

PAOLA BRUNO ARAB

Corte de rocha com jato d'água abrasivo – uma
abordagem baseada em energia

Tese apresentada à
Escola de Engenharia de São Carlos
da Universidade de São Paulo,
como parte dos requisitos para
a obtenção do título de
Doutora em Ciências

Área de concentração: Geotecnia

Orientador: Prof. Dr.
Tarcísio Barreto Celestino

São Carlos
2016

Versão corrigida

Original se encontra disponível na Unidade que aloja o Programa.

AUTORIZO A REPRODUÇÃO TOTAL OU PARCIAL DESTA TRABALHO, POR QUALQUER MEIO CONVENCIONAL OU ELETRÔNICO, PARA FINS DE ESTUDO E PESQUISA, DESDE QUE CITADA A FONTE.

Ficha catalográfica preparada pelo Serviço de Biblioteca
"Prof. Dr. Sérgio Rodrigues Fontes" da EESC/USP

A658r Arab, Paola Bruno
Rock cutting by abrasive water jet : an energy approach =
Corte de rocha com jato d'água abrasivo : uma abordagem baseada
em energia / Paola Bruno Arab ; orientador Tarcísio Barreto
Celestino -- São Carlos, 2016.

Tese (Doutorado - Programa de Pós-Graduação e Área de
Concentração em Geotecnia) - - Escola de Engenharia de São Carlos
da Universidade de São Paulo.

1. Abrasive waterjet cutting. 2. Brittleness. 3. Rock
erosion. 4. Rock fracture. 5. Specific destruction work.
6. Cutting efficiency. 7. Corte com jato d'água abrasivo.
8. Fragilidade. 9. Erosão de rochas. 10. Fraturamento de rochas.
11. Eficiência de corte. 12. Trabalho de destruição específico.
I. Título. II. Título=Corte de rocha com jato d'água abrasivo.

PAOLA BRUNO ARAB

Rock cutting by abrasive water jet – an energy approach

Thesis submitted to Escola
de Engenharia de São Carlos,
Universidade de São Paulo,
in partial satisfaction of the requirements
for the degree of
D.Sc. in Sciences

Major Field: Geotechnics

Supervisor: Prof. Dr.
Tarcísio Barreto Celestino

São Carlos
2016

AUTORIZO A REPRODUÇÃO TOTAL OU PARCIAL DESTA TRABALHO, POR QUALQUER MEIO CONVENCIONAL OU ELETRÔNICO, PARA FINS DE ESTUDO E PESQUISA, DESDE QUE CITADA A FONTE.

Ficha catalográfica preparada pelo Serviço de Biblioteca
"Prof. Dr. Sérgio Rodrigues Fontes" da EESC/USP

A658r Arab, Paola Bruno
Rock cutting by abrasive water jet : an energy approach =
Corte de rocha com jato d'água abrasivo : uma abordagem baseada
em energia / Paola Bruno Arab ; orientador Tarcísio Barreto
Celestino -- São Carlos, 2016.

Tese (Doutorado - Programa de Pós-Graduação e Área de
Concentração em Geotecnia) - - Escola de Engenharia de São Carlos
da Universidade de São Paulo.

1. Abrasive waterjet cutting. 2. Brittleness. 3. Rock
erosion. 4. Rock fracture. 5. Specific destruction work.
6. Cutting efficiency. 7. Corte com jato d'água abrasivo.
8. Fragilidade. 9. Erosão de rochas. 10. Fraturamento de rochas.
11. Eficiência de corte. 12. Trabalho de destruição específico.
I. Título. II. Título=Corte de rocha com jato d'água abrasivo.



Universidade de São Paulo

Confere com o original Janus
SVPOSGR - EESC / USP

21 / 03 / 2017

Cesar Roberto Deriasso
Chefe Administrativo de Serviço
Nº USP 204028

ATA DE DEFESA

Aluno: 18132 - 5125742 - 2 / Página 1 de 1

Ata de defesa pública de Tese do(a) Senhor(a) Paola Bruno Arab no Programa: Geotecnia, do(a) Escola de Engenharia de São Carlos da Universidade de São Paulo.

Aos 20 dias do mês de março de 2017, no(a) Sala de Seminários do SGS realizou-se a Defesa da Tese do(a) Senhor(a) Paola Bruno Arab, apresentada para a obtenção do título de Doutora intitulada:

"Corte de rocha com jato d'água abrasivo - uma abordagem baseada em energia"

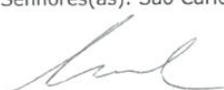
Após declarada aberta a sessão, o(a) Sr(a) Presidente passa a palavra ao candidato para exposição e a seguir aos examinadores para as devidas arguições que se desenvolvem nos termos regimentais. Em seguida, a Comissão Julgadora proclama o resultado:

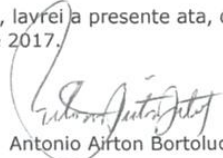
Nome dos Participantes da Banca	Função	Sigla da CPG	Resultado
Tarcisio Barreto Celestino	Presidente	EESC - USP	<u>Aprovada</u>
Cristina de Hollanda Cavalcanti Tsuha	Titular	EESC - USP	<u>Aprovada</u>
Antonio Airton Bortolucci	Suplente	EESC - USP	<u>Aprovada</u>
Antonio Carlos Artur	Suplente	IGCE-UNESP - Externo	<u>Aprovada</u>
José de Anchieta Rodrigues	Suplente	UFSCar - Externo	<u>Aprovada</u>

Resultado Final: Aprovada

Parecer da Comissão Julgadora *

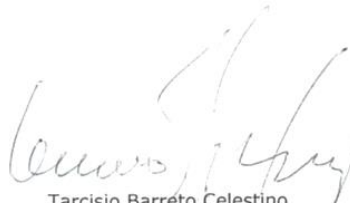
Eu, Neiva Mompean Rosalis Cardoso neiva, layrei a presente ata, que assino juntamente com os(as) Senhores(as). São Carlos, aos 20 dias do mês de março de 2017.


Cristina de Hollanda Cavalcanti Tsuha


Antonio Airton Bortolucci


Antonio Carlos Artur


José de Anchieta Rodrigues


Tarcisio Barreto Celestino
Presidente da Comissão Julgadora

* Obs: Se o candidato for reprovado por algum dos membros, o preenchimento do parecer é obrigatório.

A defesa foi homologada pela Comissão de Pós-Graduação em 21.03.2017 e, portanto, o(a) aluno(a) faz jus ao título de Doutora em Ciências obtido no Programa Geotecnia.


Presidente da Comissão de Pós-Graduação
Prof Associado Luís Fernando Costa Alberto
Presidente da CPG-EESC-USP

To those who have in some way contributed to this research, either with moral or technical support. I'm grateful for your cooperation.

ACKNOWLEDGMENTS

I would like to thank my supervisor, Prof. Dr. Tarcisio Barreto Celestino, for his professional guidance and support throughout my research.

I would also like to express my gratitude to Eng. Benedito Osvaldo de Souza, Eng. Juan Leles, Dra. Patricia Rodríguez, Prof. Dr. Antonio Airton Bortolucci, Dr. Gian Franco Napa, Eng. Oscar dos Santos Neto, José Luis Guerra and Maristela Batissaco for their technical support and for always being there to listen to me when I needed them.

Thank you to Sergio Pepino and Rogério for all of the support with the abrasive waterjet tests at ICAM Waterjet.

To Mrs. Benê for the coffee and smiles every morning and to Mrs. Damiana for always keeping the laboratory clean.

To the secretaries Álvaro Luiz Nery and Neiva Cardoso for the support.

To the postgraduate coordinator Prof. Dr. Edmundo Rogério Esquivel for the support.

To the members of my examining commission, Prof. Dr. Cristina Tsuha, Prof. Dr. Carlos Artur and Prof. Dr. José de Anchieta Rodrigues for the valuable contributions for my research.

Thank you to all of my dear colleagues from Technische Universität München, especially Prof. Kurosch Thuro, with whom I learned so much about research and life during my internship abroad. Prost!

Special thanks to my family, friends, colleagues and all those who have somehow collaborated with me so this work could be accomplished.

Thank you to my husband, Luciano Aymone Rodrigues, for his ongoing support, for understanding all of my concerns and worries, and for always being my safe haven.

Finally, I thank the CNPq for financial support throughout my PhD research and to CAPES for financial support during my doctoral interuniversity exchange.

“All things in Nature work silently. They come into being and possess nothing. They fulfil their functions and make no claim. When merit has been achieved, do not take it to yourself; for if you do not take it to yourself, it shall never be taken from you.”

Lao Tzu

ABSTRACT

ARAB, P.B. **Rock cutting by abrasive water jet – an energy approach.** Thesis (Doctorate), São Carlos Engineering School, University of São Paulo, 176 p, 2016.

Abrasive waterjet (AWJ) cutting is a versatile technique which has been effectively applied to rock cutting since the late 1980s. The complexity of the interaction between the waterjet and the rocks complicates the thorough understanding of the phenomena involved in AWJ rock cutting. On one hand, rocks are complex materials which are generated through different processes in an uncontrolled environment without human interference. On the other hand, the AWJ acts with high velocity and turbulence, complicating direct observation and the perception of details. In this respect, the present research aims to contribute to the study of AWJ cutting applied to rocks, including the analysis of qualitative and quantitative information, both of great importance regarding the study of complex materials. Concerning quantitative data, special attention is given to the investigation of the cutting efficiency, which can be analyzed by observing conditions in which the higher cutting rate is associated with the minimum energy provided by the AWJ machine per removed volume of rock. Moreover, the real efficiency can be analyzed through the investigation of the conditions in which the major part of the energy provided by the AWJ machine is used effectively for rock cutting, deducting dissipation losses. The effects of varying traverse velocity and pump pressure on cutting parameters were also investigated, in addition to the influence of rock properties on the effective energy of cutting. The effective energy was calculated based both on the specific energy and specific destruction work of the materials. With respect to the qualitative investigation, petrographic and scanning electron microscopy (SEM) analyses were conducted in order to visualize and better understand the different effects of cutting on the studied rocks. Cutting tests with a traverse velocity of 200 mm/min and a pump pressure of 400 MPa presented the most efficient rock cutting regarding both methods of efficiency analysis. Dry density and tensile strength presented fair correlations with the effective cutting energy, while the modulus ratio presented the best correlations. It was observed that brittleness plays a key role in the understanding of the phenomena involved in AWJ rock cutting.

Keywords: abrasive waterjet cutting, brittleness, rock erosion, rock fracture, specific destruction work, cutting efficiency.

RESUMO

ARAB, P.B. **Corte de rocha com jato d'água abrasivo – uma abordagem baseada em energia**. Tese (Doutorado), Escola de Engenharia de São Carlos, Universidade de São Paulo, 176 p, 2016.

O jato d'água abrasivo (AWJ) é uma técnica versátil que tem sido efetivamente aplicada ao corte de rochas desde o fim da década de 1980. A complexidade da interação entre o jato e as rochas dificulta a compreensão detalhada dos fenômenos envolvidos no corte de rochas com AWJ. Por um lado, rochas são materiais complexos gerados em ambientes sem interferência humana. Por outro lado, o AWJ age com alta velocidade e turbulência, dificultando a observação direta do procedimento. Assim, a presente tese de doutorado visa a contribuir com o estudo do corte de rochas com AWJ, incluindo análises de dados qualitativos e quantitativos, ambos de grande importância em estudos de materiais complexos. A análise quantitativa possui foco na investigação da eficiência de corte, a qual pode ser analisada por meio da observação das condições em que há a maior taxa de corte associada à mínima energia fornecida pelo AWJ por volume de rocha removido. Além disso, a eficiência real do corte pode ser analisada a partir da investigação das condições em que a maior parte da energia fornecida pelo AWJ é usada para efetivamente cortar a rocha, descontando perdas por dissipação. Os efeitos da variação da velocidade transversal de corte e da pressão da bomba nos parâmetros de corte também foram investigados, além da influência das propriedades das rochas na energia efetiva de corte. A energia efetiva de corte, denominada energia relativa de formação da ranhura (E_{KR}), foi calculada com base na energia específica e no trabalho de destruição específico dos materiais. Análises de microscopia eletrônica de varredura (SEM) e petrografia foram conduzidas para visualizar e compreender melhor os diferentes efeitos do corte nas rochas estudadas. Os testes de corte realizados com velocidade transversal do bocal de 200 mm/min e pressão da bomba de 400 MPa apresentaram as melhores eficiências de corte considerando-se ambos os métodos de análise de eficiência. Dentre as propriedades das rochas investigadas, a massa específica e a resistência à tração por compressão diametral apresentaram correlações razoáveis com E_{KR} , enquanto que o *modulus ratio* apresentou as melhores correlações. Observou-se que a ruptibilidade possui papel fundamental na compreensão dos fenômenos envolvidos no corte de rochas com AWJ.

Palavras-chave: corte com jato d'água abrasivo, fragilidade, erosão de rochas, fraturamento de rochas, eficiência de corte, trabalho de destruição específico.

LIST OF FIGURES

Figure 1 - Itaimbezinho canyon.....	5
Figure 2 - Early hydraulic mining in Idaho – U.S.A. (SUMMERS, 1995).....	6
Figure 3 - Schematic composition of the AWJ system (modified from KULEKCI, 2002).	10
Figure 4 - Scheme of a double intensifier pump (SUMMERS, 1995).	12
Figure 5 - Effect of attenuator volume on pressure fluctuation (Chalmers, 1993).	13
Figure 6 - Modern AWJ model after Vie (1983) modified from Flow Mach 2C owner’s manual.	14
Figure 7 - Parts of the abrasive metering system according to the Flow Mach 2C owner’s manual.	15
Figure 8 - Experimental results on air volume in the jet: a) plain WJ (without abrasive); b) AWJ with abrasive mass flow rate of 146 g/min (TAZIBT et al., 1996).	16
Figure 9 - Effect of the nozzle shape on the cutting performance in function of the stand-off distance (LEACH & WALKER, 1965).....	19
Figure 10 - Close-up of Venetian carnival masks on a conference table (photo courtesy Jet Edge – www.waterjets.org).....	22
Figure 11 - Sketch of the hydraulic drilling equipment developed by Summers et al. (1978).	23
Figure 12 - Main processes involved on the AWJ cutting. E_A – AWJ kinetic energy, E_{EX} – kinetic energy of the slurry that exits the cut piece, E_{DISS} - energy dissipated in the workpiece during the cutting process (modified from MOMBER & KOVACEVIC, 1998).....	27
Figure 13 - Example of a cut profile, in which it is possible to observe the areas of smooth and rough cut (quartz sandstone, Botucatu Formation).....	27
Figure 14 - Relation between absorbed fracture energy and AE_{RMS} (acoustic emission root mean square). The AE_{RMS} corresponding to different process parameters are indicated by the points (MOMBER et al., 1999).....	28
Figure 15 - General characteristics of the kerf (HASHISH, 1992).....	29
Figure 16 - Schematics of the main toughening mechanisms in cementitious composites (Momber, 2003; adapted from Shah & Ouyang, 1993).....	33
Figure 17 - Types of erosion (MOMBER, 2004).	34
Figure 18 - Amsler test machine: 1) load controller, 2) rate of sand controller, 3) engine, 4) specimen holder, 5) specimen, 6) metallic disc, 7) odometer, 8) directional brush to homogenize the distribution of sand (ABNT, 1992)	40

Figure 19 - A complete stress strain curve (HUDSON & HARRISON, 1997).....	41
Figure 20 - Stress-strain curves which describe the rock failure behavior as class I and II in uniaxial compression (modified from WAWERSIK & FAIRHURST, 1970).	42
Figure 21 - Most common methods to calculate Young’s modulus (ISRM, 1979).....	43
Figure 22 - Rock testing geometry for the Brazilian tensile test. F is the applied force and the feedback is perpendicular to it (HUDSON & HARRISON, 1997).	44
Figure 23 - Experimental set up of the END test (DONOVAN & KARFAKIS, 2004).	46
Figure 24 - Chosen rocks for the research project, from left to right: nepheline monzosyenite, syenogranite, silicified sandstone and marble.	47
Figure 25 - MTS 815 servo-controlled machine of the Rock Mechanics Laboratory at the Geotechnical Engineering Department of USP.	49
Figure 26 - Samples’ filling with the fluorescent dye resin.	50
Figure 27 - Samples after saw and polish.	50
Figure 28 - Photomicrograph of nepheline monzosyenite. Uncrossed nicols on the left, crossed nicols on the right. Ap – apatite, Bt – biotite, Hbl – hornblende, Nph – nepheline, Or – orthoclase, Aug – augite, Pl – plagioclase.	51
Figure 29 - Photomicrograph of syenogranite. Uncrossed nicols on the left, crossed nicols on the right. Bt – biotite, Or – orthoclase, Pl – plagioclase, Qz- quartz.....	53
Figure 30 - Photomicrograph of quartz sandstone. Uncrossed nicols on the left, crossed nicols on the right. Qz- quartz.....	55
Figure 31 - Photomicrograph of marble. Uncrossed nicols on the left, crossed nicols on the right. Cal – calcite, Ep – epidote, Ex – exsolution of dolomite from calcite.	56
Figure 32 - Kerf profiles of the studied rocks. The approximate depth of the kerfs is 35 mm.....	60
Figure 33 - Leica petrographic microscope with an Olympus camera attached and the image of a thin-section on the software Stream Motion 1.6.1.	61
Figure 34 - Mosaic composition scheme. The blue arrows indicate the assembly direction.	61
Figure 35 - Detail of the marble’s walls after cut, with propagation of microcracks tending to follow the orientation of cleavage planes.....	62
Figure 36 - Kerf detail on a large feldspar crystal, evincing a preferential path through its cleavage planes.	63

Figure 37 - Detail of the quartz sandstone pocket, showing potential concavities due to the impact of single abrasive particles (inside the square). The arrows indicate the removal of grains at their boundaries.	64
Figure 38 - SEM image of the nepheline monzosyenite: abrasion fatigue – a, fractures along cleavage planes – b, graded arcs – c.....	65
Figure 39 - SEM image of the syenogranite: abrasion fatigue – a, fractures along cleavage planes – b, conchoidal fractures – c, striations – d.....	66
Figure 40 - SEM image of the marble: abrasion fatigue – a, fractures along cleavage planes – b, adhering particles– c.	67
Figure 41 - SEM image of the sandstone: conchoidal fractures – a, chattermarks – b, adhering particles– c, striations – d, abrasion fatigue – e.	67
Figure 42 – Stress strain curves of the studied rocks.	80
Figure 43 – Complete stress strain curves of the studied rocks.	82
Figure 44 - AWJ machine and its main components.	87
Figure 45 - Flowchart of the AWJ operating system.	88
Figure 46 - Intensifier pump and attenuator of the cutting machine.....	89
Figure 47 - AWJ during the cutting of a granite sample.	90
Figure 48 - Detail of the top of the water tank with steel bars.....	91
Figure 49 - Grain size distribution for ICAM’s garnet abrasive material.	92
Figure 50 - Rock sample prepared to cutting tests.....	95
Figure 51 - Procedure to measure the volume of the kerfs: a) tighten specimen, b) mercury introduction.	96
Figure 52 - Example of estimation of the efficiency coefficient for $P = 400$ MPa according to the experiments described in Himmelreich (1992). In this example, $\mu=0,83$ as indicated by the blue circle.	100
Figure 53 – Variation in the removed volume of rock according to the traverse velocity.	106
Figure 54 - Variation of the specific energy of cutting according to the traverse velocity.	107
Figure 55 - Variation in the kerf generation energy according to the traverse velocity.	108
Figure 56 - Variation in the kerf generation energy according to the traverse velocity regarding W_R	109

Figure 57 - Variation in the relative kerf generation energy according to the traverse velocity.	110
Figure 58 - Variation in the relative kerf generation energy according to the traverse velocity based on W_R	111
Figure 59 – Variation in the removed volume of rock according to the pump pressure.	114
Figure 60 - Variation in the specific energy of cutting according to the pump pressure.	116
Figure 61 - Variation in the kerf generation energy according to the pump pressure.	117
Figure 62 - Variation in the kerf generation energy according to the pump pressure based on W_R	118
Figure 63 - Variation in the relative kerf generation energy according to the pump pressure.	119
Figure 64 - Variation in the relative kerf generation energy according to the pump pressure based on W_R	120
Figure 65 – Influence of the traverse velocity on the cutting rate.	122
Figure 66 – Influence of the pump pressure on the cutting rate.	123
Figure 67 - relative kerf generation energy (E_{KR}) versus Amsler abrasive wear for varying traverse velocity (mm/min). The dots from the same vertical line correspond to the same rock type.	124
Figure 68 - Relative kerf generation energy (E_{KR}) versus Amsler abrasive wear for varying pump pressure. The dots from the same vertical line correspond to the same rock type.	125
Figure 69 - Relative kerf generation energy (E_{KR}) versus Schmidt hardness for varying traverse velocity. The dots from the same vertical line correspond to the same rock type.	126
Figure 70 - Relative kerf generation energy (E_{KR}) versus Schmidt hardness for varying pump pressure. The dots from the same vertical line correspond to the same rock type.	126
Figure 71 - Relative kerf generation energy (E_{KR}) versus dry density for varying traverse velocity. The dots from the same vertical line correspond to the same rock type.	127
Figure 72 - Relative kerf generation energy (E_{KR}) versus dry density for varying pump pressure. The dots from the same vertical line correspond to the same rock type.	127
Figure 73 - Relative kerf generation energy (E_{KR}) versus degree of saturation for varying traverse velocity. The dots from the same vertical line correspond to the same rock type.	128
Figure 74 - Relative kerf generation energy (E_{KR}) versus degree of saturation for varying pump pressure. The dots from the same vertical line correspond to the same rock type.	129
Figure 75 - Relative kerf generation energy (E_{KR}) versus porosity for varying traverse velocity. The dots from the same vertical line correspond to the same rock type.	130

Figure 76 - Relative kerf generation energy (E_{KR}) versus porosity for varying pump pressure. The dots from the same vertical line correspond to the same rock type.	130
Figure 77 - Relative kerf generation energy (E_{KR}) versus tensile strength for varying traverse velocity. The dots from the same vertical line correspond to the same rock type. R^2 between 0.89 and 0.98....	131
Figure 78 - Relative kerf generation energy (E_{KR}) versus tensile strength for varying pump pressure. The dots from the same vertical line correspond to the same rock type. R^2 between 0.70 and 0.99....	132
Figure 79 - Relative kerf generation energy (E_{KR}) versus uniaxial compressive strength for varying traverse velocity. The dots from the same vertical line correspond to the same rock type. R^2 between 0.81 and 0.98.	132
Figure 80 - Relative kerf generation energy (E_{KR}) versus uniaxial compressive strength for varying pump pressure. The dots from the same vertical line correspond to the same rock type. R^2 between 0.45 and 0.92.	133
Figure 81 - Relative kerf generation energy (E_{KR}) versus brittleness for varying traverse velocity. The dots from the same vertical line correspond to the same rock type.	134
Figure 82 - Relative kerf generation energy (E_{KR}) versus brittleness for varying pump pressure. The dots from the same vertical line correspond to the same rock type.	134
Figure 83 - Relative kerf generation energy (E_{KR}) versus rock specific energy for varying traverse velocity. The dots from the same vertical line correspond to the same rock type. R^2 between 0.83 and 0.96.	135
Figure 84 - Relative kerf generation energy (E_{KR}) versus rock specific energy for varying pump pressure. The dots from the same vertical line correspond to the same rock type. R^2 between 0.63 and 0.90.	136
Figure 85 - Relative kerf generation energy (E_{KR}) versus Young's modulus for varying traverse velocity. The dots from the same vertical line correspond to the same rock type.	136
Figure 86 - Relative kerf generation energy (E_{KR}) versus Young's modulus for varying pump pressure. The dots from the same vertical line correspond to the same rock type.	137
Figure 87 - Relative kerf generation energy (E_{KR}) versus Poisson's ratio for varying traverse velocity. The dots from the same vertical line correspond to the same rock type.	138
Figure 88 - Relative kerf generation energy (E_{KR}) versus Poisson ratio for varying pump pressure. The dots from the same vertical line correspond to the same rock type.	139
Figure 89 - Relative kerf generation energy (E_{KR}) versus fracture toughness for varying traverse velocity. The dots from the same vertical line correspond to the same rock type.	140

Figure 90 - Relative kerf generation energy (E_{KR}) versus fracture toughness for varying pump pressure. The dots from the same vertical line correspond to the same rock type.	140
Figure 91 – Sandstone after uniaxial compression test.	142
Figure 92 - Marble after uniaxial compression test.	144
Figure 93 - Detail of marble sample after uniaxial compression test.....	144
Figure 94 - Granite after uniaxial compression test.	145
Figure 95 – Syenite after uniaxial compression test.	146
Figure 96 - Relative kerf generation energy (E_{KR}) versus the modulus ratio for varying traverse velocity. The dots from the same vertical line correspond to the same rock type. R^2 between 0.91 and 0.99.	147
Figure 97 - Relative kerf generation energy (E_{KR}) versus the modulus ratio for varying pump pressure. The dots from the same vertical line correspond to the same rock type. R^2 between 0.67 and 0.99. ..	147
Figure 98 - Relative kerf generation energy (E_{KRW}) versus the modulus ratio for varying traverse velocity. The dots from the same vertical line correspond to the same rock type. $R^2 = 0.37$ (100 mm/min), 0.99 (200 mm/min), 0.54 (300 mm/min) and 0.94 (400 mm/min).	148
Figure 99 - Relative kerf generation energy (E_{KRW}) versus the modulus ratio for varying pump pressure. The dots from the same vertical line correspond to the same rock type. R^2 between 0.65 and 0.99.	149
Figure 100 - Engineering classification for intact rock (DEERE & MILLER, 1966).	150
Figure 101 - Relative kerf generation energy (E_{KR}) versus the modulus ratio for varying traverse velocity. The dots from the same vertical line correspond to the same rock type. R^2 between 0.93 and 0.98.	153
Figure 102 - Relative kerf generation energy (E_{KRW}) versus the modulus ratio for varying traverse velocity. The dots from the same vertical line correspond to the same rock type. $R^2 = 0.58$ (100 mm/min), 0.87 (200 mm/min), 0.37 (300 mm/min) and 0.84 (400 mm/min).	153
Figure 103 - Relative kerf generation energy (E_{KR}) versus the modulus ratio for varying pump pressure. The dots from the same vertical line correspond to the same rock type. R^2 between 0.83 and 0.97.	154
Figure 104 - Relative kerf generation energy (E_{KRW}) versus the modulus ratio for varying pump pressure. The dots from the same vertical line correspond to the same rock type. $R^2 = 0.83$ (100 mm/min), 0.59 (200 mm/min), 0.69 (300 mm/min) and 0.79 (400 mm/min).	154

Figure 105 – Removed volume of rock (V_R) versus the modulus ratio for varying traverse velocity. The dots from the same vertical line correspond to the same rock type.	157
Figure 106 – Specific energy of cutting (SE_C) versus the modulus ratio for varying traverse velocity. The dots from the same vertical line correspond to the same rock type.	158
Figure 107 – Kerf generation energy (E_K) versus the modulus ratio for varying traverse velocity. The dots from the same vertical line correspond to the same rock type.	158
Figure 108 - Cutting rate (mm^3/s) versus the modulus ratio for varying traverse velocity. The dots from the same vertical line correspond to the same rock type.	159
Figure 109 - Removed volume of rock (V_R) versus the modulus ratio for varying pump pressure. The dots from the same vertical line correspond to the same rock type.	160
Figure 110 – Specific energy of cutting (SE_C) versus the modulus ratio for varying pump pressure. The dots from the same vertical line correspond to the same rock type.	160
Figure 111 – Kerf generation energy (E_K) versus the modulus ratio for varying pump pressure. The dots from the same vertical line correspond to the same rock type. R^2 between 0.82 and 0.98.	161
Figure 112 – Cutting rate (mm^3/s) versus the modulus ratio for varying pump pressure. The dots from the same vertical line correspond to the same rock type.	162

LIST OF TABLES

Table 1 - Effect of water treatment on water content.....	8
Table 2. Petrographic characterization summary of nepheline monzosyenite.....	58
Table 3. Petrographic characterization summary of syenogranite.	58
Table 4. Petrographic characterization summary of quartz sandstone.	59
Table 5. Petrographic characterization summary of marble.	59
Table 6 - Results of the Amsler abrasion test for the nepheline monzosyenite.	68
Table 7 - Results of the Amsler abrasion test for the syenogranite.	68
Table 8 - Results of the Amsler abrasion test for the marble.	69
Table 9 - Results of the Amsler abrasion test for the quartz sandstone.	69
Table 10 – Results of Schmidt hardness for the nepheline monzosyenite.	69
Table 11 - Results of Schmidt hardness for the syenogranite.....	70
Table 12 - Results of Schmidt hardness for the marble.	70
Table 13 - Results of Schmidt hardness for the quartz sandstone.....	71
Table 14 - Results of rock properties (ρ_d , ρ_{SAT} , S and η) for the nepheline monzosyenite.....	72
Table 15 - Results of rock properties (ρ_d , ρ_{SAT} , S and η) for the syenogranite.	72
Table 16 - Results of rock properties (ρ_d , ρ_{SAT} , S and η) for the marble.	73
Table 17 - Results of rock properties (ρ_d , ρ_{SAT} , S and η) for the quartz sandstone.	73
Table 18 - Results of the Brazilian test for the nepheline monzosyenite.	74
Table 19 - Results of the Brazilian test for the syenogranite.....	75
Table 20 - Results of the Brazilian test for the marble.....	75
Table 21 - Results of the Brazilian test for the quartz sandstone.....	75
Table 22 - Results of the <i>UCS</i> test for the nepheline monzosyenite.	76
Table 23 - Results of the <i>UCS</i> test for the syenogranite.....	76
Table 24 - Results of the <i>UCS</i> test for the marble.	77
Table 25 - Results of the <i>UCS</i> test for the quartz sandstone.	77
Table 26 - Elastic parameters for the nepheline monzosyenite.	78

Table 27 - Elastic parameters for the syenogranite.....	78
Table 28 - Elastic parameters for the marble.....	79
Table 29 - Elastic parameters for the quartz sandstone.....	79
Table 30 - Specific energy (SE_R) for the nepheline monzosyenite.....	80
Table 31 - Specific energy (SE_R) for the syenogranite.	80
Table 32 - Specific energy (SE_R) for the marble.	81
Table 33 - Specific energy (SE_R) for the quartz sandstone.	81
Table 34 - Destruction work (W_R) for the nepheline monzosyenite.....	82
Table 35 - Destruction work (W_R) for the syenogranite.	82
Table 36 - Destruction work (W_R) for the marble.	83
Table 37 - Results of fracture toughness (K_{IC}) for the nepheline monzosyenite.	83
Table 38 - Results of fracture toughness (K_{IC}) for the syenogranite.....	84
Table 39 - Results of fracture toughness (K_{IC}) for the marble.....	84
Table 40 - Results of fracture toughness (K_{IC}) for the quartz sandstone.....	84
Table 41. Summary of the properties of the rocks studied.....	85
Table 42 - Nomenclature and abbreviation of important operation parameters.	93
Table 43 - Machine parameters adopted for the tests with variation of traverse velocity.....	97
Table 44 - Machine parameters adopted for the tests with variation of pump pressure.....	97
Table 45 - Summary of the obtained data from the cutting tests varying the traverse velocity.	98
Table 46 - Summary of the obtained data from the cutting tests varying the pump pressure.	98
Table 47 - Results of V_J (WJ velocity), V_{AJ} (AWJ velocity), E_{AJ} (kinetic energy of the AWJ) and C_T (cutting time) for varying traverse velocity cutting tests.	104
Table 48 - V_R (removed volume of rock), SE_C (specific energy of cutting), E_K (kerf generation energy), E_{KW} (kerf generation energy with W_R), E_{KR} (relative kerf generation energy) and E_{KRW} (relative kerf generation energy with W_R) for traverse velocity = 100 mm/min.	104
Table 49 - V_R (removed volume of rock), SE_C (specific energy of cutting), E_K (kerf generation energy), E_{KW} (kerf generation energy with W_R), E_{KR} (relative kerf generation energy) and E_{KRW} (relative kerf generation energy with W_R) for traverse velocity = 200 mm/min.	104

Table 50 - V_R (removed volume of rock), SE_C (specific energy of cutting), E_K (kerf generation energy), E_{KW} (kerf generation energy with W_R), E_{KR} (relative kerf generation energy) and E_{KRW} (relative kerf generation energy with W_R) for traverse velocity = 300 mm/min.....	105
Table 51 - V_R (removed volume of rock), SE_C (specific energy of cutting), E_K (kerf generation energy), E_{KW} (kerf generation energy with W_R), E_{KR} (relative kerf generation energy) and E_{KRW} (relative kerf generation energy with W_R) for traverse velocity = 400 mm/min.....	105
Table 52 - Results of V_J (WJ velocity), V_{AJ} (AWJ velocity), E_{AJ} (kinetic energy of the AWJ) and C_T (cutting time) for varying pump pressure.	112
Table 53 - Results of V_R (removed volume of rock), SE_C (specific energy of cutting), E_K (kerf generation energy), E_{KW} (kerf generation energy with W_R), E_{KR} (relative kerf generation energy) and E_{KRW} (relative kerf generation energy with W_R) for pump pressure = 100 MPa.	112
Table 54 - Results of V_R (removed volume of rock), SE_C (specific energy of cutting), E_K (kerf generation energy), E_{KW} (kerf generation energy with W_R), E_{KR} (relative kerf generation energy) and E_{KRW} (relative kerf generation energy with W_R) for pump pressure = 200 MPa.	112
Table 55 - Results of V_R (removed volume of rock), SE_C (specific energy of cutting), E_K (kerf generation energy), E_{KW} (kerf generation energy with W_R), E_{KR} (relative kerf generation energy) and E_{KRW} (relative kerf generation energy with W_R) for pump pressure = 300 MPa.	113
Table 56 - Results of V_R (removed volume of rock), SE_C (specific energy of cutting), E_K (kerf generation energy), E_{KW} (kerf generation energy with W_R), E_{KR} (relative kerf generation energy) and E_{KRW} (relative kerf generation energy with W_R) for pump pressure = 400 MPa.	113
Table 57 - Classification of the studied rocks based on the classification proposal of Deere & Miller (1966).....	150
Table 58 - Equations obtained for the correlations between the relative kerf generation energy (E_{KR}) and the modulus ratio. v_T – traverse rate in mm/min, P – pump pressure in MPa, MR – modulus ratio.	155

LIST OF ACRONYMS

ABNT	Associação Brasileira de Normas Técnicas
AE	acoustic emission
AWJ	abrasive waterjet
CAD/CAM	computer-aided design/computer-aided manufacturing
CB	chevron bend test (test)
DIAJET	direct injection abrasive
EESC	Escola de Engenharia de São Carlos
END	edge notched disc wedge splitting test
ICAM	Indústria Comercializadora de Artefatos de Metal
IFSC	Instituto de Física de São Carlos
ISRM	International Society for Rock Mechanics
HDPE	high density polyethylene
PDC	Polycrystalline Diamond Compact
NBR	Normas Brasileiras
SEM	scanning electron microscopy
SP	São Paulo
SR	short rod (test)
TBM	tunnel boring machine
TUM	Technische Universität München
TS	tensile strength
UCS	uniaxial compressive strength
UNESP	Universidade Estadual Paulista “Julio de Mesquita Filho”
USP	Universidade de São Paulo
UTM	Universal Transverse Mercator coordinates
WJ	waterjet

LIST OF NOTATIONS

Latin Letters

C_T	cutting time
d_0	orifice (jewel) diameter (diâmetro da joia/orifício)
d_A	abrasive particle diameter
d_F	nozzle (focus) diameter (diâmetro do bocal/foco)
E	Young's modulus
E_{AJ}	kinetic energy of the AWJ
E_K	kerf generation energy (energia de geração da ranhura)
E_{KR}	relative kerf generation energy (energia relativa de geração da ranhura)
E_{KRW}	relative kerf generation energy based on W_R
$f(d_A)$	granulometric distribution
g	gravitational acceleration
h_S	stand-off distance (distância de afastamento)
K_{IC}	fracture toughness
m_A	abrasive mass flow rate
m_{Hg}	mass of mercury
MR	modulus ratio
m_s	mass of the syringe
m_W	water mass flow rate
P	pump pressure
P_{at}	atmospheric pressure
R^2	coefficient of determination
S	degree of saturation
SE_C	specific energy of cutting
SE_R	rock specific energy
t_E	exposure time
V	volume
V_{AJ}	abrasive waterjet velocity
V_J	waterjet velocity
V_R	removed volume of rock
v_T	traverse velocity (velocidade transversal do bocal)

v_W	velocity of the water inside the AWJ machine
W_R	specific destruction work

Greek Letters

η	porosity
μ	efficiency coefficient
ν	Poisson ratio
ρ_d	dry density
ρ_{SAT}	saturated density
ρ_w	specific mass of water
Θ	impact angle
φ	momentum transfer coefficient

SUMMARY

1. INTRODUCTION	1
1.1. OBJECTIVES	2
1.2. ORGANIZATION OF THE THESIS	3
2. LITERATURE REVIEW	5
2.1. BRIEF HISTORY AND DEVELOPMENT OF WATERJET TECHNOLOGY	5
2.2. THE BASIC MECHANISM OF THE ABRASIVE WATERJET MACHINE FOR CUTTING	10
2.2.1. The Hydraulic pump (intensifier)	11
2.2.2. The Attenuator	12
2.2.3. Abrasive Material Supply	13
2.2.4. The Nozzle	17
2.3. THE EVOLUTION OF STUDIES REGARDING WATERJETS IN ROCK CUTTING	19
2.4. PHENOMENA INVOLVED IN AWJ ROCK CUTTING	24
2.5. MECHANISMS OF ROCK DISAGGREGATION.....	30
2.6. WATERJET CUTTING MODELS BASED ON ALGEBRAIC AND REGRESSION SOLUTIONS	34
2.7. GEOTECHNICAL CHARACTERIZATION OF INTACT ROCK MATERIALS	39
2.7.1. Abrasion resistance test	39
2.7.2. Uniaxial compression test	40
2.7.3. The Brazilian tensile test	44
2.7.4. The Fracture toughness test	45
3. TESTED ROCKS AND THEIR PHYSICO-MECHANICAL PROPERTIES	47
3.1. SELECTED ROCKS.....	47
3.2. ROCKS CHARACTERIZATION METHODOLOGY	48
3.3. PETROGRAPHIC ANALYSIS.....	51
3.3.1. Nepheline Monzosyenite	51
3.3.2. Syenogranite.....	53
3.3.3. Quartz Sandstone	55
3.3.4. Marble	56
3.4. THIN-SECTION ANALYSIS OF AWJ KERFS.....	59
3.5. SCANNING ELECTRON MICROSCOPE (SEM) ANALYSIS	64
3.6. PHYSICO-MECHANICAL CHARACTERIZATION.....	68

3.6.1.	Amsler test for abrasion resistance	68
3.6.2.	Schmidt rebound hardness	69
3.6.3.	Dry density (ρ_d), saturated density (ρ_{SAT}), degree of saturation (S), porosity (η) ...	71
3.6.4.	Brazilian test for the tensile strength	74
3.6.5.	Uniaxial compressive strength from the uniaxial compression test.....	76
3.6.6.	Fracture toughness from the edge notched disc wedge splitting test (END)	83
4.	ABRASIVE WATERJET CUTTING TESTS	87
4.1.	THE ABRASIVE WATERJET MACHINE	87
4.2.	RELEVANT PARAMETERS ON AWJ CUTTING	92
4.3.	PREPARATION OF ROCK SPECIMENS FOR CUTTING TESTS.....	94
4.4.	MEASUREMENT OF THE VOLUME OF THE KERFS GENERATED BY THE AWJ MACHINE.....	95
5.	AWJ ROCK CUTTING REGARDING ENERGY CONCEPTS	99
5.1.	METHODOLOGY FOR THE CALCULATION OF THE AWJ ENERGY OF CUTTING AND THE KERF GENERATION ENERGY	99
5.2.	EFFICIENCY ANALYSIS FOR THE AWJ CUTTING TESTS.....	103
5.2.1.	Results on the cutting tests with traverse velocity variation	103
5.2.2.	Results of the cutting tests with pump pressure variation	111
5.2.3.	Efficiency analysis regarding specific energy of cutting and cutting rate	121
5.2.4.	Correlations between the relative kerf generation energy (E_{KR} and E_{KRW}) and the rock properties	123
6.	CONCLUSIONS	163
	REFERENCES.....	169

1. INTRODUCTION

Abrasive waterjet (AWJ) cutting is a versatile technique which has been effectively applied to rock cutting since the late 1980s. Phenomena involved in AWJ rock cutting are not thoroughly understood yet. This is due to the complexity of the interaction between the waterjet and the rocks, since they are composed of minerals with distinct characteristics, including peculiar textures and structures which result from their complex genesis and evolution. In contrast to most materials cut by AWJ, rocks are materials which are generated in an uncontrolled environment without human interference. Time also plays an important role in the formation of rocks. Extrusive igneous rocks like basalts may cool down and crystallize in a few hours depending on the volume of lava, while sandstones may take tens to millions of years to complete diagenesis.

The AWJ mechanism itself is not completely understood, because of the high velocity and turbulence with which it acts, complicating direct observation and the perception of details. Due to the lack of analysis and understanding of the basic phenomena involved in this technique applied to rocks, studies leading to improvement of AWJ rock cutting are not evolving properly. Furthermore, most of the literature related to the subject is produced by mechanical, mining and civil engineers, thus it is interesting to provide detailed information from a geologist's perspective, including a discussion of qualitative aspects in addition to quantitative analysis.

It is known that the AWJ action is based primarily on the impact of the abrasive material against the rock surface, which leads to the generation and propagation of cracks. Moreover, erosion occurs through friction between the abrasive material, water and rock. The combined action of impact and erosion leads to the disaggregation of the rock material in a turbulent environment. Thus, it is expected that rock characteristics have a great influence on the efficiency of cutting.

The AWJ machine operating parameters also greatly influence the efficiency of rock cutting. According to Momber & Kovacevic (1997), from a practical point of view, the applied pump pressure, traverse rate and abrasive mass flow rate are the most important for AWJ cutting.

When one speaks about “efficiency of cutting”, a discussion regarding the energy spent on the cutting process is expected, since it directly correlates with the cost per removed volume. The effective energy spent on the cutting process, i.e. the energy spent on cutting deducting losses, is also very important in order to understand the isolated phenomena which occur during the disaggregation of rocks and their relationship with rock properties and machine parameters.

Momber & Kovacevic (1999) was the first to consider that the effective energy spent on the cutting process, regarding rocklike materials such as concrete, could be determined by multiplying the removed volume by the material’s specific energy. The specific energy is equal to the area under the material’s stress strain curve when subjected to compression or tension. In fact, because of the multidisciplinary character of this theme, much confusion exists related to nomenclature. In geotechnics the area under the complete stress strain curve including the post-failure section is called *specific destruction work* (after THURO & SPAUN, 1996), while the area under the stress strain curve up to the peak strength is referred to as the *specific energy of the material*.

In this respect, the present research aims to contribute to the study of AWJ cutting applied to rocks, including the analysis of qualitative and quantitative information, both of great importance regarding the study of complex materials. Petrographic and scanning electron microscopy (SEM) analyses were conducted in order to visualize and better understand the different effects of cutting between the studied rocks. Moreover, the effect of the most important machine parameters on cutting were explored, in addition to the investigation of which rock properties exert the most influence on the effective energy spent on the cutting process. The effective energy was calculated based both on the specific energy and specific destruction work of the materials, since it was not possible to obtain the complete stress strain curve for one of the studied rocks, the sandstone.

1.1. OBJECTIVES

- Investigate and compare the effects of the AWJ on the studied rocks regarding mechanisms of cracking and erosion through petrographic and SEM analysis;

- Compare the use of the specific energy and the specific destruction work on the efficiency analysis of AWJ rock cutting;
- Analyze the effect of traverse velocity and pump pressure variations on AWJ cutting parameters, i.e. removed volume of rock, specific energy of cutting, kerf generation energy and relative kerf generation energy;
- Investigate which rock properties most influence relative kerf generation energy, which is the percentage of the total energy provided by the AWJ machine that is used for effectively cutting rocks.

1.2. ORGANIZATION OF THE THESIS

This document is arranged in the following chapters:

- Chapter 2 presents a compact literature review regarding a brief abrasive waterjet background, its evolution throughout history, operating mechanisms, applications of abrasive waterjets in geotechnics, physical phenomena involved and a brief explanation of geotechnical characterization of intact rocks;
- Chapter 3 presents the rocks studied, the petrographic analyses of intact rocks and rocks after abrasive waterjet cutting, the geotechnical characterization methodology and its results;
- Chapter 4 presents a comprehensive description of the abrasive waterjet machine used for this research, specific terms related to the machine, their definitions and the methodology and the results of the cutting tests;
- Chapter 5 covers the most important results of this research, including the analysis of the influence of traverse velocity and pump pressure on cutting parameters, always taking into account the different behavior of each type of rock. Moreover, the influence of rock properties on cutting parameters is investigated and detailed analysis regarding the most influential properties is provided;

- Chapter 6 summarizes the conclusions of this thesis and provides suggestions for future work.

2. LITERATURE REVIEW

2.1. BRIEF HISTORY AND DEVELOPMENT OF WATERJET TECHNOLOGY

Canyons are geomorphologic features characterized by deep valleys beside steep slopes and flat interfluves, which may extend for hundreds of kilometres. The Itaimbezinho is the widest canyon in Brazil, with a length of 5.800 metres and a mean depth of 600 metres (Figure 1). It is located in the State of Rio Grande do Sul, in the southern region of the country.



Figure 1 - Itaimbezinho canyon (<http://i236.photobucket.com/albums/ff11/Lbnu/rs-sc-itaimbezinho2.jpg>)

These deep features were preceded by less dissected terrains that were raised due to uplifting movements. The raise led to the emergence of a potential energy difference, allowing the beginning of intense erosion processes. The main natural agent of erosion on Earth is water. When it is in movement, like in rain or a river, water has the ability of erode and remove disaggregated soil and even the hardest rocks like granites, basalts, quartzites and amphibolites over geologic time. The Earth's actual shape is, among other things, due to the

action of water. It involves high energy systems, like alluvial fans, and low energy systems, like deltas.

Because this power of water can be seen, it can also be adapted for man's use. The first records of water being efficiently used by man date back to ancient Egypt, when the Egyptians realized that through the diversion of rivers courses, it was possible to wash soil away to procure valuable mineral deposits. Later, during the Roman Empire, power was artificially generated by storing water in specially built reservoirs on hilltops, so the water could disaggregate and carry ore downhill to facilitate its extraction (SUMMERS, 1995).

In the nineteenth century, during the industrial revolution, water was piped from rivers for the purpose of ore mining, mainly coal, in the Soviet Union and New Zealand. Shortly afterwards, the technique was adopted in the United States for the mining of gold (Figure 2), and then it spread through the world as the technique for hydraulic mining (MCMILLAN, 1962).



Figure 2 - Early hydraulic mining in Idaho – U.S.A. (SUMMERS, 1995).

One of the greatest advantages of the adoption of this technique was that it became safer for miners, since they could operate the water hoses at a safe distance from the steep ore slopes, due to the substantial availability of water power to disaggregate material. Also, in coal mines the presence of water decreased the amount of suspended particles in the air, which were – and still are – toxic and responsible for many lung diseases (SUMMERS, 1995).

When the production levels achieved with hydraulic mining became higher than with conventional techniques, research involving waterjet technologies became more common. An important improvement was discovered in the Soviet Union in attempts to disaggregate harder materials, also for mining purposes. Voitsekhovskiy (1967) developed a water cannon type of device to operate with pressures up to 700 MPa. Its nozzle design was the basis for the most efficient nozzles developed up until today.

According to Wilkins (2003), the first reports on cutting materials with waterjets date from the 1950s. In contrast with the natural processes related to alluvial fans and deltas, the waterjet cutting technique involves the transformation of pressurized water inside a cutting system into a high velocity waterjet where it exits the nozzle. One of the first reports about the capacity of waterjets to cut materials is from Dr. Norman Franz, a forestry engineer who experimented with the cutting of trees with a high velocity stream of water. He made it possible to cut trees with acceptable precision, but with great difficulty due to the necessary maintenance of a steady high pressure for long periods of time.

In the 1970s, the waterjet technique started to be modified to be used in the cleaning industry. It turned into a pistol waterjet with low flow and high pressure, which could be handled by only one working man. Its efficiency was high and it had the advantage of not using chemicals awhile sterilizing surfaces, since hot water could be used. Because of the many advantages presented, the technique became popular and grew quickly. According to Webster & Johns (2008) it also started to be applied to the cleaning of huge monuments, like the Christ the Redeemer statue in Rio de Janeiro in 1980, the granitic base of the Statue of Liberty in 1993 and Mount Rushmore in 2005.

With the introduction of waterjet systems with lower flow, large volumes of water were also gradually reduced in hydraulic mining applications, in order to reduce costs and

environmental problems. Investments were focused on new technologies to develop high capacity pumps (SUMMERS, 1995).

Concurrently in the 1970s, industrial automation began with the support and funding of several industries. As stated by Johnston (1986), the first cutting machines were installed in the United States and with its continuous use, the first operation issue emerged: premature wear of pieces of the equipment due to the quality of water. Regarding the quality of water, as it naturally presents solubilized ions, their precipitation was observed in the nozzle, which necessitated routine maintenance. In addition, the early wear of the system's valves were also attributed to precipitation. Thus, research regarding water treatment became a priority. Nowadays, the main water treatment processes are reverse osmosis and deionization, because they are the most effective options. However, in the past, softening was very common. Table 1 shows the effect of the three water treatments on tap water.

Table 1 - Effect of water treatment on water content.

	Tap water	Softened water	Reverse osmosis water	De-ionized
Alkalinity	324 mg/l	364	10	<1
Calcium	23,7 mg/l	<0,01	0,14	<0,01
Chloride	38 mg/l	56	<1	<1
Hardness	140 mg/l	<1	<1	<1
Magnesium	15,4 mg/l	<1	<0,01	<0,01
pH	7,12	7,83	6,87	6,96
Sodium	212 mg/l	241	4,02	<0,01
Sulfate	158 mg/l	163	<1	<1
Total dissolved solids	637 mg/l	652	14	<1

Hashish et al. (1987) developed one of the most important improvements concerning waterjet technology by adding an abrasive material to the waterjet, which made it possible to

cut very hard materials in an efficient way. The entire mechanism of waterjet cutting had to be adapted to support the new technology. As the abrasive waterjet could cut very hard materials, a water tank also had to be created to absorb the impact of the jet; otherwise it would cut through the floor as well. In addition, cutting materials on the top of the water tank allowed for the collection of abrasive materials, which could be reused.

From then on, it was possible to cut metals, ceramic materials and rocks, with the advantage of not damaging the areas outside the action of the jet, comparative to other conventional cutting techniques. Another advantage was the possibility of cutting with low temperatures, avoiding thermal stress. Ohadi et al. (1992) performed tests to evaluate the thermal energy distribution in specimens cut with an abrasive waterjet. They measured the temperature at several locations and observed a maximum temperature of $T - T_0 = 75^\circ\text{C}$, where T is the measured temperature and T_0 is the room temperature.

Concerning abrasive material automation issues, the AWJ produces a high volume of waste which has to be directed to a landfill for disposal. Babu & Chetty (2002) state that nearly 75% of the total operating cost of AWJ is due to the cost of abrasive material. They claim that by recycling the abrasive material, the process is more economical, effective and ecologically friendly. In their research on garnet abrasive particles, they compared the efficiency of commercial and recycled abrasive material. In general, they conclude that the reuse of abrasive materials, by blending it with new abrasive materials in a proportion of 40 to 60% of reused material, provides satisfactory results.

Despite the great advances in abrasive waterjet technology, the fragility of the equipment and its sensitivity to the quality of water still restricted its use for many geotechnics purposes. Building construction involves being in contact with dust and micro particles of soils and rocks, which may damage the cutting head of the waterjet machine. Therefore, this is one of the reasons why the technology has evolved faster in other waterjet application fields.

Currently in geotechnics, the abrasive waterjet technique is being used more for the cutting of building stones, while the plain waterjet, which is done without abrasive materials, is applied to the hydrodemolition of concrete, hydraulic mining and drilling.

2.2. THE BASIC MECHANISM OF THE ABRASIVE WATERJET MACHINE FOR CUTTING

High energy waterjets are mainly divided into plain waterjets (WJ) and abrasive waterjets (AWJ). The basic difference between them is the addition of abrasive material in order to increase the jet efficiency in abrasive waterjets. The first one has a more restricted application, which is limited by the cutting of soft materials such as rubber, food, glass fibers and some types of polymers. The second one may cut several resistant materials such as metals, ceramic, concrete, rocks and other composite materials used in building construction (KULEKCI, 2002).

The conventional AWJ cutting system is similar to the other basic types of jet. What changes is that the AWJ system presents an abrasive supply tank connected to the cutting head. Figure 3 shows its typical schematic composition.

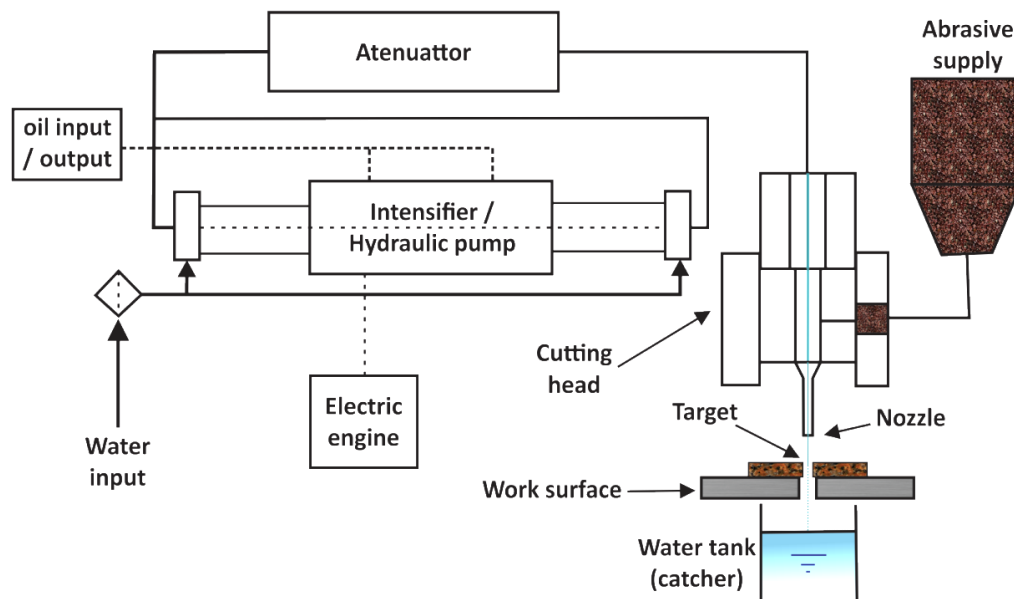


Figure 3 - Schematic composition of the AWJ system (modified from KULEKCI, 2002).

Basically, the system has an electric engine that provides energy to a hydraulic pump called an intensifier pump. Afterwards, the water passes through the attenuator so possible pressure fluctuations due to amplification will diminish. The water is then conducted to the cutting head, where it is constricted to turn it into a fine jet. It is then mixed with the abrasive

material supplied by the abrasive tank. Finally, both water and abrasive materials have some time to homogenize inside the nozzle and come out from the machine as a high velocity AWJ. After cutting through the target material, the jet impact can be absorbed by the water tank, and both water and abrasive materials may be reused after treatment. The main parts of the machine will be detailed as follows.

It is important to mention that many authors refer to the waterjet as a high pressure waterjet. In fact, this is an errored term which was spread through the scientific community. While inside the machine, the water is indeed pressurized. When it leaves the nozzle as a waterjet, the potential energy turns into kinetic energy, thus generating a high velocity or high energy waterjet. The pressure associated with the waterjet is then the ambient pressure, lower than the water pressure inside the machine. In recent years, following the work of Kovacevic et al. (1997) which presented the term “high velocity waterjet”, many authors began to use it or the term “high energy waterjet”. Therefore, the term “high pressure waterjet” and “jet pressure” is still used in this literature review due to the original terms used in several works from the past.

2.2.1. The Hydraulic pump (intensifier)

The waterjet industry deals with two main types of hydraulic pumps. The cutting of soft materials does not need high pressures, so in this case the use of a triplex pump is more common. It presents a set of three pistons which pump water from its repeated movement, made by a crankshaft. However, when higher pressures are needed, this system is not satisfactory. In this case, hydraulic pumps, called intensifier pumps, which amplify the incoming water pressure are desirable (SUMMERS, 1995).

In an ordinary intensifier pump, there is no crankshaft to move the piston. Thus, pressure is applied by oil at 20 to 35 MPa, displacing the piston in order to push the water contained inside a reservoir to the output valve. As oil can withstand more pressure than a crankshaft, water with higher pressure can be delivered to the cutting system similar to a triplex pump system (SINGH & BENSON, 1992). For the intensifier to give a quasi-continuous flow, the units are generally made double-acting, as shown in Figure 4.

The mechanism is based on a two circuit path, in which distilled water passes through one circuit while hydraulic fluid passes through the other one. The pressure applied by the hydraulic fluid moves the plunger in a way that its displacement may exert pressure against the distilled water, so it may leave the intensifier with a higher pressure. When the plunger goes the opposite way, also due to hydraulic fluid pressure, it creates suction so more distilled water can be stored to be further pressurized.

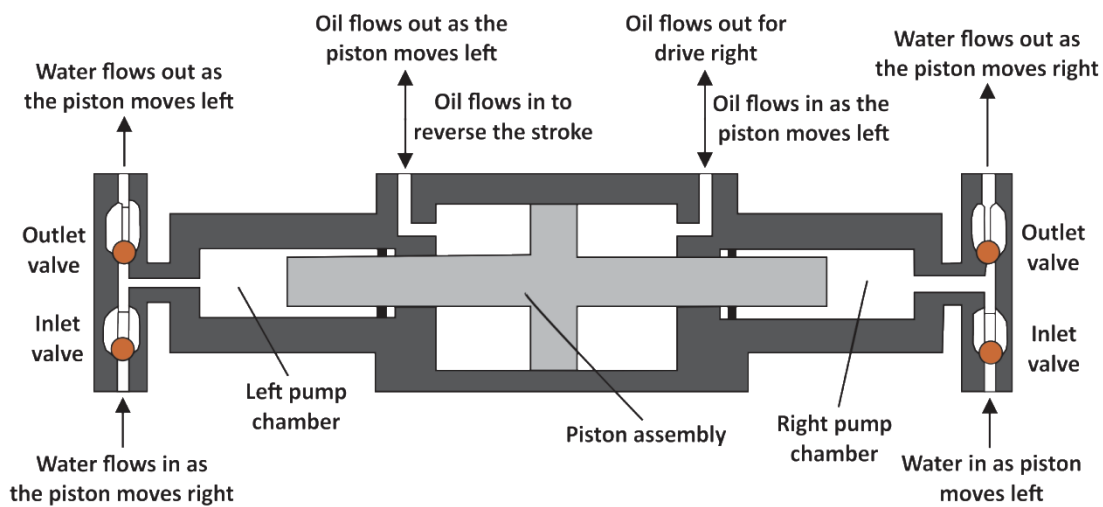


Figure 4 - Scheme of a double intensifier pump (SUMMERS, 1995).

2.2.2. The Attenuator

According to Chalmers (1993), pressure fluctuations must be avoided to ensure that the system presents the best performance possible. Excessive fluctuations may lead to early wear, fatigue or failure of components like pipes, valves and orifices. It may also affect the consistency of the jet and the quality of the cuts. Thus, the attenuator, which is simply a pressure valve set up in line with the intensifier output, uses the compressibility of water, acting like a spring, to dampen the output fluctuation. Additionally, it presents cartridge filters inside to capture loose particles that may be in the water. These particulates are generated upstream such as from seals or check valves. In the presence of an attenuator, the use of in-line filters is unnecessary.

Figure 5 presents the effect of attenuator volume on the percent pressure change considering a 359 MPa intensifier and a 0, 30 mm orifice. With an attenuator of 1.200 mL, a reduction of more than 40% on fluctuations is observed.

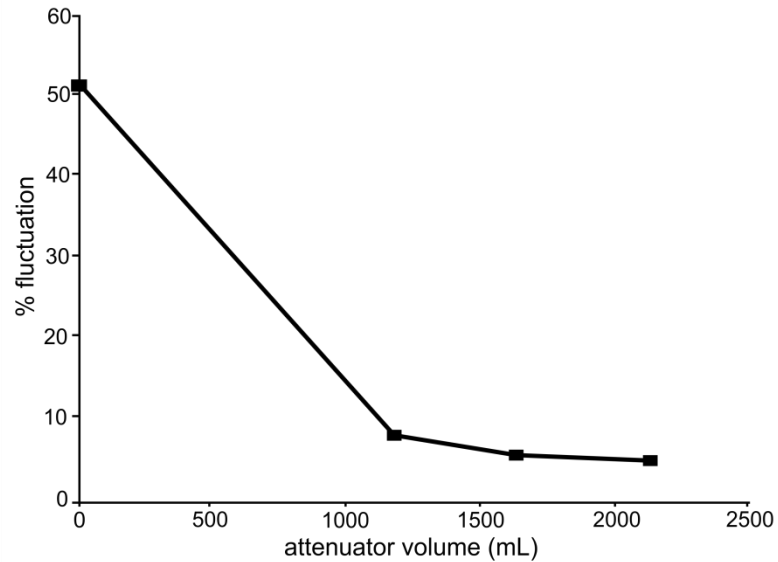


Figure 5 - Effect of attenuator volume on pressure fluctuation (Chalmers, 1993).

2.2.3. Abrasive Material Supply

At the beginning, the addition of abrasive materials in the cutting process was done through the introduction of a mixture of water and abrasive materials in the machine. The problem was that this technique led to the exaggerated wear of pieces, valves, pipes and orifices, demanding a big investment in maintenance. Therefore, companies like the pioneers Flow Industries Inc. and Fluidyne Corp. started to investigate new methods for abrasive material input.

The first detailed research on new AWJ compositions was presented by Vie (1983). The author describes the introduction of abrasive materials just after the pressurized water becomes a high energy waterjet, entering the system through suction. Through this method, the equipment wear was restricted only to the nozzle. Because of its success, the innovation was adopted on a global level.

Figure 6 shows the main components of the AWJ suction system that is part of the cutting head. Just after the pressurized water passes through the orifice, it becomes a high velocity WJ. Because of its velocity, it creates a vacuum environment inside the cutting head's body which allows the suction of the abrasive. The quantity of abrasive corresponds to a pre-defined flow through the distribution line. Afterwards, water and abrasive are homogenized inside the mixing tube which is secured by a collet and a retaining nut. The orifice has the shape of a cone in order to align it in relation to the mixing tube. At the center of the orifice, there is a little diamond or corundum disc with a smaller outlet which is called jewel. These materials are chosen due to their higher wear resistance.

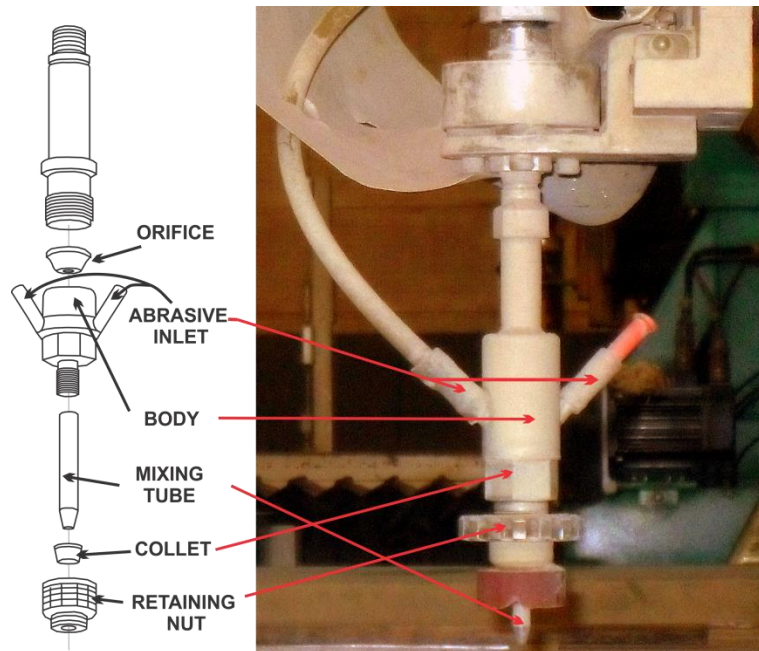


Figure 6 - Modern AWJ model after Vie (1983) modified from Flow Mach 2C owner's manual.

An important component of the AWJ is the abrasive metering system, which acts as abrasive metering and air isolator (Figure 7). According to the Flow Mach 2C owner's manual, abrasive and air, which are in the abrasive supply, enter the system through a lateral inlet port. The abrasive accumulates on the top of the air isolator and drops through an orifice at its center, passing through the seating surface and the rubber stopper, finally reaching the metering disc. During the use of the equipment, the rubber stopper is kept open and when the machine is turned off, the rubber stopper closes in order to retain the abrasive.

The control of the abrasive rate is done by the diameter of the metering disc, since the material moves by gravity. Finally, the diverter is responsible for fixing the metering disc and directing the abrasive to the water. Regarding the air inside the system, after it enters the valve, it escapes through the air cylinder and the vent.

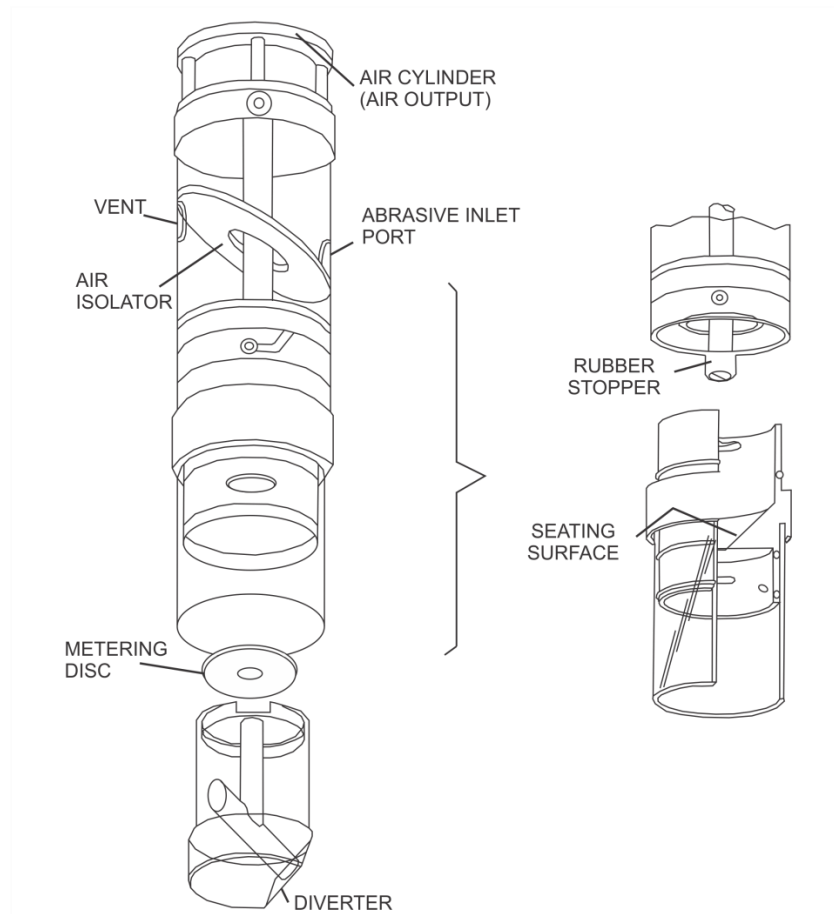


Figure 7 - Parts of the abrasive metering system according to the Flow Mach 2C owner's manual.

Tazibt et al. (1996) present data on the contribution of air in WJ and AWJ, the latter considering an abrasive suction system. According to the authors, air makes the fluid jet density low but improves the homogenizing process between water and abrasive. Figure 8 shows experimental results on air volume in the jet, evincing that the air occupies more than 90% of the volume of both WJ and AWJ. The authors state that regarding the composition by volume of the AWJ, abrasives represent 1%, water 4% and air 95%.

In addition, according to Momber & Kovacevic (1998) a typical phase distribution of an AWJ considering its mass composition is 3% air, 23% abrasive and 74% water.

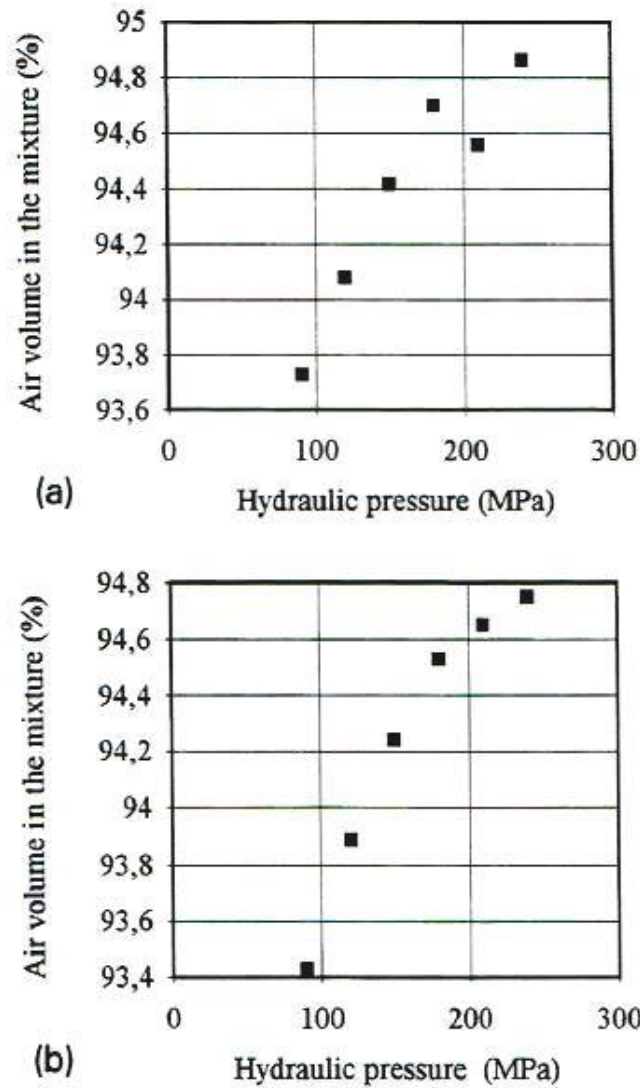


Figure 8 - Experimental results on air volume in the jet: a) plain WJ (without abrasive); b) AWJ with abrasive mass flow rate of 146 g/min (TAZIBT et al., 1996).

Ohman (1993) discusses many aspects related to abrasive material which influence the process of AWJ cutting. Abrasive material consisting of garnet has many advantages, such as high hardness levels and sharp edges due to its habit and high density. The author claims that particle size also influences the cut, and through several experiments, it was observed that an ideal size is 80 mesh with a good particle size distribution. The use of an adequate abrasive

material allows a better quality of cut, better finish, working with a less abrasive material, lower pressure and with less wear of the nozzle.

Vasek et al. (1993) studied the efficiency of cutting with different types of garnet, in order to analyse the influence of its mineralogy. Experiments were done with pirope, almandine, spessartite, grossular, andradite and uvarovite. The authors observed that, even though all of the minerals present similar properties, the almandine variety showed to be more efficient, because it presented more resistance to the impact against the target, causing less fracturing.

Fairhurst et al. (1986) developed an alternative to the mechanism of abrasive material addition to the waterjet known as direct injection abrasive – DIAJET. In this technique, the abrasive material is suspended in a polymer solution in the tank, which is pressurised through a conventional high-pressure pump. The slurry is then introduced directly inside the nozzle. Although the system provides good quality cuts, it requires periodic mixing and filling of the tank with abrasive and polymeric additives. It also requires higher water flow rates and high abrasive flow rates (KOLLÉ, 1999).

The use of garnet as the abrasive material for AWJ cutting has been the most common material since the development of this technique, though other materials such as olivine ($(\text{Mg}^{+2}, \text{Fe}^{+2})_2\text{SiO}_4$) and aluminium oxide (Al_2O_3) may be used. According to the brochure “Pressure = Productivity” by Dr. Alex Chillman from Flow International Corporation, olivine, a magnesium-iron silicate, cuts hard materials almost 50% slower, although it extends tool life. Thus, it is economical only for cutting very soft materials. On the other hand, harder than garnet there is the aluminium oxide, which cuts quickly through hard and very hard materials, but diminishes tool life.

2.2.4. The Nozzle

A successful WJ system takes into account the nozzle design, which is a key element for an optimum machine performance, since it drives the jet to the surface of the target. A good nozzle design not only influences how the target is cut, but also how it wears over time, thus the best models tend to present a lower wear rate than others.

According to Badgujar & Rathi (2014) the WJ and AWJ nozzle does not depend on the material to be cut. This is an advantage when compared to conventional mechanical machining, where the tool may have to be changed in order to satisfy the optimum conditions of cutting for each type of material. Another advantage is that the nozzle wear, the cutting head and the high pressure water components tend to be constant overtime, without changes when machining different materials.

Concurrently with the Voitsekhovsky studies on water cannon systems (which started many years before his 1967 paper), several researchers investigated improvements on nozzle design. Leach & Walker (1965) conducted a thorough study on the comparison of more than ten different types of nozzles, including the Rouse et al. (1952) design and the Shavlovskii (1972) design. The Rouse nozzle was designed for firefighting applications, which requires only lower pressures. The Shavlovskii nozzle, with its simple shape, revealed itself as the best option considering cost, performance and ease of manufacturing. Figure 9 shows the performance related to pressure, considering five of the nozzle types tested in Leach & Walker's work.

Presently, the Shavlovskii design is the most used in the world. Little has changed considering the basic nozzle shape. Most recent upgrades on WJ and AWJ machines are more related to pump and abrasive material input technologies, but the machine used in this research is from a traditional model, so further technologies will not be discussed. More details on the equipment are covered on Chapter 4.

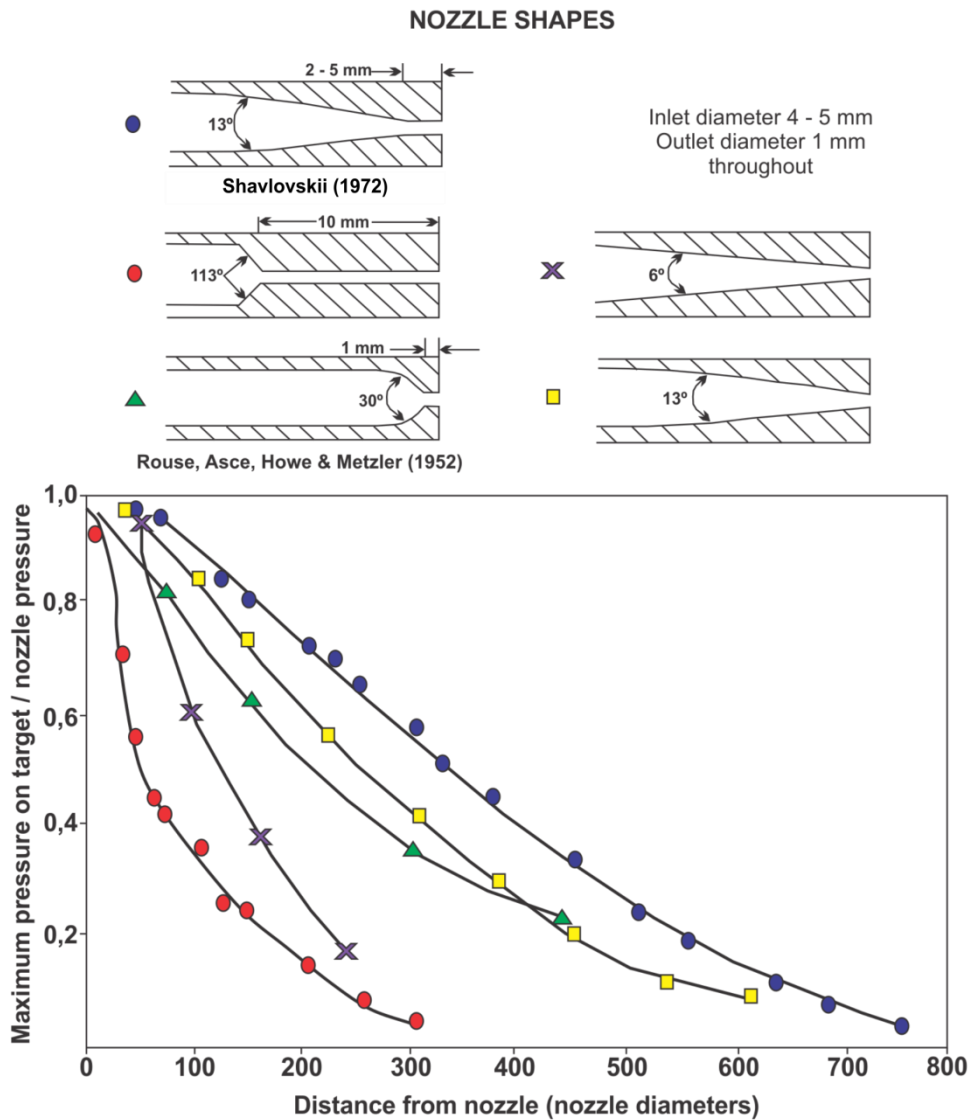


Figure 9 - Effect of the nozzle shape on the cutting performance in function of the stand-off distance (LEACH & WALKER, 1965).

2.3. THE EVOLUTION OF STUDIES REGARDING WATERJETS IN ROCK CUTTING

As previously mentioned, the application of waterjets in geotechnics started with the disaggregation of soils and soft rocks through hydraulic mining. With the refinement and spreading of the technique through the years, industrial automation was possible, and more investment in research was done.

Since the 1960s, research on WJ and AWJ applied to rock cutting has increased significantly. Experimental studies concerning the influence of equipment parameters and rock properties on cutting were the main focus (FARMER & ATTEWELL, 1964; SUMMERS, 1972; HARRIS & MELLOR, 1974; HURLBURT et al., 1975; REHBINDER, 1977; BORTOLUSSI et al., 1988; MOMBER & KOVACEVIC, 1997; SUSUZLU et al., 2004; KOLAHAN & KHAJAVI, 2009; AYDIN et al., 2013) and they still are, because of the complexity of dealing with natural materials.

The cutting of soft rocks revealed to be promising since the beginning, principally after the advent of abrasive material input (SUMMERS, 1972; SAVANICK, 1983; MIRANDA et al., 1993; MOMBER & KOVACEVIC, 1997). However, the cutting of hard rocks is still challenging, because when compared to other conventional methods, its costs are not always competitive (SUMMERS, 1995).

At present, the hard rock field in which the AWJ is primarily used is the cutting and finishing of blocks and plates of building stones. Besides more efficiency and safety than using saws and drills, the AWJ technique allows lesser material loss and the final surface of the cut is more homogeneous, presenting a better finishing (BORTOLUSSI et al., 1987; LAUAND et al., 2001). Dr. Augusto Bortolussi and Dr. David Summers were pioneers in the study of waterjets applied to quarrying of dimension stones.

Raether et al. (1983) conducted one of the first experiments completely focused on rock excavation in quarries using waterjets, motivated by the fact that conventional methods were becoming increasingly expensive in real and environmental terms. From their tests, the authors claimed that the new technology promised not only the final finish of granites, but also to isolate individual blocks still in quarries.

Bortolussi et al. (1988) analyzed the way in which the waterjets penetrate granites and it was concluded that the technique was commercially practical. A cutting rate prediction was established from the cutting of blocks to reproduce the megalith Stonehenge on the University of Missouri-Rolla campus.

Agus et al. (1991) studied the application of high velocity oscillating waterjets in cutting in order to obtain deeper kerfs in granites. They concluded that the technology is

feasible as long as enough power is applied. Also, it was observed that moderate pressures (100 MPa) were enough to achieve deeper kerfs when using adequate flow rates.

Wyatt & Peterson (1997) developed an important improvement in the waterjet machines used in quarries in order to cut very hard granites. The new equipment, the Ned-Jet-2000, cut faster, improved the automation of the machine and promoted much better recovery, and reduced the amount of waste. For those reasons, net recovery increased by 60% in sellable stone.

Carrino et al. (2001) carried out an interesting study concerning the use of waterjets on marbles to cut free-form profiles for decorative mosaic paving. It was concluded that the technique was more accurate than the traditional technology, and it was shown that it decreased more than 50% of the costs. Currently, waterjet technology is the most used for this type of work, due to its success. Figure 10 shows an example of mosaic design on rocks.

In Brazil, studies concerning the use of waterjets to cut rock materials only emerged in the late 1990s, involving researchers from the Department of Mining and Oil Engineering (Departamento de Engenharia de Minas e Petróleo) from the Polytechnic School at the University of Sao Paulo. Cortés (2003) studied the cut of Brazilian granites and marbles with high pressure waterjets, evaluating the operation costs and the quality of their finishing. In Cortés' thesis and Cortés et al. (2003), the authors claimed that monomineralic rocks presented surface quality similar to metals, and plurimineralic rocks' surface quality is influenced by the different sizes of crystals, which result in rougher planes.

The improvement in performance conditions to cut rocks led to the first conceptions of drilling with waterjets. The first drill bit design was completely hydraulic, which was described by Acheson et al. (1971), consisted of a non-rotating body with several small tilted nozzles on its tip, with the use of fluid and abrasive materials for drilling. The work exerted by the jets allowed the free rotation of the composition. The biggest problem with this design was the excessive wear of the equipment pieces due to the abrasive material flow. Also, the action of several waterjets together led to the necessity to replace the nozzle periodically. All of this imposed a much higher cost for maintenance, making this design inadequate in practice.



Figure 10 - Close-up of Venetian carnival masks on a conference table (photo courtesy Jet Edge – www.waterjets.org).

An alternative and more efficient solution was proposed by Summers et al. (1978). The new design did not use abrasive materials and, like the Acheson's model, it worked with a larger volume of water of 200 m/s. Summers' model worked with a lesser flow at 300 m/s, facilitating the propagation of cracks in rocks. Instead of several nozzles, there were only two, one in axial position, and the other one at 30 degrees from the first. The nozzles were attached to a rotating tip to cut the rock along the main axis of the machine, producing a cone-shaped cut due to the nozzles' inclination (Figure 11). Summers (1995) claims that the new model increased the penetration rate of soft rocks up to two orders of magnitude.

In the 1980s hybrid drill bits started to be developed, involving both mechanical and hydraulic compositions. Bonge & Wang (1981) developed a mechanical carbide drill with waterjets attached to its axis. The combination permitted a significant reduction of torque and thrust during drilling, besides decreasing the bit wear.

In the late 1980s a new concept of drill bit emerged, with an advanced technology which allowed a higher durability. The Polycrystalline Diamond Compact (PDC) has an operating life 200 to 600 times greater than the carbide drills. Even so, as the surface of diamonds is sensitive to high temperatures, the use of waterjets as an aid is beneficial, since it decreases the stresses and the temperature involved in the cutting of hard rocks (SUNDAE & CANTRELL, 1992).

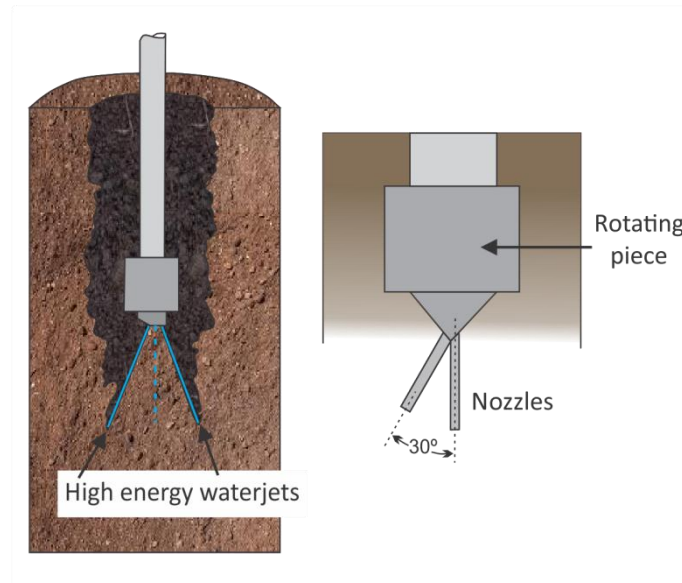


Figure 11 - Sketch of the hydraulic drilling equipment developed by Summers et al. (1978).

Even before the appearance of hybrid drills, research related to the attachment of waterjets to tunnel boring machines (TBM) being developed from the beginning of the 1970s. Hoshino et al. (1974) designed a TBM assisted by waterjets for excavations of large diameters. Their research indicated that the use of disc cutters and plain waterjets of approximately 0.3 mm in diameter at 4.000 bar pressure could increase the advance rate up to four times. The effect of the position of the jets on the TBM was also evaluated and the best efficiency was obtained with them positioned close to the face of the bit and directed to cut close to the gage of the hole.

Baumann & Henneke (1980) tested a TBM with waterjets and long-chain polymers added to the water, resulting in a 70% increase in cutting depth when compared to a system without the addition of polymers. The authors indicated that the assistance of waterjets promotes many advantages, such as the lower thrust requirement, the development of less bulky machines with easier operation, the reduction of disc cutters wear, more efficient dust suppression and the elimination of sparks which are normally generated by the contact between rocks and disc cutters.

Several studies are found in the literature regarding the performance of TBM assisted by waterjets, including different diameters, shapes, disc cutters and nozzle positions (FENN et al., 1985; KOUZMICH & MERZLIAKOV, 1986; HOOD et al., 1991; WILSON et al., 1997; CICCUCI & GROSSO, 2014).

2.4. PHENOMENA INVOLVED IN AWJ ROCK CUTTING

In brittle materials, like many rocks, erosion occurs through the propagation and intersection of cracks produced by impacting particles. As stated by Hucka & Das (1974) brittle materials can be defined as materials with: low values of elongation, fracture failure, formation of fines, high ratio of compressive to tensile strength, high resilience, high angle of internal friction and formation of cracks in indentation. Moreover, brittleness is a property of materials which rupture or fracture with little or no plastic flow. Since these materials present a tendency for microcracking, they are considered to be hard to machine by conventional tools (MOMBER et al., 1999).

In this context, as AWJs are formed by water and abrasive material, the cutting mechanism is called hydro-abrasive wear (FINNIE, 1995). Nevertheless, according to the tribology nomenclature, Ali & Wang (2011) claim that when material removal is favorable, the correct term is machining; when material removal is unfavorable, then it is called wear (e.g. damage in pipes carrying abrasive slurry). The authors also draw attention to the use of the terms erosion and abrasion. When a jet removes material from a target surface by a near-normal angle impact, it is abrasion. When the angle is near-tangent, then it is erosion. Much confusion exists in WJ research, since it is a multidisciplinary area where manufacturing, mechanical, civil and mining engineers, besides geologists work with the same subjects. Literature still does not present many detailed information on how varied rocks are disaggregated by WJ and AWJ. Most of the researches have focused on glass, ceramic and concrete materials.

According to several authors (SUMMERS, 1995; REHBINDER, 1980; CROW, 1974), the compressive force exerted by a jet creates a stress concentration which generates the nucleation of microcracks in locations as cleavage planes, pores, faults in crystals and boundaries between crystals and between crystals and the matrix. When the exerted force exceeds the tensile strength of the rock, it is observed the propagation of cracks under quasi-static regime.

Because of the high velocity of the waterjet, there is sufficient delivery of energy so that the impact leads to the nucleation and propagation of cracks. The velocity acquired by the jet is due to the pressurized water kept inside the machine, which stores potential energy.

When it is released through the jewel, the potential energy is converted into kinetic energy, producing a high velocity waterjet (ALI & WANG, 2011).

Figure 12 shows the main processes involved in the cutting of brittle materials with abrasive waterjets. The depth of cut (h) is the depth where the rock surface is smooth after the cut, while the maximum depth (h_{MAX}) is the total depth penetrated by the jet, considering both the smooth and the rough cut. Figure 13 gives an example of the typical textures presented by brittle materials when cut with WJ. They involve a flat surface on the smooth cut region and an undulated surface with striation marks on the rough cut region. Hashish (1988) proposed a division of the cut surface according to these textures. The smooth region was named cutting wear and the rough region was named deformation wear, based on the occurrence of two different material removal mechanisms. However, the explanation of the different textures observed on the cut surface is still controversial.

Raju & Ramulu (1994) suggest that the striation marks are produced when the kinetic energy of the slurry which exits the cut piece falls below a certain critical kinetic energy. In contrast, Chao & Geskin (1993) state that the striations are a result of disturbances such as machine vibrations due to the unsteady removal mechanism, which is a characteristic of WJ and AWJ cutting systems.

Hashish (1992) claims that among the theories which discuss the surface roughness generated by WJ and AWJ cutting, some hypotheses can be made: waviness may be a result inherent to the cutting process itself, in which case, all process parameters will quantitatively affect the geometry; it may also be due to dynamic parameter fluctuations (or unsteadiness) as in pressure, abrasive flow rate and traverse rate.

Gärdek & Boubker (2015) state that roughness can be reduced when higher pump pressures and higher abrasive mass flow rates are applied. In relation to pump pressure, higher kinetic energy is delivered when it is increased, thus the cutting becomes more efficient resulting in a smoother surface. Regarding the abrasive mass flow rate, it is thought that with a greater abrasive supply more brittle abrasive particles break into smaller sharp pieces when introduced into the turbulent environment of the high velocity AWJ, contributing with a better finish of the walls' surfaces.

According to Zeng & Kim (1992), direct impact of the AWJ at high angles only occurs at the top of the target material, and below where there are secondary and tertiary impacts of the deflected jet. Thus, the entire cutting front is impacted by the AWJ at low incidence angles.

Because of the impact of the jet's abrasive particles on the surface of the target, the rock is fragmented and debris is produced on the upper part of the cut, mainly as a result of the coalescence of cracks. Below this region, there is a cutting front, where a damping zone is generated, in other words, an area subjected to an impact of lesser intensity in the period in which the jet has not removed the debris yet. It is also in this area that the erosion/abrasion processes starts acting as a removal component. The damping occurs due to the accumulation of water, abrasive and debris inside the kerf (MOMBER & KOVACEVIC, 1998).

Still, according to the model proposed by Momber & Kovacevic (1998) in Figure 12, there is heat generation on the cutting front, which is due to the friction between the abrasive particles and the target. It also occurs due to the plastic deformation during the rock material removal. Finally, the jet loses kinetic energy with the depth of the cut, so it tends to become horizontal because it does not have enough energy to penetrate the material further. This threshold energy is reached when $h=h_{MAX}$. The energy dissipated (E_{DISS}) in the workpiece during the cutting process is found in the difference between the kinetic energy (E_A) of the jet (input energy) and the kinetic energy of the slurry that exits the cut piece (E_{EX} , the exit energy).

Momber & Kovacevic (1999) claims that the disaggregation process is characterized by a critical process parameter called the threshold pressure. The disaggregation of a material only initiates after the threshold pressure is exceeded. The authors assume that the threshold pressure characterizes the exit energy of the high speed slurry when the maximum depth of cut is reached, i.e. when the slurry leaves the material because it is not able to remove more material.

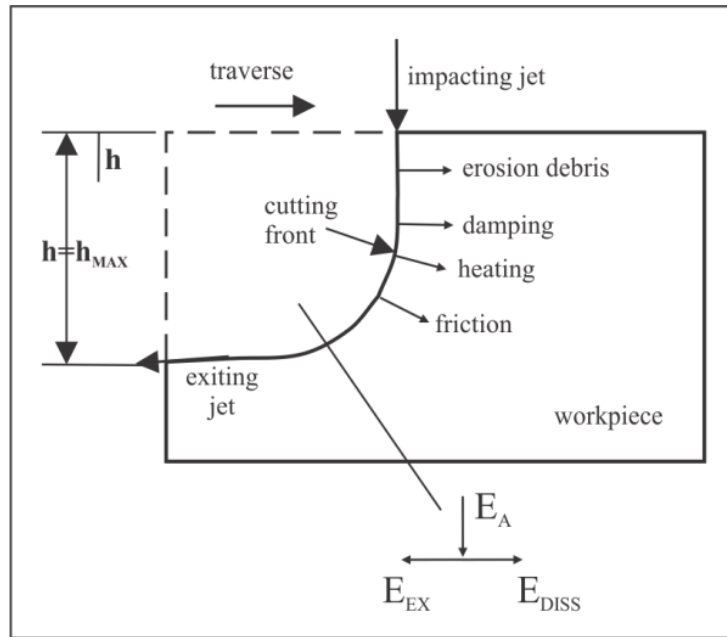


Figure 12 - Main processes involved on the AWJ cutting. E_A – AWJ kinetic energy, E_{EX} – kinetic energy of the slurry that exits the cut piece, E_{DISS} - energy dissipated in the workpiece during the cutting process (modified from MOMBBER & KOVACEVIC, 1998).

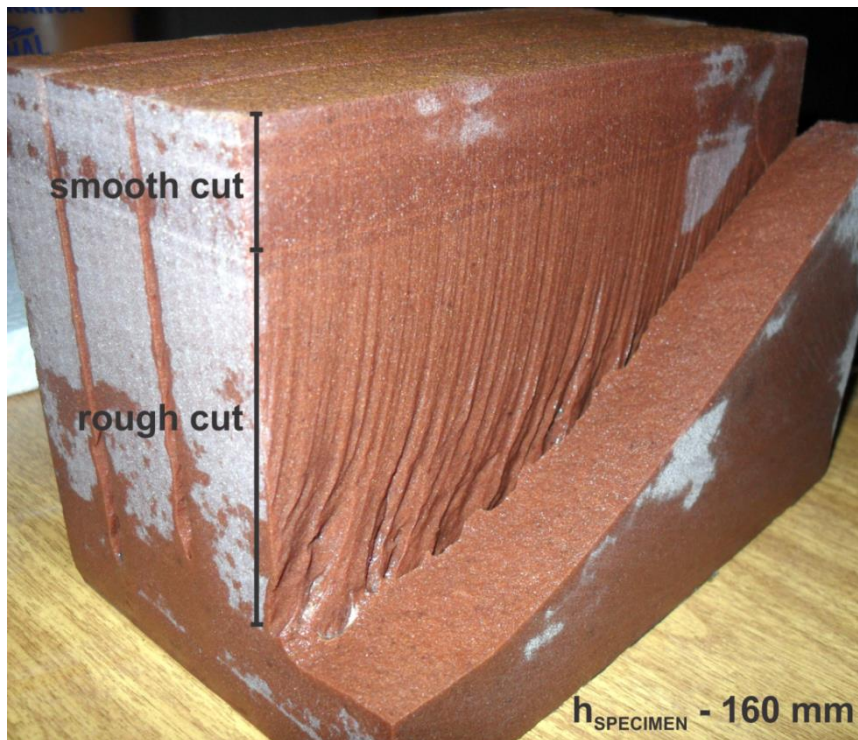


Figure 13 - Example of a cut profile, in which it is possible to observe the areas of smooth and rough cut (quartz sandstone, Botucatu Formation).

According to Momber et al. (1999), acoustic emission technique was first applied to AWJ cutting by Mohan et al. (1994), who detected relationships between acoustic emission (AE) signals, the depth cut of metals and the energy dissipated in the specimens during the procedure. The acoustic emissions are associated with crack initiation and propagation, besides deformation. Thus, it is a useful tool to assist on the understanding of the phenomena involved in AWJ cutting. The authors performed uniaxial compression tests on concrete samples in order to determine the energy absorbed (i.e. specific energy) during the compression fracture and analyzed the presented mechanisms of failure. Then, acoustic emission was applied to the material also to recognize the mechanisms of concrete disaggregation during AWJ cutting. It was found that the failure mechanisms during the compression test and the AWJ cutting are similar. Finally, Figure 14 shows the relation between the absorbed fracture energy (specific energy) obtained in compression tests and the acoustic emission root mean square (AE_{RMS}) obtained in AWJ cutting tests. It was observed a reduction of AE_{RMS} with increase in the mechanical properties of the materials. Since the intensity of the AE-signals generally decreases with a drop in the energy dissipated during the disaggregation of a material, an increasing absorbed fracture energy lead to less material removal.

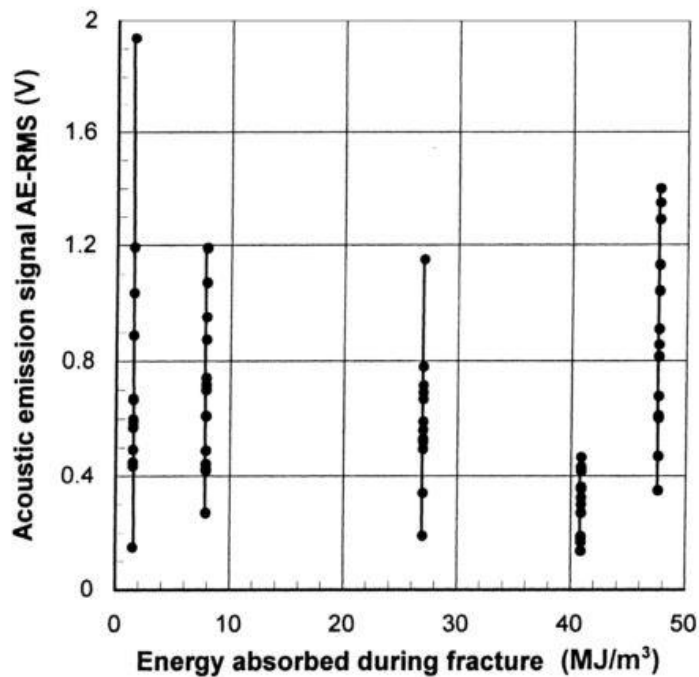


Figure 14 - Relation between absorbed fracture energy and AE_{RMS} (acoustic emission root mean square). The AE_{RMS} corresponding to different process parameters are indicated by the points (MOMBER et al., 1999)

Accuracy of WJ cutting is generally defined by the shape of the cutting gap, which is called kerf. Its shape is complex and cut surfaces are almost never really parallel. In most cases, the kerf is wider at the upper part than it is at the bottom, where the jet exits the workpiece (MAROS, 2013). The general geometrical features of cuts produced by a WJ or a AWJ are shown in Figure 15.

The decrease in the WJ energy as it gets deeper inside the rock is what explains the constriction of the kerf. Thus, W_t is the top width of the kerf, W_b is the bottom width and W is its mean value. On the tips of the WJ it is also common to have rounding processes because of the differences in energy from the center of the jet and its borders. As indicated before, the smooth cut depth is h and the total thickness is h_{MAX} . The ratio between the top and the bottom widths is called taper (HASHISH, 1992).

Momber (1995) observed the formation of large pockets in the very lower region of the cuts in soft concrete materials subjected to an AWJ. The authors suppose that the matrix material is washed away by the high-speed water flow. Nevertheless, the influence of water flow in the course of AWJ cutting is still an unsolved problem and further work is required to clarify this problem.

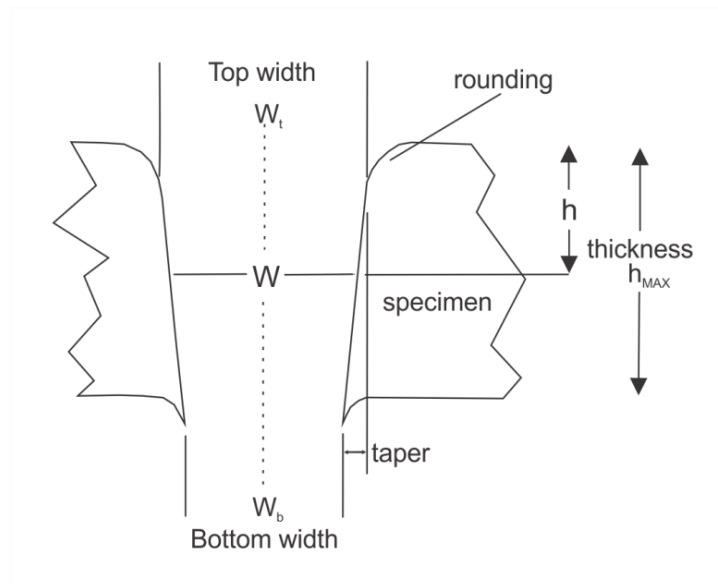


Figure 15 - General characteristics of the kerf (HASHISH, 1992).

Some authors such as Ali & Wang (2011) claim that the water does not act directly in material removal, though it has an important role in the transfer of energy to accelerate the

abrasive particles, guide and converge them through the jet, remove debris from the kerf and reduce the heat generated by friction. However, there are several authors who think that the water contributes to the effectiveness of the cut, as Harris & Mellor (1974), Hurlburt et al. (1975), Rehbinder (1977) and Hagan (1992).

2.5. MECHANISMS OF ROCK DISAGGREGATION

When brittle materials such as rocks are cut, the mechanisms involved are related to the generation of microcracks, abrasion and erosion processes. The knowledge of the mechanisms of the disaggregation of rocks is a fundamental part of the study of rock mechanics applied to cutting with AWJ. However, it is not a simple task to analyze and establish a relationship between the processes which occur in each type of rock and the action of the turbulent and fast two-stage type of jet. It is of great value to base the study on the mechanical properties of rocks and their petrology.

Simmons & Richter (1976) define a microcrack as an opening that occurs in rocks and has one or two dimensions smaller than the third. For flat microcracks, one dimension is much less than the other two. In rocks, they are generated when the local stress exceeds the local strength. The authors classify microcracks into grain boundary cracks, intragranular or intracrystalline cracks and intergranular or intercrystalline cracks. Grain boundary cracks may be coincident or non-coincident with the crystal's borders. In the last case, it may extend slightly into the crystal or be close and subparallel to its borders. This type of microcrack may be difficult to recognize, because it may be confused with the proper line of the boundaries. Intracrystalline cracks always occur inside a single crystal. When they are natural to the rock, they present a rough contouring and may be filled in by other materials like clay minerals, quartz or mica. In contrast, when they are generated by mechanical stresses, they present sharp and generally narrow walls with sharp or tapered tips (TAPPONNIER & BRACE, 1976). A special case of this type of crack is the cleavage crack, which occur along the weaker planes of a crystal, which are known as cleavages. Cleavages are lines of weakness related to the means with which the molecules are bound together in a mineral. Also, there is a tendency of the mineral to break along the cleavages, when it presents them. Intercrystalline cracks extend from the boundaries of a crystal passing inside one or more crystals. The term

transgranular crack is also used to describe a crack which goes from the boundaries of a crystal to the boundaries of the next crystal. The shape of intercrystalline cracks is very similar to the intracrystalline one.

Kranz (1983) states that under experimental and natural conditions, with which cracks are generated, mechanical stresses may lead to the formation of cracks by means of a minimum of six mechanisms: twins interactions with grain boundaries and other twins; release of stored strain energy associated with kink bands and deformation lamellae; cleavage separations; stress concentration near grain boundaries, cavities and crack tips; mismatches in elastic compliances of neighboring grains; and grain translations and rotations.

There are few studies in literature which discuss microscopically the generation of microcracks in rocks due to the action of AWJ. It's more common to find studies regarding rock-like materials as concrete and ceramics or other materials related to metallurgy.

Zeng & Kim (1992) studied patterns of microcracks in polycrystalline ceramics. A mixed material removal mode was observed, corresponding to brittle fracture and plastic deformation. In low impact angles of abrasive particles, scratching marks dominated, but also intergranular cracking appeared. At perpendicular impact angles, the main process of cutting was intergranular cracking.

Miranda & Kim (1996) investigated the action of AWJ on the cutting of calcitic rocks. It was concluded that the amount and distribution of pre-existing flaws like cracks and pores exert great influence on the process. The main observed mechanism of cracking was intergranular cracking and cleavage cracking of calcite.

Momber et al. (1999) investigated the behavior of materials with low and higher stiffness, like mortar and concrete. It was found that in mortar the failure occurred due to the erosion of the matrix and the pull-out of a separate inclusion. In contrast, high-strength concretes were eroded by intense spalling fracture with cracks covering the matrix and inclusions.

Momber (2001) characterizes the structure and behavior of materials with non-linear behavior such as concrete, mortar and hardened cement paste. After cutting, grain bridging was observed, with microcracking and crack branching as the main processes, which occur as intergranular and transgranular cracking. The author, based on fracture mechanics theory,

used the characteristic length of the fractures as a non-linear parameter to indicate the resistance of these materials against fluid jet impact, since a physical parameter alone (i.e. compressive strength or Young's modulus) cannot describe the way a material fails.

Momber (2003) applied the classification of the work: "Toughening mechanisms in quasi-brittle materials" of Shah & Ouyang (1993) to cement paste, mortar and concrete samples cut with AWJ. The approach is interesting as it provides more information about processes which occur during the generation of cracks in these types of materials. Among the quasi-brittle fracture behavior of the materials during erosion, the following behaviors were observed: microcrack shielding; aggregate bridging; crack branching; aggregate spalling; crack deflection; crack blunting; crack rim interaction and crack bridging (Figure 16).

Aydin et al. (2012) studied the influence of textural properties like grain size and its boundaries in order to investigate their effect on the AWJ cutting of coarse to fine-grained granites. The authors observed that the main types of cracks generated during the cutting were intercrystalline and grain boundary cracks.

As the subject of this thesis is multidisciplinary, it is important to provide some specific definitions which may lead to confusion. Some terms present small differences when distinct areas like civil and mechanical engineering, materials science and geology are compared. Thus, it is essential to have common sense when dealing with AWJ and define abrasion, erosion and wear.

Budinsky (1998) claims that both wear and erosion involve material removal with progressive loss due to the fracture of its surface. However, while erosion requires the contribution of a fluid to the damage, wear does not. Rabinowicz (1995) adds that if dealing with machinery, when the material removal is unfavorable to the process, it is called wear, while favorable removal is called machining. Examples of wear are damage in pipes carrying abrasive slurry and damage to turbine blades due to particles in the gas stream. When an AWJ cuts rocks to be used as building stones, then it is machining.

According to Ali & Wang (2011), erosion takes place when a jet removes material from a target by impacting at a near-normal angle. When the impact is near-tangent angle, i.e. subparallel to the surface of the target, it is called abrasion. During AWJ cutting, both processes may occur simultaneously. It is important to notice that the "abrasive" term referred

to the name of the technique – “abrasive waterjet” – refers to the nature of the solid particle, which is harder than the target material, and not to the removal mechanisms.

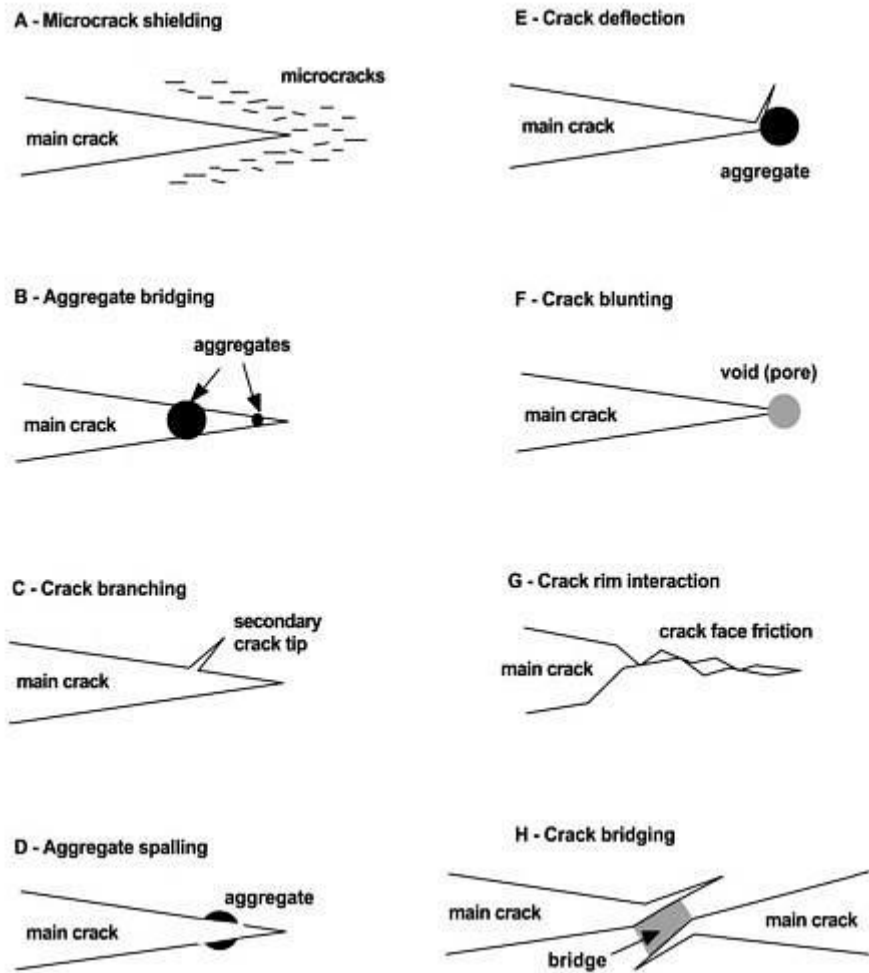


Figure 16 - Schematics of the main toughening mechanisms in cementitious composites (Momber, 2003; adapted from Shah & Ouyang, 1993).

As stated in Momber (2004), according to the tribological definition of the Deustches Institut für Normung on DIN 50323-2 (1995), the term erosion includes, among others: fluid flow erosion (material removal by flowing liquid), drop impact erosion (material removal by impacting liquid drops) and hydro-abrasive erosion (material removal by impacting particles suspended in a flowing liquid). Figure 17 shows more details on these types of erosion.

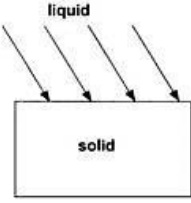
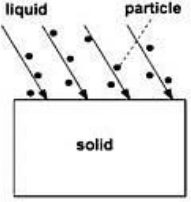
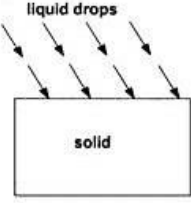
Wear type	Tribological scheme	System structure	Flow system	Wear caused by...	Wear mechanisms
Fluid flow erosion		Liquid Solid body	Flowing liquid	Liquid -Erosive	Fatigue corrosion
Hydro-abrasive erosion		Solid particles liquid Solid body	Flowing liquid/ solid particle	-Corrosive Particles	Scratching surface fatigue
Drop impact erosion		Liquid Solid body	Flowing fluid	Liquid particles	Fatigue

Figure 17 - Types of erosion (MOMBER, 2004).

2.6. WATERJET CUTTING MODELS BASED ON ALGEBRAIC AND REGRESSION SOLUTIONS

In the literature, the majority of the existing models which describe the WJ and AWJ cutting process is based on laboratory tests including algebraic solutions or regression analysis. Most of the proposed models are attempts to estimate the depth of cuts in different types of materials. The greater part of these models is focused on the cutting of ductile materials and a smaller part regards the cutting of brittle materials, mainly concrete, glass and ceramics. The variables and the conditions involved in the operation of a WJ/AWJ system are so many that it is hard to develop a single theory which describes all of the conditions that may occur from the existing WJ/AWJ test data.

The physics of the WJ/AWJ machining process is complex, and it becomes more complex when considering the cutting of rocks. Several authors developed models which may be applied to rock cutting, yet more research is needed in order to test more types of rocks and distinct combinations of parameters. This research also contributes to a better understanding

of the mechanisms of WJ cutting and the mechanisms of disaggregation of different rocks when subjected to the process.

Crow (1973) developed one of the first models considering the phenomena of WJ cutting as a continuous process with its typical traverse movement. The model is applied to granular sedimentary rocks and it was widely used in studies in comparison with empirical models. In Crow's model, the depth of cutting (h) can be estimated through Equation 1:

$$h = 2\mu_w \frac{d_0 \cdot P_0}{\tau_0} \int_0^{\theta} \frac{e^{\mu_w(\theta-\theta_0)} \text{sen}(\theta)}{1 + (\nu/c)\text{sen}(\theta)} d\theta \quad (1)$$

where μ_w is the coefficient of Coulomb friction between water and rock, d_0 is the diameter of the WJ, P_0 is the total pressure of the WJ (exit pressure), τ_0 is the shear strength of the rock, ν is the traverse velocity, c is the cutting velocity (i.e. the traverse velocity) and θ is the angle of cutting.

Rehbinder (1977) developed another theoretical model of cutting rocks based on the flow of water in a porous medium, also considering the action of a continuous WJ. The maximum depth of cutting (h) was defined through Equation 2:

$$\left(\frac{h}{D}\right)_{max} = \frac{1}{\beta} \log_n \left(\frac{P_0}{P_{th}}\right) \quad (2)$$

where D is the kerf width, β is a rock constant, P_0 is the jet pressure inside the nozzle and P_{th} is the threshold pressure required for cutting on depth h . According to the author, parameters like compressive strength, tensile strength and fracture toughness do not enter the equation explicitly, although they are embedded in the threshold pressure.

Zeng & Kim (1992) developed an elasto-plastic model for brittle material removal due to low incidence impacts of single particles to predict the depth of cut. The study was based on the observation of ceramics and on the equations previously defined by Bitter (1963). The

authors state that the removal of material occurs due to intergranular cracking as a result of impact induced stress waves. The loading period is very short due to the high velocity impacts of the AWJ, thus cracks do not have time to propagate. Lots of minute cracks begin to form along grain boundaries or other types of flaws and then they coalesce to form a crack network. Equation 3 gives the relationship for the depth of cut (h):

$$h = \left(\frac{\eta \cdot C_v \cdot C_y}{1 + R} \right)^2 \frac{Cm \cdot P_w}{\rho_w \cdot D \cdot u} \left(\frac{2f_w \cdot \beta \cdot a \cdot \sigma_f \cdot \alpha^2}{3\gamma \cdot E} + \frac{\alpha}{\sigma_f} \right) \quad (3)$$

where η is the momentum transfer efficiency, C_v is the orifice efficiency, C_y is the compressibility coefficient of the water, R is the ratio of abrasive/water mass flow rates, C is the coefficient of impact efficiency, m is the abrasive mass per time rate, P_w is the water pressure, ρ_w is the density of water, D is the diameter of the jet at the top of the target (it is assumed to be equal to the focusing diameter), u is the traverse speed, α is the incidence angle, f_w is the stress wave energy coefficient, β is a coefficient related to the stress wave energy, a is the grain size or flaw distribution parameter, σ_f is the flow stress of target material, γ is the fracture energy per unit area and E is the elastic modulus of the target material.

After some data handling, Equation 4 may be expressed as:

$$h = \frac{m \cdot m_w^2 \cdot P_w}{2670(m \cdot m_w)^2 \cdot D \cdot u \cdot R_E} \quad (4)$$

where m_w is the water mass flow and R_E is the erosion resistance.

Momber & Kovacevic (1999) developed a model based on the energy dissipation processes involved in the erosion process of the target materials, i.e. an energy-conservation model. Fracture tests, material removal experiments and measurements of the reaction forces on the exiting slurry during the cut were performed in order to analyze separately the

components of the energy dissipation parameter, like damping, friction and erosion debris generation.

In order to isolate the components of the energy dissipation parameter like damping, friction and erosion debris generation, fracture and material removal tests, and measurements of the reaction forces on the jet slurry were done. The model is based on what was discussed in Figure 12. The authors claim that with a constant input energy, its value only depends on the relative erosion depth (ϕ), which is Equation 5:

$$\phi = \frac{h}{h_{MAX}} \quad (5)$$

where h is the depth of cut and h_{MAX} is the maximum possible cut depth. Then, Equation 6 describes the energy dissipated during the cut:

$$E_{DISS}(\phi) = \chi(\phi)(E_S - E_{EX}) \quad (6)$$

where E_{DISS} is the energy dissipated on the target, E_S is the kinetic energy of the high-speed slurry flow exiting from the focusing tube (nozzle) and E_{EX} is the exit energy of the high-speed slurry. By definition, χ is 0 when ϕ is 0 and χ is 1 when ϕ is 1. The parameter $\chi(\phi)$ describes different mechanisms of energy dissipation. After a few manipulations, Equation 7 is obtained:

$$E_{DISS}(\phi) = \chi(\phi) \frac{\alpha^2 \cdot \phi^2 \cdot d_F (m_P \cdot m_W)}{v \left(1 + \frac{m_P}{m_W} \right)^2 \rho_W} (p - p_{thr}) \quad (7)$$

where α is the mixing efficiency coefficient, φ is the energy transfer in the orifice, d_F is the focusing tube diameter, m_p is the abrasive particle mass flow rate, m_w is the water mass flow rate, v is the traverse rate, ρ_w is the water density, p is the pump pressure and p_{thr} is the critical threshold pressure.

During the 2000s no relevant model emerged regarding the cutting of rocks, however it seems that since 2010 the subject regained attention. Engin (2012) focused on the development of equations based on linear and non-linear regression analysis to predict the depth of cutting for forty two types of rocks. The aim was to provide models which allow the preselection of particular operating parameters for the cutting of rocks. Among the equations presented, Equation 8 is highlighted:

$$h = 5.35x \frac{P^{1.398} x M^{0.486} x R^{0.125}}{V^{0.790} x H^{0.890} x D^{1.102}} \quad (8)$$

where P is the pump pressure (MPa), M is the abrasive flow rate (g/min), R is the bohme abrasion resistance (cm³/50 cm²), V is the traverse velocity (mm/s), H is the shore scleroscope hardness and D is the apparent density (g/cm³).

Oh & Cho (2016) developed a model for cutting granites based on the maximum kinetic energy and the depth of cut. The aim of the equation was to estimate the process time of rock cutting with an AWJ. The equation may be written as (Equation 9):

$$h = \alpha \left(\frac{E_{MAX}}{1J} \right)^\beta \quad (9)$$

where h is the cutting depth (mm), α is the cutting depth (mm) when the maximum kinetic energy (E_{MAX}) is equal to 1 J and β is a constant obtained through experimental cutting tests and can be defined as the performance efficiency of the cutting depth with increasing maximum energy. The exponent β is for cutting performance sensitivity with respect to the applied maximum energy. When β becomes 1, the relationship between the maximum energy

and the cutting depth is linear. When $\beta < 1$, this relationship becomes a convex curve. The parameters α and β are related to the properties of the abrasive material and the target material.

2.7. GEOTECHNICAL CHARACTERIZATION OF INTACT ROCK MATERIALS

In geotechnical engineering it is crucial to work together with qualitative and quantitative information about rocks. Qualitative characterization is mainly related to petrography, i.e. the description of individual minerals and the rock as a whole based on previous geological knowledge. Also, it involves the interpretation of information on the genesis of rocks. Generally, that is the main contribution which geologists provide to a geotechnical study, which no other professional provides: the detailed knowledge of the bedrock. Therefore, when dealing with geotechnical engineering it is clear that geologists will have to share this knowledge with engineers (e.g. civil and mechanical engineers), who are responsible for general constructions and maintenances, among others. The primary intersection between geology and engineering information is the geotechnical characterization of intact rocks, so that physical properties and parameters may be obtained to describe their mechanical behavior.

In this section, some information on the more elaborated laboratory characterization tests performed in the present research will be introduced, since the study of AWJ is a multidisciplinary field.

2.7.1. Abrasion resistance test

As stated in Frazão (2002), the wear of a rock can be obtained by means of the determination of its abrasion resistance. The lesser the hardness of a rock, the greater is its wear. The hardness of a rock is related to the hardness of its minerals assembly and its cohesion. It is defined as the resistance of a rock against the penetration of a harder foreign body or the resistance against being scratched by it. The direct determination of hardness is a

complex practice and the results may not reflect the real tendency of a rock to wear. This occurs due to the different hardnesses presented by the rock's individual minerals. The hardness of minerals is influenced by cleavages, crystallographic axis orientations, directions of loading, as well as the textures and the structures of the rocks themselves. Therefore, the indirect determination of hardness through abrasion resistance leads to a better reproducibility. In Brazil, one of the main laboratory tests used to determine abrasion resistance is the Amsler abrasion test, which involves the pressing of cubic specimens against a hard metallic disc. Over the disc, an abrasive material made of quartz sand is discharged, and then the specimens wear as the disc rotates. The results are calculated after 500 m and 1000 m are covered, and the measure of abrasion resistance is given according to the reduction of the specimen's height, e.g. mm/500m and mm/1000m. Figure 18 shows a scheme of the test.

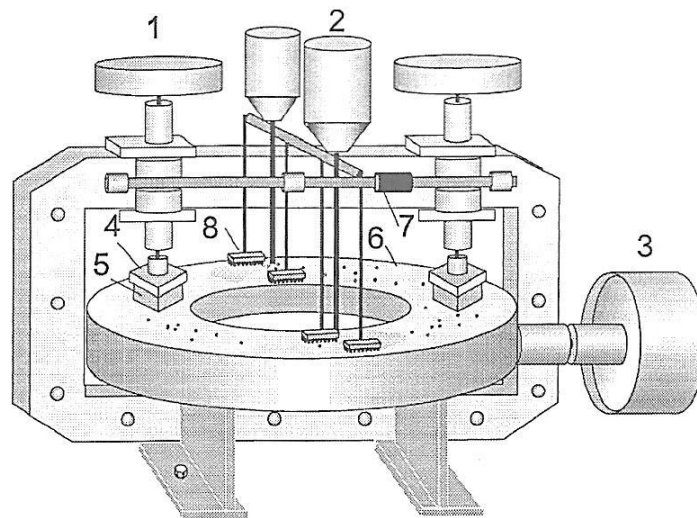


Figure 18 - Amsler test machine: 1) load controller, 2) rate of sand controller, 3) engine, 4) specimen holder, 5) specimen, 6) metallic disc, 7) odometer, 8) directional brush to homogenize the distribution of sand (ABNT, 1992)

2.7.2. Uniaxial compression test

Most of the engineering mechanics-based approaches to the solution of various rock mechanics problems require the aforementioned definition of the stress-strain behavior of rock masses. Depending on the problem to be solved, the behavior of the intact rock material may be of concern. Even the most complex solutions start with the acquisition and analysis of intact rock, before actually handling rock masses (BRADY & BROWN, 2004).

The uniaxial compression test is the main test done to obtain strength information of a regular rock specimen. The uniaxial compressive strength (σ_c) is calculated through Equation 10:

$$\sigma_c = \frac{F}{\pi D^2 / 4} \quad (10)$$

where F is the maximum force carried by the specimen during the test, D is the diameter of the specimen (ISRM, 1979; ASTM, 2014).

By conducting an instrumented uniaxial compression test, it is possible to obtain the elastic constants of rocks, e.g. the Young's modulus and the Poisson ratio, and also the stress strain curves of rocks. The apparatuses involved in obtaining this information are devices used to measure circumferential and axial displacement and a device for recording the load and the displacement produced as the force is increased. From the displacement values, it is possible to calculate strain; from the values of force, stress can be also calculated. When stress and strain are arranged on a XY scatterplot, the complete stress strain curve is obtained. (Figure 19). When the test is conducted only until the peak stress, the curve is referred to as simple stress strain curve.

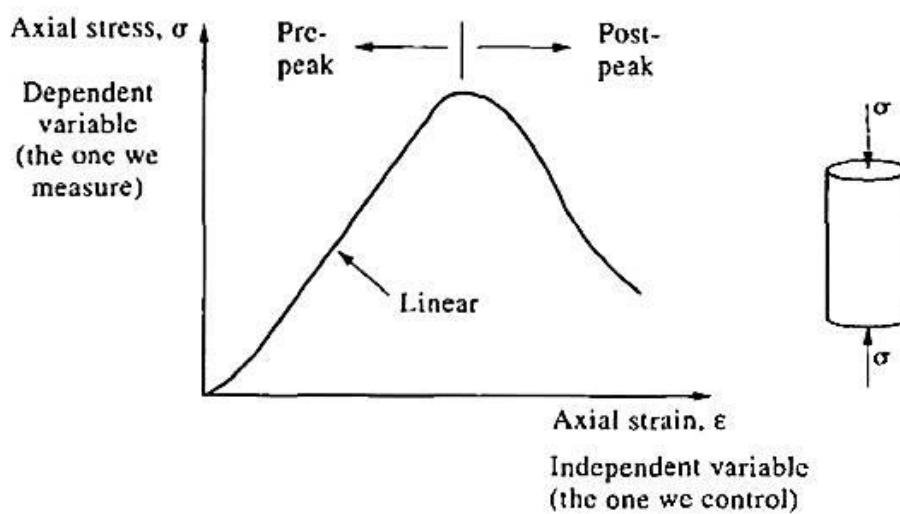


Figure 19 - A complete stress strain curve (HUDSON & HARRISON, 1997).

According to Hudson & Harrison (1997), the stress strain curve presents an initial portion at the beginning which is concave upwards, and this is due to the non-perfect shape of the specimen, i.e. non-parallel ends after its preparation, and the closing of natural microcracks of the intact rock. Then, there is a portion of linear behavior almost at the peak stress, which is called the uniaxial compressive strength, as already stated. Martin (1997) defined values of stress for crack initiation and crack damage before peak stress. If the test is conducted with stress as the independent variable, the consequence is a violent uncontrolled failure after the peak strength, because the machine applies more stress than the specimen can withstand. On the other hand, if the test is conducted with strain as the independent variable, the failure may be controlled and the interpretation of the post-peak region is that beyond a certain strain value the rock continues to suffer mechanical breakdown with progressive loss of load-bearing capacity.

Wawersik & Fairhurst (1970) developed a classification for rocks based on their behavior observed on the stress strain curves patterns (Figure 20). When considering rock behaviors on complete stress strain curves, Class I rocks are those which present increasing deformation while under decreasing loading, while class II rocks present a decrease in strain under decreasing loading. The strain may increase at first, but then decrease after the peak strength.

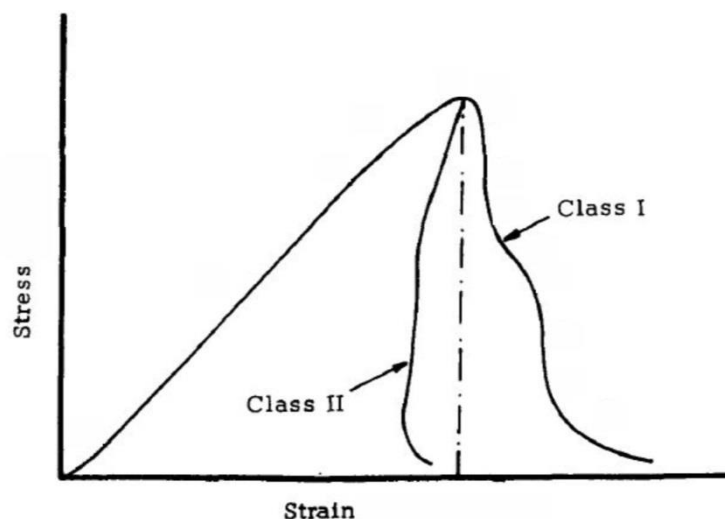


Figure 20 - Stress-strain curves which describe the rock failure behavior as class I and II in uniaxial compression (modified from WAWERSIK & FAIRHURST, 1970).

The Young's modulus is defined as the ratio of the axial stress change to axial strain produced by the stress change. In engineering problems, this elastic constant may be calculated mainly through three methods, as shown in Figure 21, where σ_u is the ultimate strength, i.e. the peak strength; ϵ_a is the axial strain, E_t is the Young's modulus obtained from the tangent method, E_{av} is the Young's modulus obtained from the average method and E_s is the one obtained from the secant method (ISRM, 1979; ASTM, 2014).

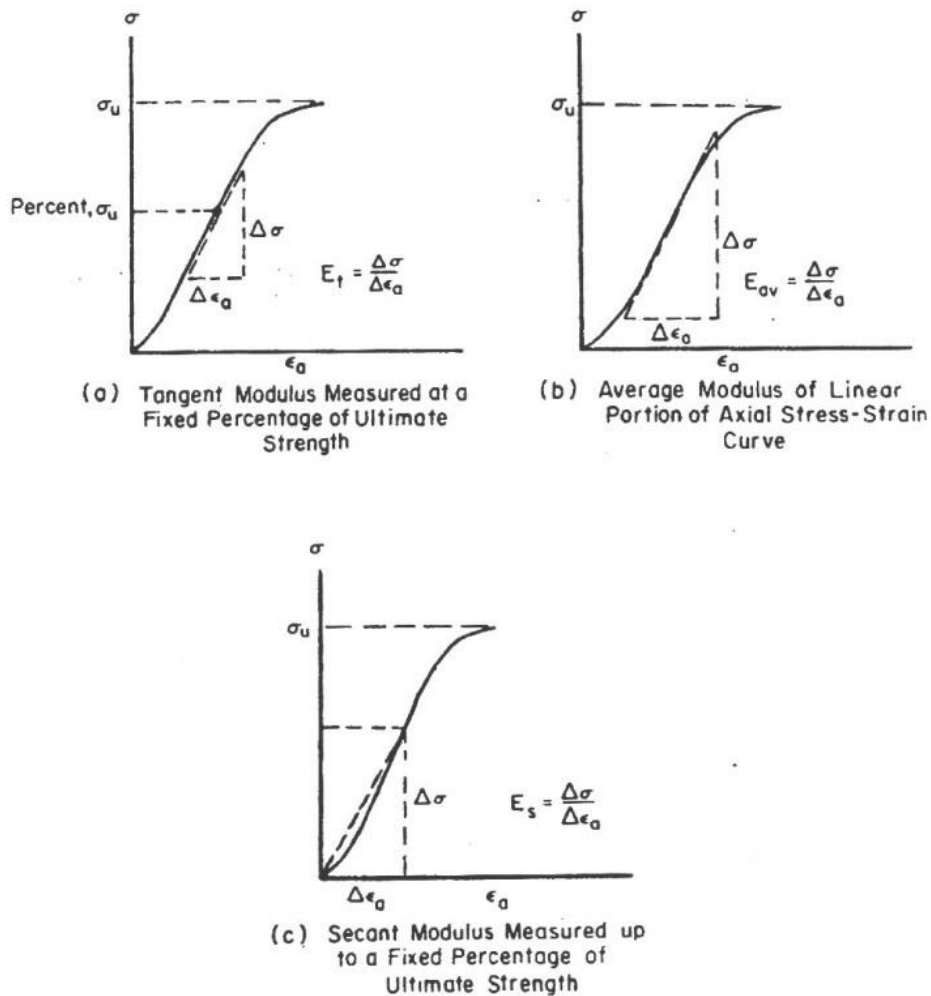


Figure 21 - Most common methods to calculate Young's modulus (ISRM, 1979).

Poisson's ratio is defined as the negative of the ratio of circumferential strain to the axial strain when an elastic material is loaded in uniaxial compression. The "Poisson effect" is the trend of a material to expand or shrink perpendicularly to the loading axis (GERCEK, 2007).

2.7.3. The Brazilian tensile test

According to ISRM (1978a), the Brazilian tensile test is intended to measure the uniaxial tensile strength indirectly through uniaxial compression. The justification for an indirect measure is that most rocks in biaxial stress fields fail in tension at their uniaxial tensile strength when one main stress is tensile and the other finite main stress is compressive with a magnitude smaller than three times that of the tensile main stress. In addition, this test is much simpler to conduct when compared to direct tensile tests.

In this test, a specimen with the shape of a disc is compressed diametrically (Figure 22) between two loading plates and the indirect tensile stress at failure is calculated from the breakdown load (HUDSON & HARRISON, 1997). Thus, the tensile strength (σ_t) may be calculated through Equation 11, where F is the load at failure, D is the diameter of the specimen and t is the thickness of the specimen measured at its center:

$$\sigma_t = \frac{0,636F}{Dt} \quad (11)$$

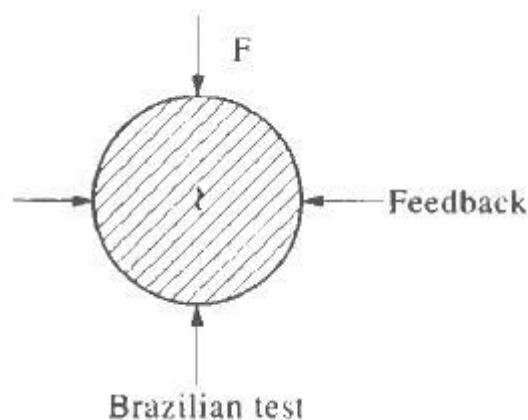


Figure 22 - Rock testing geometry for the Brazilian tensile test. F is the applied force and the feedback is perpendicular to it (HUDSON & HARRISON, 1997).

2.7.4. The Fracture toughness test

Fracture mechanics involves the study of the conditions that lead a material to collapse due to the generation and propagation of cracks, when it is subjected to a proper load. A fundamental parameter of fracture mechanics is the fracture toughness, which indicates the capacity of a brittle material to withstand local stress intensity factors due to external loads. This parameter indicates the magnitude of the fracture strength, i.e. the capacity of a rock to withstand the propagation of a crack (SCHMIDT, 1976).

ISRM suggests three tests in order to obtain the fracture toughness of rocks: chevron bend (CB), short rod (SR) and cracked chevron notched Brazilian disc (ISRM, 1988; ISRM, 1995). These methods present some difficulties regarding the shape and dimensions of the specimens and the complex installation. Non-conventional methods have been developed as alternatives to the already established ones and they seem promising. Donovan & Karfakis (2004) developed the edge notched disc wedge splitting test (END), a test which requires a simple procedure. The test involves a specimen with a diameter around 50 mm and a thickness around 25.4 mm. Then, a straight notch is made on its center according to the conditions established in the authors' work. The specimen is placed on a wedging device which has an angle of 11° (Figure 23). Vertical force is applied under displacement control by a testing machine and the fracture toughness (K_{IC}) is obtained through equation 12:

$$K_{IC} = 2\sqrt{\frac{D}{2a}} \left(\frac{F_V}{2 \tan(\alpha/2)} \frac{1 - \mu \tan(\alpha/2)}{1 + \mu \cot(\alpha/2)} \right) \left(\frac{a}{0.355715(D-a)^{3/2}} + \frac{1}{0.966528(D-a)^{1/2}} \right) \quad (12)$$

where D is the diameter of the specimen, a is the length of the notch, F_V is the vertical applied force, μ is the tangent of the angle of sliding obtained by the tilt test and α is the angle of the wedging device. According to the research of Alvarez (2004), the END test provide comparable results to the CB and SR tests suggested by the ISRM when considering some types of Brazilian granites and basalts.

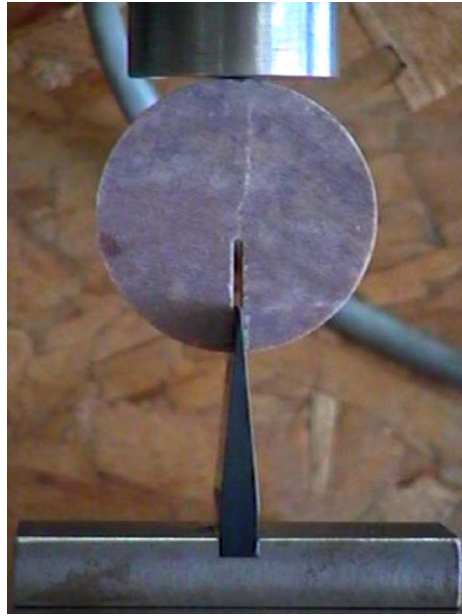


Figure 23 - Experimental set up of the END test (DONOVAN & KARFAKIS, 2004).

3. TESTED ROCKS AND THEIR PHYSICO-MECHANICAL PROPERTIES

3.1. SELECTED ROCKS

Four types of rocks were selected (Figure 24) based on their distinct geological characteristics and their ease of obtainment (previous contact with owners and supervisors, locations and transportation). Two of them are intrusive igneous rocks. A typical silicate rock – syenogranite, and an alkaline rock – nepheline monzosyenite. The silicified sandstone is a sedimentary rock and marble is a metamorphic rock. All of them were collected at the mining front of quarries in single batches. The nepheline monzosyenite is a rock from the Crystalline Coastal Complex of São Sebastião's island and it dates from 200 to 145 m.y. (SILVA et al., 1977). Samples were collected in Ilhabela – SP, UTM coordinates 464.573 m E, 7.373.750 m N, zone 23K.

The syenogranite belongs to the Itu Intrusive Suit from the Ribeira Belt, dating from 580 m.y. (HACKSPACHER et al., 2003). Samples were collected in Salto – SP, UTM coordinates 265.279 m E, 7.429.395 m N, zone 23K.



Figure 24 - Chosen rocks for the research project, from left to right: nepheline monzosyenite, syenogranite, silicified sandstone and marble.

The marble is from São Joaquim Unit, Italva Group, which also belongs to the Ribeira Belt. It dates from 501 m.y. (HEILBRON & MACHADO, 2003) and samples were collected

in Cachoeiro de Itapemirim – ES, UTM coordinates 276.404 m E, 7.691.262 m N, zone 24K. Finally, the silicified sandstone belongs to the Botucatu Formation of the Paraná Sedimentary Basin, dating from 200 to 100 m.y. (MILANI et al., 1994). Samples were collected in São Carlos – SP, UTM coordinates 207.369 m E, 7.557.755 m N, zone 23K.

3.2. ROCKS CHARACTERIZATION METHODOLOGY

Thin-sections of intact rocks were made at the Petrography Laboratory of the Universidade Estadual Paulista (UNESP), Rio Claro Campus. A petrographic analysis was conducted through polarized light microscopy on an Olympus BX40 microscope from the Geotechnical Engineering Department of the Universidade de São Paulo (USP), São Carlos Campus.

Scanning electron microscopy (SEM) was conducted in the Electron Microscopy Laboratory of the Instituto de Física de São Carlos – IFSC of the USP, São Carlos campus. The equipment is a Carl Zeiss SIGMA Advanced Analytical Scanning Electron Microscope. Images from the top of the kerfs were obtained of all four types of rocks.

The Amsler Abrasion Test was performed according to the NBR 12042 (ABNT, 2012) at the Building Stones Laboratory of UNESP, also at the Rio Claro Campus.

Dry density, saturated density, degree of saturation and porosity were conducted according to the Brazilian standard NBR 15845-2 (ABNT, 2015). This test and the following ones were performed at the Rock Mechanics Laboratory of the Geotechnical Engineering Department of USP.

The Brazilian tensile test was performed in a Rock Mechanics Test System MTS 815 servo-controlled machine (Figure 25) with a loading rate of 12 kN/min. The Uniaxial Compression Test was performed in the same machine, but with a loading rate of 100 kN/min for the syenite and 60 kN/min for the other rocks. The tests were based on the following ISRM (International Society for Rock Mechanics) standards: Suggested Method for Determining Tensile Strength of Rock Material (1978a) and Suggested Methods for Determining the Uniaxial Compressive Strength and Deformability of Rock Materials (1979).

Besides the rock strength, it was possible to obtain from this test the Young's modulus, the Poisson ratio and the specific energy of the rocks. In order to verify the isotropy of the studied rocks, the aforementioned tests were firstly conducted on specimens in three different orientations. The results of tensile and compressive strength demonstrated that the rocks could be considered isotropic, since the same range of results were obtained regardless of the tests' orientation.



Figure 25 - MTS 815 servo-controlled machine of the Rock Mechanics Laboratory at the Geotechnical Engineering Department of USP.

In order to obtain the fracture toughness of the rocks, a non-conventional test was performed, since the conventional tests which are suggested by ISRM require larger samples than possible to obtain. The test was developed by Donovan & Karfakis (2004) and is named Edge notched disc wedge splitting test (END). The specimens were prepared with approximate dimensions of 56,2 mm in diameter, 27 mm thickness, 20 mm notch length and 1,7 mm notch mean width.

The Schmidt rebound hardness was obtained with a L-type RM-710 Schmidt hammer from Soiltest. The hammer device has an impact energy of 0.735 Nm. The test was conducted according to the ISRM Suggested Methods for Determining Hardness and Abrasiveness of

Rocks (1978b). The approximate dimensions of the block specimens were 110 mm x 110 mm x 170 mm.

During a visiting doctoral student period at the Ingenieur fakultät Bau Geo Umwelt of the Technische Universität München (TUM), more thin-section analyses were performed. Samples of the studied rocks were prepared and cut with the AWJ while in Brazil, in order to be analyzed in Germany. The aim of this analysis was to observe and describe the shape of the kerf through polarized light microscopy. For this, part of the cut rock samples was filled in with a two-component epoxy resin containing a yellow fluorescent dye under vacuum conditions (Figure 26 and Figure 27). A very low viscosity resin was used to guarantee good infilling of small fissures. The fluorescent dye in the resin was used to obtain a better visualization of possible cracks under the microscope. For the analysis, a Leica microscope, an Olympus camera and the software Stream Motion 1.6.1 were used.



Figure 26 - Samples' filling with the fluorescent dye resin.



Figure 27 - Samples after saw and polish.

3.3. PETROGRAPHIC ANALYSIS

3.3.1. Nepheline Monzosyenite

Nepheline syenite is a rock with imbricated structure and inequigranular phaneritic holocrystalline texture. Bigger crystals are subhedral (0,2 to 5,0 mm) and the matrix is anhedral, presenting very fine to medium granulation. Poikilitic texture is a common feature on the bigger crystals. Its weathering grade is very low and evinced by the powdery aspect of plagioclase and feldspar crystals. Deformational effects are observed due to the undulating extinction of low to medium intensity of feldspar crystals (Figure 28).

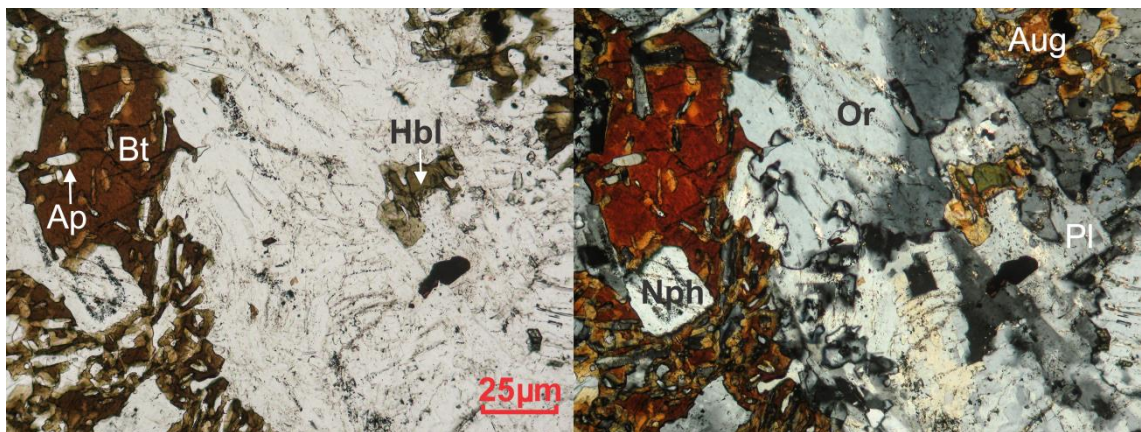


Figure 28 - Photomicrograph of nepheline monzosyenite. Uncrossed nicols on the left, crossed nicols on the right. Ap – apatite, Bt – biotite, Hbl – hornblende, Nph – nepheline, Or – orthoclase, Aug – augite, Pl – plagioclase.

Estimated mineral composition:

Alkaline feldspar (orthoclase/microcline)	40%
Plagioclase (albite/oligoclase)	20%
Augite	12%
Nepheline	12%
Apatite	5%
Opaque minerals	5%
Olivine	3%
Biotite	2%

Hornblende	1%
Zircon	traces

Description of the minerals:

The alkaline feldspar appears as colorless subhedral to anhedral crystals with up to 4,0 mm of maximum dimension and as micrometric aggregates on the rock matrix. Crystals present intensely corroded and comminuted borders. Sometimes, they have plagioclase cores, which evidences a process of feldspatization. Fracturing is observed and fractures may be filled with sericite. The powdery surface is due to the kaolinization process.

Plagioclase also appears as colorless subhedral to anhedral crystals with maximum dimension of 6,0 mm. The crystals present intensely corroded and comminuted borders and the filling of fractures with sericite is common. Polysynthetic twinning with narrow lamellae is observed on part of the crystals. The powdery surface is due to the sericitization process.

Augite occurs as brownish smoked subhedral to anhedral crystals with maximum dimension of 2,5 mm. They are fractured and present intensely corroded and comminuted borders. The mineral always occurs associated with olivine and hornblende, demonstrating a relationship according to the Bowen's reaction series.

Nepheline is colorless and occurs as prismatic subhedral to anhedral crystals with a maximum dimension of 1,0 mm. It is distinguished from plagioclase and feldspar through its higher relief. It is intensely fractured and its fractures may be filled with sericite or recrystallized plagioclase and feldspar.

Apatite is an accessory mineral and it occurs as colorless prismatic crystals with high relief. It is also possible to see its hexagonal basal section.

The opaque minerals are anhedral to subhedral and occur in association with iron-magnesium minerals.

Olivine appears as brownish smoked anhedral crystals with intensely corroded borders. It occurs as micrometric aggregates or as crystals with a maximum dimension of 1,0 mm. Some crystals present corona texture due to the weathering of its borders with augite.

Biotite occurs as brownish yellow crystals with intense pleochroism. Crystals are lamellar with corroded and comminuted borders, anhedral to subhedral with a maximum dimension of 2,5 mm.

Hornblende is greenish brown and present intense pleochroism. The crystals are prismatic, anhedral to subhedral and present corroded and comminuted borders, but with a clearer surface when compared to other iron-magnesium minerals.

Zircon appears spread in the rock as smoked prismatic crystals with high relief.

3.3.2. Syenogranite

Syenogranite is a rock with massive structure and inequigranular phaneritic holocrystalline texture. The granulation is fine to very coarse and the weathering grade is medium, evinced by the powdery aspect of feldspar and plagioclase crystals. Deformational effects are observed due to the presence of undulating extinction of medium to high intensity and it may be seen in the majority of quartz, feldspar and plagioclase crystals (Figure 29).

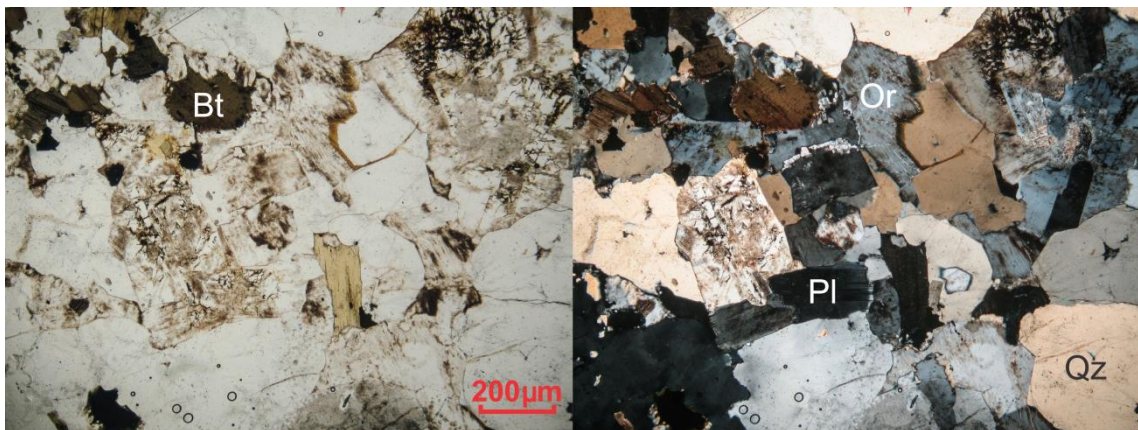


Figure 29 - Photomicrograph of syenogranite. Uncrossed nicols on the left, crossed nicols on the right.
Bt – biotite, Or – orthoclase, Pl – plagioclase, Qz- quartz

Estimated mineral composition:

Alkaline feldspar (orthoclase/microcline)	45%
Quartz	35%

Plagioclase (oligoclase)	16%
Biotite	2%
Opaque minerals	2%
Apatite	traces
Titanite (sphene)	traces
Zircon	traces
Chlorite	traces
Sericite/Moscovite	traces

Description of the minerals:

Alkaline feldspar occurs as colorless prismatic anhedral to subhedral crystals, with dimensions between 1,0 and 7,0 mm. The bigger crystals are intensely fractured and part of the fractures is filled with sericite or recrystallized quartz. Sometimes microcline presents tartan twinning and orthoclase presents Carlsbad twinning. Fine perthite and antiperthite are typical and, in some cases, in contact between feldspar and plagioclase, mirmequite is common. Crystals are powdery due to sericitization and kaolinization.

Quartz is present as colorless anhedral crystals with a maximum dimension of 3,0 mm and with irregular to lobulated contacts. It also occurs in interstitial domains as recrystallized aggregates. The majority of crystals is fractured and the bigger crystals have fractures filled with sericite and iron oxides.

Plagioclase appears as colorless prismatic anhedral to subhedral crystals with planar to irregular borders and dimensions between 1,0 and 7,0 mm. As feldspar, the bigger crystals are intensely fractured. Its weathering is of medium intensity due to sericitization. Twinning is frequent and of the polysynthetic type.

Biotite is brown with intense pleochroism. It is lamellar, anhedral to subhedral with intensely corroded borders. It is associated with opaque minerals and presents local chloritization.

The opaque minerals are euhedral to anhedral and frequently present inclusions of apatite. Apatite, zircon and titanite occur locally as euhedral to subhedral crystals.

Chlorite appears as light green anhedral lamellae, frequently on the borders of biotite crystals. Sericite/muscovite occurs as small aggregates associated with the weathering of plagioclase.

3.3.3. Quartz Sandstone

Quartz sandstone is a rock with very fine to medium granulometry, but the fine one predominates. It presents a good selection of grains and they are rounded with low sphericity. The structure of the rock is not imbricated and microcracks are rare. Contacts between grains vary from tangential to floating, rarely being concave-convex. The rock presents a cement of microcrystalline silica, thus it has low porosity (Figure 30). The red color presented by the rock is a result of the presence of iron oxides mainly as films surrounding the crystals. Regarding volume composition of the rock, it is estimated that 75% corresponds to quartz crystals, 22% to silica cement and 3% to pores.

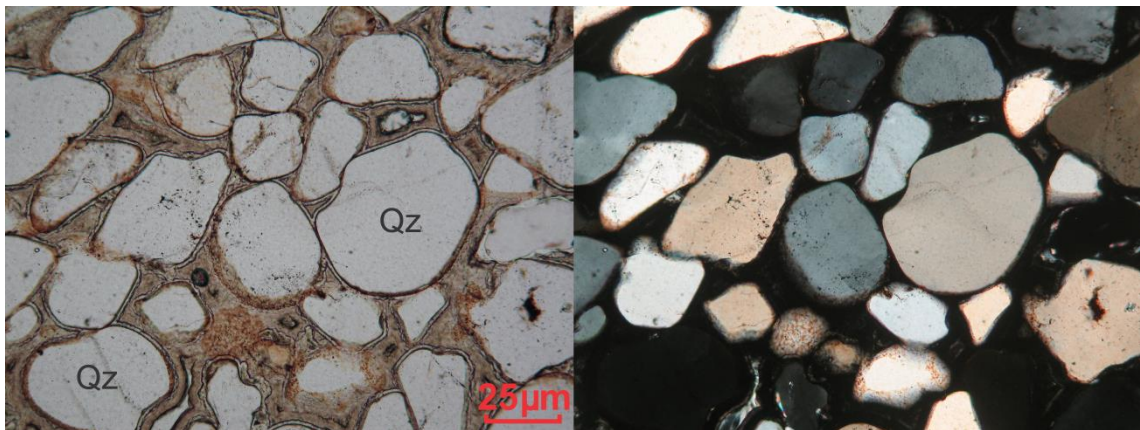


Figure 30 - Photomicrograph of quartz sandstone. Uncrossed nicols on the left, crossed nicols on the right. Qz- quartz.

Estimated mineral composition:

Quartz	100%
Microcline	traces
Lithic fragments	traces

Description of the minerals:

Quartz is colorless, with a clear aspect and brownish orange borders due to the presence of oxides and hydroxides. It rarely presents inclusions or fractures. Tenuous halos may be seen, indicating an overgrowth process. The majority of the crystals present slightly undulating extinction.

Microcline can easily be seen due to its tartan twinning. It always presents a powdery aspect, which is related to kaolinization. The lithic fragments are fewer than microcline and generally present an advanced weathering grade. However, the most common type of lithic fragment is chert, which does not occur weathered.

3.3.4. Marble

Marble is a rock with massive structure and granoblastic texture. It presents very low weathering grade revealed by the slightly powdery aspect of part of the crystals, which also present low undulating extinction. From the analysis of hand samples, it may be inferred that the rock is calcite-rich due to the intense effervescence when in contact with hydrochloric acid. Besides, it also presents dolomite, since exsolution is observed on several crystals (Figure 31). Microcracks occur spread in the rock on the inside of the crystals and also through their borders. Most of the microcracks occur as reactivation of cleavage planes.

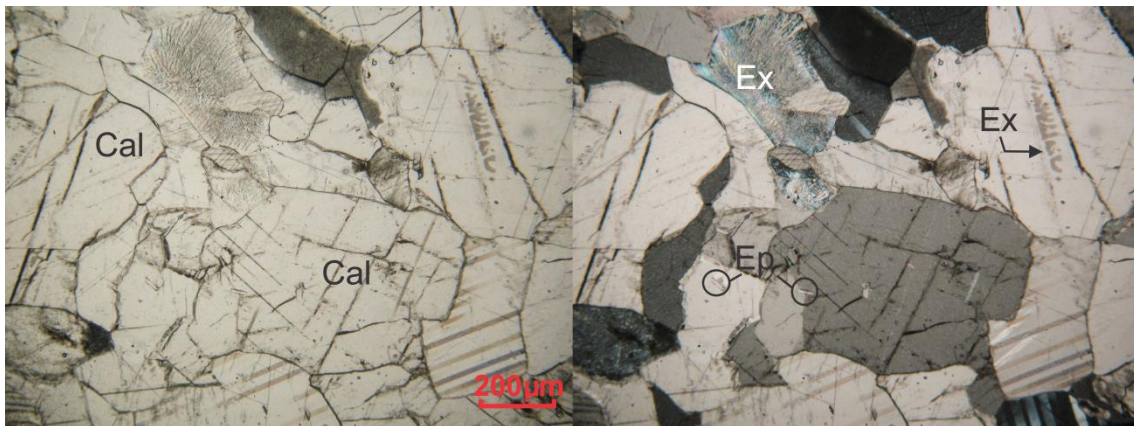


Figure 31 - Photomicrograph of marble. Uncrossed nicols on the left, crossed nicols on the right. Cal – calcite, Ep – epidote, Ex – exsolution of dolomite from calcite.

Estimated mineral composition:

Calcite/Dolomite	100%
Epidote	traces
Diopside	traces

Description of the minerals:

Calcite is colorless and presents evident romboedric cleavage. Crystals have a medium dimension of 2,5 mm and rectilinear to sinuous or lobulated contacts. Crystals have a medium fracturing grade and exsolution of dolomite from calcite is observed.

Diopside is dispersed and it occurs as colorless prismatic subhedral to anhedral crystals. It presents a corroded aspect and fractures are usual. On basal sections, it is possible to observe two cleavage directions. Its presence suggests a metamorphic peak of medium to high grade.

Epidote occurs as colorless prismatic elongated crystals with a clear aspect. Sometimes, it is possible to observe one cleavage direction parallel to the c axis of the mineral. Its presence suggests low grade retro-metamorphism.

Table 2 to Table 5 present a summary of the petrographic characteristics of the rocks studied.

Table 2. Petrographic characterization summary of nepheline monzosyenite.

General	Imbricated structure, inequigranular phaneritic texture, matrix with fine to medium granulation, bigger crystals with dimensions of 0,2 to 0,5 mm, very low weathering grade	
Mineralogy	Description	Modal (%)
Alkaline feldspar	Occurs as corroded crystals with up to 4,0 mm of maximum dimension and as microaggregates. Powdery aspect due to kaolinitization	40
Plagioclase	Occurs as corroded crystals with maximum dimension of 6,0 mm. Presents cracks filled with sericite. Powdery aspect due to sericitization	20
Augite	Occurs as fractured and corroded crystals with maximum dimension of 2,5 mm	12
Nepheline	Occurs as fractured crystals with maximum dimension of 1,0 mm. Fractures filled with sericite, plagioclase and feldspar	12
Other minerals (accessories)	Apatite, opaque minerals, olivine, biotite, hornblende, zircon	16

Table 3. Petrographic characterization summary of syenogranite.

General	Massive structure, inequigranular phaneritic texture, fine to very coarse granulation, bigger crystals with dimensions of 1,0 to 7,0 mm, medium weathering grade	
Mineralogy	Description	Modal (%)
Alkaline feldspar	Occurs as fractured crystals with up to 7,0 mm of maximum dimension. Filling with sericite and recrystallized quartz is common. Powdery aspect due to kaolinitization	45
Quartz	Occurs as fractured crystals with maximum dimension of 3,0 mm and as recrystallized aggregates. Presents cracks filled with sericite and iron oxides	35
Plagioclase	Occurs as fractured crystals with maximum dimension of 7,0 mm. Medium grade of weathering due to sericitization	16
Other minerals (accessories)	Biotite, opaque minerals, apatite, titanite, zircon, chlorite, sericite/muscovite	4

Table 4. Petrographic characterization summary of quartz sandstone.

General	No imbricated structure, very fine to medium granulometry, rounded grains with low sphericity, microcracks are rare, 22% volume corresponds to microcrystalline silica cement	
Mineralogy	Description	Modal (%)
Quartz	Occurs as clear crystals with brownish orange due to oxide films, contact between grains vary from tangential to floating	100
Other minerals (accessories)	Microcline, lithic fragments, iron oxides	traces

Table 5. Petrographic characterization summary of marble.

General	Massive structure, granoblastic texture, crystals with medium dimension of 2,5 mm, very low weathering grade, microcracks are common	
Mineralogy	Description	Modal (%)
Calcite/Dolomite	Occurs as crystals with rectilinear to sinuous or lobulated contacts, romboedric cleavage is evident, medium fracturing grade, may present powdery aspect due to incipient weathering	100
Other minerals (accessories)	Epidote, diopside	traces

3.4. THIN-SECTION ANALYSIS OF AWJ KERFS

Through thin-section analysis it was not possible to obtain detailed information regarding the processes which occur during the AWJ rock cutting. Still, it is a reasonable tool to observe the generated kerfs as a whole. Figure 32 shows mosaic compositions with examples of kerf profiles of the studied rocks.

In order to obtain the mosaic compositions, a large number of photographs of the thin-sections were taken with the aid of a guiding ruler which is positioned on the top of the petrographic microscope's rotating stage (Figure 33). The thin-section is fixed with clips which are attached to the ruler. Then, through the movement of the ruler's knobs, the thin-section can be dislocated linearly on axis X and Y, following the kerf's perimeter. The camera

is positioned on the top of the microscope and the images provided by it can be seen on the computer's screen.

In order to obtain mosaics with the correct shape and dimensions of kerfs, the photos are fitted together like a jigsaw puzzle through the connection of features of the rocks, like cleavages and crystals borders. As shown in Figure 34, the assembly begins at the left top of the kerf, goes to its bottom, and then it goes up to the right top, so that the exact kerf dimensions may be preserved.



Figure 32 - Kerf profiles of the studied rocks. The approximate depth of the kerfs is 35 mm.

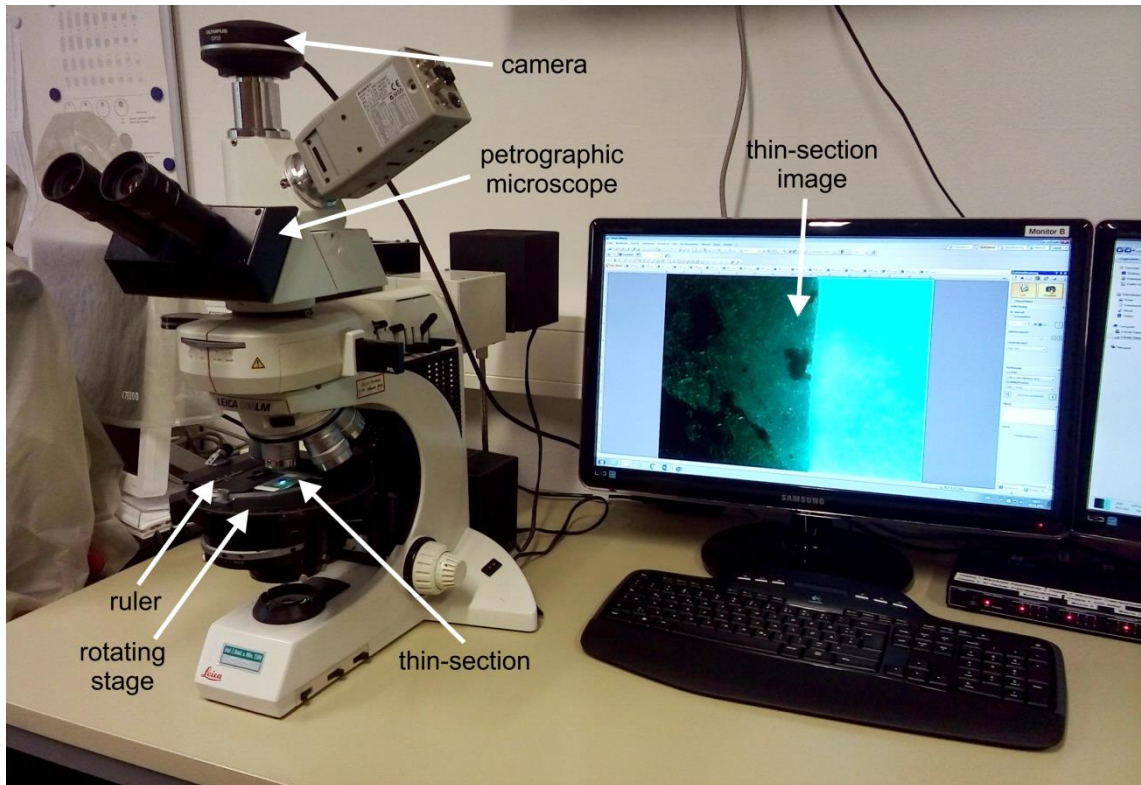


Figure 33 - Leica petrographic microscope with an Olympus camera attached and the image of a thin-section on the software Stream Motion 1.6.1.

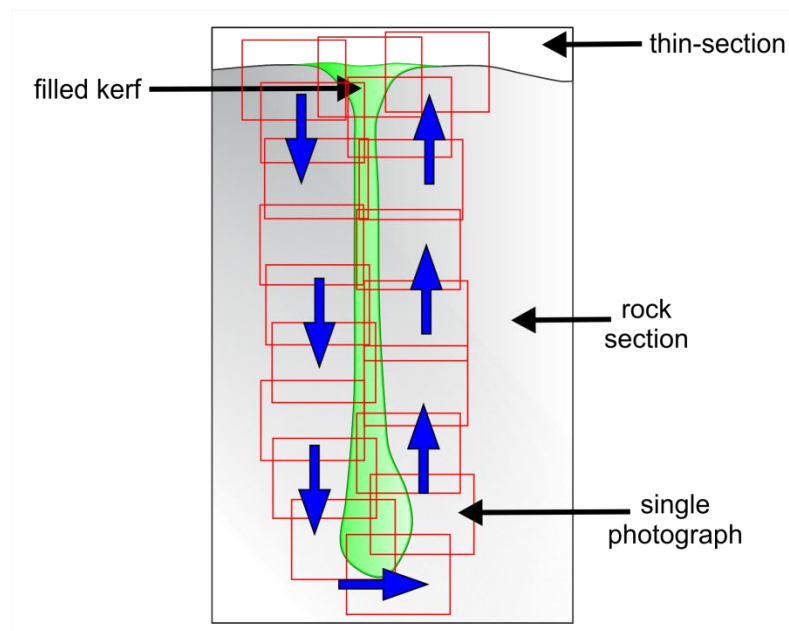


Figure 34 - Mosaic composition scheme. The blue arrows indicate the assembly direction.

The profiles of the kerfs in the nepheline monzosyenite and syenogranite have a tendency to taper from the top to the bottom, before the beginning of the pockets, which are

the domed shapes at the bottom of all kerfs. Marble has the straightest kerf profile and its width does not change drastically. It tends to get a little wider near the pocket. Quartz sandstone has the narrowest kerf of all the rocks, starting narrower at the top, getting larger gradually until the top of the pocket.

The kerfs were done in cylindrical rock samples with dimensions 50 x 50 mm. Different traverse velocities were adopted in order to obtain kerfs with approximate values of depth. Thus, they were cut with different traverse velocities, but with all other parameters as constants. It is interesting to notice that even when cut with different traverse velocities, the pockets tend to begin at similar depth. It is also noteworthy to observe that for all of the rocks except the marble, the microcracking related to the erosion of the kerf's walls is restricted to a very limited area surrounding the kerfs, since microcracks almost never propagate inside the walls. In fact, it seems that the impact due to the AWJ leads to the activation of calcite's cleavages on marble, as Figure 35 shows.

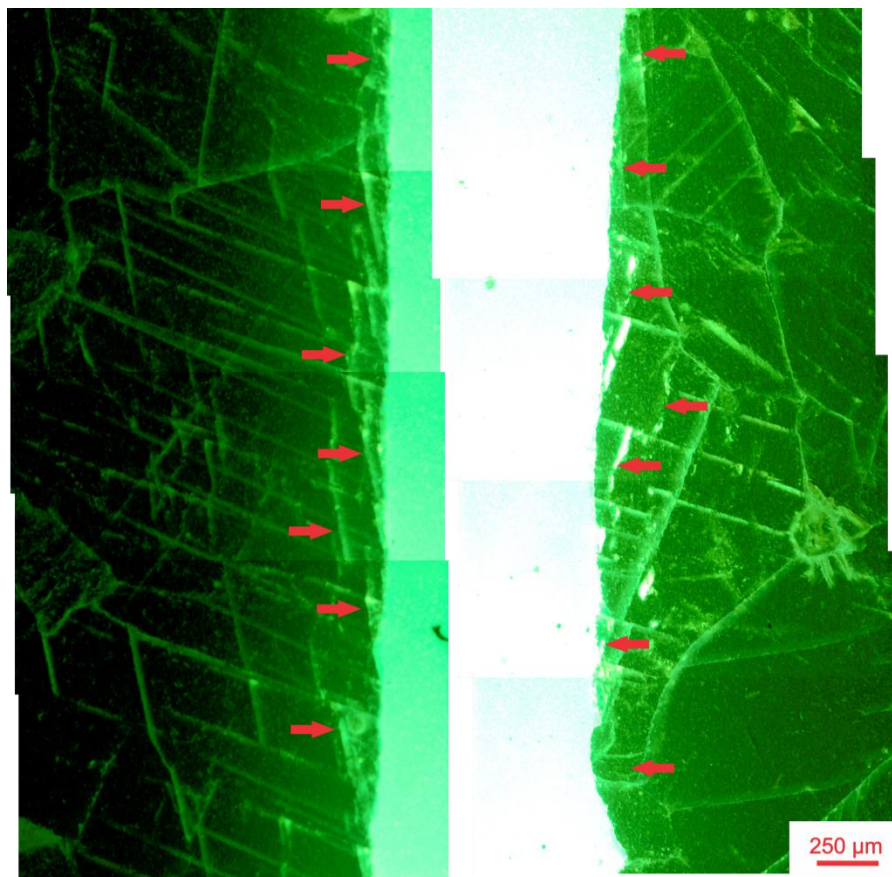


Figure 35 - Detail of the marble's walls after cut, with propagation of microcracks tending to follow the orientation of cleavage planes.

Since the AWJ is a high energy jet, it cuts through everything in its path, generally crossing all crystals and grains as transgranular and intergranular cracks with a high grade of comminution of crystals. However, with increasing depth, the AWJ loses its kinetic energy, so it is common to observe a greater preference for following planes of weakness as cleavages and crystal boundaries (Figure 36).

Something similar was observed by Momber (2003), who studied the removal mechanisms of AWJ refractory ceramics. Through SEM analysis they found that on the top region of the kerfs the material removal occurred as transgranular fracture and changed to a combination of intergranular fracture and matrix removal in the lower region of the kerfs.



Figure 36 - Kerf detail on a large feldspar crystal, evincing a preferential path through its cleavage planes.

One curious feature only observed in the quartz sandstone is the presence of concavities which may be due to the impact of single particles of abrasive. These shapes are highlighted with a square in Figure 37. The same figure shows the removal of quartz grains at their boundaries, highlighted with arrows. This process only appears in the pocket region, where the AWJ acts with lower energy.

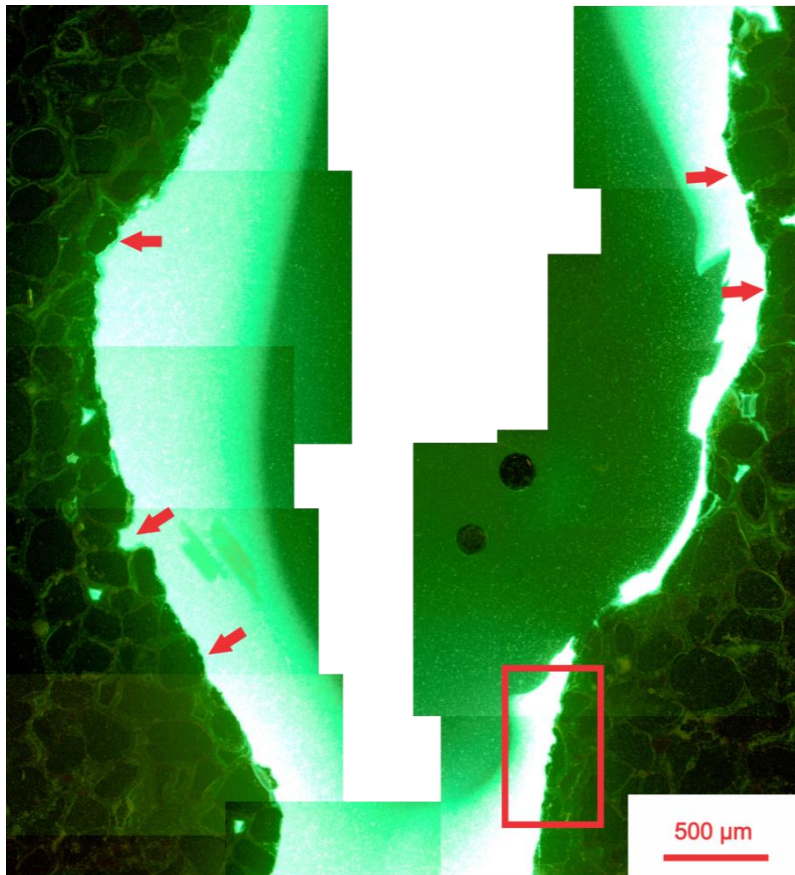


Figure 37 - Detail of the quartz sandstone pocket, showing potential concavities due to the impact of single abrasive particles (inside the square). The arrows indicate the removal of grains at their boundaries.

3.5. SCANNING ELECTRON MICROSCOPE (SEM) ANALYSIS

The SEM images of syenogranite, marble and quartz sandstone were taken with a scale of 2 μm , while the image of nepheline monzosyenite was taken with a scale of 10 μm , in order to better capture differences in the rock texture. All images are from the tops of the kerfs of the samples.

In the nepheline monzosyenite an erosive fracturing process predominates, corresponding to the rougher surface shown in Figure 38, designated as “a”. According to Vos et al. (2014) it also may be called an abrasion fatigue, which is characterized by surface irregularities created through high energetic collisions. Fracturing also can follow the cleavages of feldspar and plagioclase crystals and are represented by the parallel lines and smooth planes observed in the same image (marked as “b”).

A sort of chatter mark occurs sparsely as semi-circular arcs produced by violent shocks (marked as “c”). It looks similar to conchoidal fractures and it reflects the chip out of rock fragments due to the impact of abrasive particles. Striations may occur together with chatter marks, as shown just behind the “c”.

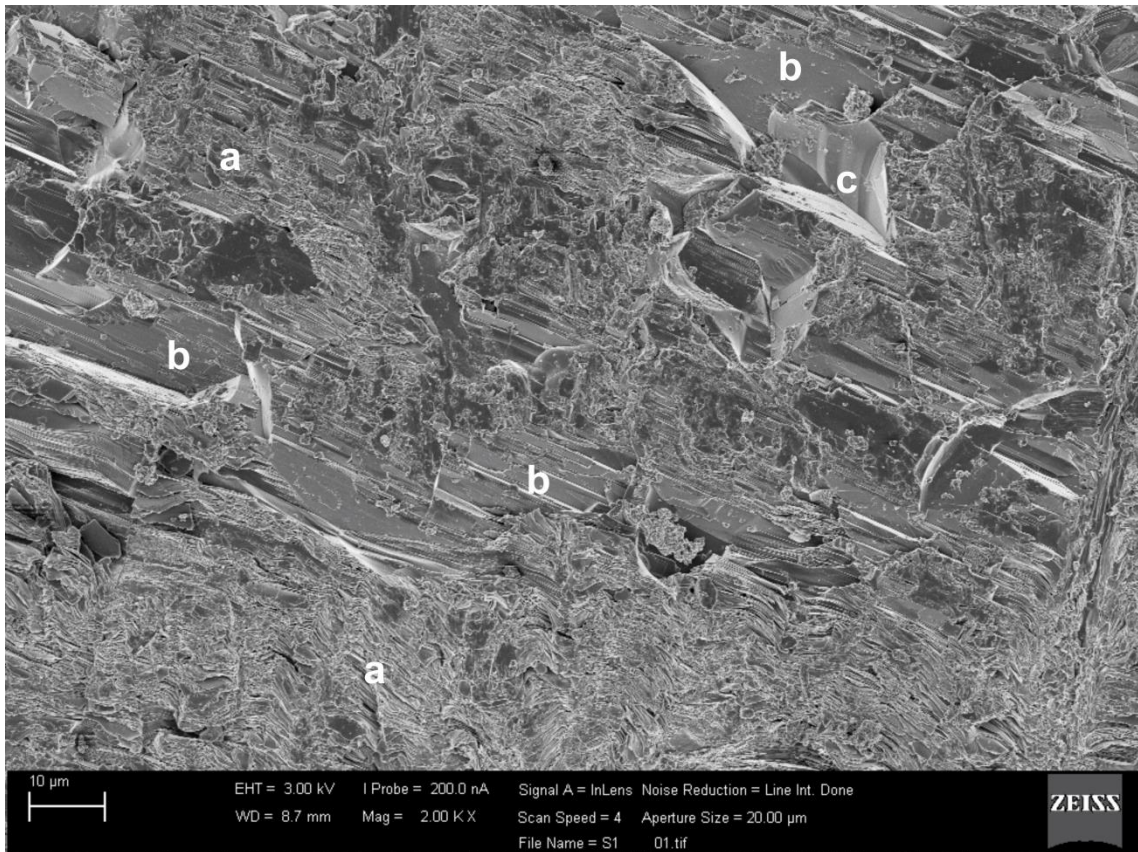


Figure 38 - SEM image of the nepheline monzosyenite: abrasion fatigue – a, fractures along cleavage planes – b, graded arcs – c.

The syenogranite also presents erosive fracturing/abrasion fatigue (Figure 39 “a”), however when compared to the nepheline monzosyenite, it shows more influence of fracturing following cleavages (Figure 39 “b”) because of the occurrence of large crystals of feldspar and plagioclase. Conchoidal fractures with both arcuate and straight steps are more common in quartz crystals (Figure 39 “c”), presenting smoother cut surfaces. Locally on the smoother surfaces it is possible to observe striations generated by the scratch of abrasive particles (Figure 39 “d”).

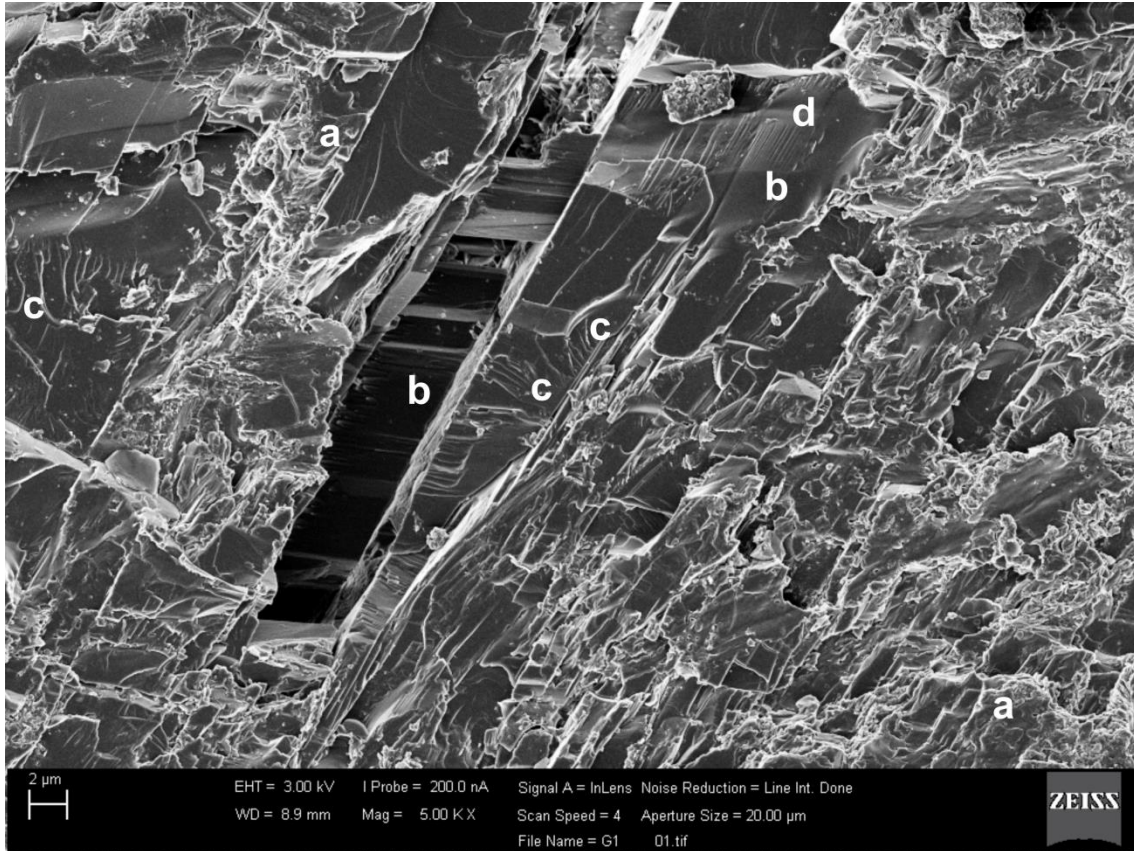


Figure 39 - SEM image of the syenogranite: abrasion fatigue – a, fractures along cleavage planes – b, conchoidal fractures – c, striations – d.

As observed in Figure 40 the removal mechanisms in the marble are guided by the cleavage planes of calcite. Most surfaces of the rock are smooth due to the precise breakage on the cleavage planes. Straight steps generated by this breakage occur all over the section. In a few areas erosive fracturing/abrasive fatigue also is present. Remnant fragments of the rock can be seen on its surface and they may be called adhering particles, since they remain attached to it as a product of abrasion fatigue. Adhering particles also occur in the nepheline monzosyenite and syenogranite, however it is more common in the marble and quartz sandstone.

In the quartz sandstone conchoidal fracturing dominates the section (Figure 41 “a”), being both straight and arcuate. Chattermarks are also common as semi-circular arcs (Figure 41 “b”), something presenting associated striations. The surface of the crystals present very sharp ridges and adhering particles are also observed. Striations occur sparsely as indicated in Figure 41 “d” and abrasive fatigue is a secondary process (Figure 41 “e”).

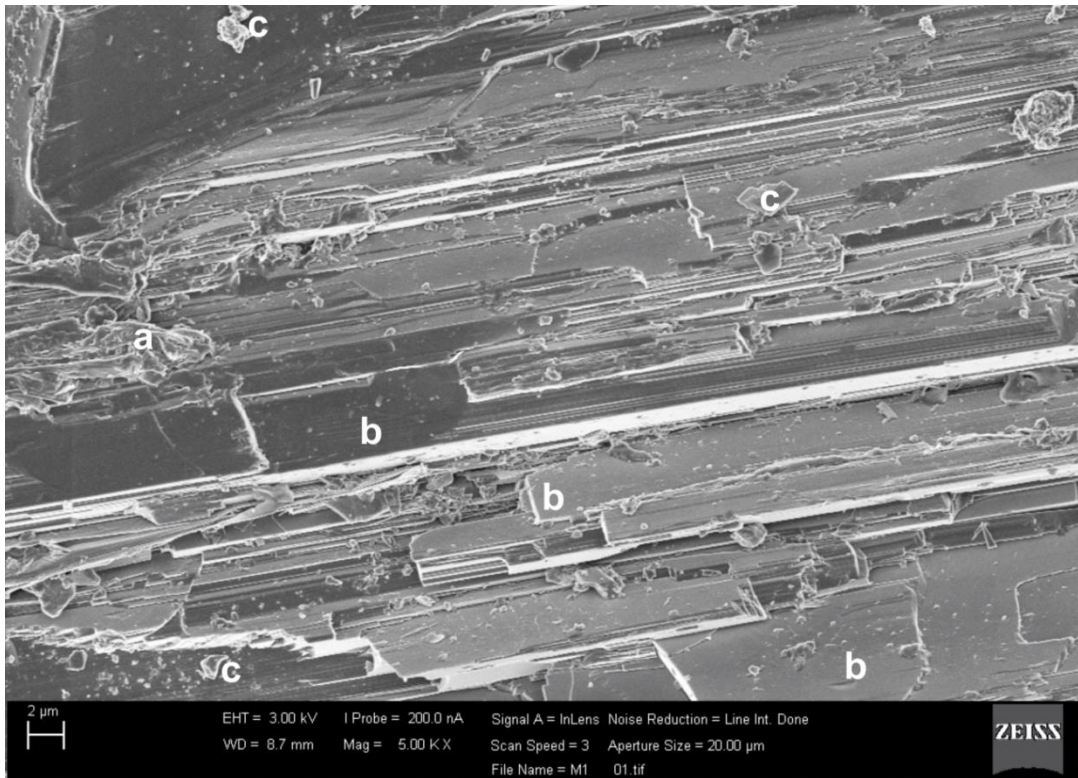


Figure 40 - SEM image of the marble: abrasion fatigue – a, fractures along cleavage planes – b, adhering particles– c.

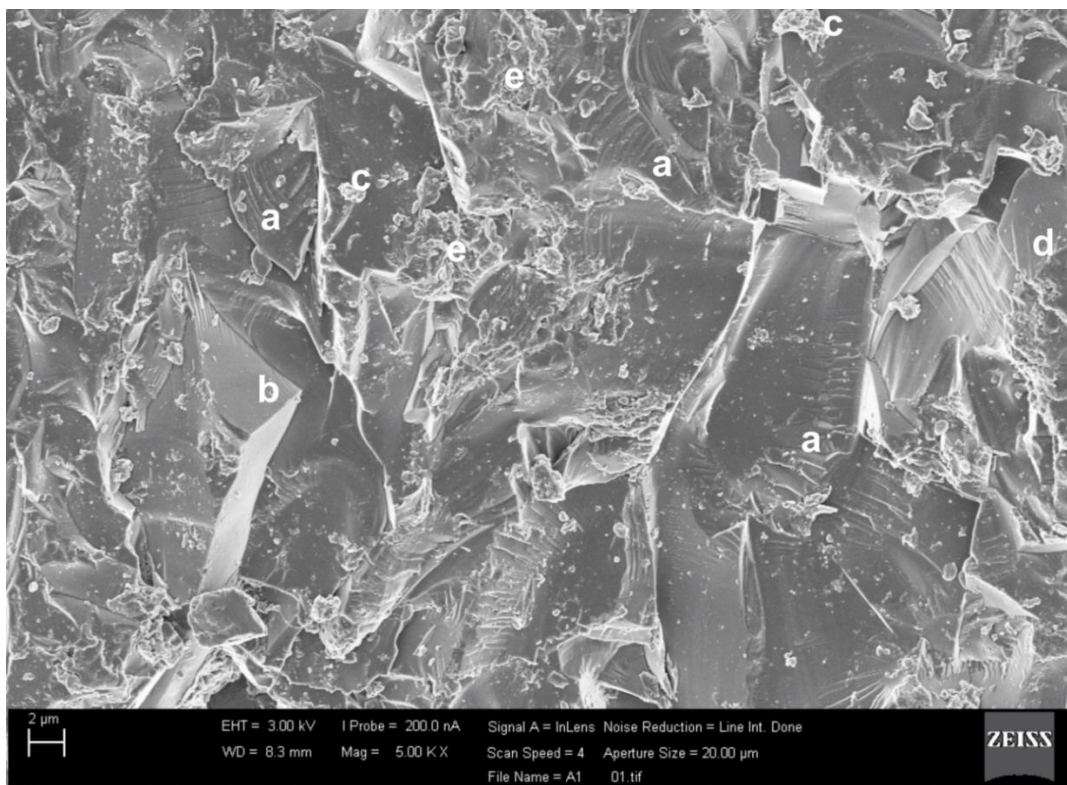


Figure 41 - SEM image of the sandstone: conchoidal fractures – a, chattermarks – b, adhering particles– c, striations – d, abrasion fatigue – e.

3.6. PHYSICO-MECHANICAL CHARACTERIZATION

3.6.1. Amsler test for abrasion resistance

The results of the Amsler abrasion test are presented in Table 6 through Table 9. Essentially, rocks which present minerals with low values of hardness tend to have a greater wear due to abrasion. Marble is composed mainly by calcite, which has a hardness value of 3 according to the Mohs scale. Thus, it presented the lowest resistance to abrasion among the studied rocks. Next, the quartz sandstone also presented low resistance to abrasion. Even being composed by quartz, it is a sedimentary rock with lower cohesion when compared to the studied igneous rocks, since its geological history did not involve great pressures in burial. Finally, the wear difference between the nepheline monzosyenite and the syenogranite is due to the fact that the first one is composed mainly by alkaline feldspars and plagioclase, which have Mohs hardness around 6, while the second one presents a high content of quartz, which has a hardness value of 7.

Table 6 - Results of the Amsler abrasion test for the nepheline monzosyenite.

Rock	Sample	Wear mm/500m	Wear mm/1000m
Nepheline Monzosyenite	1	0,38	0,84
	2	0,46	0,85
	3	0,43	0,88
	Mean	0,42	0,86
	Standard deviation	0,04	0,02
	Coefficient of Variation	9,55%	2,43%

Table 7 - Results of the Amsler abrasion test for the syenogranite.

Rock	Sample	Wear mm/500m	Wear mm/1000m
Syenogranite	1	0,23	0,68
	2	0,39	0,68
	3	0,43	0,67
	Mean	0,31	0,68
	Standard deviation	0,08	0,005
	Coefficient of Variation	26,15%	0,85%

Table 8 - Results of the Amsler abrasion test for the marble.

Rock	Sample	Wear mm/500m	Wear mm/1000m
Marble	1	3,92	8,08
	2	4,30	7,95
	3	4,07	7,84
	Mean	4,10	7,96
	Standard deviation	0,19	0,12
	Coefficient of Variation	4,67%	1,51%

Table 9 - Results of the Amsler abrasion test for the quartz sandstone.

Rock	Sample	Wear mm/500m	Wear mm/1000m
Quartz sandstone	1	0,53	1,54
	2	0,62	1,53
	3	0,76	1,53
	Mean	0,64	1,53
	Standard deviation	0,11	0,01
	Coefficient of Variation	18,20%	0,38%

3.6.2. Schmidt rebound hardness

The results of the tests are presented in Table 10 through Table 13. Values of hardness are similar between all rocks studied. Further it will be discussed that the results are not suitable for correlations because of this.

Table 10 – Results of Schmidt hardness for the nepheline monzosyenite.

Rock	Sample	Hardness
Nepheline monzosyenite	1	53
	2	53
	3	52
	4	50
	5	49
	6	48
	7	48
	8	46
	9	47
	10	46
	11	45
	12	45

	13	44
	14	44
	15	44
	Mean	47,60
	Standard deviation	3,094
	Coefficient of Variation	6,5%

Table 11 - Results of Schmidt hardness for the syenogranite.

Rock	Sample	Hardness
Syenogranite	1	56
	2	54
	3	49
	4	48
	5	47
	6	47
	7	46
	8	46
	9	45
	10	45
	11	45
	12	44
	13	44
	14	44
	15	44
	Mean	46,93
	Standard deviation	3,511
	Coefficient of Variation	7,48%

Table 12 - Results of Schmidt hardness for the marble.

Rock	Sample	Hardness
Marble	1	44
	2	42
	3	42
	4	39
	5	39
	6	40
	7	38
	8	38
	9	38
	10	38
	11	38

	12	37
	13	37
	14	37
	15	38
	Mean	39,0
	Standard deviation	2,03
	Coefficient of Variation	5,20%

Table 13 - Results of Schmidt hardness for the quartz sandstone.

Rock	Sample	Hardness
Quartz sandstone	1	48
	2	44
	3	44
	4	44
	5	42
	6	42
	7	42
	8	40
	9	40
	10	40
	11	39
	12	39
	13	38
	14	38
	15	38
	Mean	41,2
	Standard deviation	2,78
	Coefficient of Variation	6,75%

3.6.3. Dry density (ρ_d), saturated density (ρ_{SAT}), degree of saturation (S), porosity (η)

The results of the tests are summarized in Table 14 through Table 17. The values of all of the properties do not change dramatically for any of the rock types. Dry density values are very close in the igneous rocks, since both present essential minerals with similar values of dry density (alkaline feldspars and plagioclase: 2,55 to 2,76 g/cm³, quartz: 2,65 g/cm³ and nepheline: 2,55 to 2,65 g/cm³). Even so, the nepheline monzosyenite presents around 25% denser minerals than those presented by the syenogranite (augite, olivine, apatite and opaque

minerals) and the syenogranite also has more voids. The dry density of the marble is consistent with a rock which presents carbonates other than calcite, since its dry density is 2,72 g/cm³. The petrographic analysis shows that dolomite also occurs, a fact that is corroborated due to the high dry density of the marble (dolomite dry density is 2.85 g/cm³). Finally, the quartz sandstone presents the lowest value of dry density. It is less than the dry density of quartz, but this is because the rock is sedimentary, and sedimentary rocks tend to have more voids and lower degree of compaction.

Table 14 - Results of rock properties (ρ_d , ρ_{SAT} , S and η) for the nepheline monzosyenite.

Rock	Sample	ρ_d (g/cm ³)	ρ_{SAT} (g/cm ³)	S (%)	η (%)
Nepheline monzosyenite	1	2,717	2,717	0,020	0,054
	2	2,692	2,693	0,026	0,071
	3	2,697	2,697	0,026	0,071
	4	2,752	2,753	0,023	0,063
	5	2,707	2,708	0,033	0,090
	6	2,707	2,708	0,020	0,053
	7	2,716	2,717	0,023	0,063
	8	2,716	2,717	0,017	0,045
	9	2,710	2,710	0,020	0,054
	10	2,716	2,717	0,026	0,072
	Mean	2,713	2,714	0,023	0,064
	Standard deviation	0,016	0,016	0,0048	0,013
	Coefficient of variation	0,59%	0,59%	20,42%	20,26%

Table 15 - Results of rock properties (ρ_d , ρ_{SAT} , S and η) for the syenogranite.

Rock	Sample	ρ_d (g/cm ³)	ρ_{SAT} (g/cm ³)	S (%)	η (%)
Syenogranite	1	2,621	2,623	0,062	0,162
	2	2,588	2,591	0,085	0,220
	3	2,606	2,608	0,052	0,136
	4	2,602	2,603	0,069	0,178
	5	2,609	2,610	0,055	0,144
	6	2,620	2,622	0,068	0,178
	7	2,595	2,596	0,062	0,162
	8	2,618	2,620	0,082	0,215
	9	2,631	2,634	0,111	0,292
	10	2,593	2,594	0,051	0,133
	Mean	2,608	2,610	0,070	0,182
	Standard deviation	0,013	0,014	0,017	0,049
	Coefficient of variation	0,52%	0,59%	20,42%	26,83%

The saturated density values practically do not change, since all rocks have very low permeability. The values of degree of saturation and porosity also do not change substantially, being higher for the quartz sandstone because it is a sedimentary rock with lower cohesion than the other rocks.

Table 16 - Results of rock properties (ρ_d , ρ_{SAT} , S and η) for the marble.

Rock	Sample	ρ_d (g/cm ³)	ρ_{SAT} (g/cm ³)	S (%)	η (%)
Marble	1	2,828	2,831	0,115	0,326
	2	2,814	2,816	0,103	0,291
	3	2,811	2,814	0,111	0,313
	4	2,824	2,827	0,111	0,313
	5	2,831	2,833	0,092	0,260
	6	2,816	2,819	0,122	0,343
	7	2,829	2,832	0,102	0,288
	8	2,826	2,830	0,141	0,397
	9	2,812	2,815	0,110	0,309
	10	2,828	2,831	0,102	0,289
	Mean	2,822	2,825	0,111	0,313
	Standard deviation	0,0079	0,0078	0,013	0,037
	Coefficient of variation	0,28%	0,29%	12,02%	12,00%

Table 17 - Results of rock properties (ρ_d , ρ_{SAT} , S and η) for the quartz sandstone.

Rock	Sample	ρ_d (g/cm ³)	ρ_{SAT} (g/cm ³)	S (%)	η (%)
Quartz sandstone	1	2,307	2,337	1,317	3,039
	2	2,314	2,342	1,225	2,835
	3	2,305	2,333	1,228	2,830
	4	2,324	2,352	1,218	2,830
	5	2,331	2,358	1,149	2,679
	6	2,327	2,354	1,160	2,700
	7	2,296	2,325	1,292	2,965
	8	2,296	2,326	1,291	2,965
	9	2,317	2,344	1,137	2,635
	10	2,309	2,337	1,224	2,826
	Mean	2,313	2,341	1,224	2,830
	Standard deviation	0,012	0,011	0,062	0,132
	Coefficient of variation	0,53%	0,48%	5,10%	4,68%

3.6.4. Brazilian test for the tensile strength

The results of the Brazilian tests are shown in Table 18 to Table 21. The marble presents the lowest tensile strength, which may be due to the calcite's three perfect directions of cleavage, which considerably reduce the strength of the rock. Also, the marble is not as brittle as the other rocks, thus it does not accumulate very much energy before rupture. This happens because cracks in marble are developed progressively and even when the applied load is somewhat at a stage around 50% of the maximum load value (RODRÍGUEZ, 2016). In that way, coalescence is not abrupt or explosive. The second weakest strength is observed in the syenogranite and it is mainly due to the coarse granulation of the rock which facilitates the propagation of cracks through the cleavages of alkaline feldspars and plagioclase. Despite the presence of feldspar and plagioclase in the nepheline monzosyenite, this rock has a fine to medium granulation, thus the contact between minerals is more cohesive and the cleavages remain not as exposed as in the case of the syenogranite. Finally, the quartz sandstone has the second greatest tensile strength. Although it is a sedimentary rock, the presence of quartz grains and silica cement makes the rock resistant to this type of solicitation because quartz does not have weakness planes as cleavages. Thus, it accumulates relatively high energy before rupture with very little deformation.

At least five samples were tested of each type of rock. As the nepheline monzosyenite and the syenogranite are more heterogeneous, a sixth sample was tested in order to obtain a variation coefficient similar to that of the marble, around 15%.

Table 18 - Results of the Brazilian test for the nepheline monzosyenite.

Rock	Sample	Maximum load (kN)	Tensile strength (MPa)	
Nepheline Monzosyenite	1	25,85	11,29	
	2	29,11	12,75	
	3	34,82	15,30	
	4	33,91	14,96	
	5	25,85	11,41	
	6	30,68	13,46	
		Mean		13,20
		Standard deviation		1,71
		Coefficient of Variation		12,97%

Table 19 - Results of the Brazilian test for the syenogranite.

Rock	Sample	Maximum load (kN)	Tensile strength (MPa)	
Syenogranite	1	19,66	8,06	
	2	23,43	9,56	
	3	27,52	12,36	
	4	22,26	9,59	
	5	26,26	11,46	
	6	23,18	9,96	
		Mean		10,17
		Standard deviation		1,53
		Coefficient of Variation	15,01%	

Table 20 - Results of the Brazilian test for the marble.

Rock	Sample	Maximum load (kN)	Tensile strength (MPa)	
Marble	1	11,29	4,59	
	2	11,90	4,82	
	3	7,80	3,17	
	4	11,35	4,59	
	5	9,72	3,93	
		Mean		4,22
		Standard deviation		0,67
		Coefficient of Variation	15,91%	

Table 21 - Results of the Brazilian test for the quartz sandstone.

Rock	Sample	Maximum load (kN)	Tensile strength (MPa)	
Quartz sandstone	1	29,66	12,26	
	2	27,02	11,25	
	3	30,73	12,66	
	4	29,72	12,24	
	5	29,55	12,17	
		Mean		12,11
		Standard deviation		0,52
		Coefficient of Variation	4,29%	

3.6.5. Uniaxial compressive strength from the uniaxial compression test

The results of the tests are presented in Table 22 through Table 25. The uniaxial compressive strength (*UCS*) values of the rocks follow the same pattern shown in the Brazilian test, with the crescent strength of: the marble, syenogranite, sandstone and nepheline monzosyenite.

Table 22 - Results of the *UCS* test for the nepheline monzosyenite.

Rock	Sample	Maximum load (kN)	UCS (MPa)	
Nepheline monzosyenite	1	599,56	266,77	
	2	566,55	251,74	
	3	603,50	267,53	
	4	610,96	246,29	
	5	606,70	253,52	
		Mean		257,17
		Standard deviation		9,49
		Coefficient of Variation		3,69%

Table 23 - Results of the *UCS* test for the syenogranite.

Rock	Sample	Maximum load (kN)	UCS (MPa)	
Syeno granite	1	385,20	171,46	
	2	423,28	188,95	
	3	369,95	164,71	
	4	489,55	195,95	
	5	473,75	190,98	
		Mean		182,41
		Standard deviation		13,53
		Coefficient of Variation		7,42%

The values of the elastic parameters Young's modulus (*E*) and Poisson ratio (ν) for all rocks are shown in Table 26 through

Table 29. According to Goodman (1989) when the modulus value is calculated from the slope of a virgin loading curve, it embraces both recoverable and nonrecoverable deformation, thus it is more appropriated to use the term deformability modulus. In the present research, the term Young's modulus is used to follow the suggestions of the ISRM standards, however it is kept in mind that the real meaning of it involves both types of deformation.

Table 24 - Results of the *UCS* test for the marble.

Rock	Sample	Maximum load (kN)	UCS (MPa)	
Marble	1	157,76	66,19	
	2	168,29	70,71	
	3	179,59	75,91	
	4	174,74	70,44	
	5	162,53	65,52	
		Mean		69,75
		Standard deviation		4,18
		Coefficient of Variation		5,99%

Table 25 - Results of the *UCS* test for the quartz sandstone.

Rock	Sample	Maximum load (kN)	UCS (MPa)	
Quartz sandstone	1	390,89	174,32	
	2	477,93	213,56	
	3	431,16	192,40	
	4	471,23	190,64	
	5	465,46	188,31	
		Mean		191,85
		Standard deviation		14,08
		Coefficient of Variation		7,34%

The nepheline monzosyenite and the syenogranite present essentially the same Young's modulus. Non-weathered igneous rocks like syenites, granites, basalts and diabases tend to be resistant to deformation, since they are formed from the cooling of magma in more homogeneous environments, acquiring a stiffer behavior. Marble is still considered a stiff material, but not as stiff as igneous rocks because its behavior is completely dependent on the rearrangement of calcite's cleavage, which makes the rock deform more. Quartz sandstone

presents a high value of Young's modulus considering the range of sandstones. Its porosity and sedimentary character contributes to a lower value of modulus when compared to the other rocks studied.

It is interesting to compare the values of Poisson's ratio for these rocks. Again nepheline monzosyenite and syenogranite present similar values. The syenogranite has a slightly higher poisson ratio because of a tendency to expand more in a direction perpendicular to loading due to opening of cracks in the bigger crystals of feldspar and plagioclase. Marble has an even higher value because of the opening of cracks in calcite, which is facilitated by the existence of three directions of cleavage. Finally, even though quartz sandstone has a lower Young's modulus, it presents the greatest resistance to expand laterally. That may be because of the stiff behavior of quartz. In this case, it is much easier to deform parallel to loading direction than perpendicular to it. This rock may be deformed because of compaction and it stores high levels of energy. However, the same does not occur in the perpendicular direction.

Table 26 - Elastic parameters for the nepheline monzosyenite.

Rock	Sample	E (GPa)	v
Nepheline monzosyenite	1	71,78	0,30
	2	73,55	0,21
	3	79,22	0,20
	4	73,86	0,21
	5	78,31	0,23
	Mean	75,34	0,23
	Standard deviation	3,24	0,04
	Coefficient of Variation	4,30%	17,83%

Table 27 - Elastic parameters for the syenogranite.

Rock	Sample	E (GPa)	v
Syenogranite	1	73,32	0,30
	2	71,62	0,24
	3	76,57	0,27
	4	75,66	0,32
	5	72,36	0,25
	Mean	73,91	0,28
	Standard deviation	2,13	0,03
	Coefficient of Variation	2,88%	12,73%

Table 28 - Elastic parameters for the marble.

Rock	Sample	E (GPa)	v
Marble	1	55,53	0,27
	2	45,22	0,32
	3	60,71	0,28
	4	55,68	0,37
	5	57,07	0,33
	Mean	54,84	0,31
	Standard deviation	5,77	0,04
	Coefficient of Variation	10,52%	13,27%

Table 29 - Elastic parameters for the quartz sandstone.

Rock	Sample	E (GPa)	v
Quartz sandstone	1	33,79	0,11
	2	33,94	0,10
	3	33,54	0,15
	4	34,15	0,16
	5	34,72	0,12
	Mean	34,03	0,13
	Standard deviation	0,45	0,02
	Coefficient of Variation	1,31%	20,22%

From the uniaxial compression test, the stress strain curves of the studied rocks were obtained (Figure 42). A displacement rate of 0,025 mm/min and circumferential displacement control were adopted. From the steepness of the curves, it is observed that the sandstone presents the higher stiffness, although it does not present the highest uniaxial compressive strength. Then, decreasing stiffness is observed for the syenite, the granite and finally the marble. From the curves, the specific energies of the rocks (SE_R) were calculated as the area under the stress strain curve until the peak strength. The results are presented in Table 30 through Table 33.

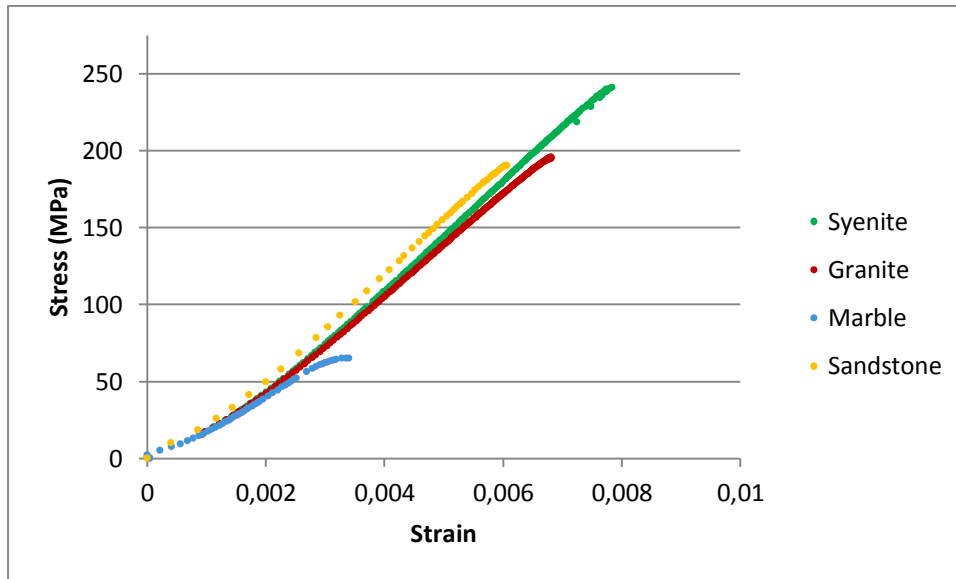


Figure 42 – Stress strain curves of the rocks studied.

Table 30 - Specific energy (SE_R) for the nepheline monzosyenite.

Rock	Sample	SE_R (kJ/m ³)
Nepheline Monzosyenite	1	859,26
	2	883,41
	3	866,28
	4	940,30
	5	907,53
	Mean	891,35
	Standard deviation	0,029
	Coefficient of Variation	30,11%

Table 31 - Specific energy (SE_R) for the syenogranite.

Rock	Sample	SE_R (kJ/m ³)
Syenogranite	1	611,01
	2	586,23
	3	611,56
	4	657,30
	5	598,89
	Mean	612,93
	Standard deviation	0,024
	Coefficient of Variation	25,52%

Table 32 - Specific energy (SE_R) for the marble.

Rock	Sample	SE_R (kJ/m³)
Marble	1	127,88
	2	115,12
	3	100,43
	4	132,68
	5	119,11
	Mean	119,03
	Standard deviation	0,011
	Coefficient of Variation	10,64%

Complete stress strain curves also were obtained for the studied rocks, except for the sandstone. It is known that the sandstone presents a class II behavior, but the servo-controlled machine was not able to control the tests in order to obtain the complete curve for this rock. Its rupture involves explosive coalescence of few cracks, thus only post-peak information until 120 MPa was acquired. The shapes of the curves reveal that the marble is the only rock with class I behavior, thus it may be called a ductile rock (or less brittle rock); and the syenite, granite and sandstone present class II behavior, with the sandstone as the most brittle rock. The obtained values of destruction work for the syenite, granite and marble are presented in Table 34 through Table 36.

Table 33 - Specific energy (SE_R) for the quartz sandstone.

Rock	Sample	SE_R (kJ/m³)
Quartz Sandstone	1	585,36
	2	564,40
	3	542,37
	4	634,69
	5	587,17
	Mean	582,79
	Standard deviation	0,030
	Coefficient of Variation	19,02%

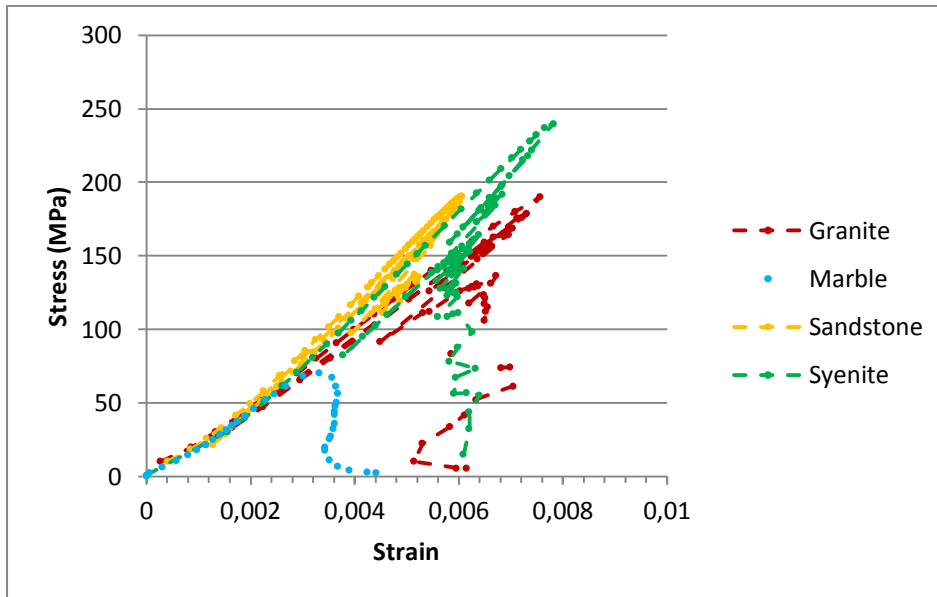


Figure 43 – Complete stress strain curves of the studied rocks.

Table 34 - Destruction work (W_R) for the nepheline monzosyenite.

Rock	Sample	W_R (kJ/m ³)
Nepheline Monzosyenite	1	332,06
	2	322,53
	3	317,26
	Mean	323,53
	Standard deviation	0,0061
	Coefficient of Variation	1,89%

Table 35 - Destruction work (W_R) for the syenogranite.

Rock	Sample	W_R (kJ/m ³)
Syenogranite	1	293,26
	2	274,47
	3	281,52
	Mean	283,08
	Standard deviation	7,750
	Coefficient of Variation	2,74%

Table 36 - Destruction work (W_R) for the marble.

Rock	Sample	W_R (KJ/m ³)
Marble	1	136,45
	2	129,11
	3	132,07
	Mean	132,54
	Standard deviation	3,015
	Coefficient of Variation	2,27%

3.6.6. Fracture toughness from the edge notched disc wedge splitting test (END)

The results of the END test are shown in Table 37 through Table 40. As usual, the nepheline monzosyenite presents the highest resistance to crack propagation, followed by the syenogranite. The quartz sandstone presents greater fracture toughness than the marble, since it is easier for a crack to propagate through calcite crystals than quartz crystals or silica cement.

Table 37 - Results of fracture toughness (K_{IC}) for the nepheline monzosyenite.

Rock	Sample	K_{IC} (MPa \sqrt{m})
Nepheline monzosyenite	1	2,447
	2	1,536
	3	1,711
	4	2,354
	5	1,467
	6	2,111
	7	2,223
	Mean	1,978
	Standard deviation	0,40
	Coefficient of Variation	20,29%

Table 38 - Results of fracture toughness (K_{IC}) for the syenogranite.

Rock	Sample	K_{IC} (MPa \sqrt{m})
Syenogranite	1	1,266
	2	1,391
	3	1,422
	4	1,661
	5	1,297
	6	1,667
	7	1,739
	Mean	1,492
	Standard deviation	0,19
	Coefficient of Variation	12,96%

Table 39 - Results of fracture toughness (K_{IC}) for the marble.

Rock	Sample	K_{IC} (MPa \sqrt{m})
Marble	1	0,410
	2	0,421
	3	0,396
	4	0,371
	5	0,444
	6	0,395
	7	0,392
	Mean	0,404
	Standard deviation	0,02
	Coefficient of Variation	5,80%

Table 40 - Results of fracture toughness (K_{IC}) for the quartz sandstone.

Rock	Sample	K_{IC} (MPa \sqrt{m})
Quartz sandstone	1	1,050
	2	0,910
	3	1,208
	4	1,102
	5	1,054
	6	0,958
	7	1,092
	Mean	1,053
	Standard deviation	0,09
	Coefficient of Variation	9,29%

Table 41 presents a summary of the properties of the rocks studied.

Table 41. Summary of the properties of the rocks studied.

	Monzosyenite	Syenogranite	Marble	Sandstone
Amsler wear (mm/500 m)	0,42	0,31	4,10	0,64
Amsler wear (mm/1000 m)	0,86	0,68	7,96	1,53
Dry density (g/cm³)	2,713	2,608	2,822	2,313
Saturated density (g/cm³)	2,714	2,610	2,825	2,341
Degree of saturation (%)	0,023	0,070	0,111	1,224
Porosity (%)	0,064	0,182	0,313	2,830
Tensile strength (MPa)	13,20	10,17	4,22	12,11
Uniaxial compressive strength (MPa)	257,17	182,41	69,75	191,85
Young's Modulus (GPa)	75,34	73,91	54,84	34,03
Poisson's ratio	0,23	0,28	0,31	0,13
Specific energy (kJ/m³)	891,35	612,93	119,03	582,79
Specific destruction work (kJ/m³)	323,53	283,08	132,54	-
Fracture toughness (MPa^{1/2}/m)	1,978	1,492	0,404	1,053

4. ABRASIVE WATERJET CUTTING TESTS

4.1. THE ABRASIVE WATERJET MACHINE

The cutting tests were executed at the company ICAM Waterjet (Indústria Comercializadora de Artefatos de Metal), which is located in São Carlos – SP. It was the first company in Brazil to acquire an abrasive waterjet machine.

The machine is a Flow Mach 2C with pressure up to 400 MPa and maximum traverse velocity of 12 m/min. The tests performed involved a pressure ranging from 100 to 400 MPa and a traverse velocity range from 100 to 400 mm/min. An attempt of working with variations of abrasive flow rate was conducted, but as the company works with a narrow range thereof, unsubstantiated results were obtained. Also, working with varying angle of the nozzle was not possible, because it cuts with a 90° fixed position. ICAM's AWJ machine and some of its main components are presented on Figure 44. Figure 45 shows a detailed flowchart of the AWJ operating system.

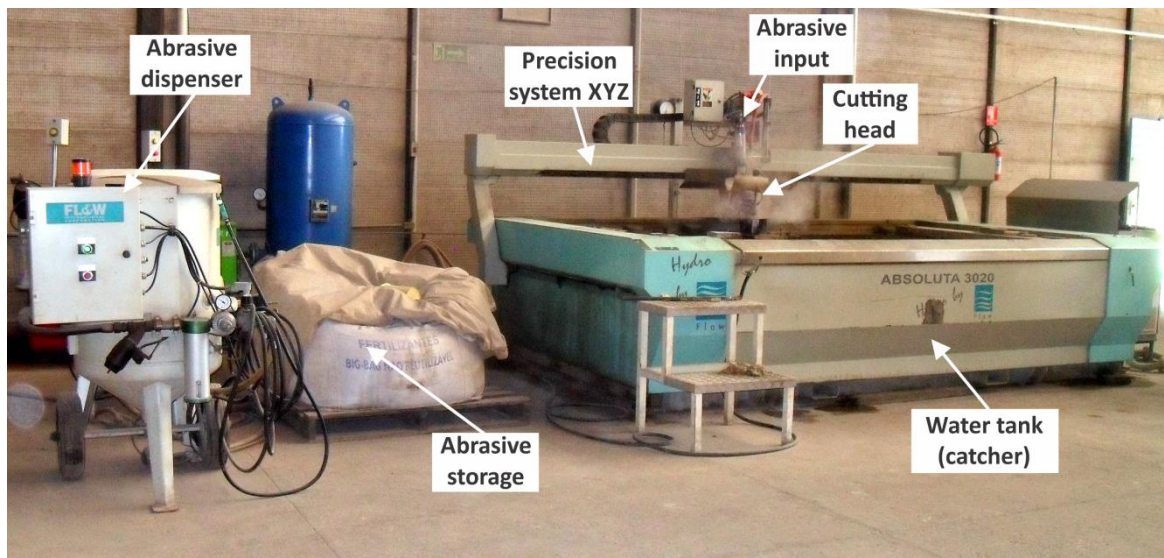


Figure 44 - AWJ machine and its main components.

The operating system consists of two main circuits which work combined: the water circuit and the hydraulic oil circuit. Initially, tap water is filtered through the inlet water filtration system, and then it travels to a booster pump, where the inlet water pressure is

maintained at approximately 620 KPa to ensure the feeding of the intensifier. As explained in chapter 2, the hydraulic pump connected to the system is called a double intensifier pump, since it is responsible for amplifying the water pressure. In the case of ICAM's machine, this pump makes it possible to deliver high pressure water (up to 400 MPa) to the nozzle, which is situated at the tip of the cutting head. Figure 46 shows in detail the intensifier pump and the attenuator composition.

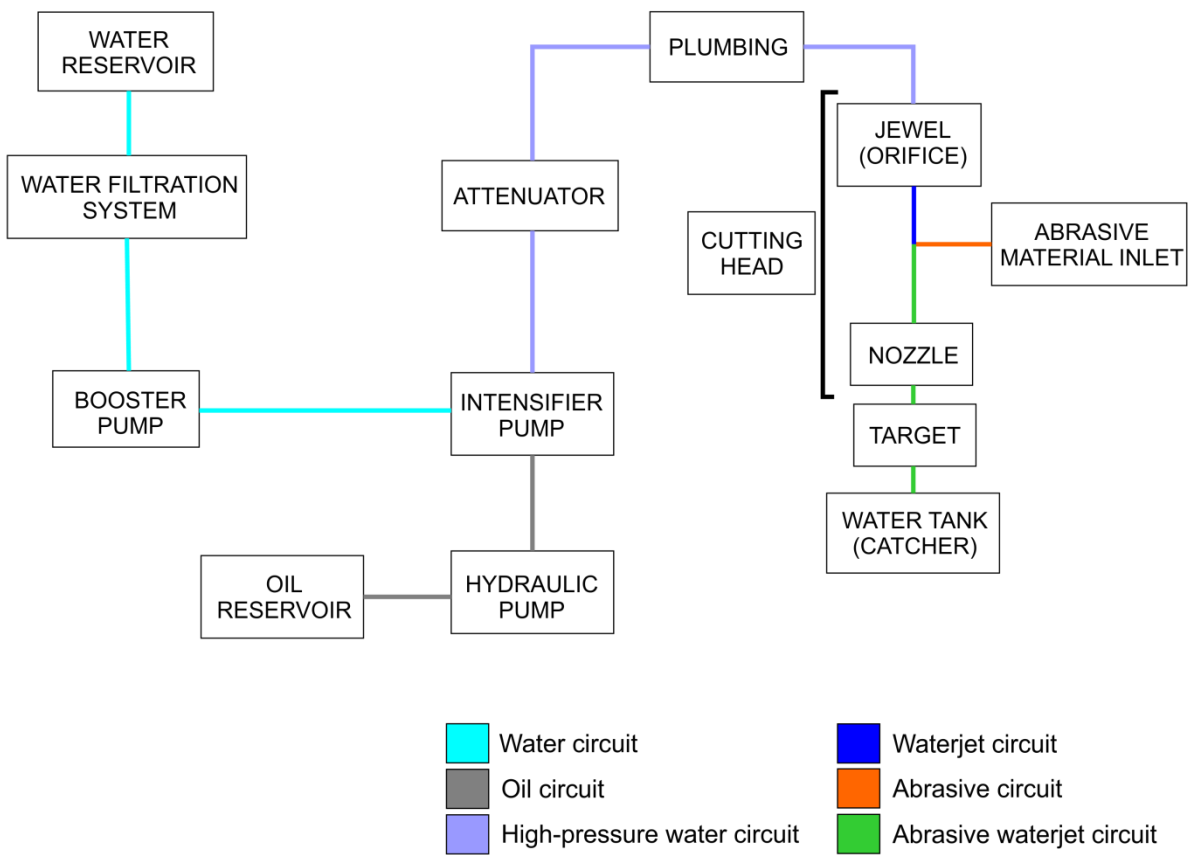


Figure 45 - Flowchart of the AWJ operating system.

Regarding the hydraulic circuit, the oil is kept inside a reservoir and a hydraulic pump powered by a 100 HP electric motor pulls it and pressurizes it to 20 MPa. The pressurized oil is pulled to the intensifier and then it acts on the amplification of the water pressure.

After leaving the intensifier pump, the water goes through the attenuator, a valve that damps pressure fluctuations to ensure a steady and consistent flow to the cutting head.

According to Summers (1995), these fluctuations interfere on the quality and depth of the kerf, besides leading to an early wear of components like pipelines, valves and orifices.

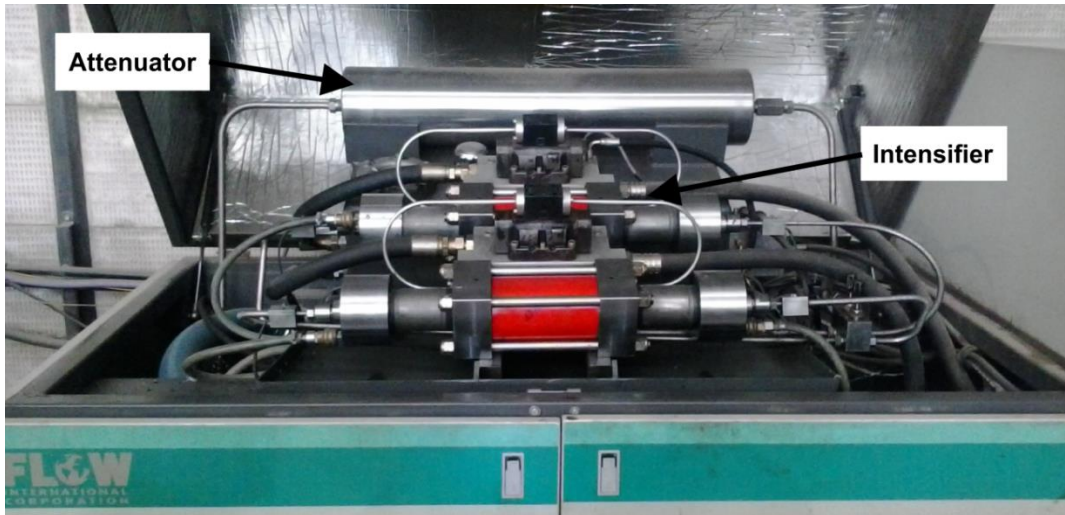


Figure 46 - Intensifier pump and attenuator of the cutting machine

The abrasive material is stored in dispensers and the main dispenser is connected to the cutting head with a hose, so it may deliver the abrasive particles to the system at predetermined flow rates.

The cutting head is responsible for driving and accelerating the abrasive particles through the orifice, generating a high velocity waterjet, which is capable of cutting even hard materials like brittle rocks. Figure 47 shows the cutting of a piece of rock, capturing the steam generation due to the large thickness of the sample and the non-traversing character of the AWJ.

Precision system XYZ is composed by a horizontal beam, which stands above the cutting area and is fixed on its sides, at the edges of the cutting table. The cutting head may move along the Y axis, parallel to the beam. Attached to the cutting head, there is an arm that allows motion along the X axis, which is on the same plane of the Y axis and perpendicular to the beam. So, the arm has a vertical motion that corresponds to the Z axis. The hydraulic pump and the cutting head controls are guided by a CAD/CAM software named Flow Lantek Expert 2010. This interface provides the high precision cut of the materials. Through a remote

control, it is also possible to control the main functions of the machine, such as the pump pressure, traverse velocity, the start and the stop.



Figure 47 - AWJ during the cutting of a granite sample.

The catcher is a water tank which absorbs the kinetic energy of the waterjet after cutting. Otherwise it would damage the floor. On the top of the catcher there are parallel steel bars where the samples to be cut are placed (Figure 48).

As presented in Figure 6, the cutting head is composed by orifice, abrasive material inlet, body, collet, retaining nut and mixing tube (nozzle). Under pressure, the water flows through the orifice to the mixing tube, creating a partial vacuum area. The vacuum sucks up a predetermined amount of abrasive material, which corresponds to a given abrasive rate, and it blends with the water, generating the high velocity abrasive waterjet.

The tapering body of the cutting head aligns the orifice and the mixing chamber. Inside the orifice, there is another tiny orifice which is called a jewel, because it is made of diamond or corundum. This is the piece that creates the high velocity waterjet by means of constriction. According to Sérgio Pepino, the owner of ICAM Waterjet (verbal communication), it is preferable to use a diamond piece; because it has a life of 500 hours, while a corundum piece has a life of 50 hours. Although the diamond jewel is more

expensive, it does not have to be replaced as many times as a piece made of corundum. The replacement action also contributes to an earlier wear of other pieces of the machine.



Figure 48 - Detail of the top of the water tank with steel bars.

The cutting head also presents two abrasive material entries, in a way that there will always be one entry closer to the abrasive material feed line after the threading, and this one is the selected one to be used. Just after the pressurized water is turned into a high velocity waterjet, the abrasive material is provided to the system through suction. Inside the mixing chamber, both water and abrasive particles have enough time to homogenize.

The abrasive material used in this research is almandine garnet, which is the abrasive material utilized most often in the waterjet industry due to its efficiency. Ohman (1993) states that garnet has several characteristics which make it a good abrasive material: high hardness (6,5 to 7,5 according to the Mohs Scale), dodecahedral to trapezohedral habit (i.e. the external shape of the mineral) with angular edges and high specific mass (3,1 to 4,3 g/cm³). The author also claims that the grain size plays an important role in the cutting efficiency, with 80 mesh as the best choice. Moreover, Vasek et al. (1993) say that almandine is the most resistant garnet variety related to impact resistance, thus it undergoes lesser comminution. The abrasive material used by ICAM comes from Canada and it is currently being recycled by the company with a reuse of 40% of the same granulometry (80 mesh) and up to 70% of smaller ones.

An abrasive grain size characterization was performed for ICAM’s abrasive material at the Soil Mechanics Laboratory of the Geotechnical Engineering Department of USP. Figure 49 presents the grain size distribution of the material, which is composed by angular almandine garnet particles. The test was done with intact abrasive particles, before being used in AWJ cutting.

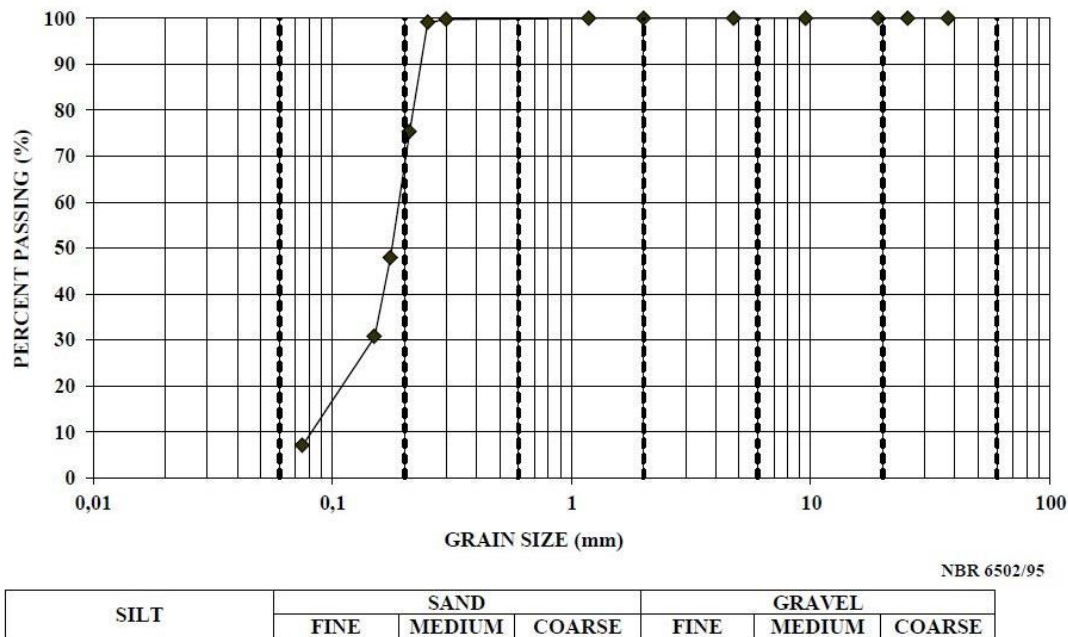


Figure 49 - Grain size distribution for ICAM’s garnet abrasive material.

4.2. RELEVANT PARAMETERS ON AWJ CUTTING

All parameters nomenclature regarding the AWJ cutting is found in the Table of Notations. As this topic belongs to a multidisciplinary area and it involves a large quantity of terms, it is also important to present its basic operation parameters and their definitions (Table 42). The presented grouping of variables is based on the nomenclature proposed by Momber & Kovacevic (1998).

The pump pressure (P) corresponds to the pressure exerted by the intensifier pump, when it pushes the water up to the cutting head. As stated before, it is important to emphasize that there is no waterjet pressure, because after the waterjet is created, it is not confined

anymore. Therefore, a high energy or high velocity waterjet is generated, not a high pressure waterjet.

The waterjet velocity (V_J) is the velocity of the waterjet at the early moment when it leaves the jewel, before incorporating the abrasive particles when it passes through the nozzle.

Table 42 - Nomenclature and abbreviation of important operation parameters.

Operation parameters	Nomenclature and abbreviation
Hydraulic Parameters	Pump pressure (P)
	Waterjet velocity (V_J)
	Orifice (jewel) diameter (d_0)
	Water mass flow rate (m_W)
Cutting parameters	Traverse velocity (v_T)
	Stand-off distance (h_S)
	Impact angle (Θ)
	Exposure time (t_E)
Mixture and acceleration parameters	Nozzle (focus) diameter (d_F)
	Abrasive waterjet velocity (V_{AJ})
Abrasive parameters	Abrasive mass flow rate (m_A)
	Abrasive particle diameter (d_A)
	Granulometric distribution ($f(d_A)$)

The orifice diameter (d_0) is the smallest diameter of the cutting head, that is to say, the inner diameter of the jewel, through where the water has to pass to become a high velocity waterjet.

The water mass flow rate (m_W) is the quantity of water mass which flows in a certain period of time.

The traverse velocity (v_T) is the velocity with which the cutting head moves along the target surface (XY plane) so that it may be cut. It is also called the nozzle displacement velocity.

The stand-off distance (h_s) is the distance between the lower tip of the cutting head and the surface of the target, while the impact angle (θ) is the one measured between the waterjet direction and the cutting surface.

The exposure time (t_E) is the time that the AWJ remains at the same location on the top of the target. In other words, it is the period of time that a little area on the top of the target is exposed to the impact of the AWJ.

The nozzle (focus) diameter (d_F) is the inner diameter of the nozzle, through which the waterjet passes after it leaves the jewel, so it may receive the abrasive particles in order to generate the AWJ.

The abrasive waterjet velocity (V_{AJ}) is the velocity of the AWJ, that is to say, the velocity acquired after the water and abrasive particles are homogenized. For further calculations on this research, this parameter is calculated as the velocity with which the AWJ impacts the target, considering losses incurred in its path.

The abrasive mass flow rate (m_A) is the quantity of abrasive mass which flows in a certain period of time.

The abrasive particle diameter (d_A) is the maximum diameter of the abrasive particles that are retained in a certain mesh. In order to be aware of the exact particle diameter, it is necessary to know its granulometric distribution ($f(d_A)$), which is obtained by means of a sieve grain size characterization.

4.3. PREPARATION OF ROCK SPECIMENS FOR CUTTING TESTS

The blocks of rocks were cut and rectified as rectangular prisms with minimum dimensions of 100 x 100 x 160 mm, with the aid of a hand-made electric saw and a grinding machine RAPH 640 from Usimaq Indústria & Comércio Ltda. Attention was paid in order to avoid blocks with apparent heterogeneities such as veins, beddings or areas with prominent weathering features, as well as cracks.

The samples had to be fixed onto wood plates so that they could be clamped at the steel supports of the AWJ machine's water tank (Figure 50). For this, epoxy adhesive was used to bond specimens and wood plates together. These clamps are used in order to reduce the effect of both the machine's and the operation's vibrations.

The machine parameters and the height of the samples were adjusted so that the AWJ did not cross over the bottom of the sample. In that way, the AWJ removed rock material from the samples, without splitting it and preserving kerfs, so that the disaggregated volume could be obtained.

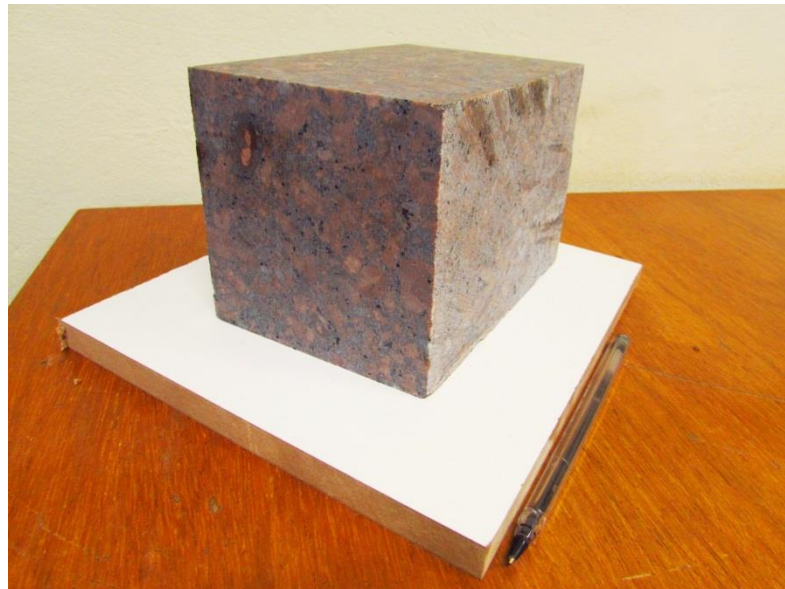


Figure 50 - Rock sample prepared to cutting tests

4.4. MEASUREMENT OF THE VOLUME OF THE KERFS GENERATED BY THE AWJ MACHINE

After the cut, the bonded wood plates were carefully removed with the aid of a chisel and a rubber hammer. In order to measure the volume of the rock kerfs, the sides of the specimens were sealed with high density polyethylene (HDPE) membranes and wood plates. Then, they were tightened with the aid of two c-clamps (Figure 51a).



Figure 51 - Procedure to measure the volume of the kerfs: a) tighten specimen, b) mercury introduction.

Thereafter, metallic mercury was introduced with a disposable syringe inside the kerfs until they were filled to the top of the samples (Figure 51b). The volume of mercury inside each kerf was then calculated, corresponding to the volumes of the kerfs themselves. In equation 13, V is the volume of the kerf (cm^3), m_{Hg} is the mass of mercury (g), m_s is the mass of the syringe (g) and 13,58 corresponds to the specific mass of mercury (g/cm^3):

$$V = \frac{m_{\text{Hg}} - m_s}{13,58} \quad (13)$$

For each condition of the tests – variation of traverse velocity and variation of pump pressure – five tests were adopted regarding the same conditions for each rock, so representative data could be acquired. The tests' conditions are presented in Table 43 and Table 44. The summary of the obtained data is observed in Table 45 and Table 46, where the volumes of the kerfs were normalized to a kerf with 150 mm of length.

Table 43 - Machine parameters adopted for the tests with variation of traverse velocity.

TEST 1: variation of traverse velocity	
P (MPa)	400
ϕ (°)	90
v_T (mm/min)	100, 200, 300, 400
h_S (mm)	5,00
d_0 (mm)	0,33
d_F (mm)	1,02
m_A (g/min)	408,23
d_A (mesh)	80

Table 44 - Machine parameters adopted for the tests with variation of pump pressure.

TEST 2: variation of pump pressure	
P (MPa)	100, 200, 300, 400
ϕ (°)	90
v_T (mm/min)	200
h_S (mm)	5,00
d_0 (mm)	0,33
d_F (mm)	1,02
m_A (g/min)	408,23
d_A (mesh)	80

Table 45 - Summary of the obtained data from the cutting tests varying the traverse velocity.

Rock	Traverse velocity (mm/min)	Mean kerf volume (cm³)	Mean cutting rate (cm³/min)
Syenite	100	17,042	11,34
Syenite	200	17,307	23,1
Syenite	300	8,268	16,56
Syenite	400	4,979	13,26
Granite	100	15,291	10,2
Granite	200	18,290	24,36
Granite	300	7,693	15,36
Granite	400	5,169	13,8
Marble	100	29,360	19,56
Marble	200	28,785	38,4
Marble	300	18,098	36,18
Marble	400	8,569	22,86
Sandstone	100	29,624	19,74
Sandstone	200	33,244	44,34
Sandstone	300	15,072	30,12
Sandstone	400	9,406	25,08

Table 46 - Summary of the obtained data from the cutting tests varying the pump pressure.

Rock	Pump pressure (MPa)	Mean kerf volume (cm³)	Mean cutting rate (cm³/min)
Syenite	100	2,54	3,387
Syenite	200	6,16	8,213
Syenite	300	9,87	13,160
Syenite	400	14,54	19,387
Granite	100	2,78	3,707
Granite	200	4,29	5,720
Granite	300	8,05	10,733
Granite	400	13,33	17,77
Marble	100	3,21	4,280
Marble	200	9,90	13,200
Marble	300	18,33	24,441
Marble	400	28,17	37,562
Sandstone	100	4,01	5,347
Sandstone	200	10,87	14,493
Sandstone	300	18,22	24,293
Sandstone	400	29,51	39,347

5. AWJ ROCK CUTTING REGARDING ENERGY CONCEPTS

5.1. METHODOLOGY FOR THE CALCULATION OF THE AWJ ENERGY OF CUTTING AND THE KERF GENERATION ENERGY

The determination of the AWJ energy of cutting depends on the calculation of the WJ velocity. To assess it, the Bernoulli's law (Equation 14) describes the energy balance of a pressurized water volume forced through an orifice, which generates a high energy waterjet (MOMBER & KOVACEVIC, 1998):

$$P_{at} + \frac{\rho_w}{2} \cdot v_J^2 + \rho_w \cdot g(h_1 - h_2) = P + \frac{\rho_w}{2} \cdot v_W^2 \quad (14)$$

where P_{at} is the atmospheric pressure (Pa), ρ_w is the specific mass of water (kg/m³), v_J is the WJ velocity (m/s), g is the gravitational acceleration (m/s²), $(h_1 - h_2)$ is the difference in elevation of the water inside the machine and when it leaves the nozzle (in m and which is negligible compared to the other terms), P is the pressure of the intensifier pump (Pa) and v_W is the velocity of water inside the equipment.

h_1 is considered equal to h_2 because their difference of less than 1 m can be neglected since the contribution of gravitational energy is minimal when compared to the high kinetic energy of the WJ cutting process. It is also considered that $P_{at} \ll P$ (notice that the pressure related to the waterjet is the atmospheric pressure itself, which is much lower than the water pressure inside the machine) and $v_J \gg v_W$ (the waterjet velocity is much higher than the water velocity inside the machine). Through the simplification of Equation 14, Equation 15 is obtained (MOMBER & KOVACEVIC, 1998):

$$v_J = \mu \cdot \sqrt{\frac{2P}{\rho_w}} \quad (15)$$

where P is the intensifier pump pressure (Pa) and μ is an efficiency coefficient related to momentum losses due to wall friction, fluid-flow disturbances and the compressibility of water.

According to Momber & Kovacevic (1998) the efficiency coefficient depends the most on the machine's pump pressure and the orifice geometry; and it may be obtained experimentally by measuring the real WJ velocities. Since it was not possible to measure it in the case of this work due to ICAM's policies, the values were estimated according to experiments conducted by Himmelreich (1992) as shown in Figure 52, which shows results considering a typical industrial machine similar to the one used for the present research. A linear extrapolation was adopted for pressure equal to 400 MPa.

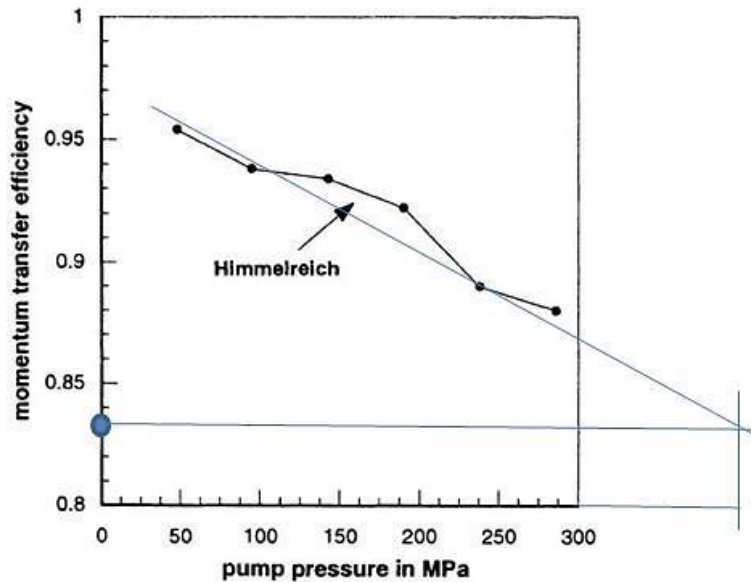


Figure 52 - Example of estimation of the efficiency coefficient for $P = 400$ MPa according to the experiments described in Himmelreich (1992). In this example, $\mu=0,83$ as indicated by the blue circle.

Subsequently, as shown through Equation 16, the WJ velocity is used to calculate the AWJ velocity, i.e. the WJ velocity after the introduction of the abrasive material (MOMBER & KOVACEVIC, 1998):

$$V_{AJ} = \varphi \cdot \frac{V_J}{1 + (m_A / m_W)} \quad (16)$$

where V_{AJ} is the AWJ velocity (m/s), φ is a momentum transfer coefficient related to the momentum transfer between the high velocity WJ at the nozzle and the incoming abrasive particles, m_A is the abrasive mass flow rate (kg/s) and m_W is the water mass flow rate (kg/s). Per the authors, literature presents typical φ values between 0,65 and 0,94. As this coefficient is also obtained experimentally, a value of 0,8 was adopted in the present thesis, as a mean value from the literature data range. It is important to mention that adopting approximated coefficient values does not compromise the development of the present thesis, since its main objective involves the determination of correlations regarding AWJ cutting tests and the studied rocks, i.e. a comparative analysis.

Then, the kinetic energy of the AWJ may be written as Equation 17:

$$E_{AJ} = \frac{1}{2} \cdot (m_A + m_W) \cdot t_E \cdot V_{AJ}^2 \quad (17)$$

where E_{AJ} is the kinetic energy of the AWJ (J), m_A is the abrasive mass flow rate (kg/s), m_W is the water mass flow rate (kg/s) and t_E is the exposure time (s).

As previously mentioned in Chapter 2, there is a similarity between the failure mechanisms observed during the uniaxial compression test and the AWJ cutting. Regarding the uniaxial compression test, the energy required to disaggregate a certain volume of rock is obtained through the determination of the specific energy (in fact, the destruction work) of the same rock, which is given by the area under the stress-strain curve to the peak strength (MOMBER & KOVACEVIC, 1999). The AWJ rock cutting process involves the disaggregation of a certain volume of rock in order to generate a kerf. Thus, by multiplying the specific energy of a rock by its removed volume for each AWJ cutting test, the energy spent to generate a kerf may be obtained, as shown in Equation 18:

$$E_K = SE_R \cdot V_R \quad (18)$$

where E_K is the kerf generation energy (J), SE_R is the rock specific energy (J/cm³) and V_R is the removed volume of rock (cm³).

It is important to take into consideration that the values of the specific energy of the rocks (SE_R) are usually obtained in laboratory tests according to ISRM procedures in which the loading rate is very low (failure takes place usually in five to ten minutes). In the AWJ cutting process the time involved to disaggregate the rock is much shorter. The effect of the loading rate on the results of unconfined compression tests has been studied by some authors (RESTNER & PLINNINGER, 2015; FUENKAJORN & KENKHUNTHOD, 2010), but it is far from being quantitatively established. It should be kept in mind that the loading rate is much higher in AWJ cutting than in UCS tests.

Thuro & Spaun (1996) introduced the specific destruction work (W_R), which is defined as the area under the complete stress strain curve of a material. It reflects the work of shape altering including the post failure section, i.e. the work required to destruct a rock sample. The authors claim that it is an interesting property to compare with the drillability of rocks, since it involves both strength and deformation conditions. As mentioned in chapter 3, it was not possible to measure the specific destruction work of the sandstone. In order to compare the results based on the specific energy (SE_R) and the specific destruction work (W_R), the kerf generation energy regarding W_R (E_{KW}) was calculated through Equation 19 for the other studied rocks:

$$E_{KW} = W_R \cdot V_R \quad (19)$$

where E_{KW} is given in J and W_R is given in J/cm³.

Finally, E_{KR} (%) is the relative kerf generation energy, which corresponds to the percentage of energy from the total E_{AJ} (*kinetic energy of the AWJ*) which is really spent on material removal in order to generate a kerf. It is calculated from the value of E_K considering E_{AJ} as 100% (Equation 20):

$$E_{KR} = \frac{E_K \cdot 100}{E_{AJ}} \quad (20)$$

where E_K is the kerf generation energy (J) and E_{AJ} is the kinetic energy of the AWJ (J).

The relative kerf generation energy (E_{KRW}) was also calculated for syenite, granite and marble based on the specific destruction work (Equation 21):

$$E_{KRW} = \frac{E_{KW} \cdot 100}{E_{AJ}} \quad (21)$$

5.2. EFFICIENCY ANALYSIS FOR THE AWJ CUTTING TESTS

5.2.1. Results on the cutting tests with traverse velocity variation

The results of the cutting tests with traverse velocity variation are presented in Table 47 through Table 51. The specific energy of cutting (SE_C) is the total energy spent by the machine to cut a certain volume of material (J/cm^3), including losses and dissipation through various means including friction, damping, heating and other mechanisms. As previously mentioned in chapter 2, damping effects are generated inside the kerf due to the difficulty for the AWJ to exit the narrow kerf, thus creating a film of water and an accumulation of abrasive particles inside of it. This effect leads to the damping of the coming water and abrasive particles. C_T is the time spent in the cutting of a rock specimen. For a better representation, C_T is considered for a normalized kerf of 150 mm length.

The WJ and AWJ velocities are constant in this case, since the parameters used to calculate them do not depend on the traverse velocity (see Equations 15 and 16). However, the kinetic energy of the AWJ does depend on the traverse velocity because this parameter changes the exposure time t_E , which is considered in the calculation of the AWJ kinetic energy (Equation 17).

Table 47 - Results of V_J (WJ velocity), V_{AJ} (AWJ velocity), E_{AJ} (kinetic energy of the AWJ) and C_T (cutting time) for varying traverse velocity cutting tests.

	V_J (m/s)	V_{AJ} (m/s)	E_{AJ} (J)	C_T (s)
$v_T = 100$ mm/min	742,37	593,99	2455,34	90
$v_T = 200$ mm/min	742,37	593,99	1227,67	45
$v_T = 300$ mm/min	742,37	593,99	818,45	30
$v_T = 400$ mm/min	742,37	593,99	613,84	22,5

Table 48 - V_R (removed volume of rock), SE_C (specific energy of cutting), E_K (kerf generation energy), E_{KW} (kerf generation energy with W_R), E_{KR} (relative kerf generation energy) and E_{KRW} (relative kerf generation energy with W_R) for traverse velocity = 100 mm/min.

	V_R (cm ³)	SE_C (J/cm ³)	E_K (J)	E_{KW} (J)	E_{KR} (%)	E_{KRW} (%)
Syenite	17,042	144,093	15,167	5,514	0,618	0,224
Granite	15,291	160,629	9,328	4,329	0,380	0,176
Marble	29,360	83,767	3,523	3,891	0,143	0,158
Sandstone	29,624	82,910	17,182	-	0,700	-

Table 49 - V_R (removed volume of rock), SE_C (specific energy of cutting), E_K (kerf generation energy), E_{KW} (kerf generation energy with W_R), E_{KR} (relative kerf generation energy) and E_{KRW} (relative kerf generation energy with W_R) for traverse velocity = 200 mm/min.

	V_R (cm ³)	SE_C (J/cm ³)	E_K (J)	E_{KW} (J)	E_{KR} (%)	E_{KRW} (%)
Syenite	17,307	70,962	15,403	5,599	1,255	0,456
Granite	18,290	67,149	11,157	5,178	0,909	0,422
Marble	28,785	42,682	3,454	3,815	0,281	0,311
Sandstone	33,245	36,949	19,282	-	1,571	-

Table 50 - V_R (removed volume of rock), SE_C (specific energy of cutting), E_K (kerf generation energy), E_{KW} (kerf generation energy with W_R), E_{KR} (relative kerf generation energy) and E_{KRW} (relative kerf generation energy with W_R) for traverse velocity = 300 mm/min.

	V_R (cm ³)	SE_C (J/cm ³)	E_K (J)	E_{KW} (J)	E_{KR} (%)	E_{KRW} (%)
Syenite	8,268	99,002	7,358	2,675	0,899	0,327
Granite	7,693	106,790	4,693	2,178	0,573	0,266
Marble	18,098	45,273	2,172	2,399	0,265	0,293
Sandstone	15,072	54,327	8,742	-	1,068	-

Table 51 - V_R (removed volume of rock), SE_C (specific energy of cutting), E_K (kerf generation energy), E_{KW} (kerf generation energy with W_R), E_{KR} (relative kerf generation energy) and E_{KRW} (relative kerf generation energy with W_R) for traverse velocity = 400 mm/min.

	V_R (cm ³)	SE_C (J/cm ³)	E_K (J)	E_{KW} (J)	E_{KR} (%)	E_{KRW} (%)
Syenite	4,979	121,800	4,489	1,632	0,731	0,266
Granite	5,169	118,810	3,153	1,463	0,514	0,238
Marble	8,569	71,817	1,028	1,136	0,167	0,185
Sandstone	9,406	65,777	5,455	-	0,889	-

Figure 53 presents the influence of the traverse velocity on the removed volume of rock. A general trend of a decrease in the removed volume along with an increase in the traverse velocity is observed, in spite of the results obtained for a traverse velocity of 200 mm/min. In this specific case, the removed volume of rock is the highest for all types of rocks.

It is interesting to notice that at higher traverse velocities, the removed volume values are closer for the studied rocks. As traverse velocity decreases, the removed volumes increase at a higher rate for the non-crystalline rocks, i.e. the marble and sandstone. Thus, in this situation it may be inferred that the removal process is more effective for the marble and the sandstone than for the syenite and the granite.

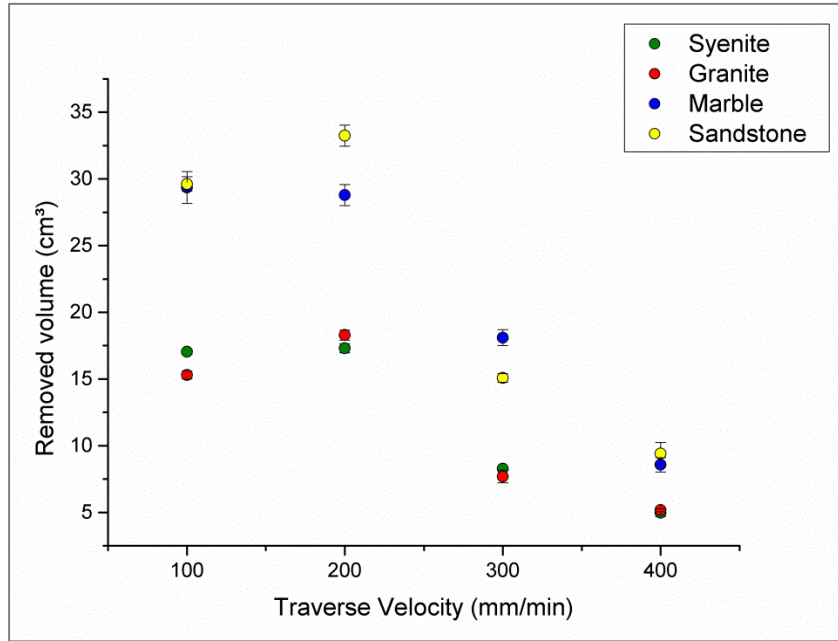


Figure 53 – Variation in the removed volume of rock according to the traverse velocity.

If the removed volume of rock is the highest at 200 mm/min, this is the optimum value of traverse velocity regarding AWJ cutting. Below 200 mm/min the exposure time is higher, thus a large removed volume of rock is expected. However, a higher exposure time also implies more loss of energy mainly due to damping effects regarding larger accumulation of water and abrasive material inside the kerf, which reduces the impact force of the AWJ. Above 200 mm/min the exposure time is lower and the damping effects are also lower. However, when comparing the removed volume of rock below and above 200 mm/min, it may be inferred that the exposure time plays a more important role in the removal of rock than the damping effects, because at a traverse velocity of 100 mm/min more rock is removed than at traverse velocities of 300 and 400 mm/min. Finally, it may be stated that the balance of the most influential factors in AWJ rock cutting allows for more efficiency at a traverse velocity of 200 mm/min.

Figure 54 presents the influence of the traverse velocity on the specific energy of cutting, i.e. the total energy provided by the machine per removed volume of rock. An opposite trend is observed in contrast with Figure 53, in spite of the results for a traverse velocity of 100 mm/min. In general, the specific energy of cutting decreases linearly with the decrease of the traverse velocity. However, the traverse velocity of 100 mm/min presents the highest values in the specific energy of cutting. It is possible to infer that cutting rocks with

very low traverse velocities may increase the inefficiency in the process due to the increase in energy loss related to damping, friction and heat resulting in a very high amount of energy to cut a small volume of rock. Thus, it may be inferred that in Figure 53 the traverse velocity of 100 mm/min is the one which deviates from the general trend and not the traverse velocity of 200 mm/min. Consequently, there is a critical traverse velocity under which the AWJ rock cutting drastically loses its efficiency, with 100 mm/min below and 200 mm/min above said limit.

Engin et al. (2012) present a correlation between the AWJ cutting depth and traverse velocity for several types of rocks with similar parameter values regarding this thesis (0,35 mm jewel diameter; 1,1 mm diameter nozzle; 80 mesh garnet; 5 mm stand-off distance and 360 MPa pressure). Unfortunately, the tests were conducted only with traverse velocities from 500 mm/min to 2000 mm/min, out of the range studied in the present thesis. Even so, the reported trend was that the highest cutting depths were obtained with 500 mm/min, decreasing exponentially until 2000 mm/min.

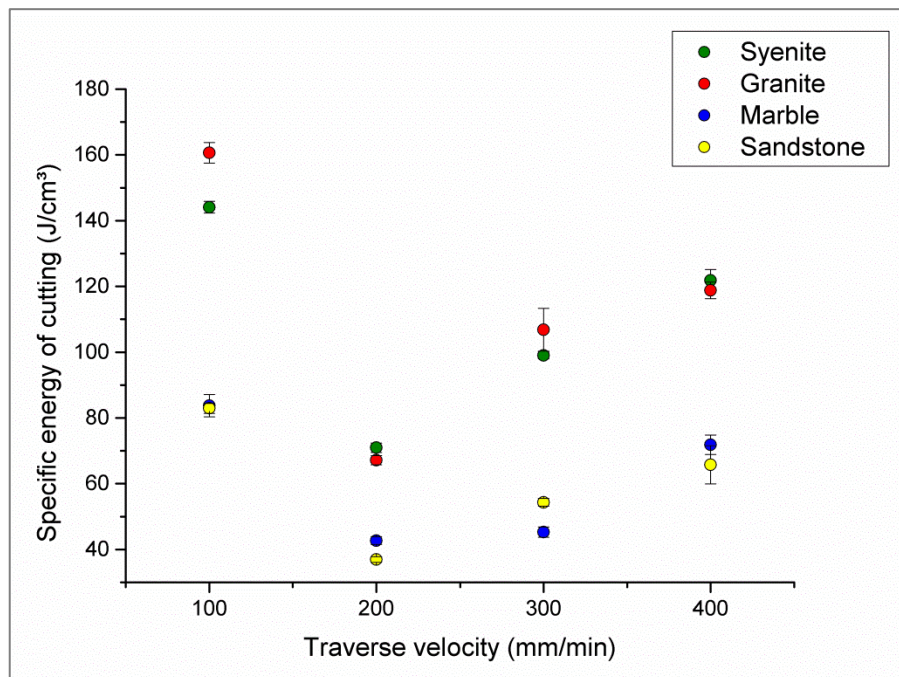


Figure 54 - Variation of the specific energy of cutting according to the traverse velocity.

Figure 55 presents the influence of the traverse velocity on the kerf generation energy. As discussed previously, the traverse velocity of 100 mm/min deviates from the general trend

due to the lower efficiency of cutting at this rate (loss of energy is higher during the cutting mainly due to the damping effect). Nevertheless, there is a decrease in the kerf generation energy with the increase in traverse velocity. Thus, since the kerf generation energy is the effective energy which is spent to disaggregate a volume of rock, more of it is spent on the rock removal with a traverse velocity of 200 mm/min.

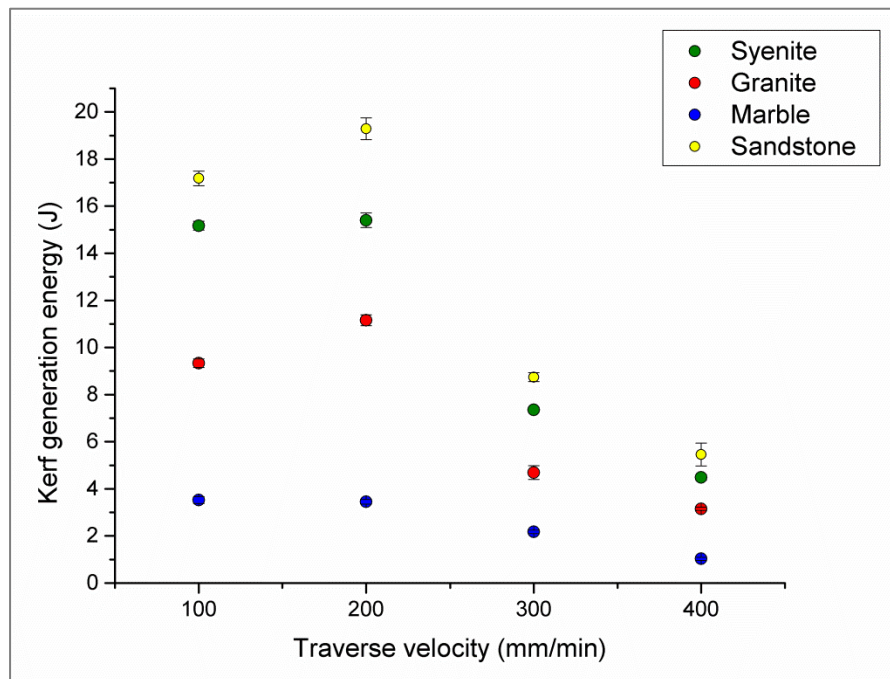


Figure 55 - Variation in the kerf generation energy according to the traverse velocity.

Figure 56 presents the same correlation for the kerf generation energy based on W_R (E_{KW}). The deviation at the traverse velocity of 100 mm/min decreases when W_R is considered, except in the case of the granite. The decrease in energy with the increase in traverse velocity is still observed, but the differences in energy at each traverse velocity decrease considerably between the rocks. The behavior of the marble does not change so much between adopting SE_R or W_R . This is because the marble continues to deform only a little after its peak strength, increasing its area under the stress strain curve from 119,03 to 132,54 kJ/m³. The opposite is observed in the case of the syenite and granite, because their areas decrease from 891,35 to 323,53 and 612,93 to 283,08 kJ/m³, respectively.

Still, in Figure 55 it is interesting to notice that the variation in the kerf generation energy with the decrease in the traverse velocity from 400 to 200 mm/min reveals a lower rate of energy increase for the marble and a higher rate of energy increase for the more brittle

rocks. This difference decreases when observing Figure 56, but it still exists in the most efficient condition (200 mm/min). Thus, two considerations are taken into account: the variation in the traverse velocity may exert a smaller influence on the effective energy spent to generate kerfs in class I materials or materials considered ductile (or yet “less brittle), e.g. marble; and a different trend is observed for marble because the SE_R is based on the stress strain curve area until the peak strength, in contrast to the specific destruction work, which considers the post-peak area for the calculation of the total energy necessary to disaggregate a volume of rock.

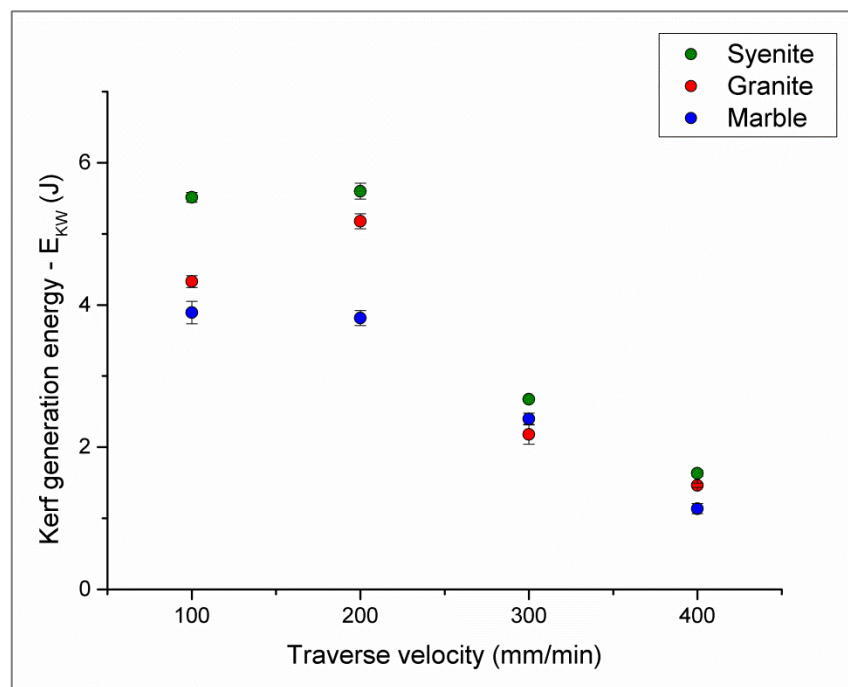


Figure 56 - Variation in the kerf generation energy according to the traverse velocity regarding W_R .

Another interesting observation regarding traverse velocities between 200 and 400 mm/min is that while Figure 54 shows the specific energy of cutting is similar for the marble and the sandstone, Figure 55 shows the lowest and the highest kerf generation energy for the marble and the sandstone, respectively. Thus, it could be interpreted that even with the machine providing nearly the same energy amount per removed volume of rock, that more energy is spent on the effective cutting of the sandstone. However, regarding the W_R values, a drop of more than a half of the kerf generation energy would be expected for the sandstone. Therefore, it would be very close to the marble’s values, probably below most of the granite’s

values. In the case of the sandstone's kerf generation energy at 100 mm/min, it would continue to be below the corresponding value of the marble, because it presents a curve shape like the other class II rocks.

Figure 57 presents the influence of the traverse velocity on the relative kerf generation energy. A higher relative kerf generation energy for a traverse velocity of 200 mm/min means that a higher percentage from the total energy provided by the AWJ machine is spent, in this case, to effectively disaggregate a rock.

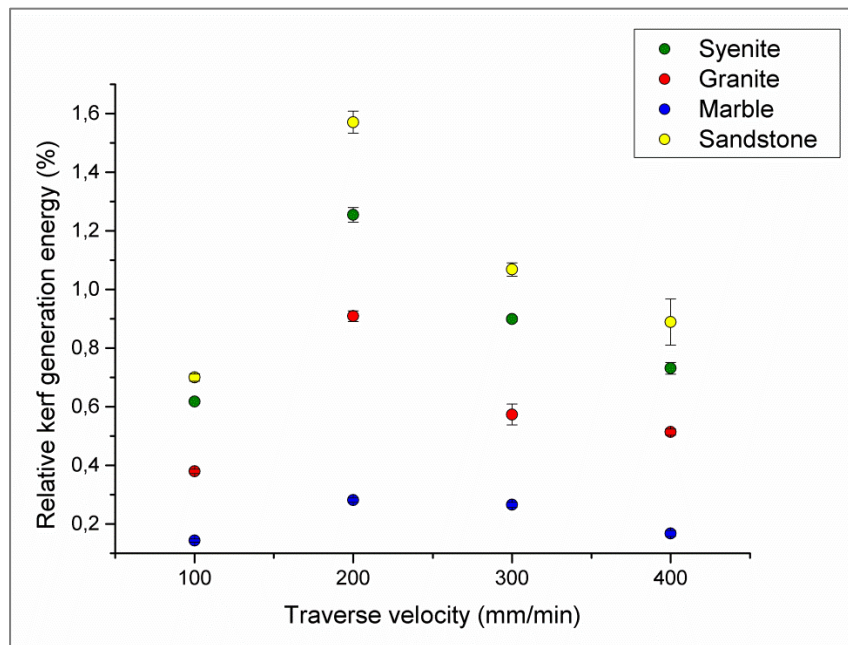


Figure 57 - Variation in the relative kerf generation energy according to the traverse velocity.

Figure 58 shows the same relationship regarding the W_R . The same general behavior from Figure 57 is observed, with a better transfer of energy at a traverse velocity of 200 mm/min. The specific destruction work (W_R) of the syenite corresponds to 36,3% of its specific energy (SE_R) while in the case of the granite this value is 46,2%. It is known that sandstone is the most brittle rock of all the rocks studied, thus it could be expected that its W_R would correspond to less than 36,3% of its SE_R . Assuming a 30% value for the sandstone, its W_R would be 174,84 kJ/m³. In said conditions, the relative kerf generation energy for the sandstone would be practically the same as that presented by the syenite. And if a 25% value is assumed ($W_R = 145,70$ kJ/m³), its values drop next to the values presented by the granite.

Thus, in general it may be concluded that the transfer of energy from the AWJ machine to the effective cutting increases with the increase in rock brittleness, or, as it will be discussed later in this chapter, with the decrease in the modulus ratio.

From the data presented in this subsection, it may be concluded that cutting the studied rocks with a traverse velocity of 200 mm/min is more efficient than with other traverse velocities. This rate provides the greatest rock volume removal, the lowest total energy provided by the machine and the greatest transfer of energy from the machine to the rock disaggregation process.

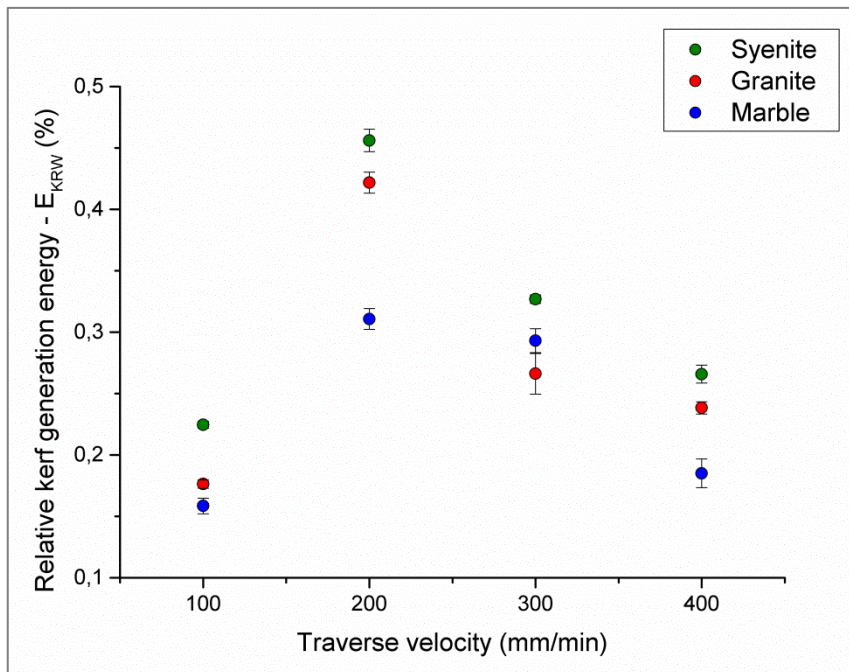


Figure 58 - Variation in the relative kerf generation energy according to the traverse velocity based on W_R .

5.2.2. Results of the cutting tests with pump pressure variation

The results of the cutting tests with pump pressure variation, which were performed with a traverse velocity of 200 mm/min, are presented in Table 52 through Table 56. The calculated WJ and AWJ velocities change because they depend on the pump pressure. The determination of the efficiency coefficient μ , which is used to calculate the waterjet velocity, also depends on the pump pressure.

Table 52 - Results of V_J (WJ velocity), V_{AJ} (AWJ velocity), E_{AJ} (kinetic energy of the AWJ) and C_T (cutting time) for varying pump pressure.

	V_J (m/s)	V_{AJ} (m/s)	E_{AJ} (J)	C_T (s)
P = 100 MPa	420,38	336,46	239,58	45
P = 200 MPa	575,53	460,54	588,19	45
P = 300 MPa	673,90	539,21	927,41	45
P = 400 MPa	742,37	593,99	1227,67	45

Table 53 - Results of V_R (removed volume of rock), SE_C (specific energy of cutting), E_K (kerf generation energy), E_{KW} (kerf generation energy with W_R), E_{KR} (relative kerf generation energy) and E_{KRW} (relative kerf generation energy with W_R) for pump pressure = 100 MPa.

	V_R (cm ³)	SE_C (J/cm ³)	E_K (J)	E_{KW} (J)	E_{KR} (%)	E_{KRW} (%)
Syenite	2,537	94,713	2,258	0,812	0,942	0,339
Granite	2,777	86,565	1,694	0,778	0,707	0,325
Marble	3,213	74,699	0,385	0,418	0,161	0,174
Sandstone	4,100	59,855	2,326	-	0,971	-

Table 54 - Results of V_R (removed volume of rock), SE_C (specific energy of cutting), E_K (kerf generation energy), E_{KW} (kerf generation energy with W_R), E_{KR} (relative kerf generation energy) and E_{KRW} (relative kerf generation energy with W_R) for pump pressure = 200 MPa.

	V_R (cm ³)	SE_C (J/cm ³)	E_K (J)	E_{KW} (J)	E_{KR} (%)	E_{KRW} (%)
Syenite	6,163	95,563	5,485	1,972	0,932	0,335
Granite	4,286	137,429	2,614	1,200	0,444	0,204
Marble	9,896	59,676	1,187	1,286	0,202	0,219
Sandstone	10,870	54,300	6,304	-	1,072	-

Table 55 - Results of V_R (removed volume of rock), SE_C (specific energy of cutting), E_K (kerf generation energy), E_{KW} (kerf generation energy with W_R), E_{KR} (relative kerf generation energy) and E_{KRW} (relative kerf generation energy with W_R) for pump pressure = 300 MPa.

	V_R (cm ³)	SE_C (J/cm ³)	E_K (J)	E_{KW} (J)	E_{KR} (%)	E_{KRW} (%)
Syenite	9,867	94,215	8,781	3,157	0,947	0,3240
Granite	8,045	115,454	4,908	2,253	0,529	0,243
Marble	18,332	50,602	2,199	2,383	0,237	0,257
Sandstone	18,218	50,971	10,566	-	1,139	-

Table 56 - Results of V_R (removed volume of rock), SE_C (specific energy of cutting), E_K (kerf generation energy), E_{KW} (kerf generation energy with W_R), E_{KR} (relative kerf generation energy) and E_{KRW} (relative kerf generation energy with W_R) for pump pressure = 400 MPa.

	V_R (cm ³)	SE_C (J/cm ³)	E_K (J)	E_{KW} (J)	E_{KR} (%)	E_{KRW} (%)
Syenite	14,539	84,733	12,939	4,652	1,054	0,379
Granite	13,329	92,147	8,131	3,732	0,662	0,304
Marble	28,167	43,600	3,380	3,662	0,275	0,298
Sandstone	29,506	41,632	17,114	-	1,394	-

Figure 59 presents the influence of the pump pressure on the removed volume of rock. For all studied rocks, the removed volume of rock increases with the increase in pump pressure. The increase in the pump pressure implies an increase in the AWJ velocity and energy. Two distinct trends are observed: one for the igneous rocks (syenite and granite) and the other for the marble and sandstone. The less steep gradient reflects the higher strength to disaggregation of those rocks and the steepest gradient reflects, consequently, the lower strength to disaggregation of the marble and sandstone. As a relationship based on a second degree polynomial equation is observed between the removed volume of rock and the pump pressure, Equation 22 through Equation 25 were fitted to the data in order to describe these relationships for the studied rocks.

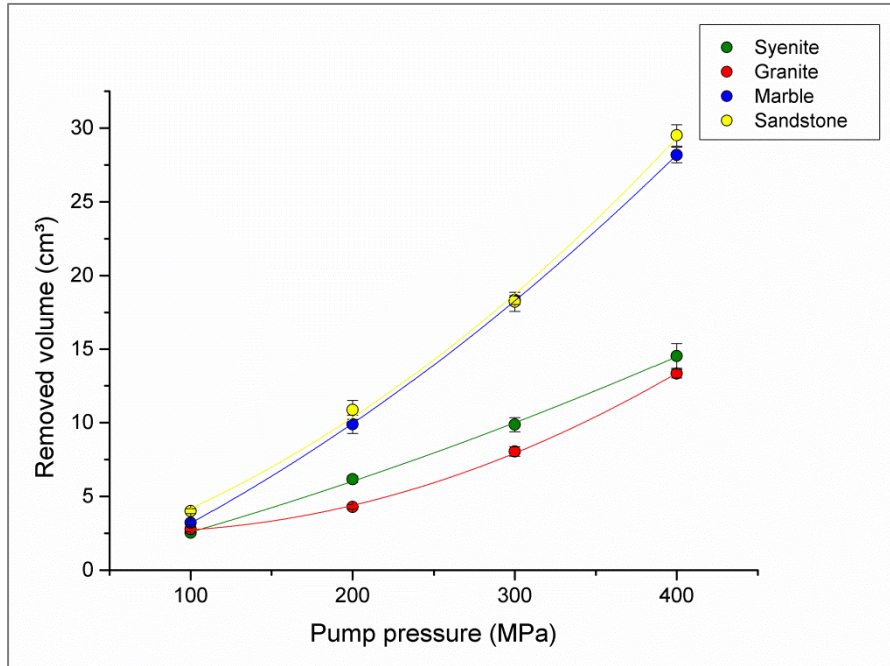


Figure 59 – Variation in the removed volume of rock according to the pump pressure.

$$\text{Syenite: } V_R = 2,6134E^{-5}P^2 + 0,0266P - 0,3444 \quad (R^2=0,99) \quad (22)$$

$$\text{Granite: } V_R = 9,4386E^{-5}P^2 - 0,0117P + 2,9747 \quad (R^2=0,99) \quad (23)$$

$$\text{Marble: } V_R = 7,8801E^{-5}P^2 + 0,0439P - 1,9829 \quad (R^2=0,99) \quad (24)$$

$$\text{Sandstone: } V_R = 1,0513E^{-4}P^2 + 0,0316P - 0,1924 \quad (R^2=0,99) \quad (25)$$

where V_R is the removed volume of rock (cm³) and P is the pump pressure (MPa).

Momber & Kovacevic (1999) state that a critical pump pressure characterizes the exit energy of the AWJ (i.e. the energy which leaves the piece of material) when the maximum possible erosion depth is reached. In this condition, the AWJ leaves the material because it is not able to remove more material. This critical pump pressure may be called the threshold pressure, which can be estimated experimentally by plotting the erosion depth versus the applied pump pressure. In the case of the present thesis, the same idea could be considered with a removed volume versus pump pressure plot. However, still regarding Figure 59, it may be misleading to extrapolate the curves linearly below 100 MPa because the fitted curves are not linear.

This would suggest that a lower threshold pressure exists for the syenite and granite, while a higher one would exist for the marble and sandstone. Since the syenite and the granite are more resistant to AWJ cutting, this method could be wrong. A non-linear behavior probably exists below the studied 100 MPa limit. Therefore, more tests would have to be done between 0 and 100 MPa in order to verify this situation.

Bortolussi et al. (1988) investigated the relationship between the depth of the cut of varied granites and the pump pressure, observing that even with 34 MPa an AWJ can cut granite with 5 mm depth. The authors performed tests with similar parameters regarding the present thesis (1 mm nozzle diameter; 0,35 mm jewel diameter and 60 mesh garnet abrasive), though the adopted traverse velocity and stand-off distance were not mentioned.

Engin (2012) studied diverse relationships between the AWJ cutting depth and the AWJ cutting parameters for diverse types of rocks. In his investigation of the relationship between the pump pressure and the cutting depth, the trend is not linear below 100 MPa.

Momber & Kovacevic (1997) studied the relationships between the depth of cut and the AWJ parameters for concrete samples. The results obtained differ from the referred studies and the present thesis. Regarding the effect of pump pressure, the threshold pressures are well-defined between 35 and 80 MPa. The depth of cut increases with decreasing steepness according to a non-linear trend. Then, it keeps steady between 300 and 350 MPa. Besides the fact that concrete and rocks have few similarities in terms of mechanical behavior; they also differ considerably when subjected to AWJ cutting.

Figure 60 presents the influence of the pump pressure on the specific energy of cutting. The general trend observed is the decrease of the specific energy of cutting with the increase of the pump pressure. Thus, when considering the energy spent by the machine on the whole cutting process for a certain volume of rock, less energy is required in rock breakage with a high pump pressure. The granite presented a deviation in the results between traverse velocities of 100 and 200 mm/min and this may be related to the greater variability of the behavior of this rock when compared to the others. Equation 26 through Equation 29 describe this relationship for the studied rocks.

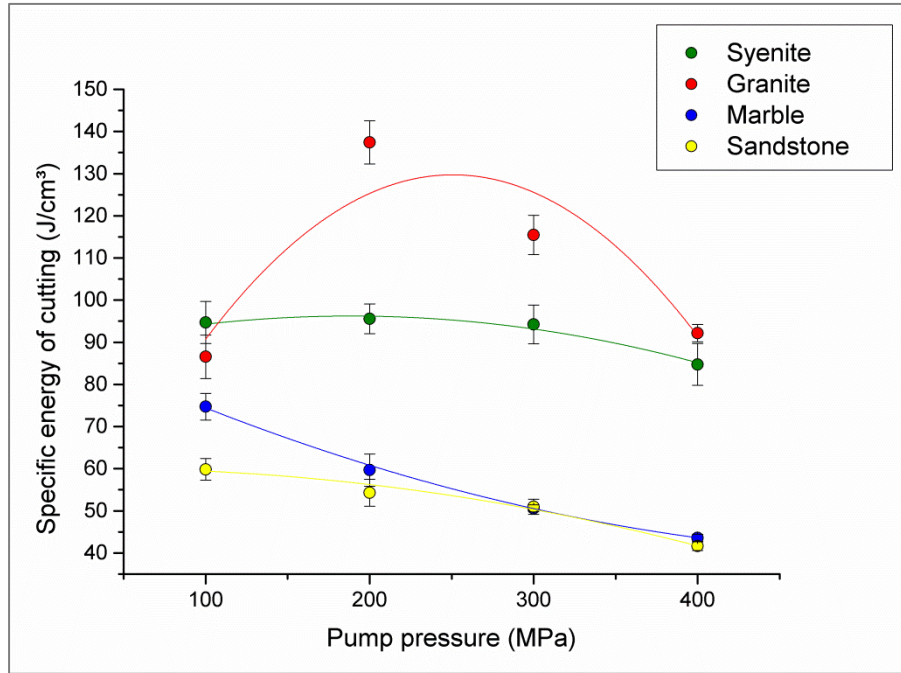


Figure 60 - Variation in the specific energy of cutting according to the pump pressure.

$$\text{Syenite: } SE_C = -2,4734E^{-4} \cdot P^2 + 0,0932 \cdot P + 87,4411 \quad (R^2 = 0,91) \quad (26)$$

$$\text{Granite: } SE_C = -0,0017 \cdot P^2 + 0,8611 \cdot P + 21,7631 \quad (R^2 = 0,61) \quad (27)$$

$$\text{Marble: } SE_C = 1,6727E^{-4} \cdot P^2 - 0,1864P + 91,4111 \quad (R^2 = 0,99) \quad (28)$$

$$\text{Sandstone: } SE_C = -1,3619E^{-4} \cdot P^2 + 0,0089 \cdot P + 59,8979 \quad (R^2 = 0,97) \quad (29)$$

where SE_C is the specific energy of cutting (J/cm^3) and P is the pump pressure (MPa).

Figure 61 presents the influence of the pump pressure on the kerf generation energy. The kerf generation energy increases with the increase in pump pressure, thus the energy transfer from the machine to the disaggregation process of the rocks is more efficient with higher pump pressures. It is also observed that the best energy transfer occurs for the sandstone, the one which presents the steepest gradient. In contrast, the worse energy transfer occurs for the marble. Equation 30 through Equation 33 describe this relationship in the cases of the studied rocks.

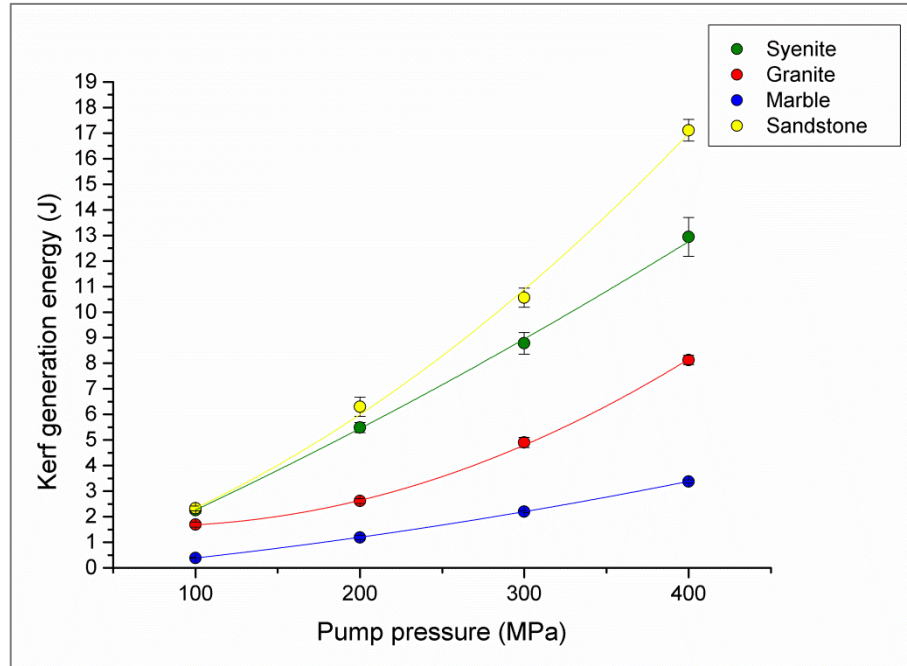


Figure 61 - Variation in the kerf generation energy according to the pump pressure.

$$\text{Syenite: } E_K = 1,5685E^{-5}P^2 + 0,0272P - 0,6107 \quad (R^2 = 0,99) \quad (30)$$

$$\text{Granite: } E_K = 6,0192E^{-5}P^2 - 0,0085P + 1,9339 \quad (R^2 = 0,99) \quad (31)$$

$$\text{Marble: } E_K = 9,3119E^{-6}P^2 + 0,0053P - 0,2413 \quad (R^2 = 0,99) \quad (32)$$

$$\text{Sandstone: } E_K = 6,0977E^{-5}P^2 + 0,0183P - 0,1116 \quad (R^2 = 0,99) \quad (33)$$

where E_K is the kerf generation energy (J) and P is the pump pressure (MPa).

The same relationship was analyzed considering the kerf generation energy calculated with the specific destruction work (W_R). As observed in Figure 62, the kerf generation energy values are similar for the granite and the marble, with slightly higher values for the granite. Syenite presents a similar value to that of the granite at 100 MPa and then it increases from 200 to 400 MPa. The data was fitted in order to obtain curves which describe the behavior of the three analyzed rocks (Equations 34 to 36). Comparing Figure 61 and Figure 62, the influence of the post-peak behavior of the studied rocks on the cutting phenomena is clear. Without considering the post-peak sections in order to calculate the kerf generation energy, the discrepancy between the rocks is large. When the post-peak is taken into account, the discrepancy decreases drastically, providing similar gradients for the syenite, granite and

marble. If a destruction work of 30% from the specific energy of the sandstone was adopted, its kerf generation energy values would be a little higher than the values obtained for the syenite. Thus, the kerf generation energy values increase with the increase in pump pressure and with the increase of rock brittleness.

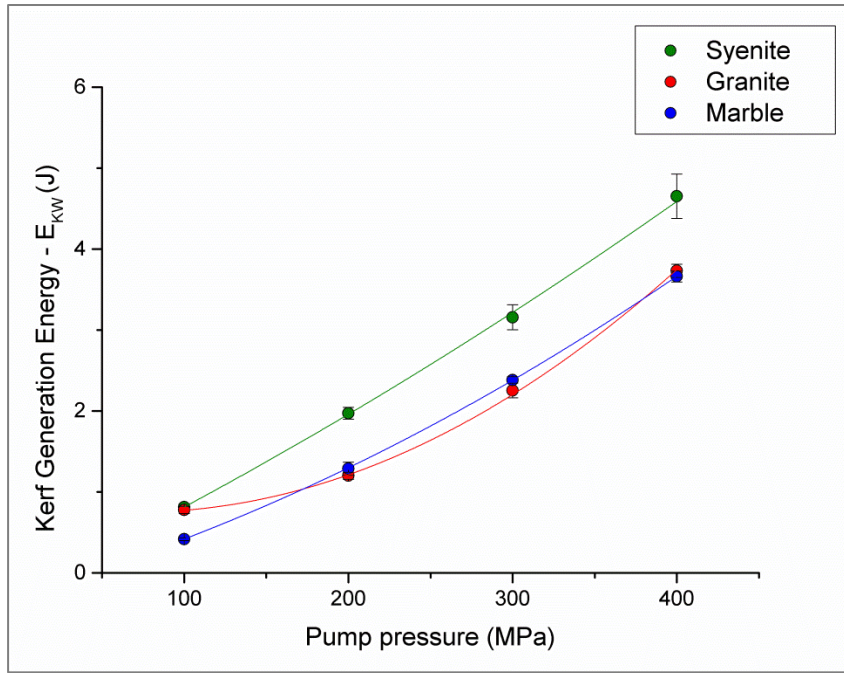


Figure 62 - Variation in the kerf generation energy according to the pump pressure based on W_R .

$$\text{Syenite: } E_{KW} = 5,6397E^{-6}P^2 + 0,0098P - 0,2196 \quad (R^2 = 0,99) \quad (34)$$

$$\text{Granite: } E_{KW} = 2,7629E^{-5}P^2 - 0,0039P + 0,8877 \quad (R^2 = 0,99) \quad (35)$$

$$\text{Marble: } E_{KW} = 1,0088E^{-5}P^2 + 0,0058P - 0,2614 \quad (R^2 = 0,99) \quad (36)$$

where E_{KW} is the kerf generation energy (J) based on W_R and P is the pump pressure (MPa).

Figure 63 presents the influence of the pump pressure on the relative kerf generation energy. The transfer of energy from the machine to the disaggregation of the sandstone is better and increases at a slightly higher rate than that of the other rocks. Equations 37 to 40

describe the relative kerf generation energy as a function of pump pressure for the rocks studied.

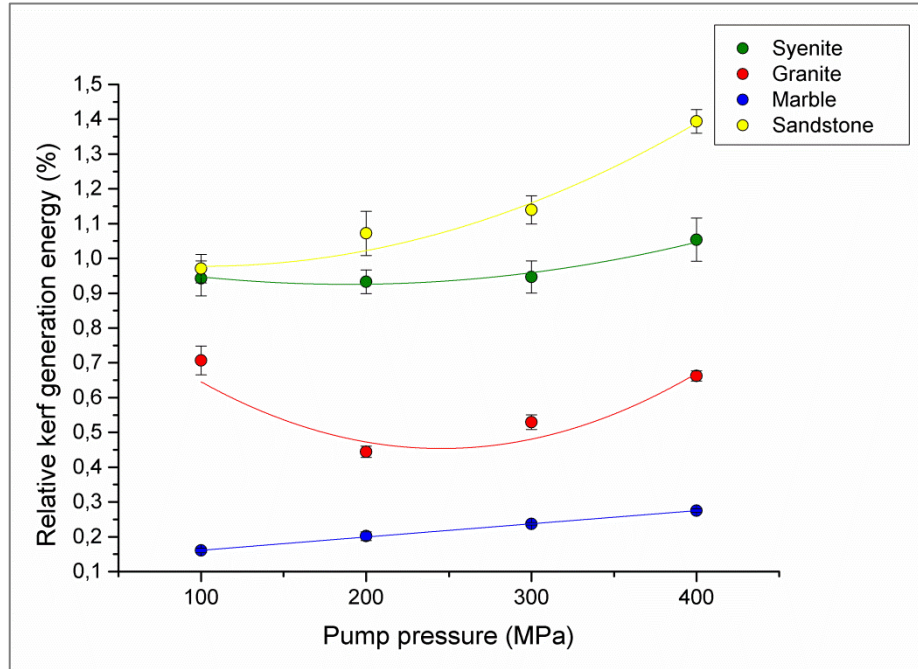


Figure 63 - Variation in the relative kerf generation energy according to the pump pressure.

$$\text{Syenite: } E_{KR} = 2,7203E^{-6}P^2 - 0,0010P + 1,0228 \quad (R^2 = 0,87) \quad (37)$$

$$\text{Granite: } E_{KR} = 9,0568E^{-6}P^2 - 0,0044P + 0,9997 \quad (R^2 = 0,72) \quad (38)$$

$$\text{Marble: } E_{KR} = -1,3184E^{-8}P^2 + 3,8671E^{-4}P + 0,1226 \quad (R^2 = 0,99) \quad (39)$$

$$\text{Sandstone: } E_{KR} = 4,6187E^{-6}P^2 - 9,3744E^{-4}P + 1,0252 \quad (R^2 = 0,96) \quad (40)$$

where E_{KR} is the relative kerf generation energy (%) and P is the pump pressure (MPa).

The same analysis was done regarding the relative kerf generation energy based on the specific destruction work (Figure 64). For the marble, the relative kerf generation energy increases linearly with the increase in pump pressure. For the granite, the same trend is observed in spite of the value for 100 MPa, which is higher. For the syenite, the relative kerf generation energy remains practically the same from 100 to 300 MPa and then increases at

400 MPa. Despite of the different observed trends, a better transfer of energy occurs at 400 MPa for the three rocks. Again, if a destruction work of 30% from the specific energy of the sandstone was adopted, it would present the higher values of relative kerf generation energy of all rocks, supporting the idea that a better transfer of energy occurs in the more brittle rocks, although the obtained values for the granite were similar to the values of the marble in this case. Equations 41 to 43 describe the relative kerf generation energy based on W_R as a function of pump pressure for the rocks studied.

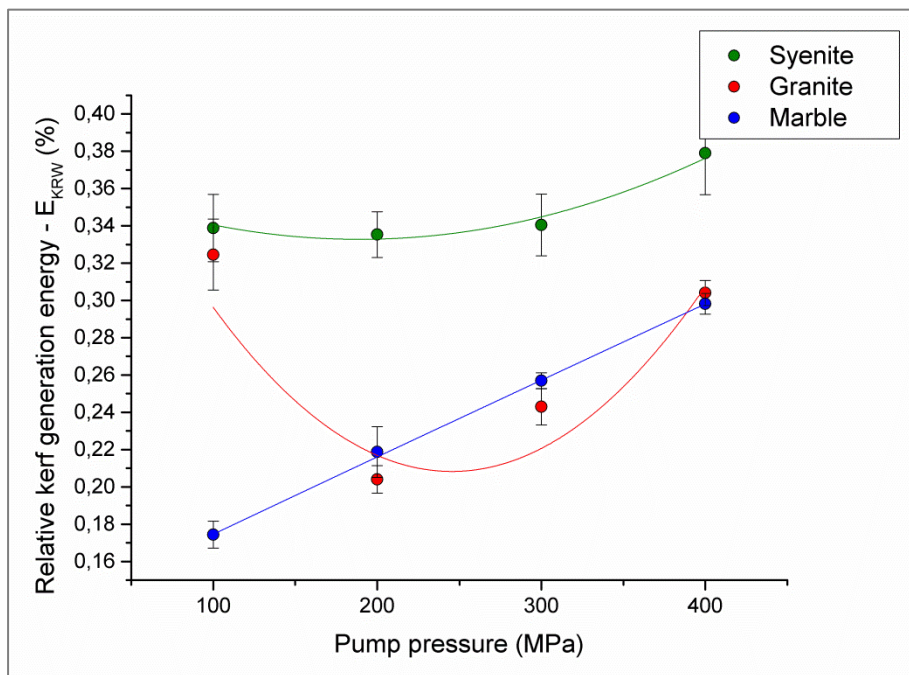


Figure 64 - Variation in the relative kerf generation energy according to the pump pressure based on W_R .

$$\text{Syenite: } E_{KRW} = 9,7809E^{-7}P^2 - 3,6982P + 0,3677 \quad (R^2 = 0,87) \quad (41)$$

$$\text{Granite: } E_{KRW} = 4,1572E^{-6}P^2 - 0,0020P + 0,94589 \quad (R^2 = 0,72) \quad (42)$$

$$\text{Marble: } E_{KRW} = -1,4283E^{-8}P^2 + 4,1893E^{-4}P + 0,1328 \quad (R^2 = 0,99) \quad (43)$$

where E_{KRW} is the relative kerf generation energy (%) based on W_R and P is the pump pressure (MPa).

It is important to observe that the kerf geometry exerts influence on the transfer of energy during the AWJ cutting. Wider kerfs facilitate the exit of the AWJ, thus less water and abrasive material accumulate inside them. Therefore, fewer losses, mainly due to damping, are expected in this case. Kerf geometry depends on rock characteristics and cutting parameters, like traverse velocity and pump pressure.

5.2.3. Efficiency analysis regarding specific energy of cutting and cutting rate

According to Atici & Ersoy (2009) a good indication of the cutting performance of rocks is given in the study of the specific energy of cutting (SE_C in the case of this thesis) and the cutting rate parameters. The cutting rate is defined as the removed volume of rock divided by the time spent on cutting, i.e. V_R/C_T . When a lower specific energy of cutting is associated with a higher cutting rate the best performance is reached, since a large volume of rock is removed without spending much energy. Also, the specific energy of cutting is directly related to the costs of production/cutting.

In this respect, taking up Figure 54, it was observed that the lowest specific energy of cutting was obtained with a 200 mm/min traverse velocity for all of the studied rocks. Figure 65 shows the influence of the traverse velocity on the cutting rate. As the higher cutting rate occurs at a traverse velocity of 200 mm/min, it may be concluded that in this condition the highest efficiency is achieved. A traverse velocity of 100 mm/min is the condition which provides the lowest efficiency, since it involves the highest specific energy of cutting in association with the lowest cutting rates.

The same line of thought may be applied to find the most efficient cutting condition regarding the pump pressure. Figure 60 presents the relationship between the specific energy of cutting and the pump pressure. For all rocks, the lowest energy is obtained when cutting with a pump pressure of 400 MPa. Figure 66 presents the effect of the pump pressure on the cutting rate and the pump pressure associated with the highest cutting rate is also 400 MPa. Gathering the results of both studied parameters, for the studied rocks the best efficiency is obtained when cutting them with a traverse velocity of 200 mm/min and a pump pressure of 400 MPa.

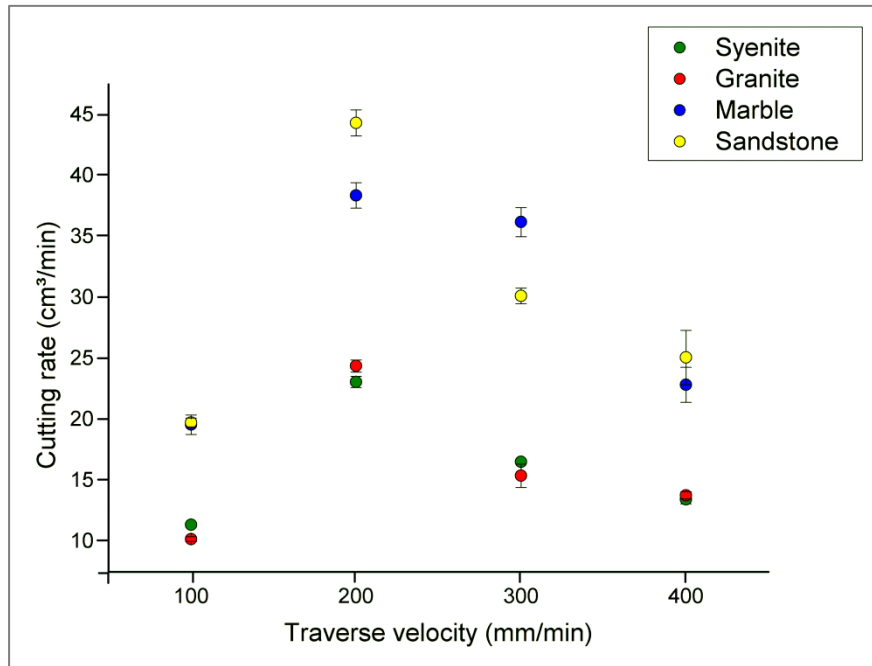


Figure 65 – Influence of the traverse velocity on the cutting rate.

The cutting tests with varying traverse velocity were conducted with a pump pressure of 400 MPa and the cutting tests with varying pump pressure were conducted with a traverse velocity of 200 mm/min. Thus, the test with conditions of 400 MPa and 200 mm/min was executed twice, each time corresponding to the production of 5 kerfs. It was expected that the mean cutting rates for both times would be similar. However, the cutting rates obtained for the studied rocks were: 384,61 and 323,08 mm³/s for the syenite; 406,45 and 296,21 mm³/s for the granite; 639,66 and 625,95 mm³/s for the marble and 738,77 and 655,69 mm³/s for the sandstone. The variability of the obtained volumes each test was low, as presented in Chapter 4, thus two situations may have occurred: local variability of the rock samples and/or, the most probable, variations due to the maintenance of the AWJ such as the change of the jewel, valves or the batch of abrasive. The last situation is more likely to have happened because all cutting rates obtained in the first batch of tests, with varying traverse velocity, were higher than the ones obtained in the tests with varying pump pressure.

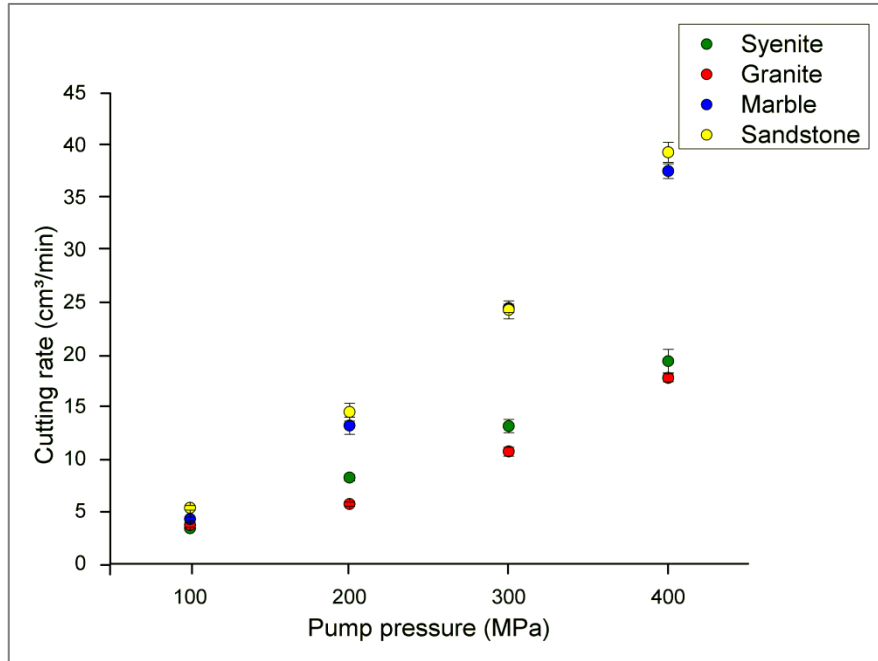


Figure 66 – Influence of the pump pressure on the cutting rate.

5.2.4. Correlations between the relative kerf generation energy (E_{KR} and E_{KRW}) and the rock properties

In this section, correlations between the relative kerf generation energy and the rock properties were investigated in order to achieve a better understanding on how rock properties may affect the AWJ cutting and its efficiency. The majority of the correlations presented in this subsection involve rock properties and E_{KR} values. The same correlations were conducted with E_{KRW} assuming a specific destruction work for the sandstone equal to 30% of its specific energy. Since the obtained trends were very similar for E_{KR} and E_{KRW} , only the significant correlations with E_{KRW} are shown. Figure 67 shows the relationship between the relative kerf generation energy and the Amsler abrasive wear for the tests with a variation in traverse velocity. Two different trends are observed: one for the marble and one for the more brittle rocks (syenite, granite and sandstone).

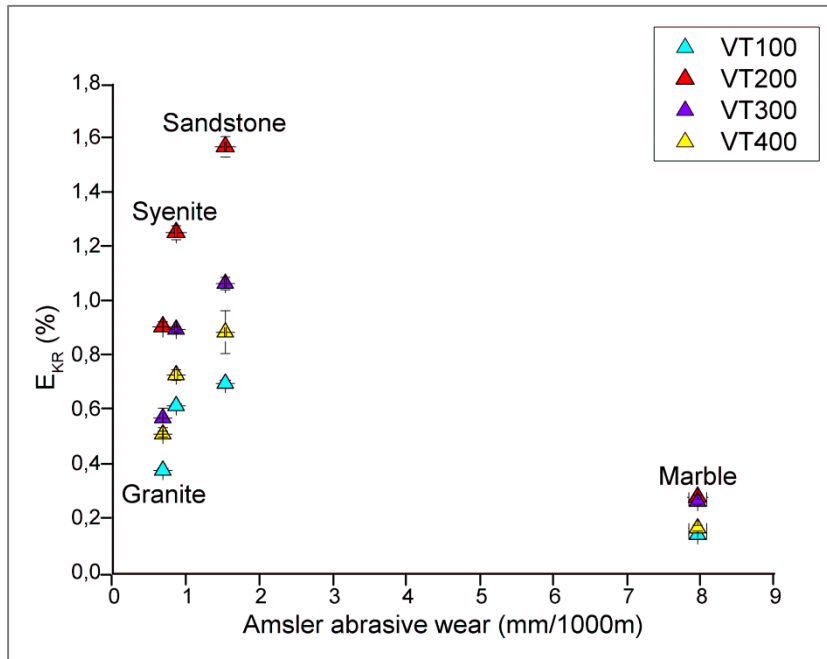


Figure 67 - relative kerf generation energy (E_{KR}) versus Amsler abrasive wear for varying traverse velocity (mm/min). The dots from the same vertical line correspond to the same rock type.

For all rocks an increase in the relative kerf generation energy from 100 to 200 mm/min is observed, and then it decreases to 400 mm/min. In the case of the marble, it seems that the increase in relative kerf generation energy is lower when compared to the more brittle rocks, but this is just an effect of adopting a correlation considering the specific energy of the rocks and not their specific destruction work. When considering the post-peak in calculations, the relative kerf generation energy range expands.

The abrasive wear did not provide a good correlation with relative kerf generation energy. The more brittle rocks show a trend of relative kerf generation energy increase with higher abrasive wear, but this is not valid for the marble (even when considering its specific destruction work). This may occur due to the fact that calcite's Mohs hardness is 3, a much lower value in comparison with the other rocks, which present essential minerals with a range of 6 to 7 according to the same scale of hardness (a logarithmic scale).

Figure 68 shows a similar analysis, but based on the tests with variation of pump pressure. The range of relative kerf generation energy values is narrower for each type of rock in comparison with the ranges observed in the tests with traverse velocity variation. It is interesting to notice that the relative kerf generation energy increases more uniformly from 100 to 400 MPa for the marble, than the granite, the syenite and the sandstone. Thus, the more

ductile the rock, the more uniform the distribution of E_{KR} is. The E_{KR} values order of increase is different for each type of rock, but for all of them the relative kerf generation energy is higher at 400 MPa. The marble and the sandstone follow the usual order, from 100 to 400 MPa. For the syenite, E_{KR} values are equal at 100 and 200 MPa and then it increases until 400 MPa is reached. The granite presents an unusual order: 200, 300, 100 and 400 MPa. Regarding the relationship between relative kerf generation energy and the rock types, it is the same as observed on Figure 67. A correlation may exist regarding the brittle rocks, but it is not valid for the marble.

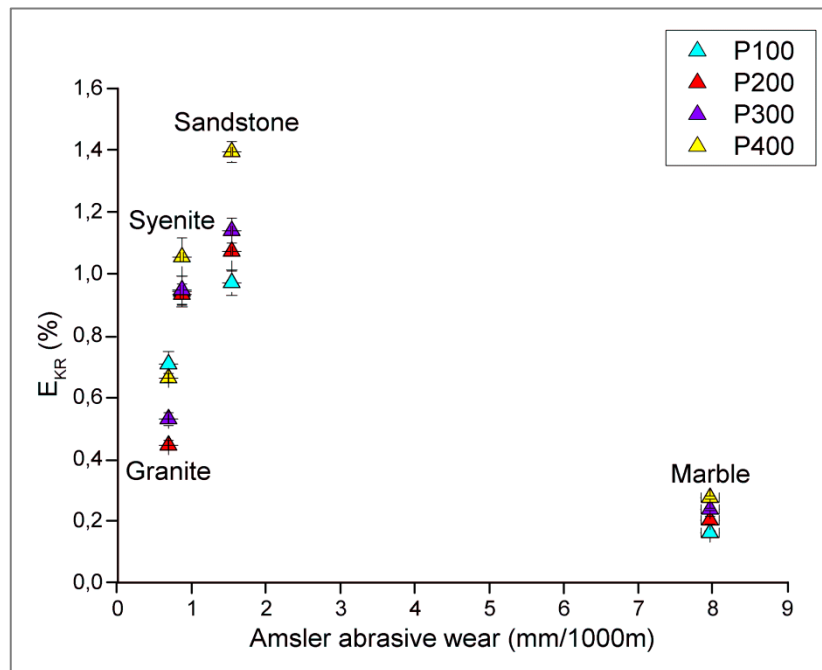


Figure 68 - Relative kerf generation energy (E_{KR}) versus Amsler abrasive wear for varying pump pressure. The dots from the same vertical line correspond to the same rock type.

Figure 69 and Figure 70 show the relationships between relative kerf generation energy and the Schmidt hardness for varying traverse velocity and pump pressure, respectively. When considering just the crystalline rocks (syenite, granite and marble), a poor trend indicates that the relative kerf generation energy increases with the increase of Schmidt hardness. However, it is not a good property to try correlations because its values present high dispersion in a narrow range for all rocks studied.

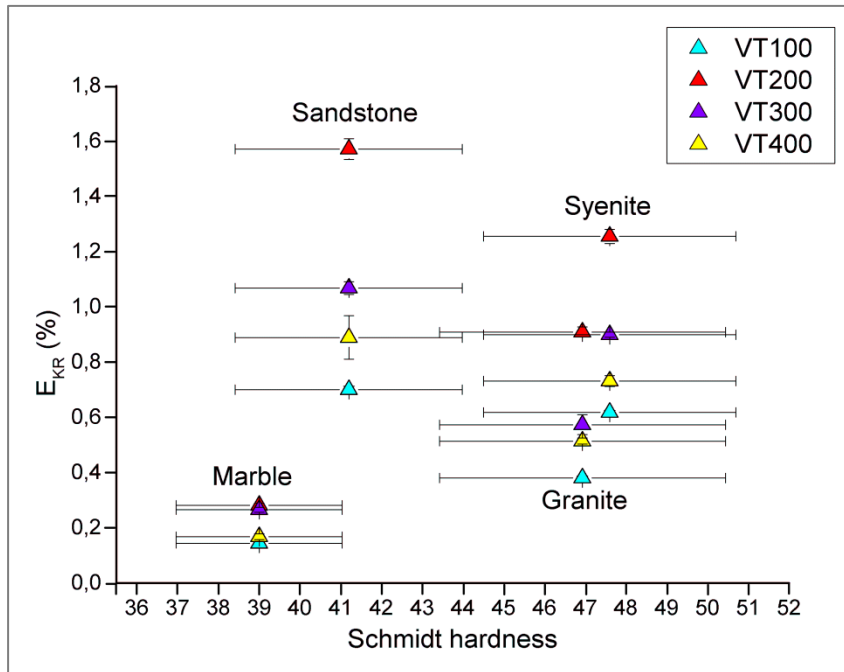


Figure 69 - Relative kerf generation energy (E_{KR}) versus Schmidt hardness for varying traverse velocity. The dots from the same vertical line correspond to the same rock type.

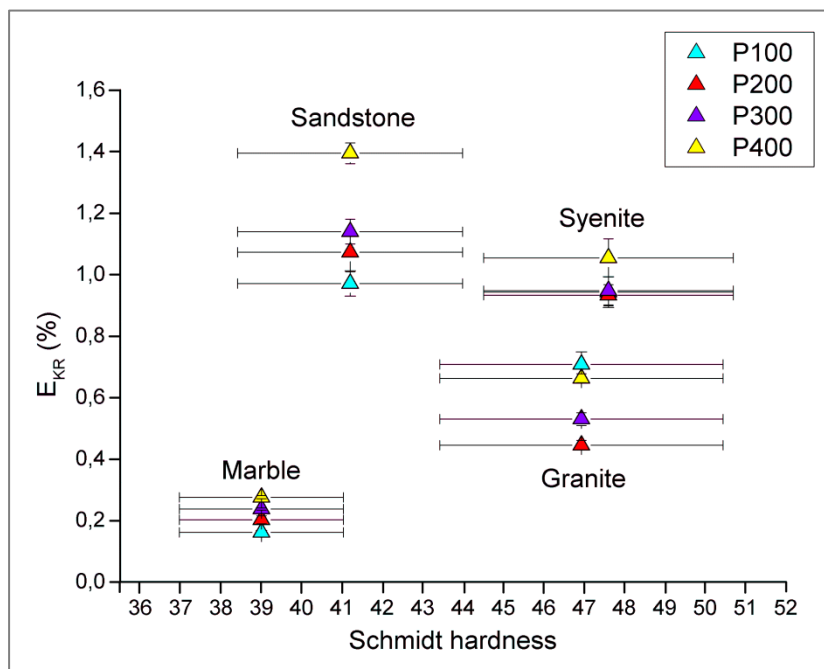


Figure 70 - Relative kerf generation energy (E_{KR}) versus Schmidt hardness for varying pump pressure. The dots from the same vertical line correspond to the same rock type.

Figure 71 shows the relationship between relative kerf generation energy and the dry density. The observed trend indicates that relative kerf generation energy increases with the decrease in dry density for all rocks. Thus, the energy transfer from the machine to the cutting

process is better when dry density is low. Figure 72 shows the same relationship regarding pump pressure variation.

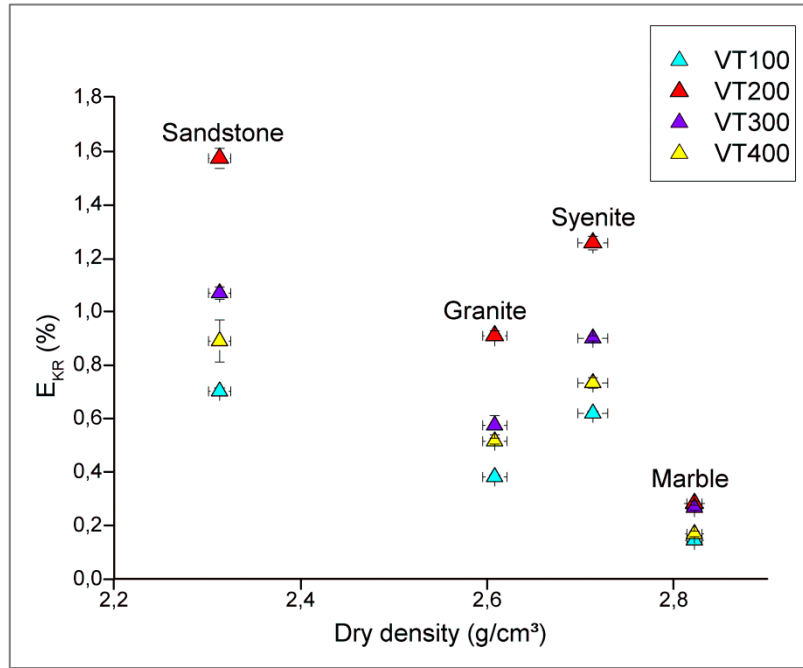


Figure 71 - Relative kerf generation energy (E_{KR}) versus dry density for varying traverse velocity. The dots from the same vertical line correspond to the same rock type.

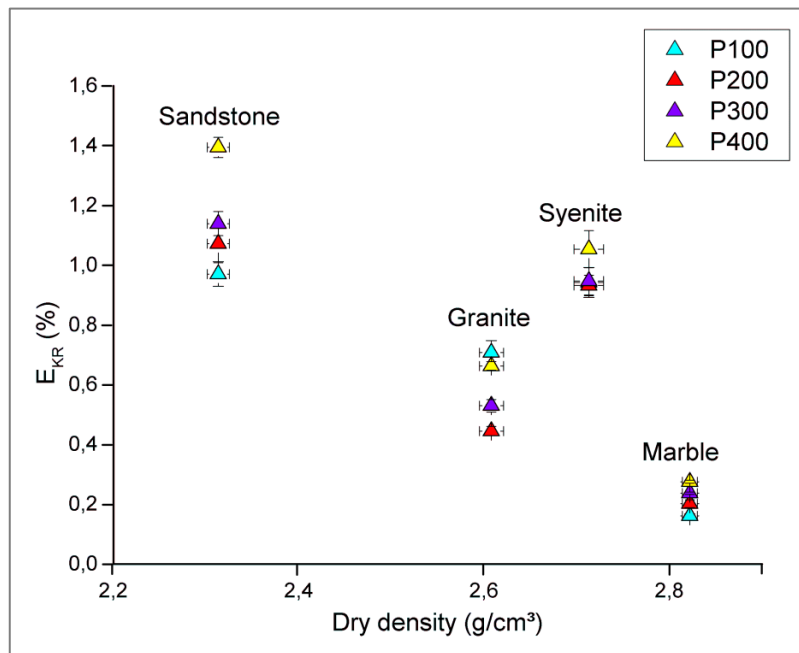


Figure 72 - Relative kerf generation energy (E_{KR}) versus dry density for varying pump pressure. The dots from the same vertical line correspond to the same rock type.

Figure 73 and Figure 74 show the relationships between relative kerf generation energy and the degree of saturation for traverse velocity and pump pressure variations, respectively. In both cases, two trends are observed, one for the crystalline rocks (syenite, granite and marble) and one for the sandstone. The degree of saturation of the sandstone differs more from the others because it is a sedimentary rock. Sedimentary rocks generally present smaller degrees of compaction due to their generation processes related to deposition environments characterized by low temperatures and low pressures. Because of that, the sandstone correlation with relative kerf generation energy cannot be interpreted together with the crystalline rocks, since the degree of saturation is highly affected by the generation conditions of the rocks.

Regarding the crystalline rocks, a weak correlation may be inferred, that is the increase in the relative kerf generation energy with the decrease in the degree of saturation.

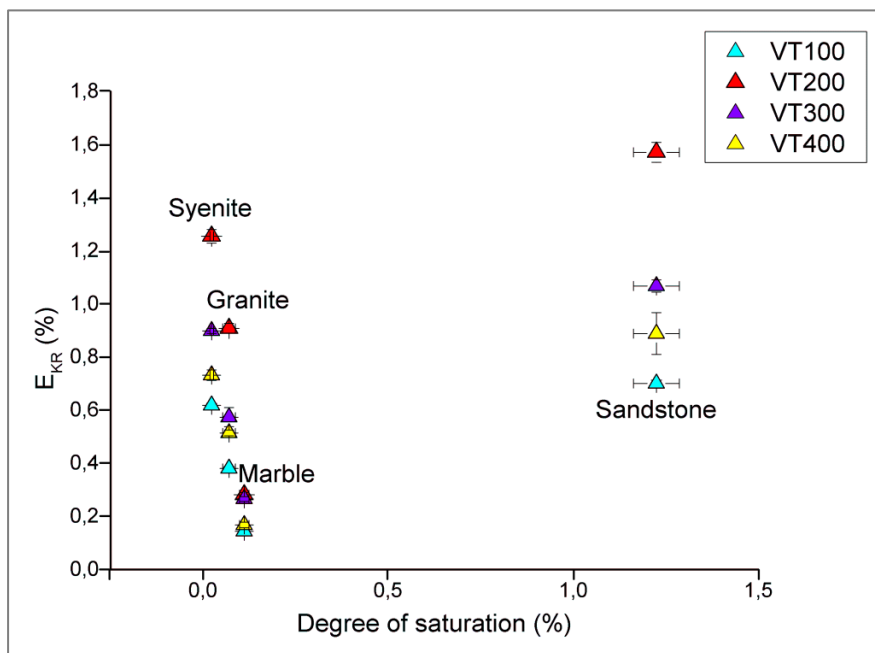


Figure 73 - Relative kerf generation energy (E_{KR}) versus degree of saturation for varying traverse velocity. The dots from the same vertical line correspond to the same rock type.

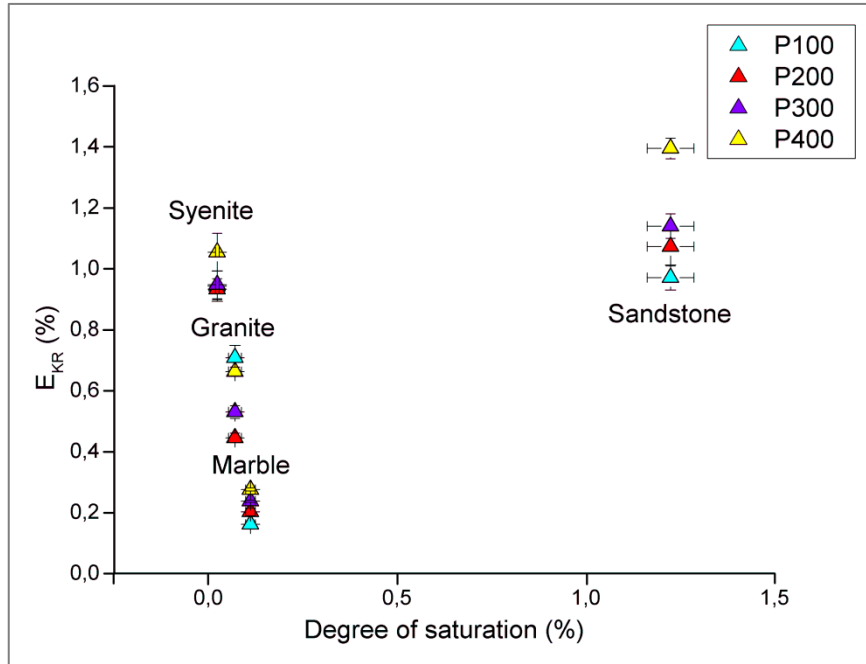


Figure 74 - Relative kerf generation energy (E_{KR}) versus degree of saturation for varying pump pressure. The dots from the same vertical line correspond to the same rock type.

Figure 75 and Figure 76 show the relationships between relative kerf generation energy and porosity for traverse velocity and pump pressure variations, respectively. Since porosity is a property based on the degree of saturation, the observed trends are similar to the ones presented in Figure 73 and Figure 74. Considering the crystalline rocks, relative kerf generation energy values increase with a decrease in porosity.

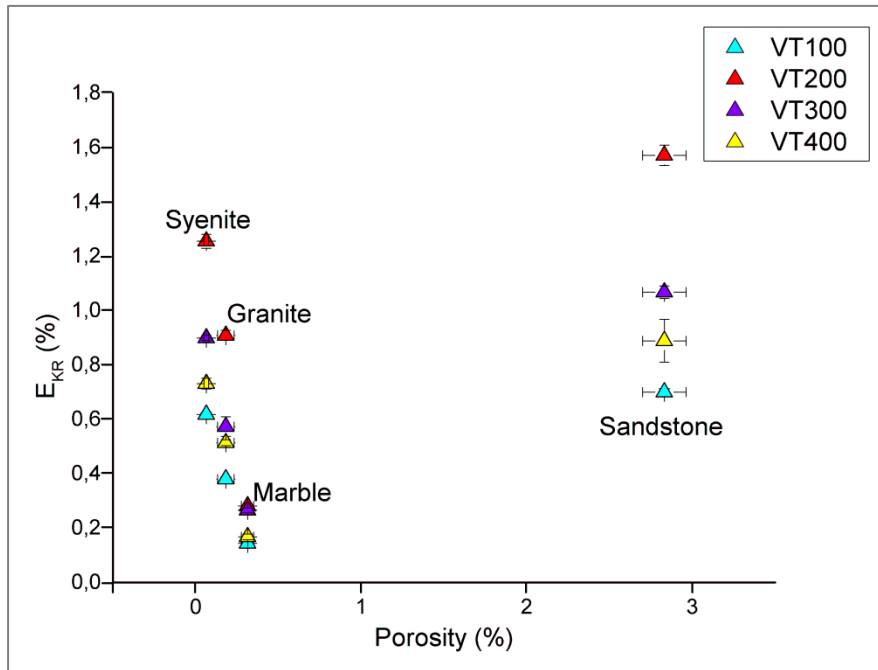


Figure 75 - Relative kerf generation energy (E_{KR}) versus porosity for varying traverse velocity. The dots from the same vertical line correspond to the same rock type.

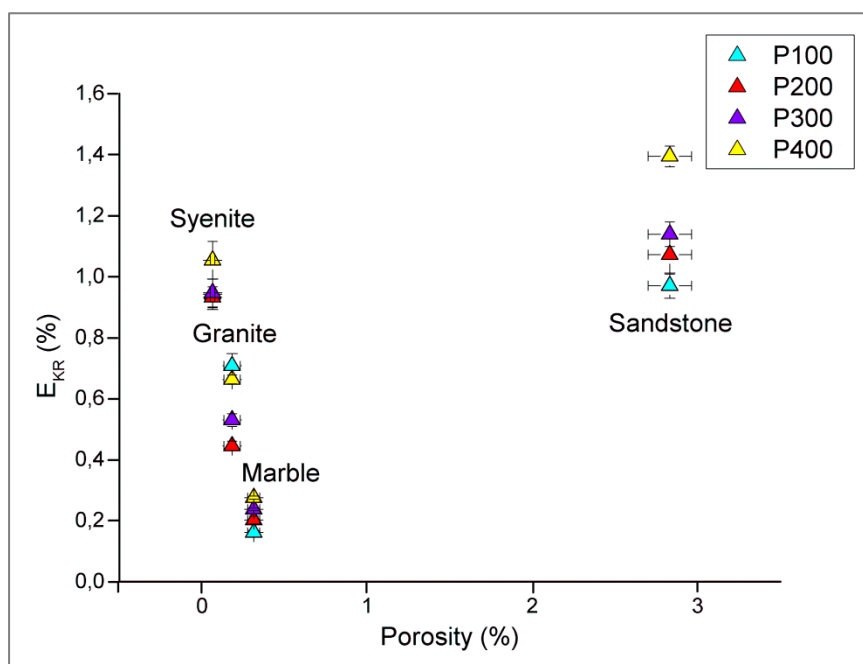


Figure 76 - Relative kerf generation energy (E_{KR}) versus porosity for varying pump pressure. The dots from the same vertical line correspond to the same rock type.

Regarding the physical properties of the rocks studied, it was observed that there was not a property with a proper correlation involving E_{KR} and E_{KRW} . From now on, the

mechanical properties are evaluated in the present thesis. Figure 77 and Figure 78 show the relationship between relative kerf generation energy and the tensile strength for traverse velocity and pump pressure variations, respectively.

A general trend of relative kerf generation energy increase with the increase of tensile strength is observed. However, the correlation involving just the crystalline rocks is more consistent, though tensile strength values disperse much for the same type of rock in a small range of tensile strength. Sandstone presents lower tensile strength than the syenite, but in association with the highest relative kerf generation energy values. These correlations regarding the E_{KRW} values presented R^2 between 0.60 and 0.99 for 100, 200 and 400 mm/min and 0.24 for 300 mm/min; 0.40 for 200, 300 and 400 MPa and 0.64 for 100 MPa.

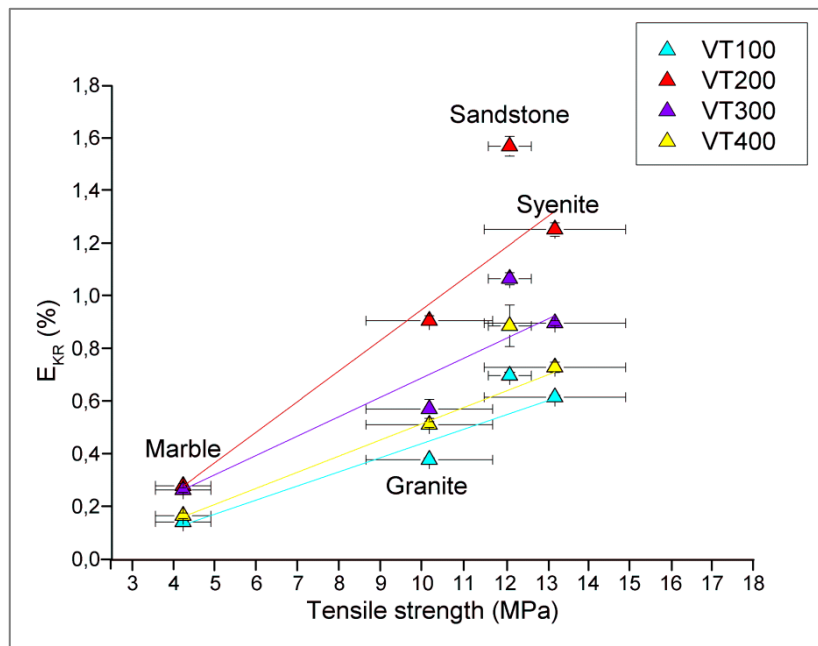


Figure 77 - Relative kerf generation energy (E_{KR}) versus tensile strength for varying traverse velocity. The dots from the same vertical line correspond to the same rock type. R^2 between 0.89 and 0.98.

A similar trend is observed in the correlation between relative kerf generation energy and the uniaxial compressive strength. There is an increase in relative kerf generation energy along with the increase in uniaxial compressive strength. However, there is a significant deviation regarding the results for the sandstone (Figure 79 and Figure 80). These correlations regarding the E_{KRW} values presented R^2 equal to 0.73 for 100, 0.96 for 200 and 400 mm/min and 0.32 for 300 mm/min; between 0.22 and 0.54 for 200, 300 and 400 MPa and 0.90 for 100 MPa.

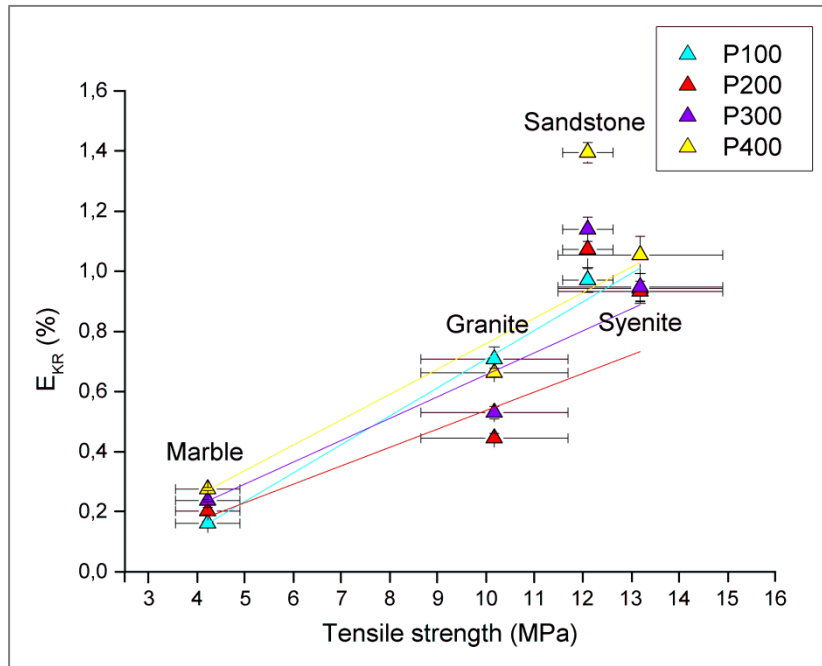


Figure 78 - Relative kerf generation energy (E_{KR}) versus tensile strength for varying pump pressure. The dots from the same vertical line correspond to the same rock type. R^2 between 0.70 and 0.99.

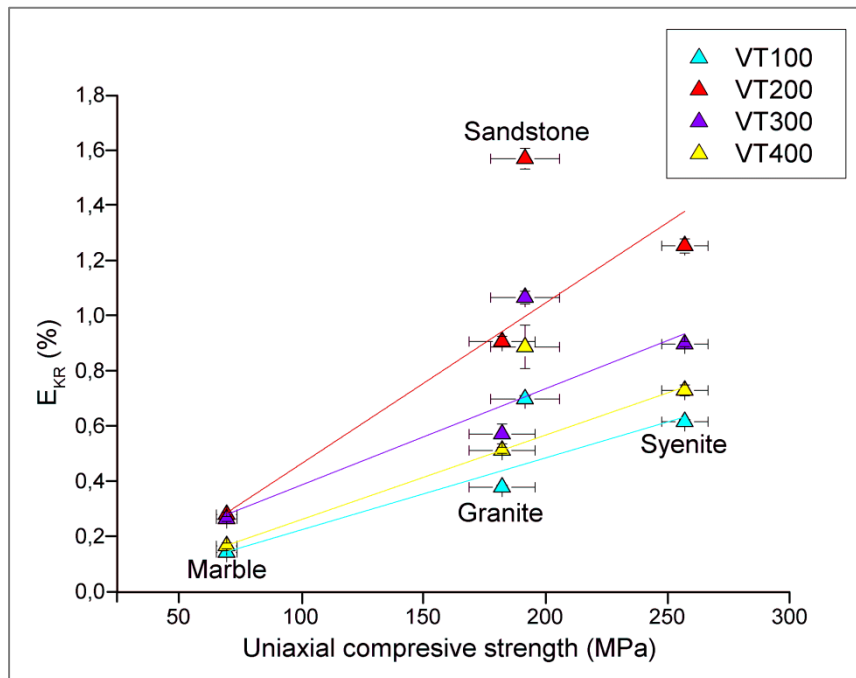


Figure 79 - Relative kerf generation energy (E_{KR}) versus uniaxial compressive strength for varying traverse velocity. The dots from the same vertical line correspond to the same rock type. R^2 between 0.81 and 0.98.

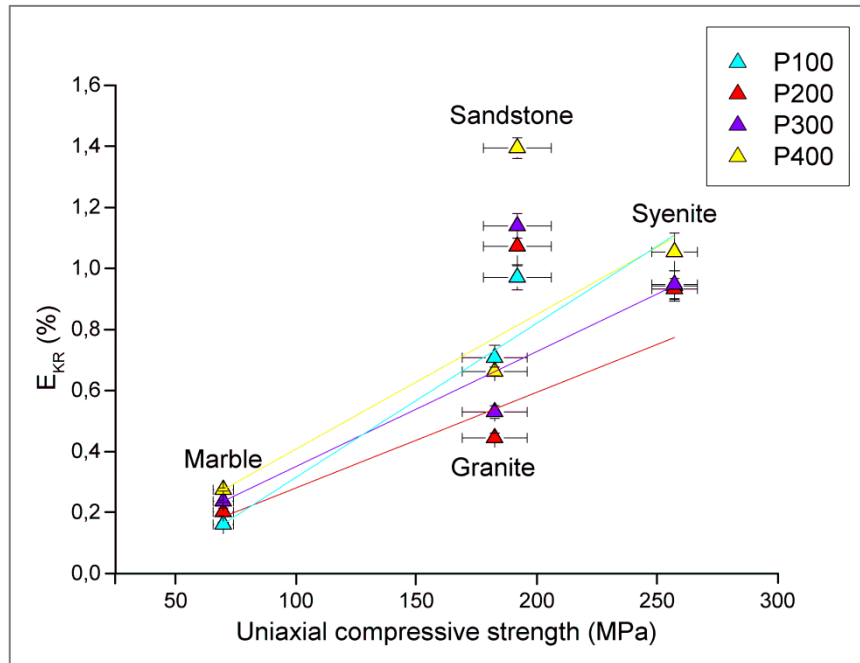


Figure 80 - Relative kerf generation energy (E_{KR}) versus uniaxial compressive strength for varying pump pressure. The dots from the same vertical line correspond to the same rock type. R^2 between 0.45 and 0.92.

Figure 81 and Figure 82 show the relationships between relative kerf generation energy and brittleness for varying traverse velocity and pump pressure, respectively. The considered brittleness is the ratio of uniaxial compressive strength divided by tensile strength, which is the most used definition of brittleness presented in literature. Relative kerf generation energy tends to increase with an increase in brittleness. However, it is clear that for the rocks studied this is not a good property to deal with, because its dispersion is too high.

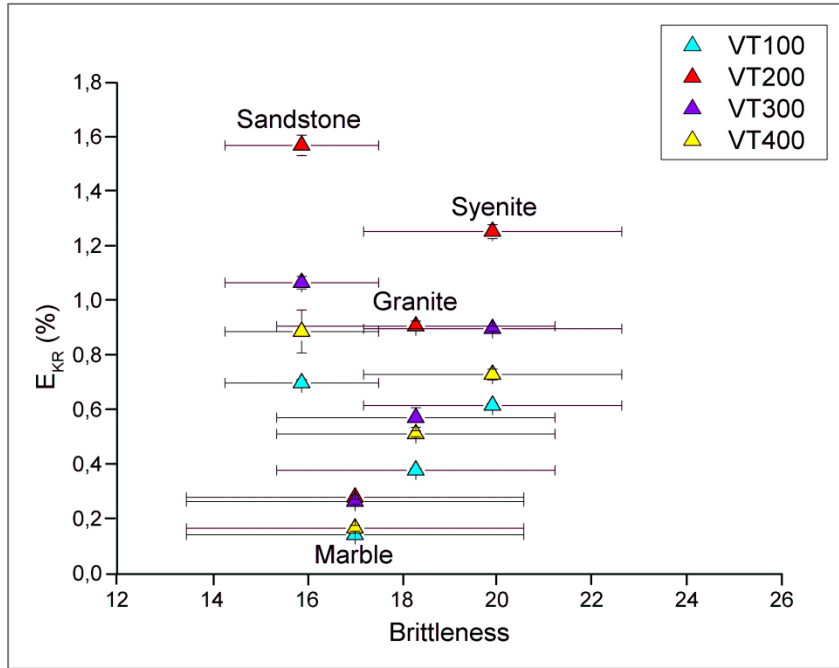


Figure 81 - Relative kerf generation energy (E_{KR}) versus brittleness for varying traverse velocity. The dots from the same vertical line correspond to the same rock type.

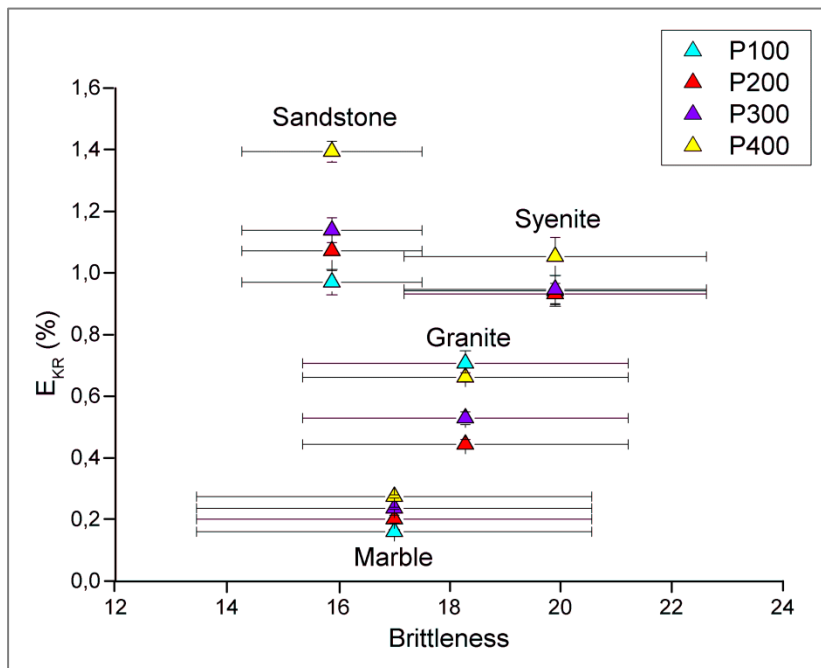


Figure 82 - Relative kerf generation energy (E_{KR}) versus brittleness for varying pump pressure. The dots from the same vertical line correspond to the same rock type.

Figure 83 and Figure 84 show the relationship between relative kerf generation energy and the rock specific energy for varying traverse velocity and pump pressure, respectively. Again, the same trend is observed with a considerable deviation in sandstone results. For the

crystalline rocks, relative kerf generation energy increases with the increase in rock specific energy. The same correlations regarding E_{KR} present R^2 equal to 0.98 for traverse velocity 200 and 400 mm/min, 0.65 for 100 mm/min and 0.27 for 300 mm/min. R^2 is lower than 0.35 for varying pump pressure.

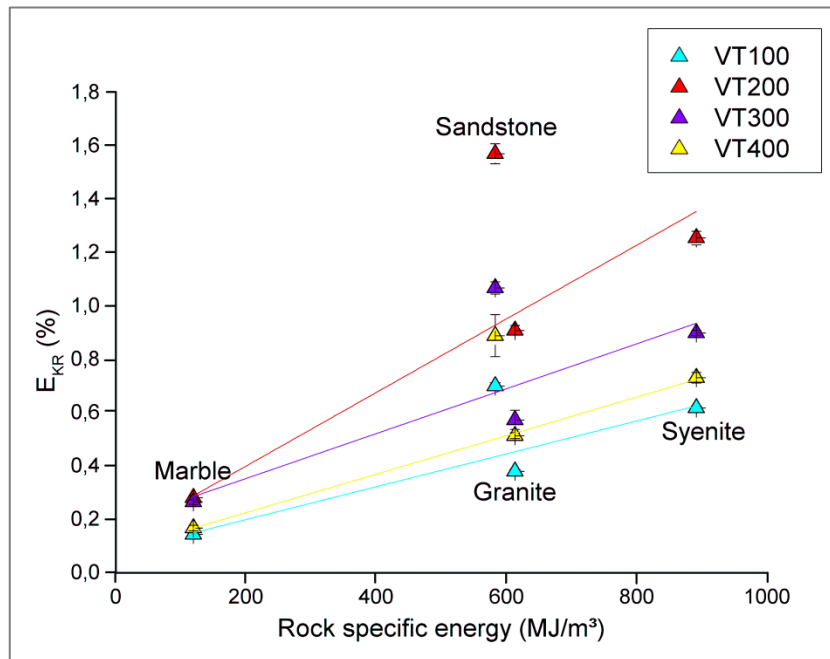


Figure 83 - Relative kerf generation energy (E_{KR}) versus rock specific energy for varying traverse velocity. The dots from the same vertical line correspond to the same rock type. R^2 between 0.83 and 0.96.

As shown in Figure 85 and Figure 86, the Young's modulus does not present a good correlation among the studied rocks. If only the crystalline rocks are considered, then relative kerf generation energy increases with the increase in Young's modulus in an exponential trend.

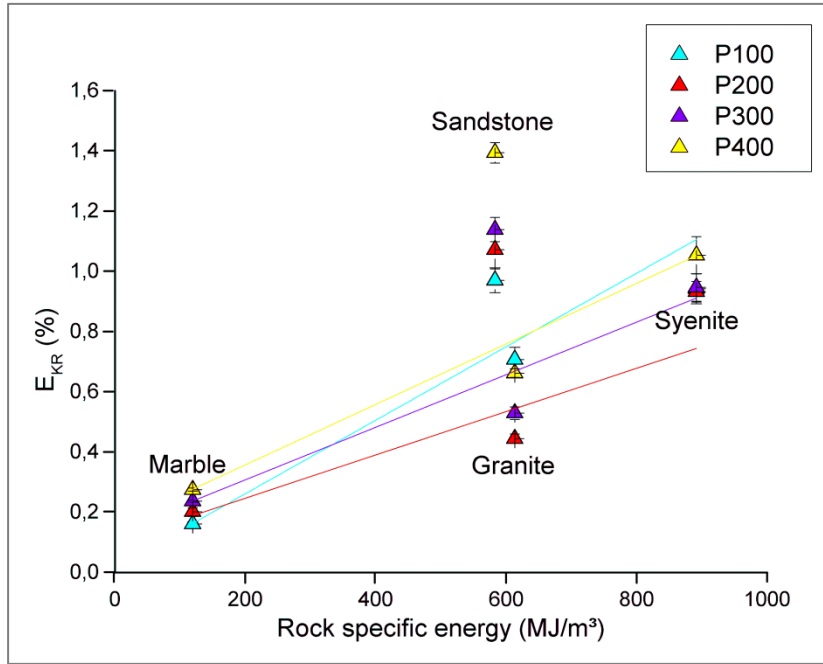


Figure 84 - Relative kerf generation energy (E_{KR}) versus rock specific energy for varying pump pressure. The dots from the same vertical line correspond to the same rock type. R^2 between 0.63 and 0.90.

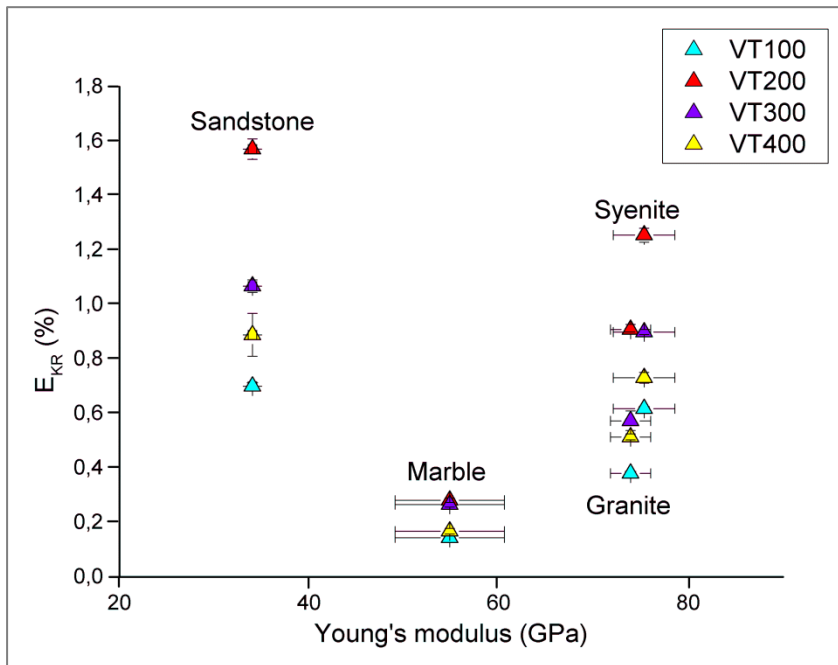


Figure 85 - Relative kerf generation energy (E_{KR}) versus Young's modulus for varying traverse velocity. The dots from the same vertical line correspond to the same rock type.

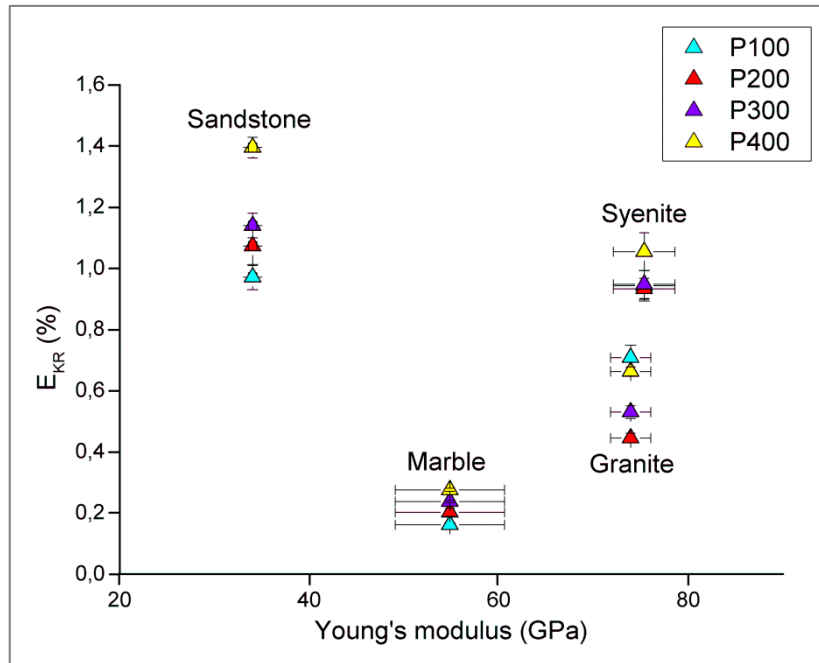


Figure 86 - Relative kerf generation energy (E_{KR}) versus Young's modulus for varying pump pressure. The dots from the same vertical line correspond to the same rock type.

Figure 87 and Figure 88 show the relationships between relative kerf generation energy and the Poisson's ratio for varying traverse velocity and pump pressure, respectively. The presented correlation is good and relative kerf generation energy increases with a decrease in Poisson's ratio. The questionable issue regarding correlations involving Poisson's ratio is that it presents a very narrow range of values, thus several types of rocks may present similar values of Poisson's ratio. In that way, this correlation may be a fortuitous event, not presenting physical consistency. Moreover, the dispersion of Poisson's ratio values are high with overlapping among the majority of the rocks studied.

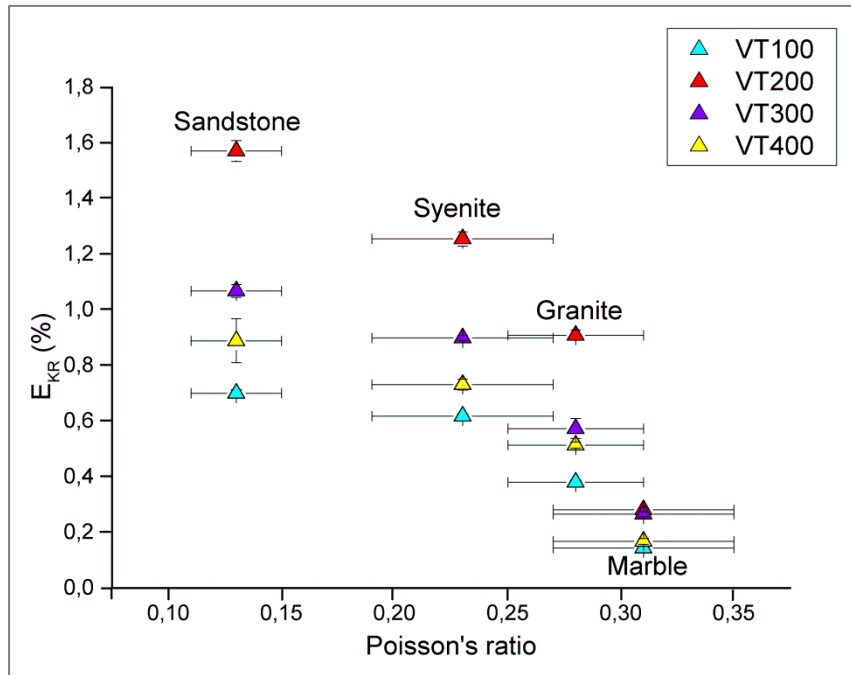


Figure 87 - Relative kerf generation energy (E_{KR}) versus Poisson's ratio for varying traverse velocity. The dots from the same vertical line correspond to the same rock type.

The relationship between relative kerf generation energy and fracture toughness K_{IC} is shown in Figure 89 and Figure 90 for varying traverse velocity and pump pressure, respectively. It is possible to observe a similar pattern to the one presented for Schmidt hardness. In the same manner, only a poor correlation was found between the variables, when only considering the crystalline rocks. Relative kerf generation energy tends to increase with increasing K_{IC} .

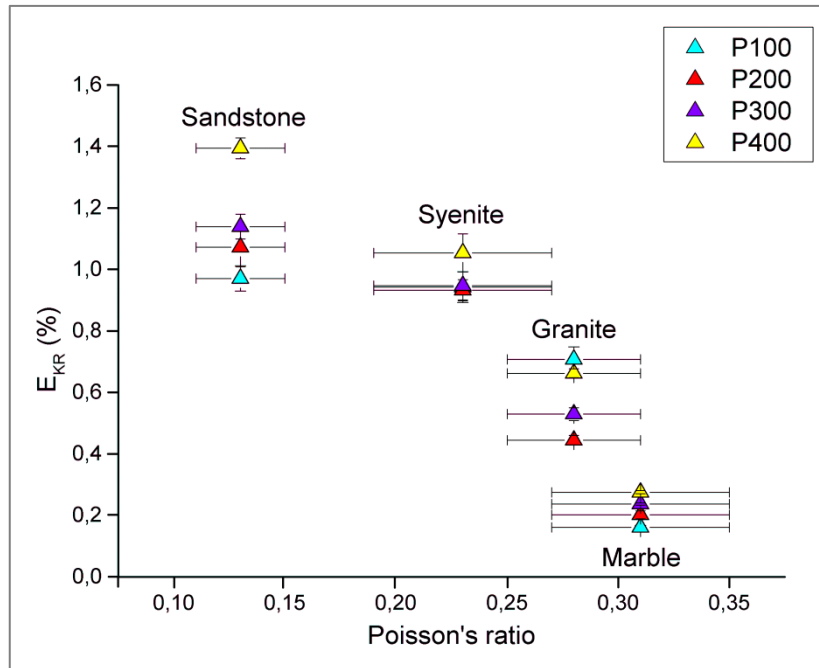


Figure 88 - Relative kerf generation energy (E_{KR}) versus Poisson ratio for varying pump pressure. The dots from the same vertical line correspond to the same rock type.

The relationship between relative kerf generation energy and fracture toughness K_{IC} is shown in Figure 89 and Figure 90 for varying traverse velocity and pump pressure, respectively. It is possible to observe a similar pattern to the one presented for Schmidt hardness. Like previous findings, only a poor correlation was found between the variables, when considering just the crystalline rocks. Relative kerf generation energy tends to increase with increasing K_{IC} .

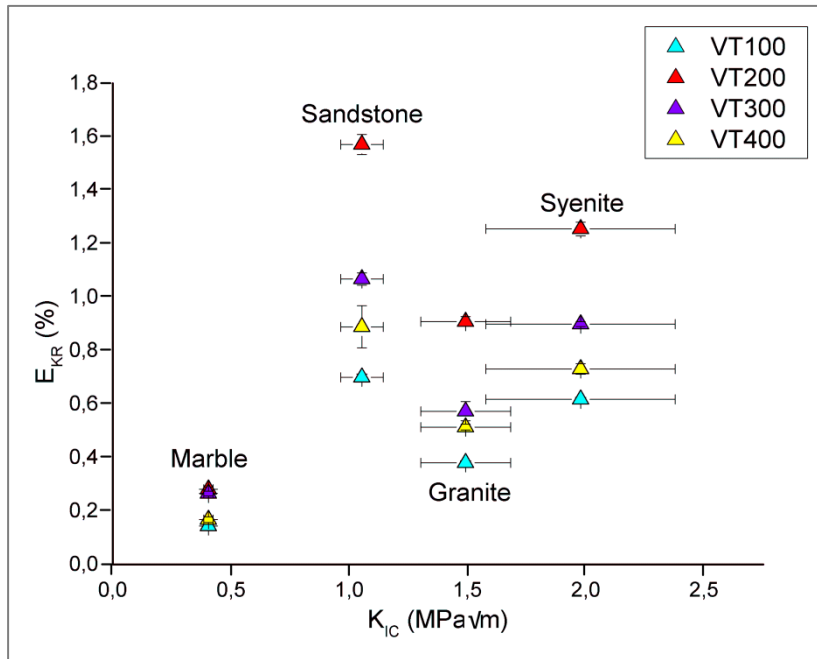


Figure 89 - Relative kerf generation energy (E_{KR}) versus fracture toughness for varying traverse velocity. The dots from the same vertical line correspond to the same rock type.

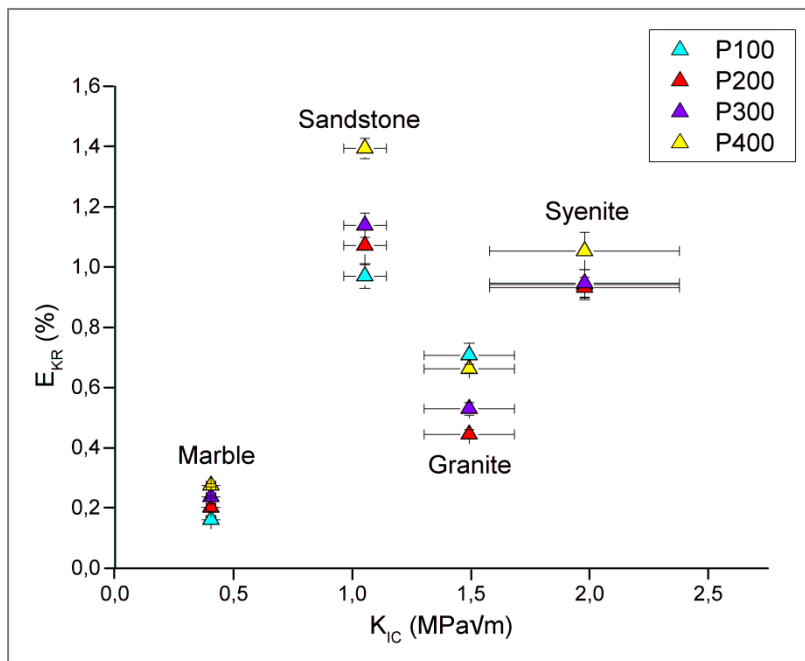


Figure 90 - Relative kerf generation energy (E_{KR}) versus fracture toughness for varying pump pressure. The dots from the same vertical line correspond to the same rock type.

Among all of the properties analyzed, none presented a real good correlation with E_{KR} and E_{KRW} . An important task is to find a property which can describe the behavior of all studied rocks involving the relative kerf generation energy. In most cases, sandstone is the

rock type which presents property values that do not conform to the trends observed for the other rock types.

Sandstone presents the highest values of relative kerf generation energy, thus the transfer of kinetic energy from the machine to the cutting process is more efficient in the case of this rock. The opposite may be stated for the marble, which is the rock which generally presents the lowest values of relative kerf generation energy (in some cases, its values are the same or a little higher than the granite's values).

The studied sandstone is a sedimentary rock which belongs to the Botucatu Formation, it is composed of quartz particles adhered with an amorphous silica cement of the same composition of quartz. The samples collected for this research present as a smooth bedding planes structure with approximately 40 cm spacing. It is considered an atypical sedimentary rock due to its high compressive and tensile strengths. Regarding its generation, it belongs to a desert depositional environment dominated by sandstone. The Botucatu Formation's upper boundary is formed through the interdigitated contact with the Serra Geral Formation, a unit characterized by volcanic rocks such as basalts and diabases (MONTANHEIRO et al., 2011).

The origin of the silicification process is still controversial. Some researchers claim that it is related to the Mesozoic volcanism which generated the Serra Geral Formation, the one associated with the separation between Africa and South America. In that way, Washburne (1930) believes that the silicification is a result of the direct action of lava and igneous intrusions through contact metamorphism. In contrast, Leinz (1938) claims that a metasomatism process took place, modifying the previous sandstone through its interaction with silica-rich juvenile water, resulting in the crystallization of silica as cement. Wernick (1966) goes against the previous theories, explaining that it could not be possible since the silicification process occurred to a great extent, vertically and laterally, in a homogeneous manner. Thus, the author believes that the silicification happened due to variations in the groundwater level over geologic time. For the states of São Paulo and Paraná, Mineropar (2003) recognizes two theories: a) igneous genesis with the Mesozoic volcanism as a source of silica-rich solutions; b) physico-chemical genesis with quartz crystals as a source of silica after their dissolution by contact with residual solutions of basaltic lava.

Sandstone is resistant to abrasion wear and presents relatively high tensile and compressive strength. On the other hand, its Young's modulus and Poisson ratio are low.

When subjected to uniaxial compression, the sandstone deforms more on the longitudinal axis and very little along the transverse axis. Since quartz does not present prominent weak planes and the silica cement is well-attached to the quartz particles, the rock withstands stress with little development of cracks, until a moment near the peak strength when more cracks nucleate, propagate and coalesce in bursts. In contrast to the other studied rocks, sandstone rupture generates less fines and larger pieces, as shown in Figure 91. On the left, many large pieces of rock and a small amount of fines are seen. On the right, larger sharp pieces of the sandstone specimen are presented.



Figure 91 – Sandstone after uniaxial compression test.

Regarding the better transfer of energy in the case of the sandstone, it is possible to draw a comparison between the AWJ cutting and the uniaxial compression test. This rock takes a longer time to start developing cracks when subjected to uniaxial compression, a process which occurs with low and constant loading rates. When it does not support stress any longer, cracks develop quickly and propagate to an explosive coalescence, generating large pieces of rock with little fines. In this case, the transfer of energy from the servo-controlled machine to the rock is efficient because the breakage involves the creation and propagation of cracks without intense comminution or deformation. Also, crack propagation through quartz and silica cement occurs with comparatively high velocities and in a much less stable condition than in the cases of the other studied rocks. The behavior of the sandstone suggests a typical class II behavior according to the classification of Wawersik & Fairhurst (1970). As already mentioned, an attempt to obtain the complete stress-strain curve of the sandstone was

carried out, but its burst behavior did not allow the servo-controlled machine to register all relevant data after the peak strength. It may be inferred that the sandstone is the most brittle rock among the studied rocks. The marble presents a typical class I behavior, i.e. ductile behavior, and the syenite and the granite present class II behavior, but involving more deformation than the sandstone.

In the case of the AWJ cutting, the removal action involves very high velocities and impact forces. The sandstone withstands high stresses under low rate loading in a controlled environment, without involving high impact processes. However, it does not present a high strength against high impact because of the lack of weak features which could absorb and dissipate part of the provided energy.

On the contrary, the transfer of energy in the case of the marble is worse due to the high dissipation that the created net of cracks promotes during its breakage. For this rock, the net of cracks is very dense due to the three cleavage planes presented by calcite crystals. Thus, it is easier to break a rock when fewer cracks propagate for longer distances and under unstable conditions than in a condition where lots of little cracks have to propagate in all directions, connect themselves and then promote coalescence. Moreover, much energy dissipates because of the marble's ductile behavior, which implies more deformation.

Figure 92 shows the marble's conditions after a uniaxial compression test. On the left there is a detail of the particles generated after rupture. Most of them are fine and disaggregate very easily when pressed between fingers. On the right the sample after the test is shown. It is possible to observe that a dense net of cracks is responsible for the rupture of the rock; otherwise it would present more intact areas.

Figure 93 shows a detail of the disaggregation of the marble when subjected to uniaxial compression. The sample had to be secured with adhesive tape in order to maintain its integrity.



Figure 92 - Marble after uniaxial compression test.



Figure 93 - Detail of marble sample after uniaxial compression test.

The syenite and the granite present intermediate behaviors between the sandstone and the marble. Both are feldspar-rich rocks (the feldspar group contain minerals like orthoclase, microcline, albite and oligoclase), thus the two cleavage planes presented in this mineral group influence the transfer of energy on the AWJ cutting and they also influence how these rocks break under uniaxial compression. Although granite presents a considerable amount of quartz crystals, its feldspar crystals have wide dimensions, being larger than the feldspar crystals in the syenite. That may be the main reason why the energy transfer in the granite is

worse than in the syenite. In the granite, cracks propagate throughout its large feldspar crystal cleavages. In the syenite, the process occurs through small and imbricated feldspar crystals.

Figure 94 presents details of a granite specimen after a uniaxial compression test. On the left, it is possible to observe fines, coarser particles and larger elongated pieces of the rock. On the right, a dashed black line marks the main plane of rupture. The specimen remains unsplit, but intense comminution is associated with the main plane of rupture.



Figure 94 - Granite after uniaxial compression test.

The conditions of syenite after uniaxial compression tests are seen in Figure 95. On the left the large elongated pieces predominate. Fines and coarser particles are also parts of syenite disaggregation. The specimen on the right reveals several well-defined planes of rupture, which generated the large pieces shown on the left. Most of these planes pass through the entire specimen, a feature that was not observed in the case of the marble and the granite.



Figure 95 – Syenite after uniaxial compression test.

Comparing the behavior of the studied rocks when subjected to uniaxial compression tests, the broken marble specimen was intensely comminuted due to the dense net of cracks developed through the cleavages of calcite, while the broken granite was partially comminuted but already presented an incipient main plane of rupture. Several planes of rupture were developed in the syenite specimen, with less production of fines. Finally, the sandstone broke explosively generating a very little number of fines and a large number of large pieces with almost no comminution.

The last attempt of correlation was done through the modulus ratio of the rocks, defined by Deere & Miller (1966) as the Young's modulus divided by the uniaxial compressive strength. Fortunately, a better result was obtained for both varying traverse velocity and pump pressure, as shown in Figure 96 through Figure 99. Modulus ratio values present considerable standard deviation mainly for the granite and marble, but the total range of values covered by modulus ratio is wide. Taking into account the mean values and the deviation for the rocks studied, there is no overlapping between them. Correlations between E_{KR} (relative kerf generation energy) and modulus ratio are linear for both types of tests (varying traverse velocity and pump pressure). The decrease in modulus ratio implies in the increase of E_{KR} .

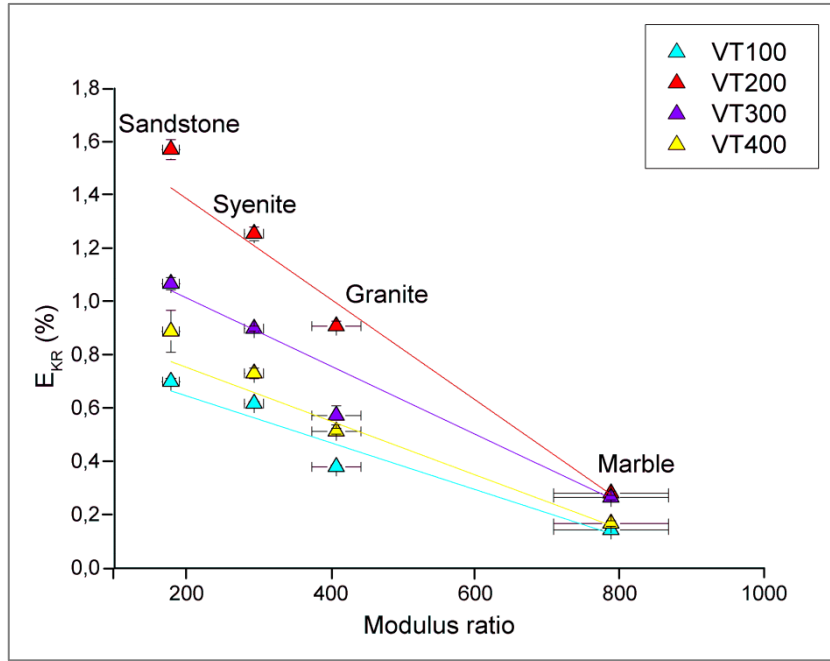


Figure 96 - Relative kerf generation energy (E_{KR}) versus the modulus ratio for varying traverse velocity. The dots from the same vertical line correspond to the same rock type. R^2 between 0.91 and 0.99.

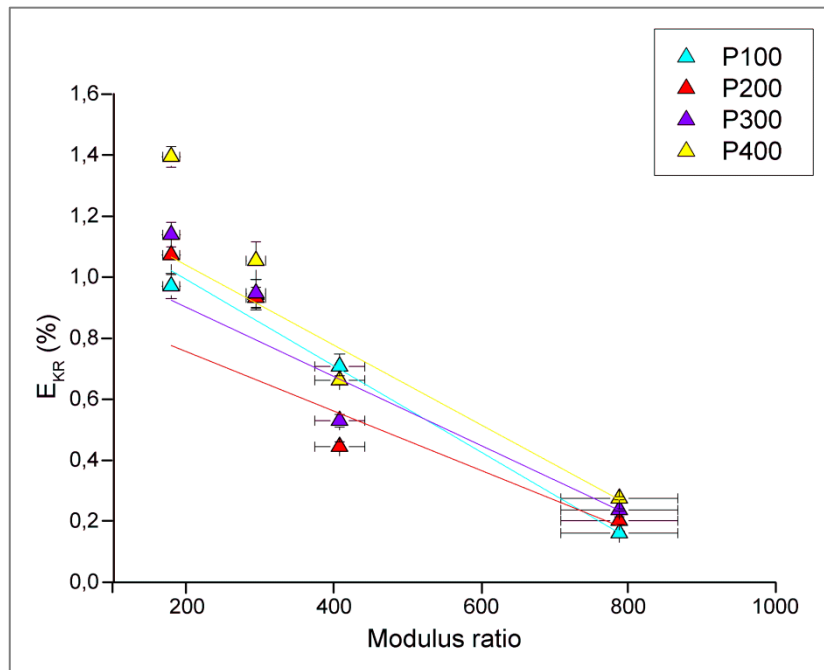


Figure 97 - Relative kerf generation energy (E_{KR}) versus the modulus ratio for varying pump pressure. The dots from the same vertical line correspond to the same rock type. R^2 between 0.67 and 0.99.

In the case of correlations between E_{KRW} and modulus ratio the trends are not the same for varying traverse velocity and pump pressure. Regarding varying traverse velocity, there is a general trend of increase of E_{KRW} with the decrease of modulus ratio. This trend is clear for 200 mm/min, which is the most efficient traverse velocity. For the tests with 100 and 400 mm/min the trend is the same, except for the sandstone, which tends to present lower E_{KRW} values than expected. However, the E_{KRW} values obtained for the sandstone were calculated based on an assumption of its W_R , thus this value may vary a little. For tests with 300 mm/min the trend would be similar, except for the marble, which presented E_{KRW} values similar to those obtained with 200 mm/min.

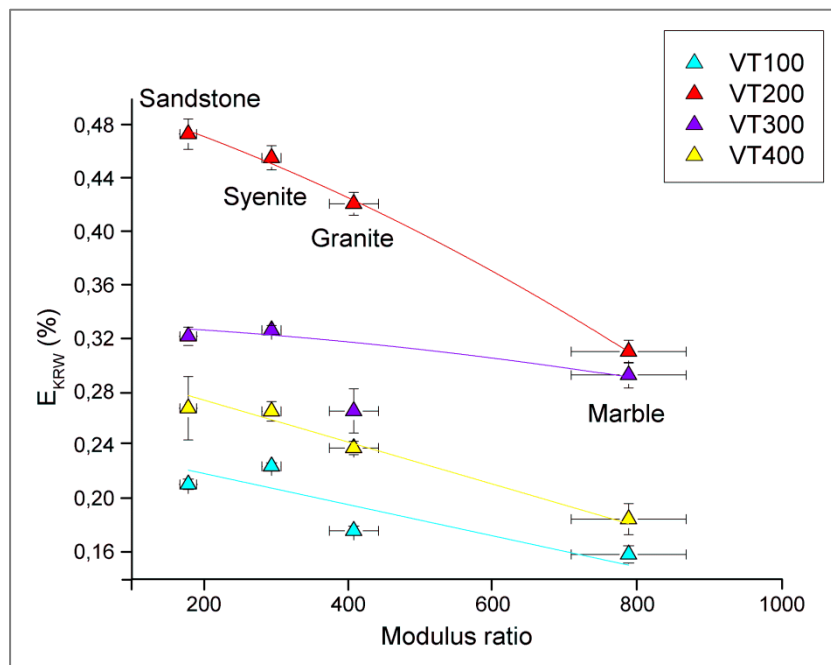


Figure 98 - Relative kerf generation energy (E_{KRW}) versus the modulus ratio for varying traverse velocity. The dots from the same vertical line correspond to the same rock type. $R^2 = 0.37$ (100 mm/min), 0.99 (200 mm/min), 0.54 (300 mm/min) and 0.94 (400 mm/min).

In the case of the tests with varying pump pressure, the trend of increase of E_{KRW} with the decrease of modulus ratio is true for all rocks but the marble, which presents a high modulus ratio and class I behavior.

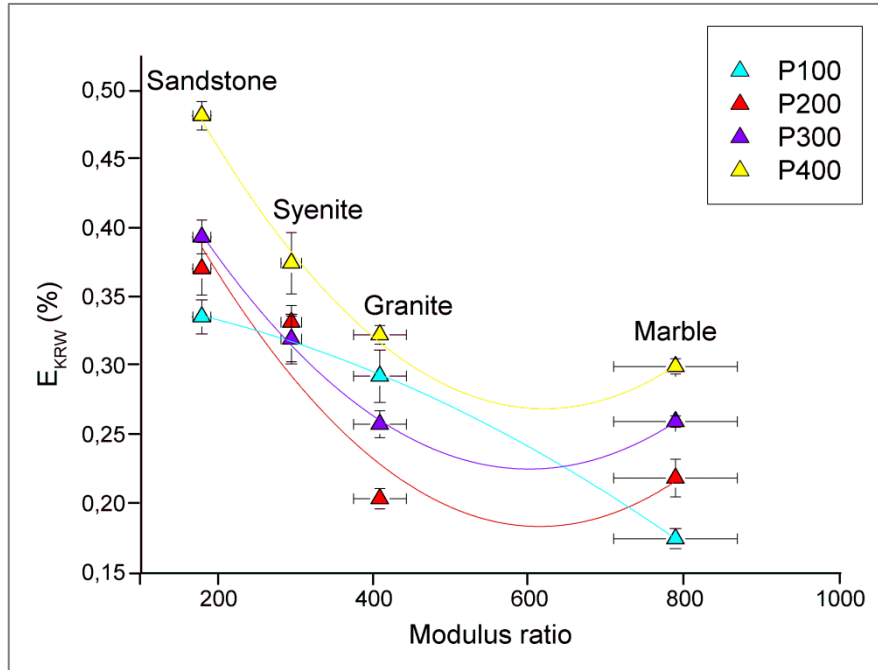


Figure 99 - Relative kerf generation energy (E_{KRW}) versus the modulus ratio for varying pump pressure. The dots from the same vertical line correspond to the same rock type. R^2 between 0.65 and 0.99.

The modulus ratio is an interesting rock property since it considers both strength and deformation behaviors, representing a good measure of brittleness. The concept of brittleness was briefly discussed in Chapter 2. A rock with a high brittleness or low modulus ratio suggests lack of ductility, a concept which is compatible with the behavior of the studied rocks. Rocks with low brittleness present ductile behavior and high modulus ratio values, like marble. Rocks with high brittleness present very brittle behavior, low modulus ratio values and class II behavior like sandstone. However, the property also presents limitations, because if rocks with increasing uniaxial compressive strength and the same Young's modulus are considered, they will present modulus ratio varying from low to high strength.

According to the engineering classification for intact rock of Deere & Miller (1966), the studied rocks may be sorted as indicated in Table 57 and Figure 100.

Table 57 - Classification of the studied rocks based on the classification proposal of Deere & Miller (1966).

Rock	Strength criterion	Modulus ratio criterion
Syenite	very high strength	average modulus ratio
Granite	high strength	average modulus ratio
Marble	medium strength	high modulus ratio
Sandstone	high strength	low modulus ratio

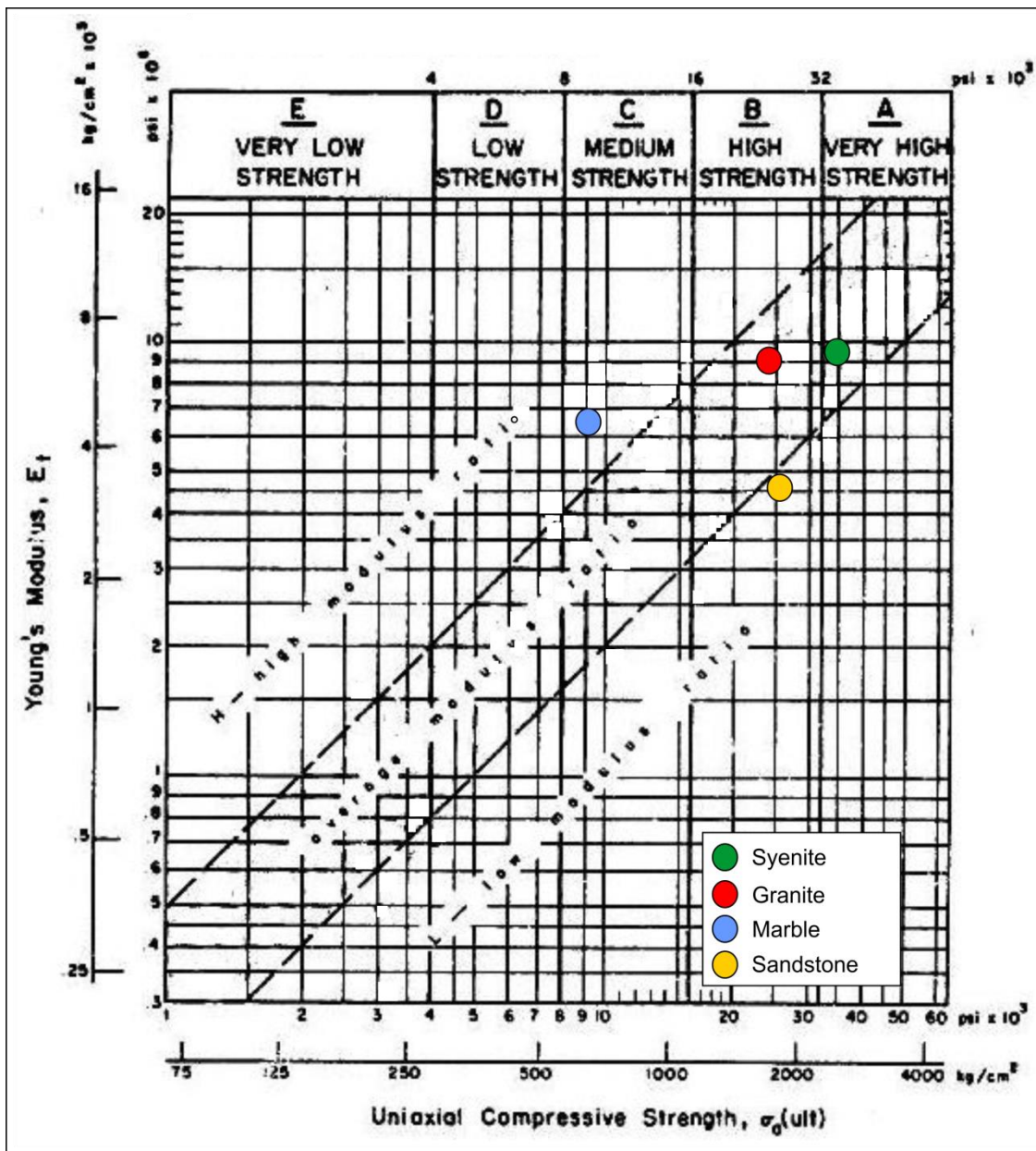


Figure 100 - Engineering classification for intact rock (DEERE & MILLER, 1966).

As discussed in Deere & Miller (1966), low to average modulus ratio values are expected for sandstones due to their higher porosity. In addition, although it is a high strength rock, the studied sandstone does not present interlocking texture. These features contribute to the better transfer of energy during the AWJ cutting. A rock with interlocking texture such as syenite and granite, makes it more difficult for a crack to cross over a sample, since it needs to deviate more from the main cracking path in order to avoid more resistant – or interlocked – areas. Thus, energy is lost due to deviation.

Regarding the marble, the authors show that the same trend of high modulus ratio is observed in limestones, dolomites and marbles. The two first types of rocks are sedimentary while the last one is a metamorphic rock. However, they are all monomineralic rocks composed of calcite. Thus, the main influence on the modulus ratio in this case is the mineralogy, especially the specific crystalline structure of calcite, i.e. its prominent cleavage planes. The marble does not present interlocking texture because calcite has a prismatic to rhomboedrical habit and its intergranular contacts are generally planar regarding other calcite crystals. However, as discussed before, the transfer of energy during AWJ cutting is compromised by the dissipation of energy due to the marble's deformation related to calcite's cleavages. As the cleavages open with ease, the rock is comminuted because of the generation of a widely spread number of small cracks which propagate in little distances. Therefore, the energy dissipated in this situation is greater than in a situation where fewer cracks are generated and propagate greater distances.

It is interesting to notice that a relationship exists between the modulus ratio values of the studied rocks, the transfer of energy in breakage (in both AWJ cutting and uniaxial compression tests) and the manner with which they break in uniaxial compression. The smaller the modulus ratio, the greater is relative kerf generation energy and the smaller the comminution during a rock's breakage, in other words, fewer and well-developed cracks are created and propagate throughout the entire specimen to break it.

Returning to the information shown in Figure 65 and Figure 66 on the efficiency based on the relationship between the specific energy of cutting and cutting rate, there are two trends: one for marble and sandstone, the other for syenite and granite. In the first case, generally the sandstone presents the higher cutting rate in association with the lower specific energy of cutting, an observation that corroborates what has been discussed about general efficiency of cutting. Thus, the cutting of sandstone grants the most efficiency, since the

transfer of energy is better, the specific energy of cutting smaller and the cutting rate are higher, even this rock, which presents higher abrasive, tensile and compressive strength. In the case of the igneous rocks, this line of reasoning is not applied, since cutting rate and specific energy of cutting are heterogeneous for both syenite and granite.

Regarding the study of pre-cracked multiphase materials, Momber & Kovacevic (1997) found very good correlations between depth of cut and mechanical properties, such as uniaxial compressive strength and Young's modulus, for concrete. This was not observed in the present research, neither for volume removal nor for relative kerf generation energy. Good correlations are more difficult to obtain for rock samples, since their behaviors are far more heterogeneous and their generation processes are very distinct, without man's interference. Many authors conduct research considering concrete samples as rock-like materials, however, in reality they present similar behavior to a restricted range of rocks. It seems that the modulus ratio may be the property which better describes the phenomena involved in AWJ rock cutting.

The results obtained for the correlation between relative kerf generation energy and the modulus ratio were linearized and adjusted in order to obtain equations which describe the relative kerf generation energy behavior for the diverse tests conditions (Figure 101 through Figure 104). The equations and R^2 (coefficient of determination) values are shown in Table 58. As discussed before, it is reasonable to assume a specific destruction work of 174,84 kJ/m³ for the sandstone, thus the correlations were also linearized for all studied rocks regarding E_{KRW} .

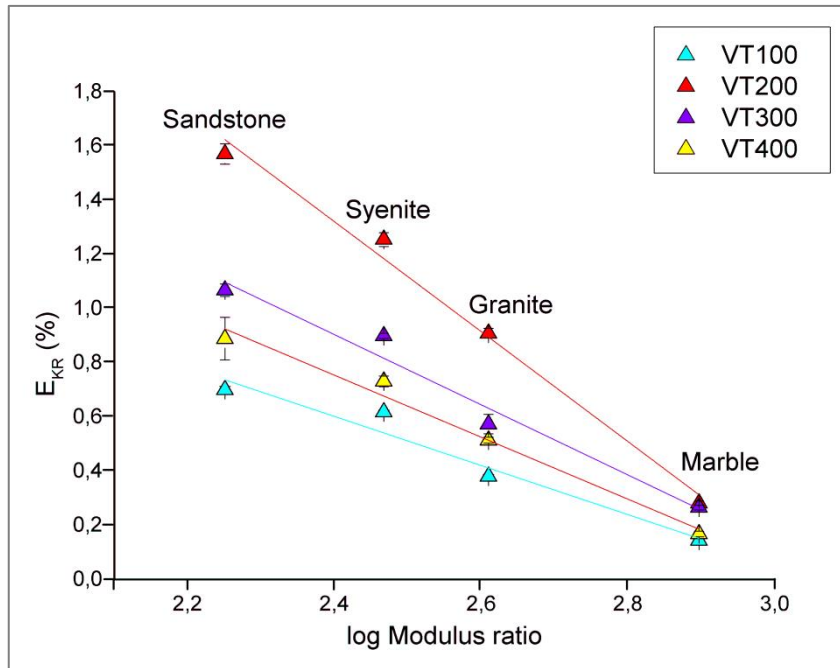


Figure 101 - Relative kerf generation energy (E_{KR}) versus the modulus ratio for varying traverse velocity. The dots from the same vertical line correspond to the same rock type. R^2 between 0.93 and 0.98.

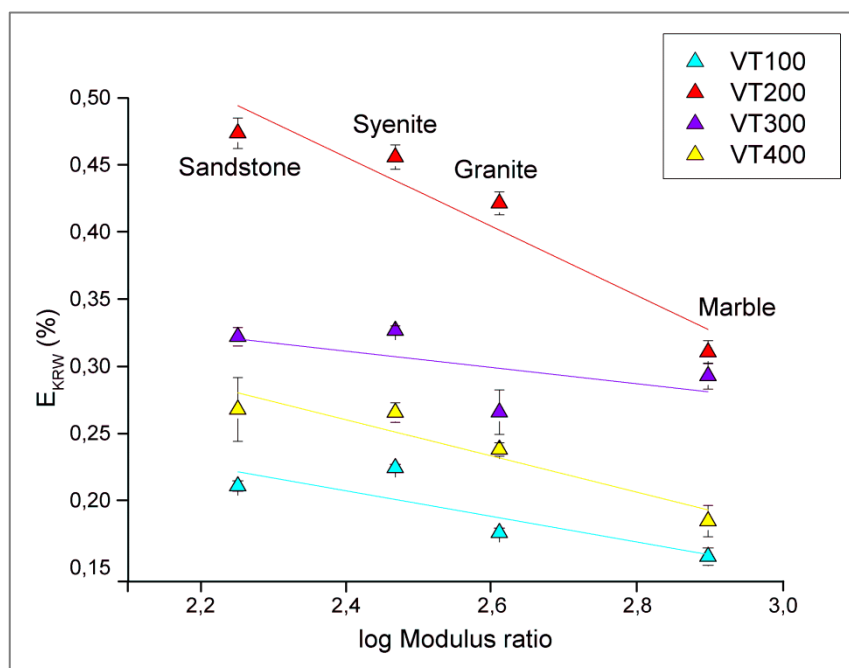


Figure 102 - Relative kerf generation energy (E_{KRW}) versus the modulus ratio for varying traverse velocity. The dots from the same vertical line correspond to the same rock type. $R^2 = 0.58$ (100 mm/min), 0.87 (200 mm/min), 0.37 (300 mm/min) and 0.84 (400 mm/min).

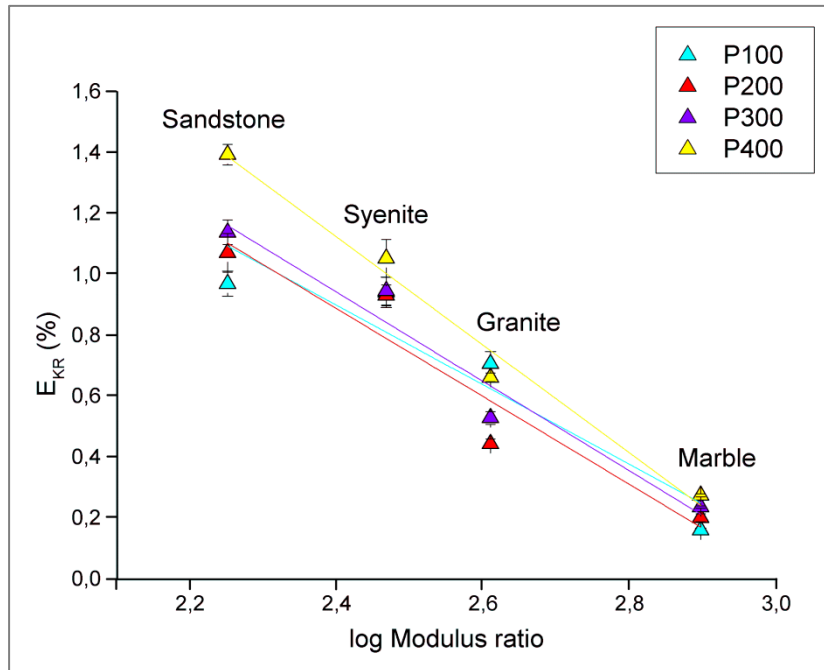


Figure 103 - Relative kerf generation energy (E_{KR}) versus the modulus ratio for varying pump pressure. The dots from the same vertical line correspond to the same rock type. R^2 between 0.83 and 0.97.

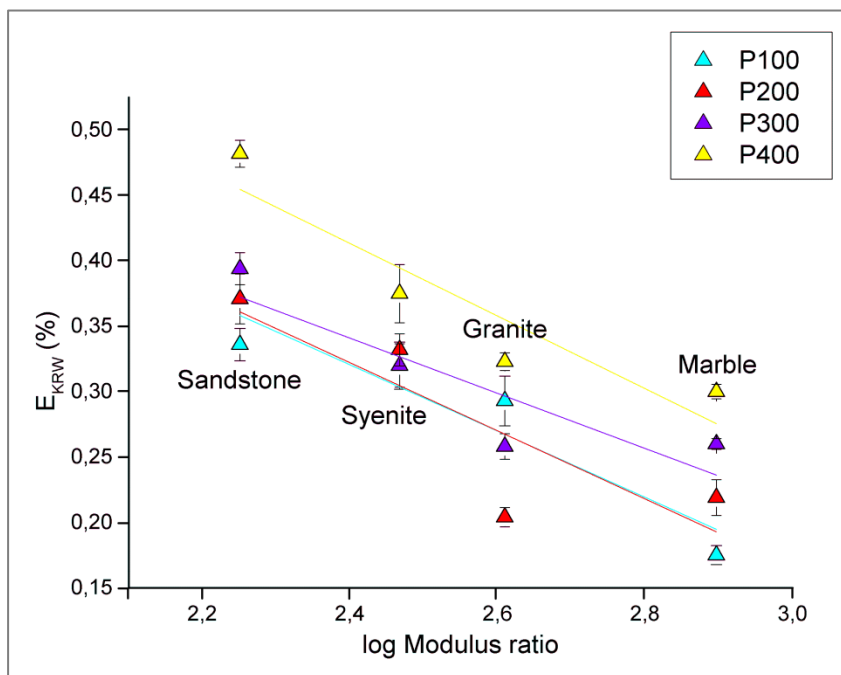


Figure 104 - Relative kerf generation energy (E_{KRW}) versus the modulus ratio for varying pump pressure. The dots from the same vertical line correspond to the same rock type. $R^2 = 0.83$ (100 mm/min), 0.59 (200 mm/min), 0.69 (300 mm/min) and 0.79 (400 mm/min).

Table 58 - Equations obtained for the correlations between the relative kerf generation energy (E_{KR}) and the modulus ratio. v_T – traverse rate in mm/min, P – pump pressure in MPa, MR – modulus ratio.

Test condition	Equation	R^2
v_T 100	$E_{KR} = 2,7765 - \log(MR).0,9061$	0,93
v_T 200	$E_{KR} = -6,1923 - \log(MR).2,0298$	0,98
v_T 300	$E_{KR} = 4,0125 - \log(MR).1,2953$	0,96
v_T 400	$E_{KR} = 3,5008 - \log(MR).1,1445$	0,98
P 100	$E_{KR} = 4,0348 - \log(MR).1,3065$	0,83
P 200	$E_{KR} = 4,3532 - \log(MR).1,4438$	0,87
P 300	$E_{KR} = 4,4653 - \log(MR).1,4679$	0,93
P 400	$E_{KR} = 5,3789 - \log(MR).1,7732$	0,97
v_T 100	$E_{KRW} = 0,436 - \log(MR).0,095$	0,58
v_T 200	$E_{KRW} = 1,0753 - \log(MR).0,2581$	0,87
v_T 300	$E_{KRW} = 0,4574 - \log(MR).0,0608$	0,37
v_T 400	$E_{KRW} = 0,5845 - \log(MR).0,1350$	0,84
P 100	$E_{KRW} = 0,9283 - \log(MR).0,2533$	0,83
P 200	$E_{KRW} = 0,9471 - \log(MR).0,2604$	0,59
P 300	$E_{KRW} = 0,8468 - \log(MR).0,2108$	0,69
P 400	$E_{KRW} = 1,0790 - \log(MR).0,2774$	0,79

Brittleness is a property well investigated in the field of mechanical rock cutting. Most of the studies investigate the correlations between brittleness and the specific energy of cutting (SE_C) or cutting rate. Diverse studies suggest that brittleness plays an important role in the drillability of rocks, since the increase in rock brittleness supposedly causes an increase in penetration rate (ALTINDAG, 2002). The problem is that there is no agreement on a precise definition and calculation of brittleness in the scientific community, thus the available data seems to be scattered and non-conclusive. Most of the studies focus on definitions of brittleness which involve only strength properties like tensile and compressive strength (KAHRAMAN, 2002; ALTINDAG, 2002; COPUR et al., 2003; GOKTAN & YILMAZ, 2005; YARALI & SOYER, 2011), but the obtained correlations are generally poor rarely

good. As already mentioned, Thuro & Spaun (1996) introduced the specific destruction work as a new rock property, which is defined as the area under the complete stress strain curve of a material. It reflects the work of shape altering including the post failure section, i.e. the work required to destruct a rock sample. It is an interesting property to correlate with the drillability of rocks, since it involves both strength and deformation conditions. The authors obtained very good correlations between this property and the drilling rates of drill hammers. Thuro & Plinninger (1999) obtained very good results in the correlation of the specific destruction work and the cutting rate of roadheader bits. Atici & Ersoy (2009) also found good correlations between the property and the drilling rates of circular diamond saws and drilling bits.

In the field of WJ and AWJ cutting, brittleness is poorly investigated. El-Domiaty et al. (1996) state that low and high brittleness are conditions which result in different types of erosive behavior during WJ and AWJ cutting. However, no attempts of correlation between the property and the AWJ cutting parameters were performed by the authors.

Kahraman (2003) claims that in general the modulus ratio is poorly investigated. The author analyzed the influence of the modulus ratio on the penetration rate of mechanical rock cutting. The author found strong correlations between the modulus ratio and the penetration rates of rotary and diamond drills. A significant correlation was found for percussive drills, however in one of the cases this correlation was only good when rocks with a porosity higher than 1,23% were excluded from the analysis.

In the present thesis, good correlations were found between the modulus ratio (as a brittleness measure) and the relative kerf generation energy (E_{KR} and E_{KRW}). However, the property does not present good correlations regarding other parameters, like the removed volume of rock (V_R), the specific energy of cutting (SE_C) and the cutting rate. Figure 105 through Figure 112 present the relationship between the modulus ratio and the other AWJ cutting parameters related to energy. In the case of the kerf generation energy (E_K), a good correlation exists for the tests with traverse velocity variation (Figure 107 and Equations 44 through 47) and the tests with pump pressure variations (Figure 111 and Equations 48 through 51). The poor correlations presented below are related to a conflict which exists between the sandstone and the marble. They present modulus ratio values very low and very high, respectively. However, their removed volumes, cutting rates and specific energy of cutting are very similar. The difference between the kerf generation energy, the relative kerf generation

energy and the other mentioned parameters is that the last parameters are not related to the effective energy spent in their disaggregation, thus other properties have to be investigated. Through the analysis of the correlations between the parameters which consider the total amount of energy (V_R , SE_C and CR) and the modulus ratio, it is observed that the best efficiency of cutting regarding large removal of rock in association with low energy expenditure of energy occurs for the extremes of brittleness: The most brittle rock – sandstone, and the most ductile rock – marble.

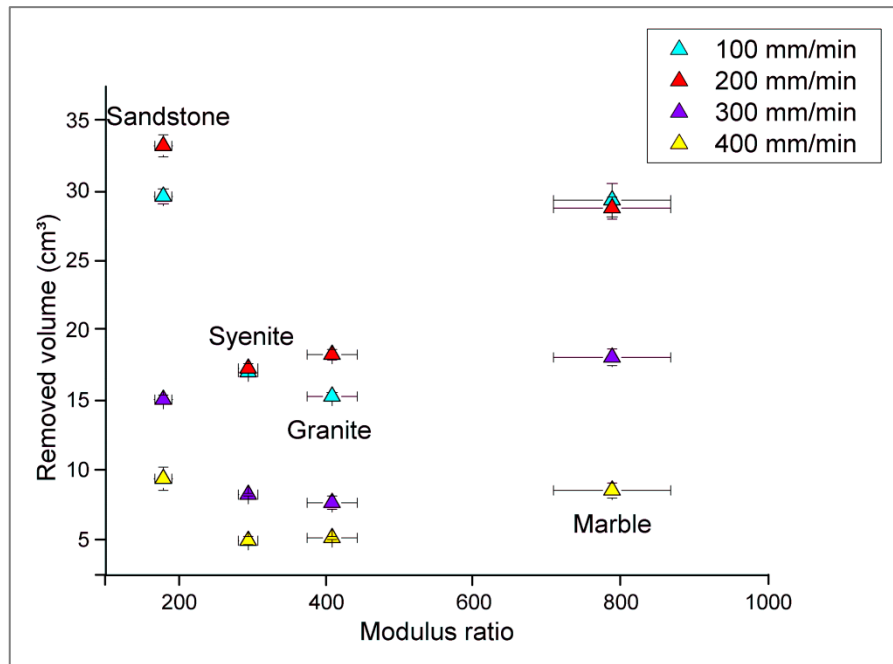


Figure 105 – Removed volume of rock (V_R) versus the modulus ratio for varying traverse velocity. The dots from the same vertical line correspond to the same rock type.

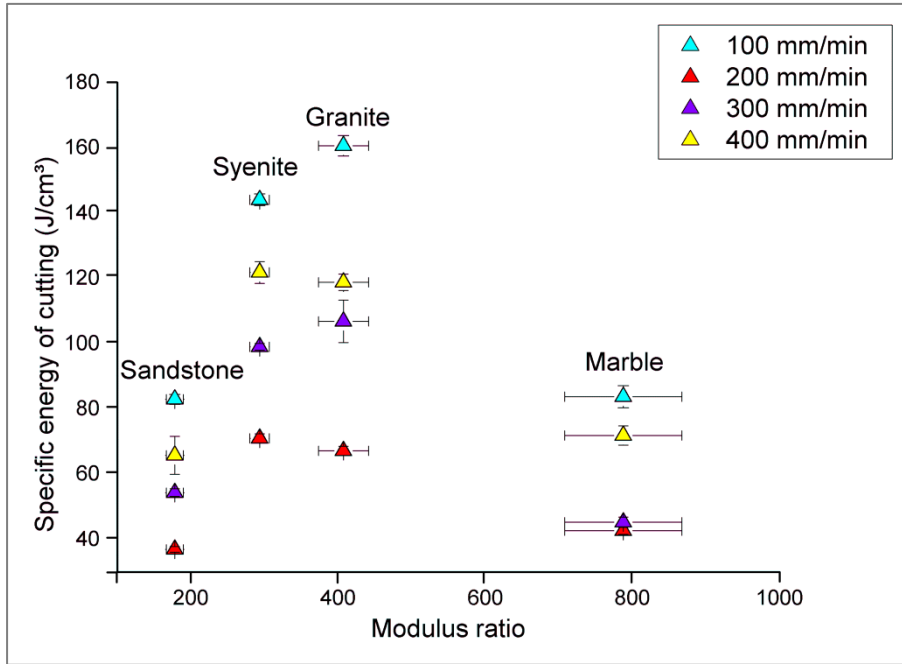


Figure 106 – Specific energy of cutting (SE_C) versus the modulus ratio for varying traverse velocity. The dots from the same vertical line correspond to the same rock type.

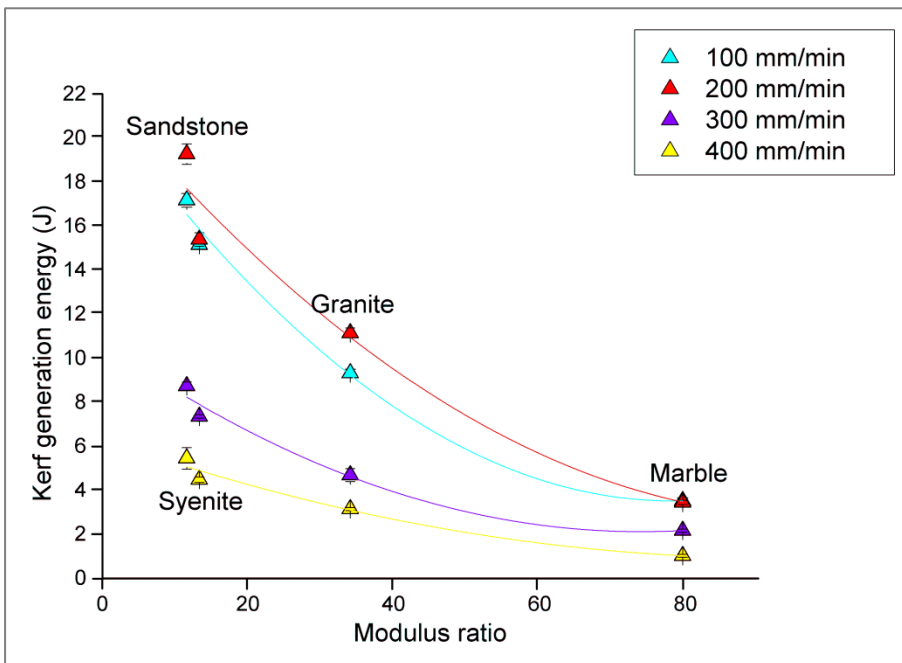


Figure 107 – Kerf generation energy (E_K) versus the modulus ratio for varying traverse velocity. The dots from the same vertical line correspond to the same rock type.

$$VT100: E_K = 21,4592 - 0,4589.MR + 0,0029.MR^2 \quad (R^2 = 0.97) \quad (44)$$

$$VT200: E_K = 22,0023 - 0,3930.MR + 0,0020.MR^2 \quad (R^2 = 0.88) \quad (45)$$

$$VT300: E_K = 10,7281 - 0,2329.MR + 0,0022.MR^2 \quad (R^2 = 0.93) \quad (46)$$

$$VT400: E_K = 6,3429 - 0,1164.MR + 6,24152E^{-4}.MR^2 \quad (R^2 = 0.91) \quad (47)$$

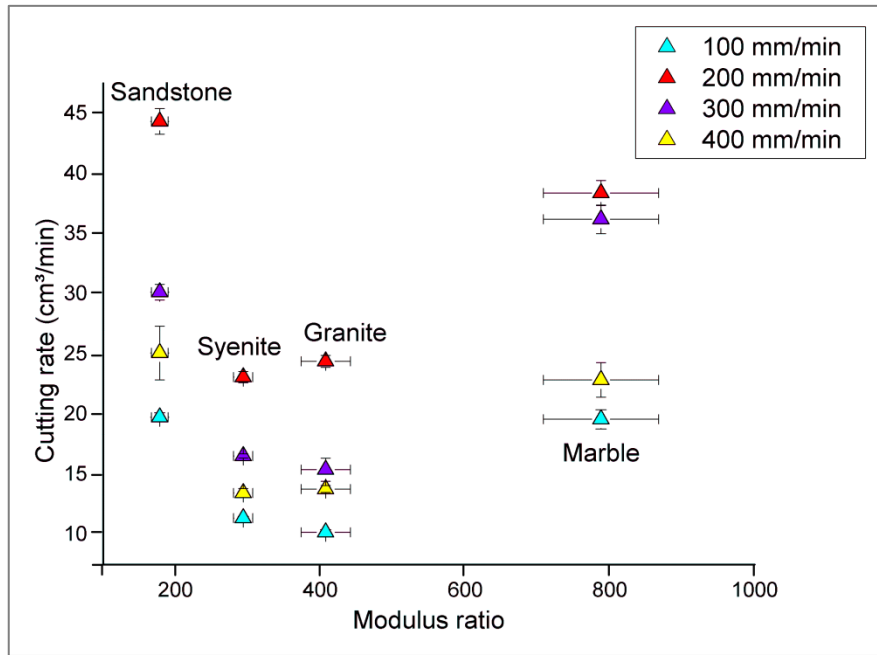


Figure 108 - Cutting rate (mm³/s) versus the modulus ratio for varying traverse velocity. The dots from the same vertical line correspond to the same rock type.

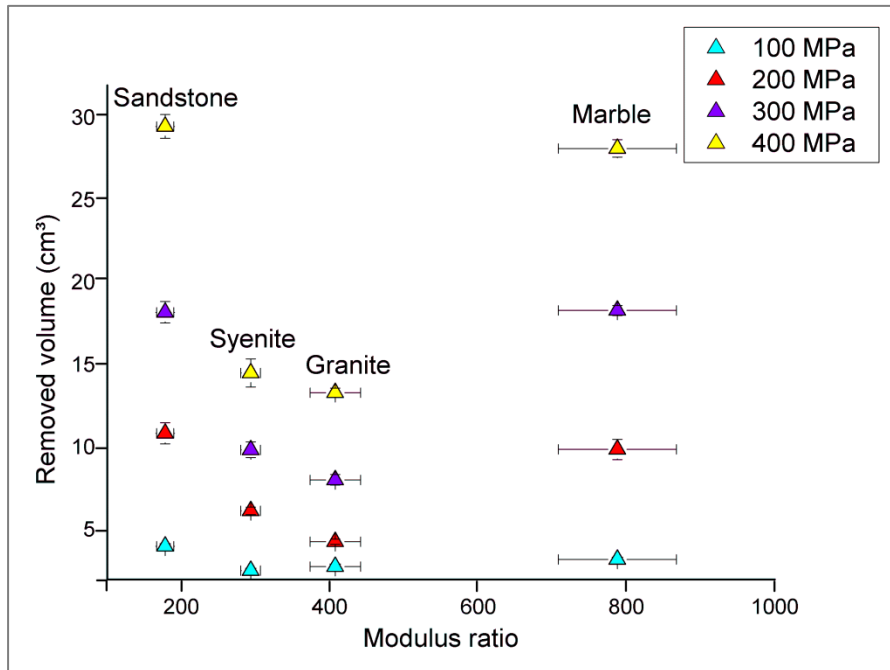


Figure 109 - Removed volume of rock (V_R) versus the modulus ratio for varying pump pressure. The dots from the same vertical line correspond to the same rock type.

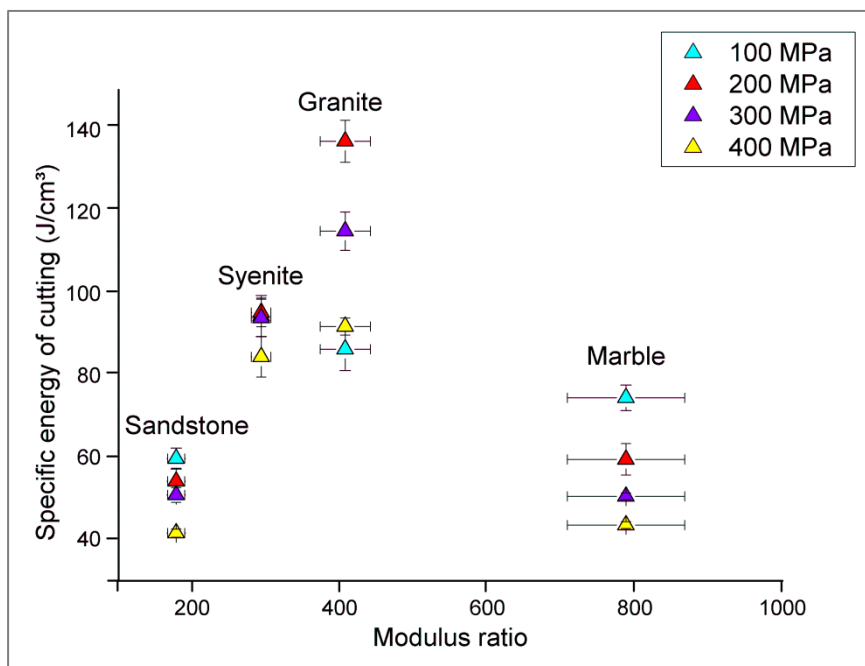


Figure 110 – Specific energy of cutting (SE_C) versus the modulus ratio for varying pump pressure. The dots from the same vertical line correspond to the same rock type.

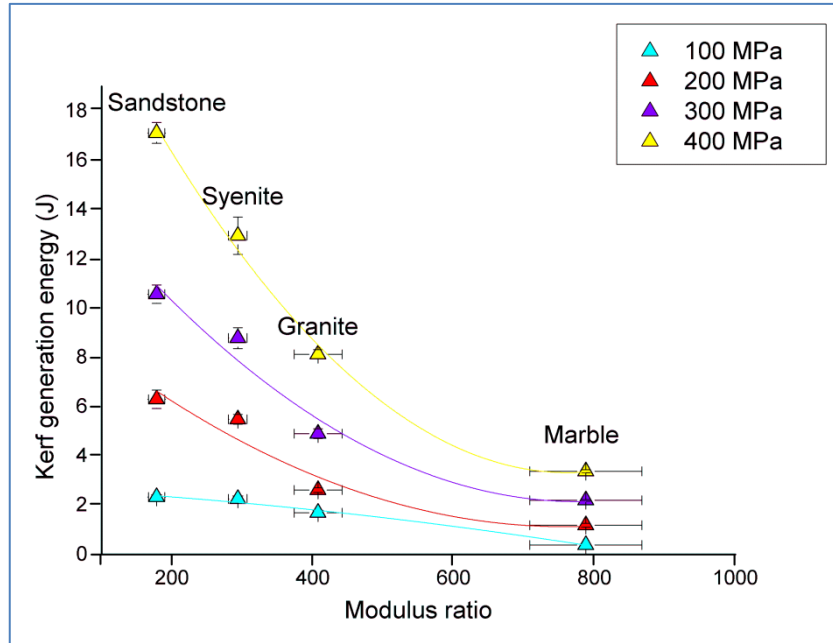


Figure 111 – Kerf generation energy (E_K) versus the modulus ratio for varying pump pressure. The dots from the same vertical line correspond to the same rock type. R^2 between 0.82 and 0.98.

$$P100: E_K = 2,7147 - 0,0015MR - 1,83103E^{-6}MR^2 \quad (R^2 = 0.96) \quad (48)$$

$$P200: E_K = 10,5271 - 0,0248MR + 1,6306E^{-5}MR^2 \quad (R^2 = 0.82) \quad (49)$$

$$P300: E_K = 16,9282 - 0,038MR + 2,44594E^{-5}MR^2 \quad (R^2 = 0.91) \quad (50)$$

$$P400: E_K = 27,1921 - 0,0626MR + 4,10306E^{-5}MR^2 \quad (R^2 = 0.98) \quad (51)$$

Other correlations were explored regarding parameters V_R , SE_C and CR . For them, fair linear correlations with R^2 between 0.67 and 0.99 were found with Young's modulus and shear modulus, but without any significant physical relevance.

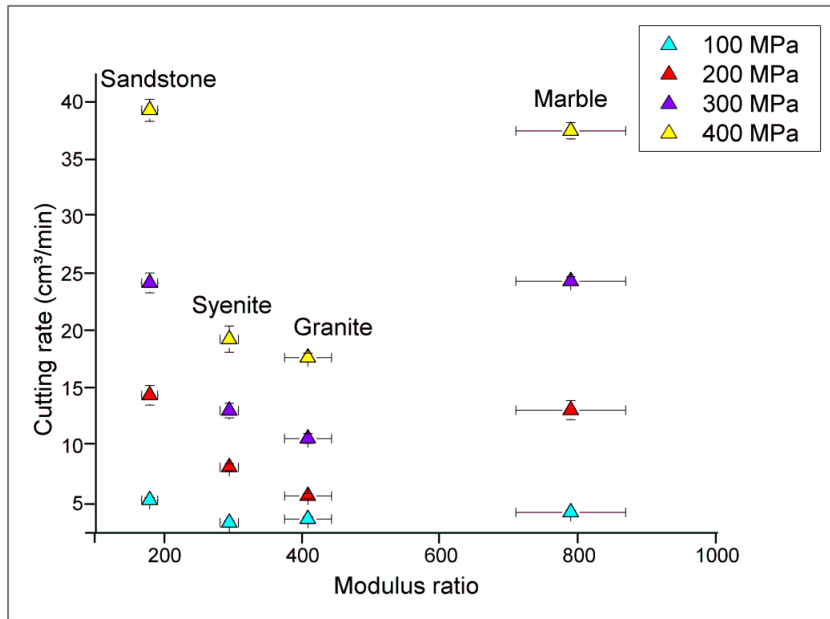


Figure 112 – Cutting rate (mm³/s) versus the modulus ratio for varying pump pressure. The dots from the same vertical line correspond to the same rock type.

6. CONCLUSIONS

The present study sought to contribute with the development of the knowledge in the field of AWJ applied to rock cutting. The study of complex materials requires detailed analysis of both qualitative and quantitative data. Thus, the effect of AWJ on rock cutting was investigated qualitatively through SEM and petrography analyses and quantitatively by means of cutting tests with the determination of the removed volume of rocks, cutting rates and energy-based parameters of both the jet and the rock.

- *Conclusions regarding the qualitative analysis*

Based on thin-section analysis, it was observed that the rock characteristics exert great influence on the shape of the kerfs. While syenite and granite have a tendency to taper from the top to the bottom as a V-shape profile, marble has the straightest kerf profile and sandstone has the narrowest one, starting narrower at the top, getting larger gradually until the top of the pocket (i.e. the larger portion of the kerf at its bottom). Thus, the rocks with larger resistance to AWJ erosion, i.e. syenite and granite, present a V-shape profile, while marble and sandstone present a straight to conical shape. Concerning the shape of the pockets, they are similar in all rock types.

For all of the rocks except the marble, microcracking related to the erosion of the walls of the kerf is restricted to a very limited area surrounding it. In the case of the marble, cracks propagate a slightly more, because the impact of the AWJ leads to the activation of calcite cleavages.

In relation to the SEM analyses, erosive fracturing (i.e. abrasion fatigue) is the process which predominates in syenite and granite cutting. In the case of marble, abrasion fatigue and fractures along cleavage planes predominate. Finally, in sandstone the conchoidal fracturing is the leading process.

- *Conclusions regarding the influence of traverse velocity and pump pressure on AWJ rock cutting*

It was observed that the traverse velocity exerts great influence on the efficiency of cutting. From the results, it is observed that an optimum point of cutting efficiency exists close to 200 mm/min. Below the optimum point, the efficiency is disturbed by large losses mainly due to effects of damping, which is caused by the accumulation of water and abrasive material inside the kerf. Above the optimum point, damping effects decrease substantially, however the efficiency also decreases because the nozzle passes too fast through the rock surface.

The pump pressure also greatly influences the efficiency of cutting. For all studied rocks, the removed volume of rock increases with an increase in pump pressure. The less steep gradient between the removed volume of rock and the pump pressure reflects the higher resistance to disaggregation of those rocks and the steeper gradient reflects, consequently, the lower resistance to disaggregation of the non-crystalline rocks. As second degree polynomial equations were adopted for the relationship between the removed volume of rock and the pump pressure, it is not possible to extrapolate data under 100 MPa in order to obtain threshold pressures. More tests are needed between 0 and 100 MPa to refine the fitted curves and obtain more accurate data.

Except for the granite results, all the other rocks tested present good correlations between pump pressure and the specific energy of cutting. Good correlations are also observed between pump pressure and the kerf generation energy. In the case of relative kerf generation energy, correlations were good when considering the specific energy of the rocks, but not their destruction work values.

Regarding the relationship between cutting rate and specific energy of cutting as a measure of cutting performance, it was observed that the minimum expenditure of total energy associated with the maximum cutting rates occurs when cutting the studied rocks with a traverse velocity of 200 mm/min and a pump pressure of 400 MPa.

The specific destruction work (W_R) of the syenite corresponds to 36,3% of its specific energy (SE_R), while for the granite this value is 46,2%. It is known that sandstone is the most

brittle rock of all rocks studied, thus a value of 30% could be assumed for this rock. For this condition, the relative kerf generation energy (E_{KRW}) for the sandstone would be practically the same presented by that of the syenite. Thus, some considerations can be made when analyzing the relationship between the traverse velocity and both kerf generation energy (E_K) and relative kerf generation energy (E_{KR}). The trends presented by these relationships are similar, but when the destruction work (W_R) is taken into account the range of energy between the rocks decreases considerably. In general, it is observed that both E_K and E_{KR} tend to increase following the order: marble, granite, syenite and sandstone (in the latter case, considering a destruction work equal to 30% of its specific energy). Thus, based on the observation of the behavior of these rocks and their modulus ratio values, it can be concluded that the energy transfer from the AWJ machine to the effective cutting process increases with an increase in rock brittleness.

Still regarding correlations with traverse velocity, the removed volume of rock (V_R) specific energy of cutting (SE_C) values are very similar for marble and sandstone. However, marble presents the lowest kerf generation energy (E_K) and relative kerf generation energy (E_{KR} and E_{KRW}) while sandstone presents the highest values of both parameters. Thus, although the energy transfer is better for the most brittle rock, i.e. the sandstone, the energy provided by the AWJ machine to cut a certain volume of rock is similar for both rocks, implying a similar cost of production.

Regarding pump pressure correlations, the removed volume of rock (V_R) is similar for both the marble and the sandstone, and for the syenite and the granite. In the case of the specific energy of cutting (SE_C) the marble and the sandstone present similar values at higher pressure values and deviate at lower values. The syenite and the granite present very different trends. When analyzing the relationship between the kerf generation energy (E_K) and the pump pressure, E_K increases following the order marble, granite, syenite and sandstone. When the destruction work (W_R) is taken into account, the range of energy values decrease between the rocks, as observed in the case of the traverse velocity analysis. However, in the case of pump pressure analysis the range is shorter. The marble and the granite present similar values and the syenite present higher values. If a destruction work (W_R) of 30% from the specific energy (SE_R) of the sandstone was adopted, its E_K values would be a little higher than the syenite E_K values.

The relationship between the relative kerf generation energy (E_{KR}) and the pump pressure shows an increase in energy with an increase in pump pressure. In addition, energy tends to increase following the order marble, granite, syenite and sandstone. Therefore, the energy transfer is better in the less brittle rocks. However, when the destruction work (W_R) is considered, the marble and the granite present similar energy values while the syenite present higher values. If the destruction work (W_R) of the sandstone was considered, its energy values would be a little higher than the syenite energy values.

Even with a better transfer of energy from the AWJ machine to the effective cutting process for the sandstone and syenite, the specific energy of cutting (SE_C) is lower and the removed volume of rock (V_R) is higher for the sandstone and the marble. Thus, the cost of production is lower for the last two rocks.

- *Conclusions regarding correlations between the relative kerf generation energy and rock properties*

Most of the rock properties investigated did not provide good correlations with the relative kerf generation energy. Most of them presented deviations concerning the results of the marble or the sandstone, the rocks which have, respectively, the more ductile and the more brittle behavior. Regarding the physical properties, none presented a best correlation with relative kerf generation energy. The trend indicates that relative kerf generation energy increases with a decrease in dry density for all rocks. Thus, the energy transfer from the machine to the cutting process is better when the dry density is low.

Among the usual mechanical rock properties, the tensile strength presented the best correlation with the relative kerf generation energy (E_{KR}). A general trend is observed in which the relative kerf generation energy increases with an increase in tensile strength. However, the correlation considering just the crystalline rocks is more consistent, because the sandstone presents a deviation from the general trend. The same correlation with the relative kerf generation energy based on the specific destruction work was good concerning the tests with traverse velocity variation, but poorer regarding the tests with pump pressure variation.

The best correlation was achieved with the modulus ratio, which is defined as the ratio between the Young's modulus and the uniaxial compressive strength. The modulus ratio is an interesting rock property since it considers both strength and deformation behaviors, serving as a good measure of brittleness. However, the property also presents limitations.

The modulus ratio values of the rocks studied are closely related to their behavior and to "how they look like" under uniaxial compression. The marble presents the highest modulus ratio value and is the most ductile of the rocks studied. It is the only rock studied which presents class I behavior under compression. The modulus ratio values decrease and the brittleness increase following the order marble, granite, syenite and sandstone. As previously noted, the marble presents class I behavior while the granite, syenite and sandstone present class II behavior. In addition, the granite presents the "least class II behavior" while the sandstone presents the "highest class II behavior".

The modulus ratio presented good correlations concerning the AWJ cutting parameters which are related to the effective energy applied to rock cutting. In the case of removed rock volume, specific energy of cutting and cutting rate presented a good correlation with Young's modulus and shear modulus, although no significant physical relevance was observed.

- *Suggestions for future work*

The present thesis has demonstrated that much progress is still to come in the field of AWJ applied to rock cutting, since the study of complex materials requires great effort and thoroughness. The main limitation of the conducted research was to work with an AWJ machine which does not belong to the university. Thus, it was not possible to make modifications to it nor work beyond the controlled conditions established by the company.

Suggestions for further investigations are as follows:

- Work with an AWJ machine which can be modified, so that the efficiency coefficient and the momentum transfer coefficient may be determined experimentally and precisely for a broad range of cutting conditions;

- Work with a wider variety of rocks, trying to embrace rocks also with wide ranges of modulus ratio and specific destruction work values;
- Perform a detailed SEM analysis of various types of rocks contemplating images from the top to the bottom of the kerfs, so that the erosion and cracking mechanisms may be compared between different types of rocks;
- Try to correlate the mechanisms observed through detailed SEM analysis and the total energy provided by the machine and the effective energy spent in cutting;
- Perform a detailed petrographic analysis of the shape of the kerfs regarding distinct types of rocks and variations of traverse velocity, pump pressure and abrasive mass rate.

REFERENCES

- ACHESON, W.; GARDNER, G. H. .; MESSMER, J. H. **Hydraulic Jet Drill Bit**, 1971.
- AGUS, M.; BORTOLUSSI , A.; CICCUCI, R.; MANCA, P.P.; MASSACCI, G; BOSU, M. Jet Impingement Tests on Mineral Crystals. **First Asian Conference on Recent Advances in Jetting Technology**, 1991.
- ALI, Y.; WANG, J. **Impact abrasive machining**. In: JACKSON, M. J.; DAVIM, J. P. (Eds.). **Machining with Abrasives**.p. 385–419, 2011.
- ALTINDAG, R. The evaluation of rock brittleness concept on rotary blast hole drills. **The Journal of the South African Institute of Mining and Metallurgy**, January/February, p. 61–66, 2002.
- ALVAREZ, H. I. P. **Ensaio Não Convencionais Para Determinação da Tenacidade à Fratura em Rochas: Análise E Comparação**. Dissertação (Mestrado), Escola de Engenharia de São Carlos, Universidade de São Paulo, 2004.
- ASSOCIAÇÃO BRASILEIRA DE NORMAS TÉCNICAS (ABNT), NBR 7181: **Solo – Análise Granulométrica – Método de ensaio**, 1984.
- ASSOCIAÇÃO BRASILEIRA DE NORMAS TÉCNICAS (ABNT), NBR 12042: **Materiais inorgânicos – Determinação do Desgaste por Abrasão**, 2012.
- ASSOCIAÇÃO BRASILEIRA DE NORMAS TÉCNICAS (ABNT), NBR 15845-2: **Rochas para revestimento - Parte 2: Determinação da Densidade Aparente, Porosidade Aparente e Absorção d'água – Métodos de Ensaio**, 2015.
- ASTM D7012-14: **Standard Test Methods for Compressive Strength and Elastic Moduli of Intact Rock Core Specimens under Varying States of Stress and Temperatures**. ASTM International, West Conshohocken, PA, 2014.
- ATICI, U.; ERSOY, A. Correlation of specific energy of cutting saws and drilling bits with rock brittleness and destruction energy. **Journal of Materials Processing Technology**, v. 209, n. 5, p. 2602–2612, 2009.
- AYDIN, G.; KARAKURT, I.; AYDINER, K. Performance of Abrasive Waterjet in Granite Cutting: Influence of the Textural Properties. **Journal of Materials in Civil engineering**, v. 24, n. 7, p. 944–949, 2012.
- AYDIN, G.; KARAKURT, I.; AYDINER, K. Prediction of the cut depth of granitic rocks machined by abrasive waterjet (AWJ). **Rock Mechanics and Rock Engineering**, v. 46, n. 5, p. 1223–1235, 2013.
- BABU, M. K.; CHETTY, O. V. K. A study on recycling of abrasives in abrasive water jet machining. **International Journal of Advanced Manufacturing Technology**, v. 19, n. 697, p. 697–703, 2002.
- BADGUJAR, P. P.; RATHI, M. G. Analysis Of Surface Roughness In Abrasive Waterjet Cutting Of Stainless Steel. **International Journal of Engineering Research & Technology**,

v. 3, n. 6, p. 209–212, 2014.

BAUMANN, L.; HENNEKE, J. Attempt of Technical-Economical Optimization of High Pressure Jet Assistance for Tunnelling Machines. **5th International Symposium on Jet Cutting Technology**, p. 119–140, 1980.

BONGE, M. J.; WANG, F. D. Advanced Applications of Water Jets to Small Hole Drilling. **1st U.S. Water Jet Symposium**. p. III-3.1–III-3.14, 1981.

BORTOLUSSI, A; CICCUCI, R.; MANCE, P.P.; MASSACCI, G. Prospects of Water Jet Technology in Granite Quarrying. **13th World Mining Congress**, p.149-159, 1987.

BORTOLUSSI, A.; YAZICI, S.; SUMMERS, D. A. The use of waterjets in cutting granite. **9th International Symposium on Jet Cutting Technology**, Paper E3, 15 p., 1988.

BRADY, B.; BROWN, E. **Rock mechanics for underground mining**. Third edit ed. [s.l.] Kluwer Academic Publishers, 645 p., 2004.

BUDINSKI, K. G. **Friction, Wear, and Erosion Atlas**. [s.l.] Taylor & Francis Group, 310 p., 1998.

CARRINO, L. et al. AWJ to machine free form profiles in natural stone. **WJTA American Waterjet Conference**, p. 309-327, 2001.

CHALMERS, E. J. Pressure Fluctuation and Operating Efficiency of Intensifier Pumps. **7th WJTA American Waterjet Conference**, 327-336. 1993.

CHAO, J.; GESKIN, E. S. Experimental study of the striation formation and spectral analysis of the abrasive generated surfaces. **Seventh American Waterjet Conference**, p. 27-41, 1993.

CICCUCI, R.; GROSSO, B. Improvement of Disc Cutter Performance by Water Jet Assistance. **Rock Mechanics and Rock Engineering**, v. 47, p. 733–744, 2014.

COPUR, H. et al. A set of indices based on indentation tests for assessment of rock cutting performance and rock properties. **The Journal of the South African Institute of Mining and Metallurgy**, n. November, p. 589–600, 2003.

CORTÉS, G. R. M. **Métodos de cortes de rochas com jato de água abrasivo**. Tese (Doutorado), Escola Politécnica, Universidade de São Paulo, São Paulo, 132 p., 2003.

CORTÉS, G. R. M. et al. Waterjet Researches at São Paulo University: Part 4 Dimension Stone Exploitation with High-Pressure Waterjets. **WJTA American Waterjet Conference**, 194 - 202, 2003.

CROW, S. C. A theory of hydraulic rock cutting. **International Journal of Rock Mechanics and Mining Sciences & Geomechanics Abstracts**, v. 10, p. 567–584, 1973.

CROW, S. C. The Effect of Porosity on Hydraulic Rock Cutting. **International Journal of Rock Mechanics and Mining Science and Geomechanics Abstracts**, v. 11, p. 103–105, 1974.

DONOVAN, J. G.; KARFAKIS, M. G. Adaptation of a simple wedge test for the rapid determination of mode I fracture toughness and the assessment of relative fracture resistance. **International Journal of Rock Mechanics and Mining Sciences**, v. 41, n. 4, p. 695–701,

2004.

EL-DOMIATY, A. A. et al. On the Modelling of Abrasive Waterjet Cutting. **Advanced Manufacturing Technology**, v. 12, p. 255–265, 1996.

ENGIN, I. C. A correlation for predicting the abrasive water jet cutting depth for natural stones. **South African Journal of Science**, v. 108, n. 9–10, p. 1–11, 2012.

FAIRHURST, R. M.; HERON, R. A.; SAUNDERS, D. H. Diajet™—A New Abrasive Waterjet Cutting Technique. **8th International Symposium on Jet Cutting Technology**, p. 395-402, 1986.

FARMER, I. W.; ATTEWELL, P. B. Rock Penetration by High Velocity Water Jet. **International Journal of Rock Mechanics and Mining Sciences**, v. 2, p. 135–153, 1964.

FENN, O.; PROTHEROE, B. E.; JOUGHIN, N. C. Enhancement of roller cutting by means of water jets. **7th Rapid Excavation and Tunneling Conference**, p. 341-356, 1985.

FINNIE, I. Some Reflections on the Past and Future of Erosion. **Wear**, v. 186–187, p. 1–10, 1995.

FRAZÃO, E. B. **Tecnologia de Rochas na Construção Civil**. Associação Brasileira de Geologia de Engenharia Ambiental, 132 p., 2002.

FUENKAJORN, K.; KENKHUNTHOD, N. Influence of Loading Rate on Deformability and Compressive Strength of Three Thai Sandstones. **Geotechnical and Geological Engineering**, v. 28, n. 5, p. 707–715, 2010.

GÄRDEK, H.; BOUBKER, O. **A State of the Art Report and Comparison with Conventional Methods of Abrasive Waterjet Machining Technology**, 32 p., 2015.

GERCEK, H. Poisson's ratio values for rocks. **International Journal of Rock Mechanics and Mining Sciences**, v. 44, n. 1, p. 1–13, 2007.

GOKTAN, R. M.; YILMAZ, N. G. A new methodology for the analysis of the relationship between rock brittleness index and drag pick cutting efficiency. **The Journal of The South African Institute of Mining and Metallurgy**, v. 105, n. 10, p. 727, 2005.

HACKSPACHER, P.C.; FETTER, A.H.; EBERT, H.D.; JANASI, V.A.; OLIVEIRA, M.A.F.; BRAGA, I.F.; NEGRI F.A. Magmatismo há ca. 660-640 M.a. no Domínio Socorro: Registros de Convergência Pré-Colisional na Aglutinação do Gondwana Ocidental. **Revista do Instituto de Geociências - USP**. Série científica, 3:85-96, 2003.

HAGAN, P. C. The cuttability of rock using a high pressure water jet. **Western Australian Conference on Mining Geomechanics**, p. 1-12, 1992.

HARRIS, H. D.; MELLOR, M. Cutting Rock with Water Jets. **International Journal of Rock Mechanics and Mining Science and Geomechanics Abstracts**, v. 11, p. 343–358, 1974.

HASHISH, M. Visualization of the abrasive-waterjet cutting process. **Experimental Mechanics**, v. 28, n. 2, p. 159–169, 1988.

HASHISH, M. A. **Method and Apparatus for Forming a High Velocity Liquid Abrasive**

Jet, 1987.

HASHISH, M. A. On the modelling of surface waviness produced by abrasive waterjets. In: LICHTAROWICZ, A. (Ed.). . **Jet Cutting Technology**, p. 17–34, 1992.

HEILBRON, M.; MACHADO, N. Timing of terrane accretion in the Neoproterozoic-Eopaleozoic Ribeira Orogen (SE Brazil). **Precambrian Research**, v.125, p.87-112, 2003.

HOOD, M. et al. An Advanced System for Rock Tunnelling—Results from a Field Experiment. **6th American Water Jet Conference**, p. 63-70, 1991.

HOSHINO, K.; NAGANO, T.; TAKAGI, K. Rock Cutting and Breaking using high speed waterjets together with a TBM cutter. **2nd International Symposium on Jet Cutting Technology**, p. E3-19–E3-29, 1974.

HUCKA, V.; DAS, B. Brittleness determination of rocks by different methods. **International Journal of Rock Mechanics and Mining Sciences & Geomechanics Abstracts**, v. 11, n. 10, p. 389–392, 1974.

HUDSON, J. A.; HARRISON, J. P. **Engineering Rock Mechanics: An Introduction to the Principles**. [s.l.] Pergamon, 444 p., 1997.

HURLBURT, G. H.; CROW, S. C.; LADE, P. V. Experiments in hydraulic rock cutting. **International Journal of Rock Mechanics and Mining Sciences & Geomechanics Abstracts**, v. 12, p. 203–212, 1975.

INTERNATIONAL SOCIETY OF ROCK MECHANICS (ISRM). Suggested methods for determining tensile strength of rock materials. **International Journal of Rock Mechanics and Mining Sciences & Geomechanics Abstracts**, v.15, n.3, p.99-103, 1978a.

INTERNATIONAL SOCIETY FOR ROCK MECHANICS (ISRM). Suggested Method for Determination of the Schmidt Rebound Hardness; 1978b.

INTERNATIONAL SOCIETY OF ROCK MECHANICS (ISRM). Suggested methods for determining the uniaxial compressive strength and deformability of rock materials. **International Journal of Rock Mechanics and Mining Sciences & Geomechanics Abstracts**, v.16, n.2, p.135-140, 1979

INTERNATIONAL SOCIETY OF ROCK MECHANICS (ISRM). Suggested methods for determining the fracture toughness of rock. **International Journal of Rock Mechanics and Mining Sciences**, v.25, p.71-96, 1988.

INTERNATIONAL SOCIETY OF ROCK MECHANICS (ISRM). Suggested methods for determining mode I fracture toughness using cracked chevron notched brazilian disc (CCNBD) specimens. **International Journal of Rock Mechanics and Mining Sciences**, v.32, p.57-64, 1995.

JOHNSTON, C. E. Effect of Water Quality on the WaternifeTM. [s.l: s.n.], **Water-Resources Investigations Report 88-4200**, 63 p., 1986

KAHRAMAN, S. Correlation of TBM and drilling machine performances with rock brittleness. **Engineering Geology**, v. 65, n. 4, p. 269–283, 2002.

- KAHRAMAN, S. Performance analysis of drilling machines using rock modulus ratio. **Journal of the South African Institute of Mining and Metallurgy**, n. October, p. 515–522, 2003.
- KOLAHAN, F.; KHAJAVI, A. H. Modeling and Optimization of Abrasive Waterjet Parameters using Regression Analysis. **World Academy of Science, Engineering and Technology**, v. 59, p. 488–493, 2009.
- KOLLÉ, J. **A Comparison of Water Jet , Abrasive Jet and Rotary Diamond Drilling in Hard Rock, Tempress Technologies Inc.** [s.l: s.n.], p. 1-8, 1999.
- KOUZMICH, I. A.; MERZLIAKOV, V. G. Coal Massif Breakage with Disc Cutter and High Speed Water Jet. **8th International Symposium on Jet Cutting Technology**, p. 147-155, 1986.
- KOVACEVIC, R. et al. State of the Art of Research and Development in Abrasive Waterjet Machining. **Journal of Manufacturing Science and Engineering**, v. 119, p. 776–785, 1997.
- KRANZ, R. L. MICROCRACKS IN ROCKS : A REVIEW. **Tectonophysics**, v. 100, p. 449–480, 1983.
- KULEKCI, M. K. Processes and apparatus developments in industrial waterjet applications. **International Journal of Machine Tools and Manufacture**, v. 42, p. 1297–1306, 2002.
- LAUAND, C. T. MARTÍN, C. G. R.; HENNIES, W. T.; AGUS, M. Performance of Abrasive Waterjet in Granite Cutting: Influence of the Textural Properties. **WJTA American Waterjet Conference**, p. 427-449, 2001.
- LEACH, S. J.; WALKER, G. L. The Application of High Speed Liquid Jets to Cutting. **Philosophical Transactions of the Royal Society of London**, p. 295–310, 1965.
- MAROS, Z. Energy Approach of the Taper At Abrasive. **Production Processes and Systems**, v. 6, n. 1, p. 89–96, 2013.
- MARTIN, C. D. The effect of cohesion loss and stress path on brittle rock strength. **Canadian Geotechnical Journal**, v.34, n.5, p. 698-725, 1997.
- MCMILLAN, E. R. Hydraulic jet mining shows potential as new tool for coal men. **Mining Engineering**, v. 14, n. 6, p. 41–45, 1962.
- MILANI, E. J. et al. Bacia do Paraná. **Boletim de Geociências da Petrobras**, v. 15, n. 2, p. 265–287, 1994.
- MIRANDA, R. M. et al. Abrasive Water Jet Cutting of Portuguese Marbles,. **7th American Water Jet Conference**, p. 443-458, 1993.
- MIRANDA, R. M.; KIM, T. J. Abrasive waterjet cutting of marble and calcareous stones : a phenomenological study. **13th International Symposium on Jet Cutting Technology**, p. 415-424, 1996.
- MOMBER, A. W. A Generalized Abrasive Water Jet Cutting Model. **Proceedings of the 8th American Water Jet Conference**, v.1, n.5, p. 359-371, 1995.
- MOMBER, A. W. Stress–strain relation for water-driven particle erosion of quasi-brittle

- materials. **Theoretical and Applied Fracture Mechanics**, v. 35, n. 1, p. 19–37, 2001.
- MOMBER, A. W. An SEM-study of high-speed hydrodynamic erosion of cementitious composites. **Composites Part B: Engineering**, v. 34, p. 135–142, 2003.
- MOMBER, A. W. Wear of rocks by water flow. **International Journal of Rock Mechanics and Mining Sciences**, v. 41, p. 51–68, 2004.
- MOMBER, A. W.; KOVACEVIC, R. Test parameter analysis in abrasive water jet cutting of rocklike materials. **International Journal of Rock Mechanics and Mining Sciences**, v. 34, n. 1, p. 17–25, 1997.
- MOMBER, A. W.; KOVACEVIC, R. **Principles of Abrasive Water Jet Machining**. [s.l.] Springer, 418 p., 1998.
- MOMBER, A. W.; KOVACEVIC, R. An energy balance of high-speed abrasive water jet erosion. **Proceedings of the Institution of Mechanical Engineers, Part J: Journal of Engineering Tribology**, v. 213, p. 463–472, 1999.
- MOMBER, A. W.; MOHAN, R. S.; KOVACEVIC, R. On-line analysis of hydro-abrasive erosion of pre-cracked materials by acoustic emission. **Theoretical and Applied Fracture Mechanics**, v. 31, n. 1, p. 1–17, 1999.
- OH, T. M.; CHO, G. C. Rock Cutting Depth Model Based on Kinetic Energy of Abrasive Waterjet. **Rock Mechanics and Rock Engineering**, v. 49, n. 3, p. 14, 2016.
- OHADI, M. M.; ANSARI, A. I.; HASHISH, M. Thermal Energy Distribution in the Workpiece During Cutting with an Abrasive Waterjet. **ASME Journal of Engineering for Industry**, v. 114, p. 67–73, 1992.
- OHMAN, J. L. Abrasives: their characteristics and effect on waterjet cutting. **Proceedings of the 7th American WaterJet conference**, p. 363-374, 1993.
- RABINOWICZ, E.; TANNER, R. I. Friction and Wear of Materials. **Journal of Applied Mechanics**, v. 33, n. 2, p. 479, 1995.
- RAETHER, R. J.; ROBINSON, R. G.; SUMMERS, D. A. Use of High Pressure Water Jets for Cutting Granite. **2nd US Water Jet Conference**, p. 203-209, 1983.
- RAJU, S. P.; RAMULU, M. Predicting Hydro-Abrasive Erosive Wear During Abrasive Waterjet Cutting: Part II-Experimental Study and Model Verification. **Manufacturing Science and Engineering**, v. 68, p. 339–351, 1994.
- REHBINDER, G. Slot cutting in rock with a high speed water jet. **International Journal of Rock Mechanics and Mining Science**, v. 14, p. 229–234, 1977.
- REHBINDER, G. A theory about cutting rock with a water jet. **Rock Mechanics**, v. 12, n. 3–4, p. 247–257, 1980.
- RESTNER, U.; PLINNINGER, R. J. Rock mechanical aspects of roadheader excavation. **EUROCK 2015 & 64th Geomechanics Colloquium**, p. 249-254, 2015.
- RODRÍGUEZ, P.; ARAB, P. B.; CELESTINO, T. B. Characterization of rock cracking patterns in diametral compression tests by acoustic emission and petrographic analysis.

International Journal of Rock Mechanics and Mining Sciences, v. 83, p. 73–85, 2016.

ROUSE, H.; HOWE, J. W.; METZLER, D. E. Experimental Investigation of Fire Monitors and Nozzles. **Transactions of the American Society of Civil Engineers**, v. 117, n. 1, p. 1147–1175, 1952.

SAVANICK, G. A. **Borehole Mining Of Deep Phosphate Ore In St . Johns County , Florida**. SME Preprint 83–104, Annual Meeting, p. 83-104, 1983.

SILVA, A.T.S.F.; CHIODI FILHO, C.; CHIODI, D.K.; PINTO FILHO, W.D. Projeto Santos Iguape. Geologia. Convênio DNPM-CPRM, v.1, 639p.,1977.

SCHMIDT, R. A. Fracture-toughness testing of limestone. **Experimental Mechanics**, v. 16, n. 5, p. 161–167, 1976.

SHAVLOVSKII, S. Hydrodynamics of High Pressure Fine Continuous Jets. **1st International Symposium on Jet Cutting Technology**, paper A6, p.81-92, 1972.

SIMMONS, G.; RICHTER, D. Microcracks in rock. In: **The Physics and Chemistry of Minerals and Rocks**. [s.l: s.n.]. p. 105–137, 1976.

SINGH, P. J.; BENSON, D. Development of Phased Intensifier for Waterjet Cutting. In: LICHTAROWICZ, A. (Ed.). . **Jetcutting Technology**. [s.l.] Kluwer Academic Publishers, 1992. p. 305–318.

SUMMERS, D. A. **Water Jet Cutting Related to Jet & Rock Properties**. [s.l: s.n.], 13 p., 1972.

SUMMERS, D. A.; MAZURKIEWICZ, M.; BUSHNELL, D. J.; BLAINE, J. **Method and Apparatus for Water Jet Drilling of Rock**, 6 p. 1978.

SUMMERS, D. A. **Waterjetting Technology**. First Edit ed. [s.l.] Chapman & Hall, 624 p., 1995.

SUNDAE, L.; CANTRELL, B. K. Breakthrough in Roof Bolt Drill Technology Provides 200 to 600 times greater Bit Life. **4th Conference on Ground Control in Midwestern U.S. Coal Mines**, p. 291-313, 1992.

SUSUZLU, T.; HOOGSTRATE, A. M.; KARPUSCHEWSKI, B. Initial research on the ultra-high pressure waterjet up to 700 MPa. **Journal of Materials Processing Technology**, v. 149, n. 2004, p. 30–36, 2004.

TAPPONNIER, P.; BRACE, W. F. Development of stress-induced microcracks in Westerly Granite. **International Journal of Rock Mechanics and Mining Sciences and**, v. 13, n. 4, p. 103–112, 1976.

TAZIBT, A.; PARSY, F.; ABRIAK, N. Theoretical analysis of the particle acceleration process in abrasive water jet cutting. **Computational Materials Science**, v. 5, n. 1–3, p. 243–254, 1996.

THURO, K.; PLINNINGER, R. J. Roadheader excavation performance - geological and geotechnical influences Le progrès des machines de percement - influences géologiques et géotechniques **Vortriebsleistung von Teilschnittmaschinen - geologische und geotechnische Einflußgrößen Excavation** p. p. 1241–1244, 1999.

THURO, K.; SPAUN, G. Introducing the “destruction work” as a new rock property of toughness referring to drillability in conventional drill- and blast tunnelling. **Eurock 1996**, p. 707-713, 1996.

VASEK, J. et al. Influence of properties of garnet on cutting process. **Proceedings of the 7th American WaterJet Conference**, p.375-387, 1993.

VIE, G. G. Cutting Hard Rock With Abrasive-Entrained Waterjet at Moderate Pressures. **Proceedings of the Second U.S. Water Jet Conference**, p. 407-420, 1983.

VOITSEKHOVSKY, B. **Jet Nozzle For Obtaining High Pulse Dynamic Pressure Heads**, 3 p., 1967.

VOS, K.; VANDENBERGHE, N.; ELSSEN, J. Surface textural analysis of quartz grains by scanning electron microscopy (SEM): From sample preparation to environmental interpretation. **Earth-Science Reviews**, v. 128, p. 93–104, 2014.

WAWERSIK, W. R.; FAIRHURST, C. A study of brittle rock fracture in laboratory compression experiments. **International Journal of Rock Mechanics and Mining Sciences and**, v. 7, n. 5, p. 561–575, 1970.

WEBSTER, P.; JOHNS, S. The Space Needle Gets a Shower : Kärcher Cleans Seattle ' s Famous Landmark. **WJTA Jet News**, n. August, p. 28, 2008.

WILKINS, C. Waterjet Cutting : the other non-traditional process. **EDM Today**, p. 11–16, 2003.

WILSON, J. W.; SUMMERS, D. A.; GERTSCH, R. E. The development of waterjets for rock excavation. **4th International Symposium on Mine Mechanisation and Automation**, 10 p., 1997.

WYATT, P.; PETERSON, M. Development of Water Jet Cutting in Extremely Hard Granite. **9th American Waterjet Conference**, p. 485-496, 1997.

YARALI, O.; SOYER, E. The effect of mechanical rock properties and brittleness on drillability. **Scientific Research and Essays**, v. 6, n. 5, p. 1077–1088, 2011.

ZENG, J.; KIM, T. J. Development of an abrasive waterjet kerf cutting model for brittle materials. In: LICHTAROWICZ, A. (Ed.). **Jet Cutting Technology**. [s.l: s.n.]. p. 483–501, 1992.